

**POROELASTIC AND SEISMIC CHARACTERIZATION OF
HETEROGENEOUS RESERVOIR ROCKS**

A Dissertation Presented to
the Faculty of the Department of Earth and Atmospheric Sciences
University of Houston

In Partial Fulfillment
of the Requirements for the Degree
Doctor of Philosophy

By
Luanxiao Zhao
May 2014

**POROELASTIC AND SEISMIC CHARACTERIZATION OF
HETEROGENEOUS RESERVOIR ROCKS**

Luanxiao Zhao

APPROVED:

Dr. De-hua Han, Chairman

Dr. Robert Stewart, Co-Chairman

Dr. John Castagna

Dr. Mosab Nasser

**Dean, College of Natural
Sciences and Mathematics**

ACKNOWLEDGEMENTS

The journey to get a Ph.D. degree from University of Houston has been the most exciting and enriching experience for me. I am indebted to all the people who have made this possible.

First and foremost, I would like to extend my deepest gratitude to my advisor, Dr. De-hua Han, for his guidance, constructive criticism, and encouragements. He taught me to approach scientific investigations with critical eye, consider all the theoretical work geologically meaningful, and always look for simple and lasting insights. I would also like to thank my doctoral committee members, Dr. Robert Stewart, Dr. John Castagna, and Dr. Mosab Nasser for their constructive comments and excellent suggestions. Special thanks also go to Dr. Leon Thomsen for the illumination discussions on the topics of effective medium theories and poroelasticity.

I thank Dr. Qiuliang Yao for his physical insights, brilliant ideas, and advices on many of the technical details. Endless scientific discussions with him have always been a great source of scientific inspiration for me. I also thank my colleagues and friends for their support: Fuyong Yan, Min Sun, Huizhu Zhao, Rui Zhou, Lun Li, Ayato Kato, Tommy Ringo, Hui Li, Xuan Qin, Hemin Yuan, Zhiwei Qian, Malleswara Yenugu, Qi Huang, Anna Khadeeva, Kirstie Haynie, and many others.

I would like to thank Fluids/DHI consortium and its sponsors for financial support. I acknowledge Maersk oil for a wonderful summer time and their permission to use the dataset from Campos Basin, offshore Brazil. I also thank Michael Matheney, Enru Liu, Xin Zhan, and Tetyana Vdovina for the fruitful summer with ExxonMobil Upstream

Research Company. I also benefited from many discussions and an exciting summer time working with Elizabeth L'Heureux, Hans Sugianto, Zhiyong Jiang, Brain Hornby, and Rosemarie Geetan in Reservoir Geophysics Group of BP.

I thank FC Barcelona and Lionel Messi for their amazing and virtuoso performances in the numerous football games. Without the joy and beauty they bring to me, the past four years would be a lot less fun. I am indebted to my parents and my sisters for their support and encouragement during all the easy and tough time of my life. Finally, I would like to thank my girlfriend, Ling, for her love, support, patience, and four years' lonely time in China.

**POROELASTIC AND SEISMIC CHARACTERIZATION OF
HETEROGENEOUS RESERVOIR ROCKS**

A Dissertation Presented to
the Faculty of the Department of Earth and Atmospheric Sciences
University of Houston

In Partial Fulfillment
of the Requirements for the Degree
Doctor of Philosophy

By
Luanxiao Zhao
May 2014

ABSTRACT

The primary focus of this dissertation is to link the poroelastic model that couples rock's elastic and hydraulic properties to seismic characterization of the heterogeneous reservoirs.

I have presented how to incorporate the dynamic poroelastic responses of microscopic and mesoscopic flow into the classical Biot theory. The resulting effective Biot media can capture the characteristics of velocity dispersion and wave attenuation in heterogeneous media. On the basis of this effective Biot media, I developed an approach to quantify the impact of both global flow and local flow simultaneously on the signatures of seismic reflectivity. The computed poroelastic reflections not only depend on the elastic properties contrast and incident angle, but also rely on the fluid mobility and observational frequency. For a typical shale-sand reflector, we find that the effect of local flow causes reflection amplitude variations in frequency to be as high as 40%, and a maximum phase shift as high as 12 degrees at the seismic exploration frequency band. However, the global flow effect on reflectivity is almost trivial ($<1.5\%$) and occurs mainly at ultrasonic frequency band.

Poroelastic seismic analysis shows that ignoring the dispersion behavior of seismic reflection can lead to inaccurate seismic imaging and misleading interpretation of reservoir properties. I further demonstrate that the AVO response at the interface is strongly impacted by the reflection dispersion behavior: the bright spot (Class III AVO) gets brighter at lower frequency, the dim spot (Class I AVO) gets dimmer at lower frequency, and the Class II AVO reservoir exhibits significant phase distortion

in the frequency domain. It is found that, for certain permeability ranges (about 2 orders of magnitude), seismic amplitude can exhibit an almost linear relationship with permeability variation. For Class III AVO reservoir scenario, high fluid mobility zones usually enhance the seismic amplitude; while for Class I AVO reservoir scenario, high fluid mobility zones weaken the seismic amplitude.

Finally, a field case study on the Offshore Brazil data set shows that poroelastic reflection from the interface of underlain carbonate with overburden marlstone exhibits considerably different frequency behavior at two nearby wells. Based on the poroelastic modeling, this discrepancy is likely to be caused by the fact that the fluid mobility in the underlain grainstone at well A is remarkably greater than that in the underlain packstone at well B.

CONTENTS

1. Introduction.....	1
1.1. Porous Media and Poroelasticity	1
1.2. Heterogeneity and Scales	3
1.3. Heterogeneity and Seismic Properties.....	4
1.3.1. Effective Medium Approximation	6
1.3.2. Wave-induced Fluid Flow	8
1.3.3. Effects of Scattering Attenuation	10
1.4. Motivations.....	11
1.5. Chapter Organization and Description	13
1.6. References	16
2. Characterizing the Effect of Elastic Interactions in the Complex Porous Media	20
2.1. Abstract	20
2.2. Introduction	21
2.3. Biot-Gassmann Consistency	25
2.4. Revisiting Interaction Energy Approach to Eshelby's Theory	27
2.5. A Numerical Experiment on Stress Interaction.....	32
2.6. DEM and SCA: Modeling Elastic Interactions Implicitly	37
2.6.1. DEM and SCA to Biot-Gassmann Consistency	39
2.7. T-matrix To Characterize Elastic Interactions	39
2.7.1. T-matrix Formulation	39
2.7.2. Effect of Spatial Distribution on Effective Stiffness.....	44
2.7.3. T-matrix to Biot-Gassmann Consistency	45
2.8. Comparison of Different Effective Medium Theories	46
2.9. Discussion	53
2.10. Conclusions	57
2.11. Acknowledgement.....	58

2.12.	Appendix A-- Evaluation of Eshelby Tensor	58
2.13.	Appendix B-- Evaluation of Tensor \bar{G}_{ijkl}	59
2.14.	References	61
3.	Extended Biot Theory with Local Flow in Heterogeneous Porous Rocks	67
3.1.	Abstract	67
3.2.	Introduction	68
3.3.	Brief Review of Biot Theory.....	70
3.3.1.	Poroelastic Constitutive Relations	71
3.3.2.	Poroelastic Wave Propagation	72
3.4.	Extended Biot Theory with Squirt Flow	73
3.4.1.	Theoretical Formulation.....	73
3.4.2.	Shear-wave Dispersion.....	75
3.4.3.	Numerical Results and Analysis	76
3.4.4.	Squirt Flow Effect on Interpretation of Well Log Data	83
3.5.	Extended Biot Theory with Mesoscopic Flow	84
3.5.1.	Double-porosity Dual-permeability Theory.....	85
3.5.2.	Governing Equation of DPDP.....	87
3.5.3.	Reduction to Single-porosity Biot Theory	90
3.5.4.	Numerical Examples and Analysis	91
3.6.	Discussion	95
3.6.1.	What Decide Magnitude of Dispersion	95
3.6.2.	Characteristic Frequency and Diffusion Equation	97
3.6.3.	Multi-scale Heterogeneity and Dispersion Coverage.....	100
3.7.	Concluding Remarks	102
3.8.	Acknowledgement.....	103
3.9.	References	103

4. Seismic Reflection Dispersion Due to Wave-induced Fluid Flow: A Theoretical Study	110
4.1. Abstract	110
4.2. Introduction	110
4.3. Effective Biot Media	116
4.4. Reflection Coefficients from the Boundary of Effective Biot Media	119
4.5. A Numerical Example.....	125
4.5.1. Geological Model.....	126
4.5.2. Velocity Dispersion and Attenuation Characteristics	128
4.5.3. Reflection Dispersion Signatures	133
4.6. Discussion	139
4.7. Conclusions	146
4.8. Acknowledgement.....	147
4.9. Appendix – Derivation of Reflection Coefficients from the Boundary of Effective Biot Media	147
4.10. References	153
 5. Poroelastic Seismic Analysis and Its Implications for Reservoir Imaging and Characterization	161
5.1. Abstract	161
5.2. Introduction	162
5.3. Spectral Signatures of Poroelastic Reflectivity.....	164
5.3.1. Class I AVF -Low frequency Dim-out.....	167
5.3.2. Class II AVF--Phase-shift Reservoir.....	168
5.3.3. Class III AVF--Low-frequency Bright-spot.....	170
5.4. Poroelstic Effect on Angle-dependent Reflectivity.....	170
5.5. Poroelastic Effect on Seismic Wavelet	176
5.6. Permeability Impact on Seismic Properties	190
5.6.1. High-permeability Dim-spot Reservoir.....	190
5.6.2. Permeability-dependent Phase Shift Reservoir	193

5.6.3.	High-Permeability Bright-spot Reservoir	197
5.6.4.	Seismic-Sensitive Permeability Zone.....	200
5.7.	Combined Effect of Anisotropy and WIFF on Reflection Coefficients.....	202
5.8.	Discussion	204
5.9.	Conclusions	207
5.10.	Acknowledgement.....	209
5.11.	References	209
6.	Poroelastic Seismic Interpretation: A Real Case Study	213
6.1.	Abstract	213
6.2.	Introduction	213
6.3.	Background and Reservoir Properties Description	216
6.3.1.	Geological Background.....	216
6.3.2.	Lithofacies and Heterogeneity Description.....	217
6.3.3.	Fluid Mobility Characteristics.....	222
6.4.	Illuminating the Poroelastic Reflections from Real Seismic	224
6.4.1.	Non-stationary Convolution Model for Attenuated Seismic Trace ..	225
6.3.2.	Comparison of Spectral Signatures	227
6.5.	Poroelastic Seismic Reflection Analysis Based on Theoretical Modeling	232
6.5.1.	Velocity Dispersion and Attenuation Characteristics	235
6.5.2.	Seismic Reflection Dispersion Analysis	235
6.6.	Discussion	242
6.7.	Conclusions	244
6.8.	Acknowledgement.....	245
6.9.	References	245

LIST OF FIGURES

Figure 1.1 A schematic illustration of the reservoir heterogeneity that occur to various extents and scales (Morad et al., 2010).....	4
Figure 1.2 Scales and frequencies for various geophysical measurement methods..	5
Figure 1.3 A schematic illustration of the concept of the scale-dependent heterogeneity and homogeneity (after Ba, 2008)..	5
Figure 1.4 Waves were propagated through periodic media created by stacking plastic and steel disks (Marion et al., 1994)..	7
Figure 1.5 The scale of heterogeneity that is typically responsible for the corresponding wave-induced fluid flow ranging from microscopic grain sizes to mesoscale heterogeneities to seismic wavelengths that are tens of meters.....	9
Figure 1.6 Intrinsic P-wave attenuation $1/Q$ plotted as a function of frequency on rocks at the Imperial College test site at various depths (Sams et al., 1997). Estimations regarding the VSP and sonic log measurements have been corrected for scattering attenuation (after Pride et al., 2006; Wenzlau, 2009)..	10
Figure 1.7 A schematic illustration of wave velocity dispersion due to scattering effect in heterogeneous media (Mavko et al., 2009) ..	11
Figure 1.8 A schematic illustration of the workflow and framework that is implemented in this thesis.....	15
Figure 2.1 Comparison of (a) C_{11} , (b) C_{33} , (c) C_{44} , (d) C_{66} , and (e) C_{13} as a function of crack density predicted by different non-interacting effective medium theories.	32
Figure 2.2 Comparison of the first principal stress distribution by introducing different set of cracks into the homogeneous solid matrix: (a) No cracks, (b) Cracks are far apart from each other, (c) Coplanar cracks, and (d) Stacked cracks. The host solid matrix is set as 2D circle geometry. The color-bar indicate the magnitude of stress in the unit of Pa.	35
Figure 2.3 Schematic illustrations of stress concentration and dilution on one crack in the homogeneous solid matrix..	36
Figure 2.4 Schematic illustrations of stress interaction between two cracks: (left) coplanar cracks, (right) stacked cracks.	36
Figure 2.5 The effective elastic stiffness C_{11} as a function of crack density simulated by (a) SCA, (b) DEM.	42

Figure 2.6 Schematic illustration of a 2D cross section through the 3D ellipsoidal crack distribution in the T-matrix model.....	43
Figure 2.7 An example to illustrate the concept of aspect ratio of spatial distribution as the conditional probability to find another inclusion given the position of an inclusion.....	43
Figure 2.8 Effective elastic properties of cracked carbonate as a function of crack density. C11, C33, C13, C44 and C66 represent five independent elastic stiffness constants in HTI medium.....	45
Figure 2.9 Computed elastic stiffness C11 as a function of aspect ratio of inclusion and aspect ratio of spatial distribution..	47
Figure 2.10 The effective elastic stiffness C11 (a), and C33 (b) as a function of crack density. Blue line represents elastic response of dry rock simulated by T-matrix. Black asterisk and red line indicate elastic stiffness for saturated rock predicted by T-matrix and Brown-Korringa relations, respectively...	48
Figure 2.11 Comparison of C11 as a function of crack density predicted by different effective medium theories.....	49
Figure 2.12 Elastic modulus of rocks containing dry, randomly distributed spherical pores, according to various effective medium theories....	51
Figure 2.13 Comparisons of predictions of Thomsen's anisotropic parameters as a function of crack density: (a) Epsilon, (b) Gamma, and (c) Delta.....	52
Figure 2.14 Variation of the elastic stiffness C11 with increasing crack density. The solid matrix is calcite and the matrix (stiff) porosity is 0.2. The aspect ratio of the matrix porosity and cracks are set as 0.5 and 0.05, respectively..	55
Figure 3.1 Schematic of pore-crack model to describe the squirt flow mechanism. The pore pressure change p in the pore space is caused by an external stress p_e (taken from Tang et al., 2012).	76
Figure 3.2 Illustration of effect of viscosity on (a) dispersion (b) attenuation of fast P-wave in a cracked porous rock.....	79
Figure 3.3 Illustration of the effect of viscosity on (a) dispersion (b) attenuation of slow P-wave in a cracked porous rock.	81
Figure 3.4 Illustration of the effect of (a) crack density and (b) aspect ratio on attenuation of fast P-wave in a cracked porous rock..	82

Figure 3.5 Illustration of the effect of permeability on attenuation of fast P-wave in a cracked porous rock.	83
Figure 3.6 A rock physics template presented as cross-plots of V_p/V_s versus P-impedance, which is used to illustrate the dispersion effect. All of the scattering data points are from the log data in a heterogeneous carbonate reservoir, offshore Brazil. The core photos in the right of figure indicate the heavily cracked carbonates in the corresponding depth.....	85
Figure 3.7 A schematic illustration of double-porosity dual-permeability model (after Pride and Berryman, 2003a). Phase 1 and Phase 2 are isotropic porous continua, and a is the characteristic length of mesoscopic scale heterogeneity.	87
Figure 3.8 Fractured reservoirs are typical example for elucidation of double-porosity dual-permeability model. The photo is the outcrop of Marcellus shale..	88
Figure 3.9 Illustration of the effect of (a) viscosity and (b) heterogeneity size on attenuation of fast P-wave in a double porosity composite. The peak to the left for each curve corresponds to mesoscopic loss, while the peak to the right corresponds to the Biot-loss... ..	89
Figure 3.10 The permeability and frequency dependence on the P-wave attenuation in a double porosity composite. The heterogeneity size is assumed 10cm in this case... ..	94
Figure 3.11 The permeability dependence of the fast P-wave attenuation in seismic exploration band. The red line, black line, and blue line represent 10Hz, 40Hz, and 80Hz, respectively.....	94
Figure 3.12 Comparisons of the effect of modeling effective elastic properties on the attenuation of fast P-wave.....	96
Figure 3.13 A schematic illustration of velocity dispersion associated with different mechanism. The potential geological features that cause the flow are also listed in the corresponding position.....	101
Figure 4.1 A schematic illustration of the P-wave incident upon an interface between two fluid-saturated heterogeneous porous media..	114
Figure 4.2 A schematic illustration of the plane wave reflection and transmission at the interface of double-porosity dual-permeability media.....	117
Figure 4.3 Schematic of the concept of effective Biot media that is simplified from heterogeneous porous media.....	119

Figure 4.4 Reflection and transmission of a compressional plane wave at an interface between two effective Biot medium. The effective single-porosity Biot medium is reduced from double-porosity medium.....	121
Figure 4.5 (a) Phase velocity dispersion (b) Attenuation of the effective fast P-wave in the upper and lower double-porosity medium..	130
Figure 4.6 (a) Phase velocity dispersion (b) Attenuation of effective slow P-waves in the upper and lower double porosity medium.	131
Figure 4.7 (a): Phase velocity dispersion (b): Attenuation of effective S-waves in the upper and lower double porosity medium.	132
Figure 4.8 (a) Reflection amplitude and (b) phase variation of fast PP as a function of frequency and incidence angle. Phase variation here indicates the deviation of the phase in the poroelastic reflection from the constant phase in the elastic reflection..	134
Figure 4.9 Reflection (a) amplitude and (b) phase of fast PP as a function of frequency at normal incidence angle. The red dashed line indicates (a) amplitude and (b) phase computed for elastic reflection. The frequency bands for seismic, VSP, sonic log, and ultrasonic lab are highlighted in the plot.....	137
Figure 4.10 AVO relationship with different frequency in the seismic band. The central frequency band for the field observation is often centered at around 40-60Hz.....	138
Figure 4.11 Comparison of PS reflectivity dispersion at incident angles of 0 degree, 15 degree, and 30 degree..	139
Figure 4.12 The effect of permeability of overburden shale on PP reflection dispersion at normal incident angle.....	142
Figure 4.13 A comparison of (a) reflection amplitude and (b) phase shift with attenuation contrast as a function of frequency at normal incidence angle. The red dashed line indicates (a) amplitude and (b) phase computed for elastic reflection.	143
Figure 4.14 Comparison of poroelastic reflection (black line) and reflection calculated based on classical Zoeppritz equation for each-frequency component (blue dashed line) at normal incidence angle.	146
Figure 5.1 P-impedance versus frequency for the overburden shale (circle) and overlying sandstone (diamond) in Model 1(red), Model 2(black), and Model 3(green).	166
Figure 5.2 V_p/V_s ratio versus frequency for Model 1 sand (square), Model 2 sand(diamond), and Model 3 sand (triangle).	166

Figure 5.3 Scatters for the real and imaginary part of the poroelastic reflection coefficients at normal incident angle. The data points are color coded by log of the frequency.....	167
Figure 5.4 (a) Magnitude and (b) Phase angle of fast PP versus frequency for the geological scenario corresponding to Class 1 AVO (square), Class 2 AVO (diamond), and Class 3 AVO (triangle).....	169
Figure 5.5 Magnitude of fast PP reflectivity versus incident angle with specific seismic frequency band for (a) Class I AVO model, (b) Class II AVO model, and (c) Class III AVO model.....	173
Figure 5.6 Phase angle of fast PP reflectivity versus incident angle with specific seismic frequency band for (a) Class I AVO model, (b) Class II AVO model, and (c) Class III AVO model.....	174
Figure 5.7 Ricker wavelets with different central frequencies used to simulate synthetic seismic trace.....	177
Figure 5.8 (a) Model 1 (Class I AVO) impulse responses convolved with 10-, 30-, 50-, and 80-Hz Ricker wavelets for seismic reflections at normal incident angle. (b) Normalized spectrum comparisons for impulse responses convolved with elastic reflection (black line) and poroelastic reflection (red line).	179
Figure 5.9 (a) Model 1 (Class I AVO) impulse responses convolved with 10-, 30-, 50-, and 80-Hz Ricker wavelets for seismic reflections at 30 degrees incident angle. (b) Normalized spectrum comparisons for impulse responses convolved with elastic reflection (black line) and poroelastic reflection (red line).	180
Figure 5.10 RMS amplitude ratio of poroelastic impulse responses over elastic impulse responses at normal incident angle for Class I AVO geological scenario.....	181
Figure 5.11 RMS amplitude ratio of poroelastic impulse responses over elastic impulse responses at 30 degrees incident angle for Class I AVO geological scenario.....	181
Figure 5.12 (a) Model 2 (Class II AVO) impulse responses convolved with 10-, 30-, 50-, and 80-Hz Ricker wavelets for seismic reflections at normal incident angle. (b) Normalized spectrum comparisons for impulse responses convolved with elastic reflection (black line) and poroelastic reflection (red line).	183
Figure 5.13 (a) Model 2 (Class II AVO) impulse responses convolved with 10-, 30-, 50-, and 80-Hz Ricker wavelets for seismic reflections at 30 degrees incident angle. (b) Normalized spectrum comparisons for impulse responses convolved with elastic reflection (black line) and poroelastic reflection (red line).	184

Figure 5.14 RMS amplitude ratios of poroelastic impulse responses over elastic impulse responses at normal incident angle for Class II AVO geological scenario.....	185
Figure 5.15 RMS amplitude ratios of poroelastic impulse responses over elastic impulse responses at 30 degrees incident angle for Class II AVO geological scenario.....	185
Figure 5.16 (a) Model 2 (Class III AVO) impulse responses convolved with 10-, 30-, 50-, and 80-Hz Ricker wavelets for seismic reflections at normal incident angle. (b) Normalized spectrum comparisons for impulse responses convolved with elastic reflection (black line) and poroelastic reflection (red line).	187
Figure 5.17 (a) Model 2 (Class III AVO) impulse responses convolved with 10-, 30-, 50-, and 80-Hz Ricker wavelets for seismic reflections at 30 degrees incident angle. (b) Normalized spectrum comparisons for impulse responses convolved with elastic reflection (black line) and poroelastic reflection (red line).	188
Figure 5.18 RMS amplitude ratios of poroelastic impulse responses over elastic impulse responses at normal incident angle for Class III AVO geological scenario.	189
Figure 5.19 RMS amplitude ratios of poroelastic impulse responses over elastic impulse responses at 30 degrees incident angle for Class III AVO geological scenario.	189
Figure 5.20 (a) Magnitude and (b) phase angle of fast PP poroelastic reflection versus frequency at normal incident angle with different matrix permeability k_1 . The geological scenario corresponds to Class I AVO response.	191
Figure 5.21 (a) Magnitude and (b) phase angle of fast PP poroelastic reflection versus permeability at normal incident angle for specific frequencies. The geological scenario corresponds to Class I AVO response..	192
Figure 5.22 Poroelastic seismic synthetics (30-Hz Ricker wavelet) at normal incident angle for permeabilities (10^{-3} D, 10^{-2} D, 10^{-1} D, and 1 D). The geological scenario corresponds to Class I AVO response	193
Figure 5.23 (a) Magnitude and (b) phase angle of fast PP poroelastic reflection versus frequency at normal incident angle with different matrix permeability k_1 . The geological scenario corresponds to Class II AVO response.	195
Figure 5.24 (a) Magnitude and (b) phase angle of fast PP poroelastic reflection versus permeability at normal incident angle for specific frequencies. The geological scenario corresponds to Class II AVO response.....	196
Figure 5.25 Poroelastic seismic synthetics (30-Hz Ricker wavelet) at normal incident angle for permeabilities (10^{-3} D, 10^{-2} D, 10^{-1} D, and 1 D). The geological scenario is corresponding to Class II AVO response	197

Figure 5.26 (a) Magnitude and (b) phase angle of fast PP poroelastic reflection versus frequency at normal incident angle with different matrix permeability k_1 . The geological scenario corresponds to Class III AVO response.....	198
Figure 5.27 (a) Magnitude and (b) phase angle of fast PP poroelastic reflection versus permeability at normal incident angle for specific frequencies. The geological scenario corresponds to Class III AVO response..	199
Figure 5.28 Poroelastic seismic synthetics (30-Hz Ricker wavelet) at normal incident angle for permeabilities (10^{-3} D, 10^{-2} D, 10^{-1} D, and 1 D). The geological scenario is corresponding to Class III AVO response	200
Figure 5.29 A schematic illustration of the VTI Anisotropy and WIFF impact on the reflection coefficients.....	203
Figure 5.30 Phase-shift versus frequency for the geological scenario corresponding to Class 1 AVO (black square) and Class 3 AVO (green triangle).....	206
Figure 6.1 Section of the near-angle stacked seismic data, Well A is located at the position of CDP 367 and Well B is located at the position of CDP 211..	218
Figure 6.2 Log data from well A in the carbonate reservoir offshore Brazil. The lithology content, P-wave velocity, S-wave velocity, density, bulk porosity, and water saturation are displayed as a function of time converted from depth..	219
Figure 6.3 Log data from well B in the carbonate reservoir offshore Brazil. The lithology content, P-wave velocity, S-wave velocity, density, bulk porosity, and water saturation are displayed as a function of time converted from depth.	220
Figure 6.4 Lithofacies correlation between the well A and well B..	221
Figure 6.5 OMRI-CAST borehole images in well A and Well B used to illustrate the strong heterogeneities in the overburden marlstone and underlain limestone. Here, (a), (b), and (c) correspond to the marlstone formation, and (c), (d), and (e) correspond to the limestone formation...	223
Figure 6.6 Permeability-porosity are cross-plotted for the Albian carbonate reservoir rocks. The permeability and porosity measurements are based on the core analysis...	224
Figure 6.7 Schematic illustration of a workflow used to illuminate the poroelastic reflection from real seismic data.	226
Figure 6.8 Comparisons of field seismic data at location of well A (CDP 366) with synthetic seismic trace at normal incident angle. (a) Field near-angle stacked seismic, (b) elastic, (c) $Q=2000$, (d) $Q=100$, (e) $Q=30$, and (f) $Q=10$	228

Figure 6.9 Spectral decomposition results of field seismic data at location of well A and attenuated seismic trace with different Q	229
Figure 6.10 Comparison of normalized seismic spectral signatures at the interface of interest for: (a) real seismic at the location of well A , and (b) the attenuated seismic trace ($Q=100$).....	229
Figure 6.11 Comparisons of field seismic data at location of Well B (CDP 211) with synthetic seismic trace at normal incident angle. (a) Field near-angle stacked seismic, (b) elastic, (c) $Q=2000$, (d) $Q=100$, (e) $Q=30$, and (f) $Q=10$	230
Figure 6.12 Spectral decomposition results of field seismic data at location of well B and attenuated seismic trace with different Q	231
Figure 6.13 Comparison of seismic spectral signatures at the interface of interest for: (a) real seismic at the location of well B, and (b) the attenuated seismic trace ($Q=100$)..	231
Figure 6.14 (a) Phase velocity dispersion (b) Attenuation of the effective fast P-wave for the overburden muddy limestone, the underlain grainstone at well A, and the underlain packstone at well B.....	236
Figure 6.15 (a) Phase velocity dispersion (b) Attenuation of the effective slow P-wave for the overburden muddy limestone, the underlain grainstone at well A, and the underlain packstone at well B.	237
Figure 6.16 (a) Phase velocity dispersion (b) Attenuation of the effective shear-wave for the overburden muddy limestone, the underlain grainstone at well A, and the underlain packstone at well B.....	238
Figure 6.17 Fast PP reflectivity for the interface of interest at the position of well A and well B as a function of frequency at normal incidence angle. The dashed line indicates PP reflection coefficients computed based on Zoeppritz equation.....	240
Figure 6.18 Fast PP reflectivity for the interface of interest at well A as a function of incident angle with different frequency in the seismic exploration band..	240
Figure 6.19 Fast PP reflectivity for the interface of interest at well B as a function of incident angle with different frequency in the seismic exploration band.	241
Figure 6.20 A comparison of normalized seismic spectral signatures at the interface of interest between real poroelastic modeling seismic at the location of well A.....	241
Figure 6.21 A comparison of normalized seismic spectral signatures at the interface of interest between real poroelastic modeling seismic at the location of well B.....	242

LIST OF TABLES

Table 2.1 Comparison of normalized volumetric strain that corresponds to different stress interaction situation in Figure 2.2..	37
Table 3.1 Input parameters to calculate the characteristics of velocity dispersion and wave attenuation of squirt flow.....	78
Table 3.2 The related parameters for the double-porosity dual-permeability modeling in the section 3.5..	93
Table 4.1 The related parameters for rock frame properties of upper medium and lower medium.	128
Table 4.2 The related parameters for the pore fluid properties of upper medium and lower medium.	128
Table 5.1 The related parameters for rock frame properties of upper medium and lower medium corresponding to three types of AVO responses.	165
Table 6.1 Properties of fluids in reservoir rock from lab measurements.....	224
Table 6.2 Mineral bulk modulus , shear modulus , and density used in the calculations (references in Mavko et al., 2009)..	233
Table 6.3 The related parameters for rock frame properties of upper medium (marlstone) and lower medium(limestone).	234
Table 6.4 The related parameters for the pore fluid properties of upper medium(marlstone) and lower medium(limestone).....	234

Chapter 1

Introduction

The principal goal of geophysical measurements is to describe geology. Distinguishing reservoir rocks and fluids from the recorded wave-field and understanding the flow characteristics by their seismic signatures are typically the responsibility of exploration seismology. Consequently, it is essential to establish a relationship to link the physical properties of rocks and their interactions with fluids to seismic signatures. We call this “Seismic Rock Physics” (Han, 2002; Zimmerman, 2011) because it is rock physics that determines how the seismic wiggles waggle. It is also the key to optimizing the value of seismic data for reservoir evaluation, reservoir monitoring, and providing drilling solutions. Seismic Rock Physics will be the framework that guides the topics covered in this dissertation.

1.1 Porous Media and Poroelasticity

The Earth’s subsurface rocks, by their very nature, are generally heterogeneous, porous, and saturated with fluids (oil, gas, or water) which are of great interest to us. The presence of the fluid modifies the mechanical response of the porous rock. Two basic physical phenomena that underlie the poroelastic behavior are:

- (i) The static effect, which has been quantified by Gassmann (1951), and is widely applied for fluid substitution. Generally, when a rock is loaded under an increment of compression, the induced pore-pressure change plays a role in

resisting being compressed and therefore stiffens the rock (Han and Batzle, 2004; Mavko et al., 2009). Consequently, the bulk compressibility is reduced. Since pore fluid cannot contribute any additional shear stiffness to the rock, the shear modulus of the saturated rock is practically not affected. The Gassmann equation requires two essential assumptions (Yao, 2013): one assumption is that the pore pressure should be locally equilibrated, and the other assumption is that the fluids cannot escape and should be trapped in a closed porous system.

- (ii) The dynamic poroelasticity (known as Biot theory), which gives a complete and general description of the mechanical behaviour of a poroelastic medium, is attributed to a series of papers published by Biot (1956a, b; 1962). He theoretically formulated the propagation of stress waves in a porous elastic solid containing a compressible viscous fluid. Pore fluid is forced to participate in a solid's oscillatory motion by viscous friction and inertial coupling, and consequently causes the energy dissipation. One of the key findings in Biot theory is the prediction of a slow P-wave in a porous saturated media. This second P-wave is thought to be diffusive in the low frequency range and has been experimentally observed in synthetic water-saturated sandstone by Plona (1980) and real sandstone by Kelder and Smeulders (1997). Another important contribution that comes from Biot theory is the establishment of the link between rock permeability and fluid viscosity with wave propagation characteristics. Note that the low-frequency limit of Biot theory is consistent with the predictions by Gassmann equation.

1.2 Heterogeneity and Scales

Sedimentary rocks are naturally produced with complicated but traceable geological processes (Han, 2002). They are often initially controlled by patterns of depositional textures, and then constantly undergo cementation and diagenesis which are strongly influenced by factors such as temperature, pressure, and atmospheric environment. The geological processes and the statistical fluctuation in geological history can cause sedimentary rocks to exhibit heterogeneities occurring at various extents and scales, ranging from micrometer grain and pore scale, to basin scale at tens to hundreds of kilometers (Figure 1.1). These heterogeneities contain variations in lithology, porosity, pore fluid properties, permeability, saturation, pore pressure, stress, and so on (Mukerji, 1995). Correspondingly, scales and frequencies of geophysical measurements also cover a wide frequency range, from ultrasonic measurements to low frequency surface seismic (Figure 1.2). Undoubtedly, the integration of the geophysical measurement at different scales aids in fully understanding the complexity and heterogeneity of the geological world.

In general, heterogeneity is a relative concept that depends on the scale to describe it. If the wavelength is substantially long, most of the geological feature is considered to be homogeneous, since the wave can only “see” the average behavior of geological feature within the wavelength. However, if the wavelength is shorter than the geological feature to be described, the wave can “see” the variations and

heterogeneities. A schematic illustration of the concept of the scale-dependent heterogeneity and homogeneity is illustrated in Figure 1.3.






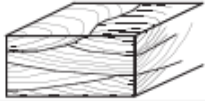

Scale	Reservoir heterogeneity types	
Giga (>300 m)	Sealing to nonsealing faults	
	Fracturing	
Mega (10–100 m)	Genetic unit boundaries	
	Permeability zonation within genetic units	
Macro (in meters)	Baffles within genetic units	
	Sedimentary structures	
Micro (μm)	Microscopic heterogeneity	

Figure 1.1. A schematic illustration of the reservoir heterogeneity that occur to various extents and scales (Morad et al., 2010).

1.3 Heterogeneity and Seismic Properties

Due to the variations in terms of geometry, elastic properties, and hydraulic properties, heterogeneity can significantly affect the signatures of elastic wave propagation. The effect mainly lies in two aspects. On the one hand, the elastic properties of porous medium can be influenced. For example, the presence of cracks can considerably reduce the elastic moduli of the porous rocks. On the other hand,

heterogeneity often causes the fluid-pressure difference, and consequently the induced fluid flow will lead to the velocity dispersion and wave attenuation. Interestingly, the degree of heterogeneity is difficult to be estimated from the elastic properties but it potentially can be deciphered from the intrinsic dispersion and attenuation.

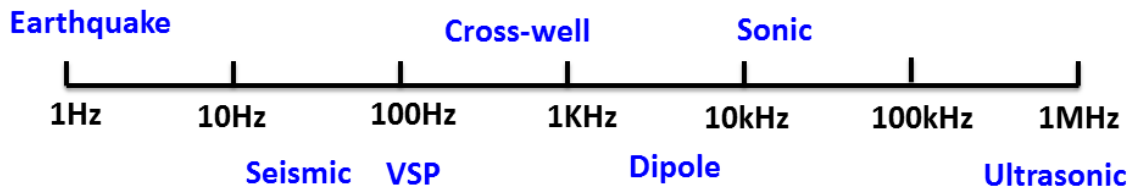


Figure 1.2. Scales and frequencies for various geophysical measurement methods.

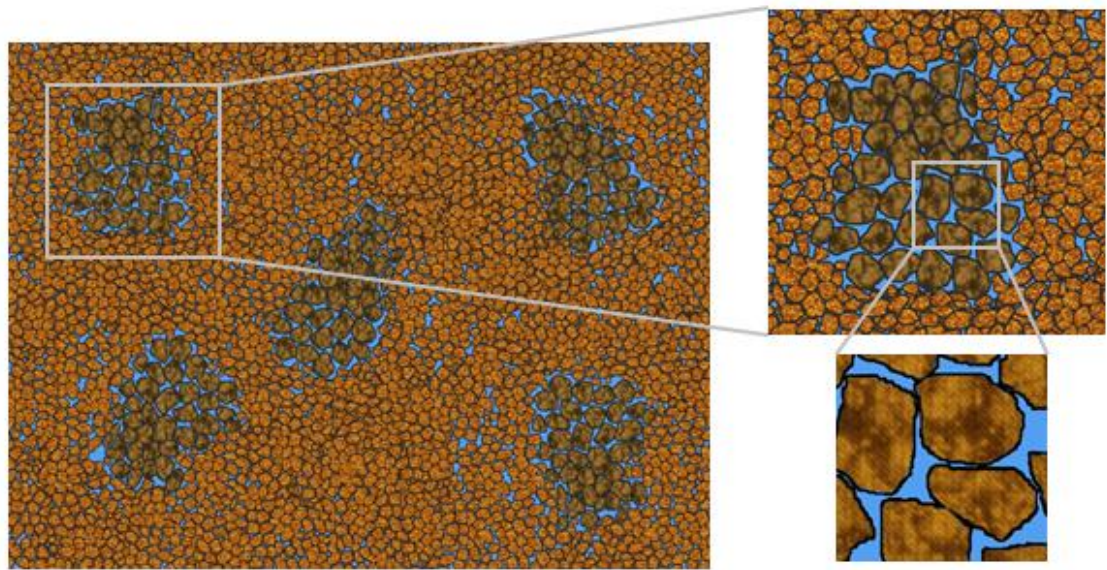


Figure 1.3. A schematic illustration of the concept of the scale-dependent heterogeneity and homogeneity.

1.3.1 Effective Medium Approximations

In porous media, since the wavelength of seismic wave is often much larger than the heterogeneity size, seismic waves cannot sense the physical behavior of individual heterogeneity but only an averaged or homogenized structure. Therefore, we often use the effective medium approximations or effective medium theory (sometimes abbreviated as EMA or EMT) to describes the macroscopic properties of composite materials in heterogeneous porous media. Conversely, the ray theory is always used to describe the physical behavior by short-wavelength. The transition from the domains of the ray to the effective medium theories is experimentally observed by Marion et al. (1994).

In this dissertation, effective elastic properties of complex porous media will be explored. Under the assumption that elastic strain is infinitesimal, the local stress tensor $\sigma(x)$ is linearly proportional to the strain tensor $\varepsilon(x)$, as given by:

$$\sigma(x) = C(x)\varepsilon(x), \quad (1.1)$$

where $C(x)$ is the fourth-rank elastic stiffness tensor at local position x . Note that $C(x)$ varies randomly with x in the composite, on a scale that is smaller compared with the wavelength scale of elastic wave. If we treat the heterogeneous materials as macroscopic homogeneous materials, the averaged stress tensor $\langle \sigma(x) \rangle$ and strain tensor $\langle \varepsilon(x) \rangle$ can be related by:

$$\langle \sigma(x) \rangle = C^*(x) \langle \varepsilon(x) \rangle, \quad (1.2)$$

where the tensor $C^*(x)$ is the effective elastic constants that reflect the elastic properties and the relative fractions of each component in the composite. Generally, if we consider a volume of heterogeneous porous materials, the angular brackets $\langle \rangle$ in equation (1.2) denote the volume average (Jackbosen et al., 2003).

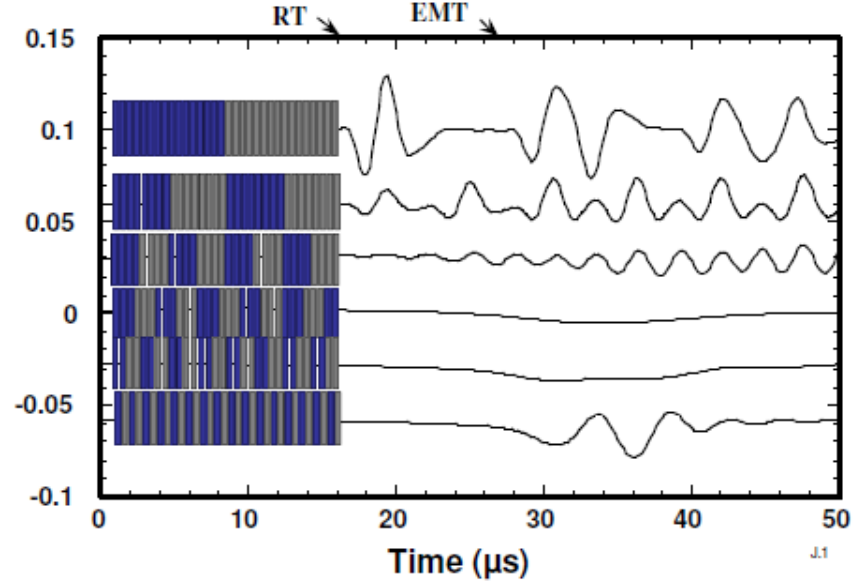


Figure 1.4. Waves were propagated through periodic media created by stacking plastic and steel disks (Marion et al., 1994).

Indeed, the concept of effective properties in exploration seismology is very important. For example, we usually need averages to provide the in-situ estimate of reservoir properties. However, the effective elastic properties offer less help in providing estimates of the heterogeneities in the complex porous media. This is because a heterogeneous composite consisting of extremely contrasting materials and a relatively homogeneous composite can exhibit quite similar elastic properties.

1.3.2 Wave-induced Fluid Flow and Intrinsic Attenuation

Seismic waves propagating in fluid-saturated porous media are subject to intrinsic dispersion and attenuation, where the mechanical energy is dissipated into heat (Aki and Richards, 1980). It is commonly accepted that the intrinsic dispersion and attenuation are caused by the mechanism broadly known as wave-induced fluid flow (WIFF).

Biot first studied the wave-induced fluid flow (WIFF) due to wavelength-scale pore-pressure equilibration and the resulting viscous-inertial attenuation (Biot, 1956a, 1956b, 1962). WIFF associated with wavelength-scale pressure gradients is often called global or macroscopic flow. However, Biot's theory has been limited by its explicit assumption that the porosity is homogeneous. When transient passage of a seismic wave through a porous system containing elastic heterogeneities, an internal equilibration takes place with fluid flowing from the more compliant high-pressure regions to the relatively stiffer low-pressure regions (Batzle et al., 2006). Based on the heterogeneities of various scale, such local fluid flow can be categorized as “squirt flow” and “mesoscopic flow”. Squirt flow typically occurs at microscopic pore scale, while mesoscopic flow is created by the heterogeneities on a scale much larger than the typical pore size but smaller than the wavelength. Squirt flow is usually considered to be important at ultrasonic frequencies, while mesoscopic flow is increasingly considered as the dominant cause of fluid-related attenuation in the seismic-exploration band (Pride et al., 2004; Müller et al., 2010). The qualitative

description of wave-induced fluid flow when a seismic wave propagates through heterogeneous porous media is sketched in Figure 1.5.

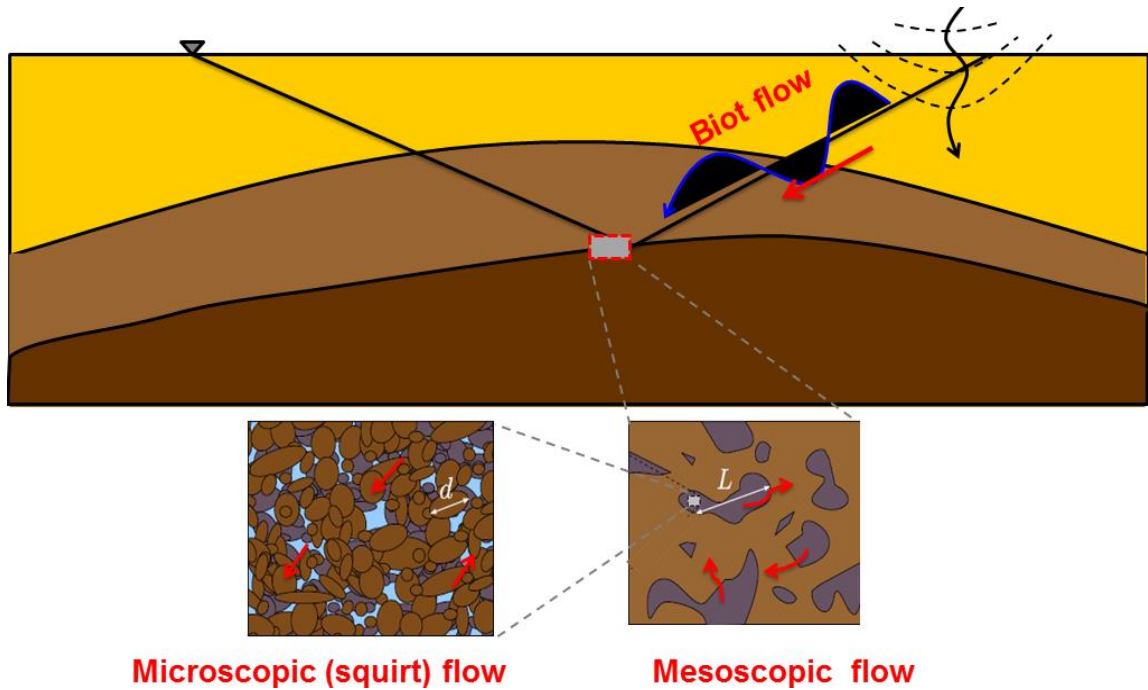


Figure 1.5. The scale of heterogeneity that is typically responsible for the corresponding wave-induced fluid flow ranging from microscopic grain sizes to mesoscale heterogeneities to seismic wavelengths that are tens of meters.

Figure 1.6 shows the frequency-dependent intrinsic attenuation of compressional waves determined from a series of experiments conducted at the Imperial college test site (Sams et al., 1997). These experimental results compare the P-wave attenuation estimated from ultrasonic core measurements (300-900 kHz), sonic logs (8-24 kHz), crosswell (0.2-2.3 kHz), and VSP data (30-280 Hz), suggesting that there exists a significant amount of energy loss at a broad frequency range.

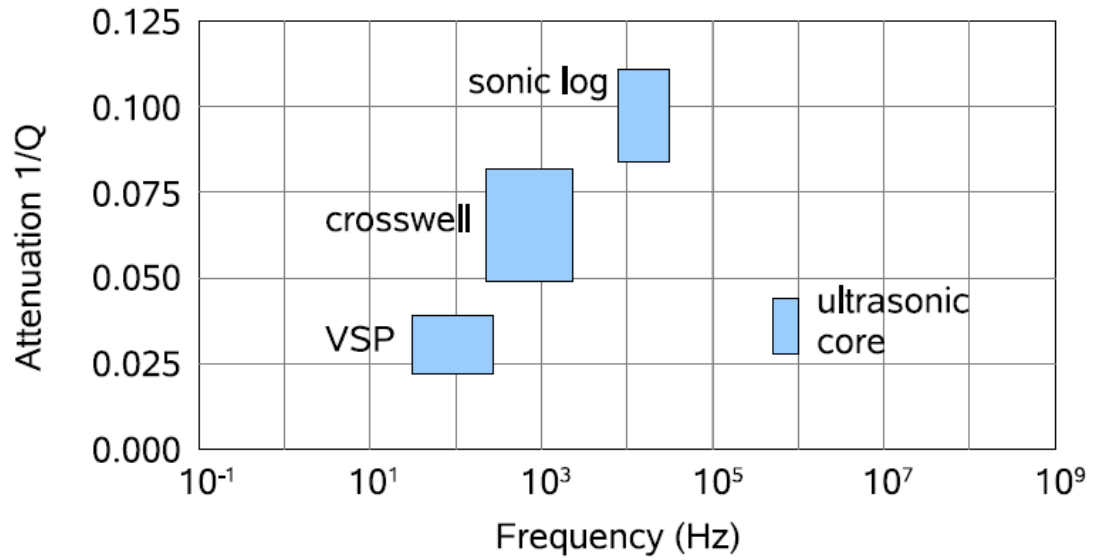


Figure 1.6. Intrinsic P-wave attenuation $1/Q$ plotted as a function of frequency on rocks at the Imperial College test site at various depths (Sams et al., 1997). Estimations regarding the VSP and sonic log measurements have been corrected for scattering attenuation (after Pride et al., 2006; Wenzlau, 2009).

1.3.3 Effect of Scattering Attenuation

In contrast to the aforementioned intrinsic attenuation mechanisms, the scattering of seismic waves in an elastic medium is not based on absorption but on the redistribution of wave-field energy caused by irregularities in the heterogeneous media. The impact of scattering attenuation is dependent on the ratio of the seismic wavelength to the length of the scattering heterogeneity (Mavko et al., 2009). The relationship between wave velocity and scale dependence due to scattering attenuation in heterogeneous media is schematically illustrated in Figure 1.7. The elastic scattering of seismic energy attenuates most when the seismic wavelength approximately equals the characteristic size of the

scattering heterogeneity. The velocity is non-dispersive or weakly dispersive when the wavelength is much bigger or smaller than the heterogeneity size, which respectively corresponds to the domain of effectively medium theories and ray theory. The issue of scattering attenuation due to the presence of heterogeneities in porous medium will not be discussed in this thesis.

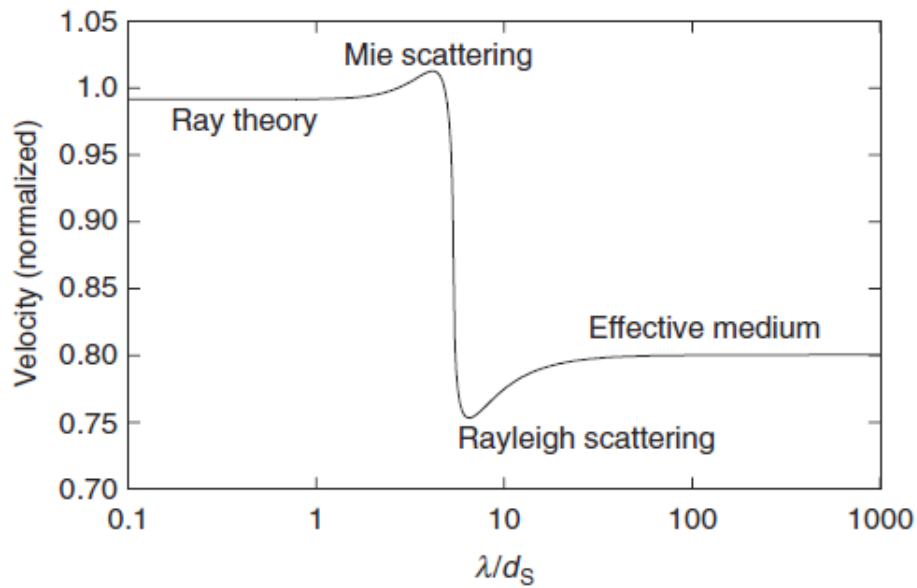


Figure 1.7. A schematic illustration of wave velocity dispersion due to scattering effect in heterogeneous media (Mavko et al., 2009).

1.4 Motivations

The heterogeneities and complexity of the subsurface rocks distort and attenuate propagating seismic waves, which makes image focusing and reservoir characterization challenging. Therefore, understanding how the presence of

heterogeneities affects the elastic properties and seismic signatures is one of the fundamental problems to be investigated in exploration seismology. The present work constitutes a contribution to solving this problem. Three key questions to address are:

1. What is the physical condition for an effective medium theory to satisfy the requirement of Biot-Gassmann consistency? This is an essential question concerning about the application of effective medium theories in porous media. We find that the key condition lies in whether elastic interactions between the inhomogeneity of porous media (such as pores and cracks) are characterized in a physically reasonable way. Actually, studying the elastic interactions is physically meaningful, because they reflect how the pores and cracks are organized or spatially distributed due to the rock's geological imprints. We demonstrate that the varying spatial distribution of pores and cracks can significantly affect a rock's elastic response and the resulting seismic anisotropy, and this impact cannot be ignored when the inclusion concentration increases beyond the dilute limit.
2. How does the wave-induced fluid flow affect the seismic reflections in heterogeneous poroelastic media? From a theoretical point of view, seismic reflection in elastic non-dissipative media (classical Zoeppritz equation) and porous homogeneous media (Dutta and Ode, 1983) are not applicable in the heterogeneous reservoir rocks. We propose and perform how to compute the poroelastic reflection from the boundary of heterogeneous porous media. The core of our methodology is to reduce the heterogeneous porous media into an effective

Biot media by incorporating the effect of local flow into the frequency-dependent poroelastic parameters such as drained bulk modulus. The reflectivity approach presented here places no restriction on the material-property contrast, the frequency, and the angle of incidence.

3. How does the dispersion behavior of poroelastic reflection facilitate our interpretation of seismic data in heterogeneous reservoir rocks? The poroelastic seismic reflection signatures, which primarily represent contrast in the poroelastic response between the individual layers, contain information about fluid mobility and heterogeneity characteristics that cannot be gained from classical seismic interpretation based on elasticity. This is of prime importance for reservoir development and production, because fluid mobility and heterogeneity properties strongly influence reservoir performance by controlling fluid flow and recovery factors.

1.5 Chapter Organization and Description

This dissertation consists of seven chapters, including this introduction. A schematic illustration of the workflow and framework that link the chapters in this dissertation is shown on Figure 1.8.

Chapter 2 discusses the physical importance of considering and characterizing the elastic interactions in complex porous media. We use the Biot-Gassmann consistency as a constraint to select a physically sound effective medium theory to characterize the elastic interactions based on a critical review and comparison of the existing

inclusion and crack theories. We further illustrate that the T-matrix theory is consistent with the Biot-Gassmann theory, and can produce physically plausible results even at large concentrations of pores and cracks.

Chapter 3 introduces the fundamental physics concerning the wave-induced flow in heterogeneous porous rocks. The extended Biot theory with squirt flow and mesoscopic flow, which are distinguished depending on the scale of the pressure gradient, are separately explored in this chapter. A rock physics template taking into account the dispersion effect caused by squirt flow is developed to interpret the sonic data in a heterogeneous carbonate reservoir. The numerical results also show that double-porosity dual-permeability model taking into account the mesoscopic heterogeneity can be responsible for the considerable attenuation determined in seismic frequency band.

Chapter 4 presents the theoretical framework used to compute the seismic reflection from the boundary of heterogeneous poroelastic media. To simplify the mathematical derivations, we replace the heterogeneous porous medium with effectively homogeneous porous medium by reducing the internal local flow term into a set of poroelastic parameters in classical Biot theory. The computed poroelastic reflection not only depends on the elastic properties contrast and incident angle, but also relies on the observational frequency, fluid mobility, and heterogeneity features. Seismic reflections exhibit negligible dispersion due to Biot flow. However, the local flow can cause a significant amount of dispersion for seismic reflections in the exploration band. Such dispersion effects can't be ignored, otherwise quantitative seismic interpretation of the reservoir properties will be biased.

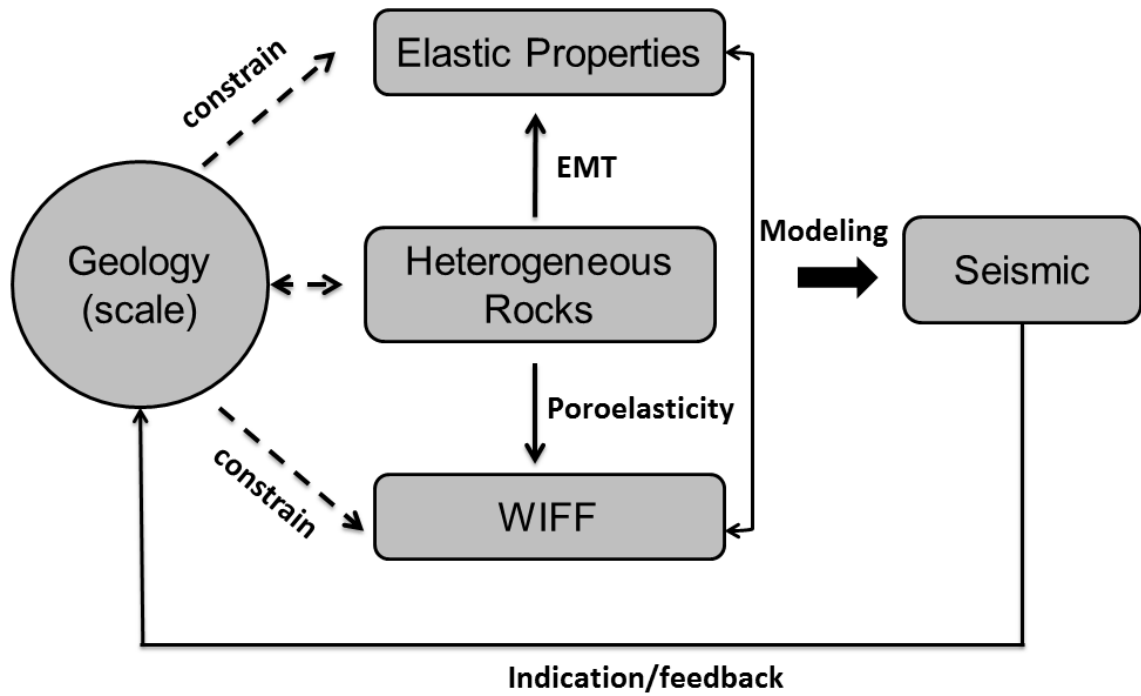


Figure 1.8. A schematic illustration of the workflow and framework that is implemented in this thesis

Chapter 5 extends the classical seismic interpretation to a heterogeneous porous medium based on an analysis of frequency and angle-dependent poroelastic reflectivity. We use spectral intercept and spectral gradient to characterize the reflection dispersion signatures. To guide the interpretation of frequency-dependent seismic anomalies, we define three types of amplitude-versus-frequency features corresponding to different geological circumstances. We demonstrate that the poroelastic reflection can significantly affect the seismic response. It not only influences the RMS amplitude of seismic traces, but also yields a noticeable phase shift compared with purely elastic seismic response. In

addition, we systematically investigate how the fluid mobility impacts the seismic signatures under different geological scenarios.

Chapter 6 presents a field case study regarding the seismic reflection dispersion due to wave-induced fluid flow in a heterogeneous carbonate reservoir, offshore Brazil. We have proposed and implemented a workflow to illuminate the poroelastic reflection characteristics from real seismic, by comparing the spectral signature of field seismic with the synthetic seismic that takes into account the attenuation and tuning effect. We explain that the discrepancy of poroelastic reflections from the interface of interest at two wells is likely to be caused by the fact that the fluid mobility in the underlain lithology is remarkably different. The case study here promises a solution to estimate hydraulic properties from field seismic, which is often considered to be extremely challenging.

1.6 References

- Aki, K., and P. G. Richards, 1980, *Quantitative Seismology: Theory and Methods*: W. H. Freeman & Co.
- Batzle, M. L., D. H. Han, and R. Hofmann, 2006, Fluid mobility and frequency-dependent seismic velocity—Direct measurements: *Geophysics*, 71, no. 1, N1–N9.
- Biot, M. A., 1956a, Theory of propagation of elastic waves in fluid-saturated porous solid. I. Low-frequency range: *Journal of the Acoustical Society of America*, 28, 168–178.

- , 1956b, Theory of propagation of elastic waves in a fluid-saturated porous solid. II. Higher frequency range: *Journal of the Acoustical Society of America*, 28, 179–191.
- , 1962, Mechanics of deformation and acoustic propagation in porous media: *Journal of Applied Physics*, 33, 1482–1498.
- Dutta, N. C., and H. Odé, 1983, Seismic reflections from a gas-water contact: *Geophysics*, 48, 148–162.
- Gassmann, F., 1951, Über die elastizität poroser medien: *Vierteljahresschr. Naturforsch. Ges. Zurich*, 96, 1–21.
- Han, D., 2002, Introduction of Reservoir Rock and Hydrocarbon Fluid Properties—Foundation for Reservoir Exploration and Exploitation (Lecture Notes): Department of Earth and Atmospheric Sciences, University of Houston, Houston, USA.
- Han, D., and M. L. Batzle, 2004, Gassmann's equation and fluid-saturation effects on seismic velocities: *Geophysics*, 69, 398–406.
- Jakobsen, M., J. A. Hudson, and T. A. Johansen, 2003, T-Matrix approach to shale acoustics: *Geophysical Journal International*, 154, 533–558.
- Kelder, O., and D. M. J. Smeulders, 1997, Observation of the Biot slow wave in water-saturated Nivelsteiner sandstone, *Geophysics*, 62, 1794–1796.
- Marion, D., Mukerji, T., and Mavko, G., 1994, Scale effects on velocity dispersion: From ray to effective medium theories in stratified media: *Geophysics*, 59, 1613–1619.
- Mavko, G., T. Mukerji, and J. Dvorkin, 2009, *The Rock Physics Handbook*, 2nd ed.: Cambridge University Press.

- Morad, S., J. M. Ketzer, and L. F. De Ros, 2010, The impact of diagenesis on the heterogeneity of sandstone reservoirs: A review of the role of depositional facies and sequence stratigraphy: *American Association of Petroleum Geologists Bulletin*, 94(8), 1267-1309.
- Mukerji, T., 1995, *Waves and Scales in Heterogeneous Rocks*: Ph.D. Thesis, Stanford University.
- Müller, T. M., B. Gurevich, and M. Lebedev, 2010, Seismic wave attenuation and dispersion resulting from wave-induced flow in porous rocks- A review, *Geophysics*, 75, 75A147-75A164.
- Plona, T. J., 1980, Observation of a second bulk compressional wave in a porous medium at ultrasonic frequencies: *Applied Physics Letters*, 36, 259–261.
- Pride, S. R., and J. G. Berryman, 2003, Linear dynamics of double-porosity and dual-permeability materials. I. Governing equations and acoustic attenuation: *Physical Review Letters*, 68, 036603.
- Pride, S. R., J. G. Berryman, and J. M. Harris, 2004, Seismic attenuation due to wave-induced flow: *Journal of Geophysical Research*, 109, B01201.
- Sams, M. S., J. P. Neep, and M. H. Worthington, 1997, The measurement of velocity dispersion and frequency-dependent intrinsic attenuation in sedimentary rocks: *Geophysics*, 62, 1456–1464.
- Thomsen, L., 1985, Biot-consistent elastic moduli of porous rocks: low frequency limit: *Geophysics*, 50, 2797– 2807.
- Wenzlau, F., 2009, *Poroelastic Modelling of Wavefields in Heterogeneous Media*: Ph.D. Thesis, Universität Karlsruhe (TH).

Yao, Q., 2013, Velocity dispersion and attenuation in reservoir: Ph.D. Thesis, University of Houston.

Zimmerman, R., 2011, Seismic Rock Physics (Lecture Notes for MSc in Petroleum Geophysics): Department of Earth Science and Engineering, Imperial College London, London, United Kingdom.

Chapter 2

Characterizing the Effect of Elastic Interactions in Complex Porous Media

2.1 Abstract:

The elastic interactions between the pores and cracks reflect how they are organized or spatially distributed due to rock's geological imprints. The first goal of this paper is to discuss the physical importance of considering and characterizing the elastic interactions. We perform a finite element modeling to quantitatively study how the stress amplification and stress shielding affect the stress distribution and the resulting overall elasticity. Our second goal is to propose a guideline on how to select a physically sound effective medium theory to characterize the elastic response for porous, cracked rock, based on a critical review and comparison of the existing inclusion and crack theories. By revisiting the interaction energy approach to Eshelby's dilute inclusion problems, we give the physical insights into why both the first-order Hudson's theory and compliance-based non-interacting approximation (NIA) can't produce physically plausible results at high crack density. Contrary to what has been assumed by NIA, two types of approaches to characterize the elastic interactions are explored, and we use Biot-Gassmann consistency (Thomsen, 1985) to test whether the elastic interactions are simulated with physical foundation. We find that the differentiate effective medium (DEM) and the self-consistent approximation(SCA) theories are not satisfied with the Biot-Gassmann consistency criteria, implying the elastic interactions mimicked by those two schemes lack

physical foundation. We further illustrate that the T-matrix theory is consistent with the Biot-Gassmann theory, suggesting that the pores and cracks interactions are characterized in a physically reasonable way. Numerical results also suggest that, when the concentrations of the cracks increase beyond the dilute limit, the single parameter crack density is not sufficient to characterize the contribution of the cracks to the effective elasticity. The spatial distribution of the pores and cracks can significantly affect the stress interaction, and thus influence the elastic response and seismic anisotropy. Additionally, such elastic interaction effects are also dependent on both the aspect ratio of the pores and the fluid infill.

2.2 Introduction

Sedimentary rocks are generally porous, and often fractured or cracked to some extent. Understanding their elastic behavior is essential to interpret and predict sonic measurement and seismic response in terms of rock properties. Such understanding comes primarily from the effective medium theories that relate the microstructural parameters of rocks (mineral composition, porosity, microstructure, etc.) to the effective elastic response. Consequently, many theoretical models have emerged, seeking to predict the effective elastic properties in porous, cracked media. Most of them are on the basis of strong assumptions with idealizations and simplification of the complexity of real rocks.

The most popular approaches are to use the non-interaction approximation (NIA) to predict the overall compressibility of rocks containing finite concentration of pores and cracks, owing to the difficulty of solving elastic interactions between pores and cracks. The pioneering work concerning about NIA is initiated by the paper of Eshelby (1957), in which he presented the solution to the strain field of an ellipsoidal inclusion in an infinite, homogeneous solid. Generally, there are two approaches to formulate the NIA theory. The first type of NIA approach directly estimates the effective stiffness as a function of porosity and crack density (Walsh, 1965; O'Connell and Budiansky, 1974; Kuster and Toksoz, 1974; Hudson, 1980, 1981, 1994). Walsh (1965) predicted the compressibility of dry rocks with spherical pores and narrow cracks, and found that pore shapes and their volume concentration can be combined together to affect the overall elasticity. By applying a long-wavelength, first-order scattering theory, Kuster and Toksoz (1974) calculated the effective moduli for randomly oriented inclusions. Their results are considered to be valid only for a small volume fraction of inclusions, since the multiple scattering effects are ignored in their methods. Based on a scattering-theory analysis of the mean wave-field in an elastic solid with thin, penny-shaped ellipsoidal cracks or inclusions, Hudson derived the first-order correction and second-order correction to compute the effective moduli for the cracked media (Hudson, 1980, 1981, 1994). The first-order Hudson's model which ignores the crack interactions can only work at low crack density. The second-order expansion of Hudson's model takes into account the pairwise interactions between cracks, but gives physically unreliable predictions at high

crack density. The dilute limit in Hudson's theory for both the first- and second-order terms is less than 0.1.

The second type of NIA approach considers the effective compliance as a sum of the contributions from the matrix compliance and excess compliances from pores and cracks (Schoenberg, 1980, 1983; Kachanov, 1992; Kachanov et al., 1994; Sayers and Kachanov, 1995; Liu et al., 2000; Kachanov, 2003; Grechka and Kachanov, 2006; Vernik and Kachanov, 2010). Kachanov (1992, 2003) concluded that compliance-based NIA remain sufficiently accurate at large crack density and strong interactions. He stated that the two competing interaction effects of stress shielding and stress amplification can counteract and cancel each other, so the pores and cracks interactions can be neglected. Another argument for the proponents of the compliance-based NIA is that this theory can yield reasonable estimate at high volume concentration of pores and cracks, while the stiffness-based NIA typically fail. Rather than assuming that fracture is a cluster of penny-shaped cracks, Schoenberg (1980, 1983) suggested to describe the fractures as planes of weakness with linear-slip boundary conditions, and the relations between the geometry of penny-shaped cracks and the fracture compliance have been derived by Schoenberg and Douma (1988), Sayers and Kachanov (1995).

So far, we have to bear in mind that the above mentioned NIA inclusion and crack theories ignore the elastic interactions between pores and cracks. Hence, theoretically, they can work only for dilute concentrations. However, these dilute limits (roughly, porosity less than 10 percent, crack density less than 0.1) make NIA theory not applicable for most sedimentary rocks. In reality, we usually deal with the rocks of

interest with porosity as high as 40 percent and/or crack density as high as 0.3 or more (Thomsen, 1985). As a result, it is of great interest to study how the pores and cracks interaction affect the elastic behavior of rocks.

To put it more specifically, the pore and cracks interactions reflect how the pores and cracks are organized or spatially distributed. As we know, the geometrical arrangement of the pores and cracks can have large variations due to their deposition and diagenesis history in geological time. Physically, such spatial distribution and correlation of pores and cracks can affect the local stress field and the resulting overall elastic properties. In order to study the effect of pores and cracks interactions, some rock physics schemes, such as self-consistent (SC) theory (Budiansky, 1965; Hill, 1965; Wu, 1966; Berryman, 1980, 1995; Hornby, 1994) and differential effective medium (DEM) theory (Norris, 1985; Zimmerman, 1991; Berryman, 1992; Nishizawa, 1982; Xu, 1998; Hornby, 1994), are proposed to handle large concentration of pores and cracks. These two rock physics schemes, simulating the pore and cracks interactions in a mathematical way, are relatively successful and certainly popular in the past decades. In contrast to DEM and SC that consider the elastic interactions implicitly, Jakobsen et al. (2003, 2004, 2009) formulates the effective stiffness using the T-matrix language to explicitly characterize the pore interactions. However, from the view of the practical application, it is hard to determine which is better. Because both can produce physically plausible results at large concentrations of inclusions. In this paper, we propose to use Biot-Gassmann consistency (Thomsen, 1985) to examine the physical foundation of elastic interaction accounted by DEM and SC, as well as T-matrix.

This chapter is organized as follows: First, to understand the physical assumption of NIA theories, we revisit the interaction energy approach to Eshelby's theory for calculating effective elastic constants under two boundary conditions. Then, we perform a finite element modeling to show how the stress amplification and stress shielding affect the stress distribution and the overall elasticity. Next, we discuss two rock physics schemes that characterize pores and cracks interactions: DEM and SC simulating the elastic interactions implicitly, and T-matrix theory taking into account the elastic interactions explicitly. Finally, we numerically compare the performance of different effective medium theories in modeling elastic response and the resulting anisotropy of the porous, cracked rock. We end up with the discussions and conclusions.

2.3 Biot-Gassmann Consistency

Biot-Gassmann theory (Gassmann, 1951; Biot, 1956) put a clear constraint between the elastic moduli of dry rock and saturated rock, without any restrictions on the specific pore geometry. To be specific, if the porosity is uniform and thus the pore pressure can be equilibrated, Biot-Gassmann theory can always work. Hence, when any effective medium theories meet such assumptions (no pore heterogeneities exist), theoretically, they should be a special case of Biot-Gassmann theory (Thomsen, 1985). Biot-Gassmann consistency should be naturally considered as a constraint to test the physical foundation of an effective medium theory. That is to say, if an effective medium theory is physically sound, it should predict the relationship between the

elastic response of dry rock and saturated rock as that predicted by Biot-Gassmann theory.

The low-frequency Biot-Gassmann (Gassmann, 1951; Biot, 1956) theory predicts the relationship between the rock's dry bulk modulus and the effective saturated bulk modulus using the following equation:

$$K_{sat} = K_{dry} + \frac{\alpha^2}{(\alpha - \phi) / K_0 + \phi / K_f} \quad (2.1)$$

$$\mu_{sat} = \mu_{dry} \quad (2.2)$$

Where K_{dry} is the effective bulk modulus of dry rock, K_{sat} is the effective bulk modulus of the rock with pore fluid, K_0 is the bulk modulus of mineral material making up rock, K_f is the effective bulk modulus of pore fluid, ϕ is the porosity, μ_{dry} is the effective shear modulus of dry rock, and μ_{sat} is the effective shear modulus of rock with pore fluid.

Biot-Gassmann equation can be extended into anisotropic media (Brown and Korrington, 1975; Mavko et. al, 2009), which is given below as:

$$s_{ijkl}^{sat} = s_{ijkl}^{dry} - \frac{(s_{ijaa}^{dry} - s_{ijaa}^0)(s_{bbkl}^{dry} - s_{bbkl}^0)}{(s_{ccdd}^{dry} - s_{ccdd}^0) + \phi(\beta_{fl} - \beta_0)} \quad (2.3)$$

where s_{ijkl}^{dry} is the effective elastic compliance tensor element of dry rock, s_{ijkl}^{sat} is the effective elastic compliance element of rock saturated with pore fluid, s_{ijkl}^0 is the

effective elastic compliance element of the solid mineral, β_f is the fluid compressibility = $1/\kappa_f$, and β_0 is the mineral compressibility.

2.4 Revist Interaction Energy Approach to Eshelby's Theory

By assuming the ellipsoidal inclusion in an infinite, homogeneous solid, Eshelby (1957) proposed to use interaction energy approach to calculate the effective elastic constants of the composite permeated with dilute concentrations of inhomogeneity. He suggested to formulate the solution under two boundary conditions: the constant load and the constant displacement at infinity. The following two equations are corresponding to the above two boundary conditions (Eshelby, 1957; Nishizawa, 1982; Xu, 1998), respectively:

$$\frac{1}{2} S_{ijkl}^* \sigma_{ij}^0 \sigma_{kl}^0 = E_0 - E_{\text{int}} , \quad (2.4)$$

$$\frac{1}{2} C_{ijkl}^* \sigma_{ij}^0 \sigma_{kl}^0 = E_0 + E_{\text{int}} , \quad (2.5)$$

where S_{ijkl}^* and C_{ijkl}^* are the effective compliance and the effective stiffness of the medium including elastic inhomogeneity, respectively. σ_{ij}^0 and e_{ij}^0 represent the stress and elastic strain of inhomogeneity-free medium, respectively; E_0 is an initial elastic energy, which can be expressed with applied stress or elastic strain at infinity; E_{int} is an interaction energy between the inhomogeneity and the applied elastic field, which can be calculated by the introduced “stress-free strain” (Eshelby, 1957) or eigenstrain (Mura, 1987). Note that the equation 2.4 and 2.5 hold only in the case of dilute

concentration of inclusions, where the change of elastic field caused by the presence of one inclusion does not affect the elastic energy of other inclusions (Eshelby, 1957; Nishizawa, 1982). The effective compliance under the constant load condition and the effective stiffness under the constant displacement condition can be derived from equation 2.4 and 2.5 as (Nishizawa, 1982; Xu, 1998):

$$S^* = S^0 + \sum_{r=1}^N v^r [(C^0 - C^r)E^r - C^0]^{-1} (C^r - C^0) S^0, \quad (2.6)$$

$$C^* = C^0 - \sum_{r=1}^N v^r C^0 [(C^0 - C^r)E^r - C^0]^{-1} (C^r - C^0), \quad (2.7)$$

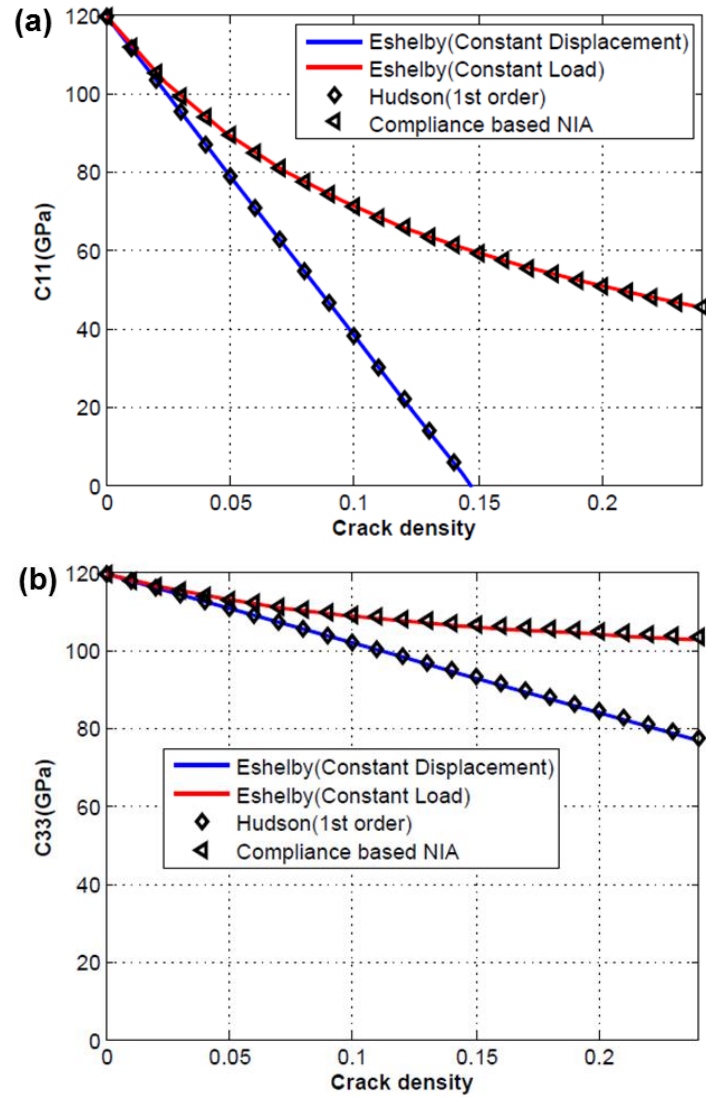
where C^0 and S^0 is the fourth-rank stiffness and compliance tensor of the host rock, respectively; v^r is the volume fraction of the inclusions ($r=1, 2, \dots, N$); C^r represents the stiffness tensor of the r th inclusion; E^r is the well-known Eshelby tensor (see **Appendix A**) of the r th inclusion, which relates the eigenstrain to the total strain (Mura, 1987). All those denotation will be also effective for the other equations in the later section.

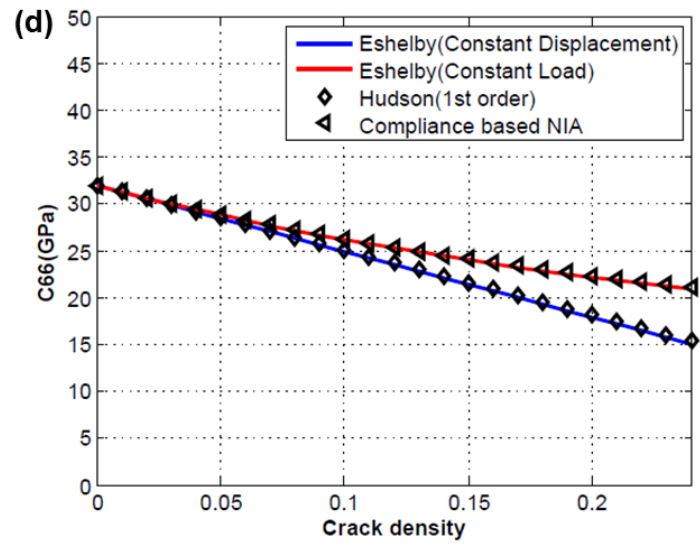
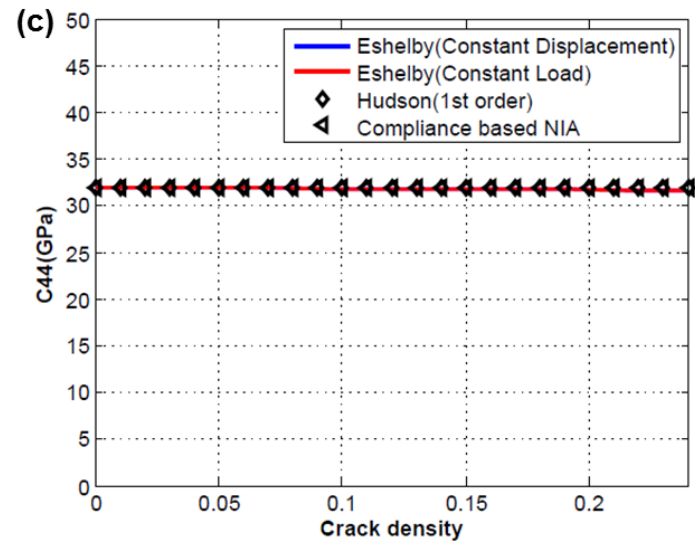
The comparison of the effective stiffness C11, C33, C44, C66, and C13 as a function of crack density predicted by different NIA approaches are displayed in Figure 2.1. In our modeling, cracks are vertically aligned and parallel to each other in an isotropic host rock, the resultant cracked rock is transversely isotropic with a horizontal symmetry axis (HTI). The host matrix is assumed to be calcite ($K = 76.8 \text{ GPa}, \mu = 32 \text{ GPa}$), and the aspect ratio of the cracks is set as 0.01. There are five independent components in the effective elastic stiffness tensors, C11 and

C33 correspond to the P-wave propagating perpendicular and parallel to the crack plane, and C44 and C66 are related to the polarization of the S-wave parallel and perpendicular to the crack plane. The volume crack density ε (O'Connell and Budiansky, 1974; Hudson, 1980) is determined by the crack aspect ratio and the crack-induced porosity. If no other specific instructions, all the numerical simulations in this paper will be based on this cracked model.

As we can see in Figure 2.1, the effective stiffness predicted by the first-order Hudson's theory are functionally equivalent to Eshelby's formulation under the constant displacement boundary condition (Equation 2.7). And the effective stiffness predicted by compliance-based NIA (or linear-slip theory) are functionally equivalent to the Eshelby's formulation under the constant load boundary condition (Equation 2.6). It is important to be aware that such equivalence can only be valid when the aspect ratio is very small. Because, in this way, the ellipsoidal inclusions can be considered as penny-shaped cracks, and hence satisfy the assumption for the geometry of fractures in Hudson's theory and compliance-based NIA. Remember that the interaction energy approach under the constant load and constant displacement boundary condition to calculate the effective elastic constants can only work in dilute concentrations. In other words, we can state that, the two most popular fracture models - the first-order Hudson's theory and the compliance-based NIA - can only predict physically reasonable effective elastic response at dilute concentrations. This is consistent with our numerical observation that the stiffness-based NIA and compliance-based NIA are basically in agreement with each other at very small crack density. However, they start to deviate from each other when the crack density

increases beyond around 0.03. In addition, at high crack density, the stiffness-based NIA typically breaks down, while the compliance-based NIA seems to still produce reasonable estimates. In the later section, we will use a numerical example to demonstrate that this mathematically reasonable estimate by compliance NIA is misleading.





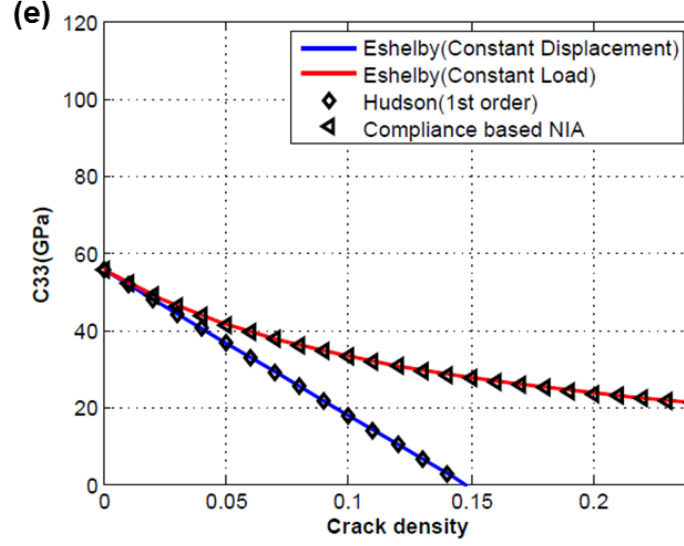


Figure 2.1. Comparison of (a) C_{11} , (b) C_{33} , (c) C_{44} , (d) C_{66} , and (e) C_{13} as a function of crack density predicted by different non-interacting effective medium theories. Blue line, red line, left triangle symbol, and diamonds symbol represents prediction based on Eshelby's formulation under constant displacement boundary condition, Eshelby's formulation under constant load boundary condition, first order Hudson theory, and compliance-based NIA, respectively.

2.5 A Numerical Experiment on Stress Interaction

In this section, finite-element modeling (Software COMSOL) is employed to investigate the stress interactions between cracks. We simulate the remote stress boundary conditions by applying a constant load (70,000Pa) to a homogeneous 2D solid matrix ($E=70$ GPa, $\nu = 0.33$). The aspect ratio of the ellipsoidal inclusion is set as 0.1 to mimic the geometry of cracks. Figure 2.2 shows the first principal stress behavior by introducing different sets of cracks into the homogeneous solid matrix, and Table 1 shows the corresponding normalized volumetric strain. Figure 2.2(b)

shows the stress distribution when the two introduced cracks are far apart to each other, to mimic the non-interacting situation. For each crack, we observe that the stress concentration (stress magnitude is greater than the background) occurs at crack tips and stress dilution (stress magnitude is less than the background) takes places at crack faces. Stress field concentration and dilution for one crack is schematically illustrated using the iso-stress lines in Figure 2.3. To depict the stress field, the density of iso-stress lines at certain location indicates the intensity of stress magnitude. For example, the density of iso-stress line at crack tips are much higher than that at the crack face, which suggests that the stress magnitude is much more intense at the crack tips. As shown in Table 1, the normalized volumetric strain consequently increases to 13.2 from 1 due to the extra strain of two non-interacting cracks. Figure 2.2(c) shows the stress distribution when crack tips approach closely to each other. As expected, the local stress magnitude between the tips of the cracks increases dramatically. Note that the resulting volumetric strain increases to 17, which is higher than the non-interacting situation. This can be understood, because the stress amplification dominates the stress interaction and thus increases the overall strain. Similarly, the stress shielding dominates the stress interaction when the crack faces approach closely to each other as shown in Figure 2.2(d), and hence the volumetric strain decreases considerably compared with the non-interacting situation. As a result, the effective stiffness tends to be higher when stress shielding dominates the stress interactions, while the effective stiffness tends to be lower when stress amplification dominates the stress interactions. Those stress amplification and stress shielding phenomenon are schematically illustrated using iso-stress lines in Figure 2.4.

Based on this numerical experiment, we can infer that, for the dilute concentration of pores and cracks, stress interactions can be reasonably ignored, since the pores and cracks have high chance to be far apart to each other in a representative volume. However, for large concentration of pores and cracks, both stress amplification and stress shielding are getting stronger as pores and cracks have high chance to approach to each other, and therefore the elastic interactions should be taken into account to calculate the elastic response. This also explains why NIA can work in dilute concentration of pores, while producing unreasonable prediction when the inclusion concentration increases beyond the dilute limit. Furthermore, as illustrated in the numerical experiment, whether the stress shielding or amplification dominates the overall effect on the final effective stiffness depends on the spatial arrangements of the pores and cracks. Therefore, it is necessary to find a way to characterize such spatial arrangement in order to properly model the elastic interactions.

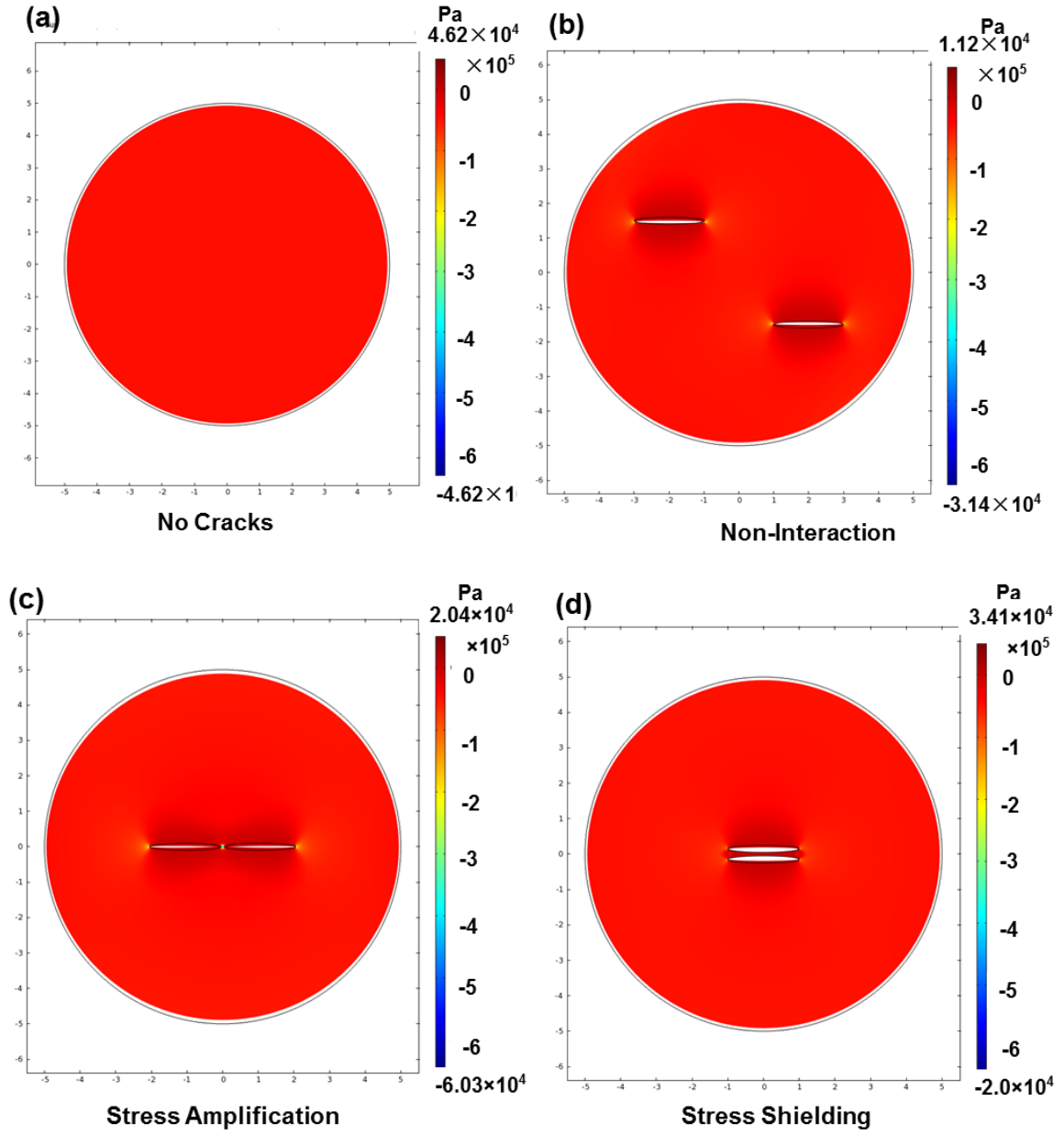


Figure 2.2. Comparison of the first principal stress distribution by introducing different set of cracks into the homogeneous solid matrix: (a) No cracks, (b) Cracks are far apart from each other, (c) Coplanar cracks, and (d) Stacked cracks. The host solid matrix is set as 2D circle geometry. The color-bar indicate the magnitude of stress in the unit of Pa.

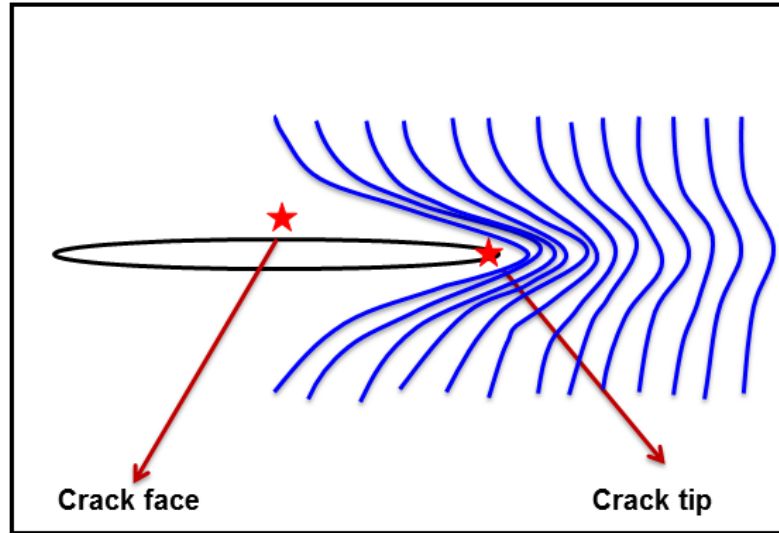


Figure 2.3. Schematic illustrations of stress concentration and dilution on one crack in the homogeneous solid matrix. Blue line indicates the iso-stress line. These lines are not physical lines that are actually present at certain locations, but are merely used to represent the stress field magnitude.

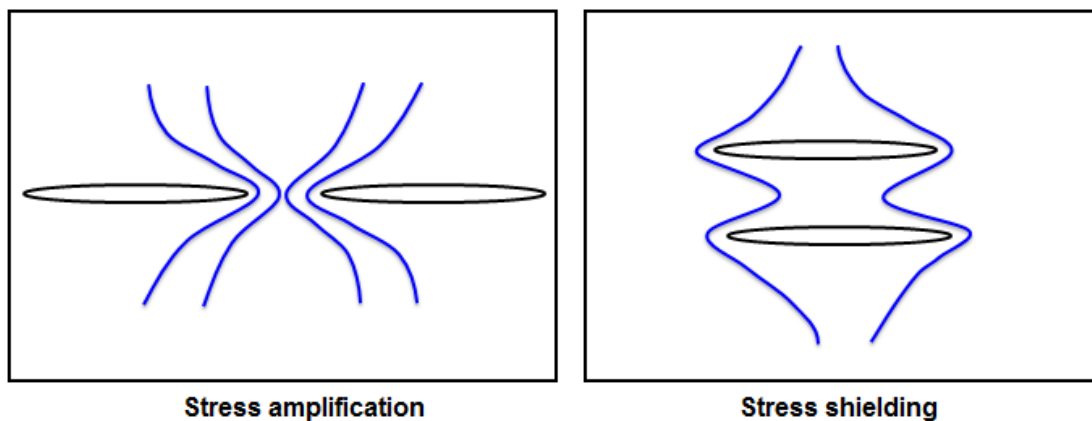


Figure 2.4. Schematic illustrations of stress interaction between two cracks: (left) coplanar cracks, (right) stacked cracks. Blue line indicates the iso-stress line as displayed in Figure 2.3.

Table 2.1. Comparison of normalized volumetric strain that corresponds to different stress interaction situation in Figure 2.2.

No cracks	Non-interaction	Stress Shielding	Stress Amplification
1	13.2	9.3	17.1

2.6 DEM AND SC: Modeling Elastic Interactions Implicitly

To overcome the dilute limit of NIA, two popular rock physics schemes, self-consistent approximation (SCA) and differential effective medium (DEM) theories, are developed to indirectly include the pores and cracks interactions. In SCA, the contribution of excess strain due to deformation of the ellipsoidal inclusion is still employed, but the elastic interactions of inclusions are approximated by replacing the background medium with the as-yet-unknown effective medium (Berryman, 1995). Through an iterative manner, SCA yields the effective estimate through mixing all phases, including minerals and pores, present in the rock. The effective stiffness tensor in the SCA model can be expressed as (Hornby et al., 1994; Bandyopadhyay, 2009):

$$\sum_{r=1}^N v_r (C^r - C^{SCA}) \left[1 + G^r (C^r - C^{SCA}) \right]^{-1} = 0. \quad (2.8)$$

Here, C^{SCA} indicates the self-consistent effective elastic stiffness, G^r is a fourth-rank tensor given by the strain Green's function integrated over characteristic inclusion shape (Mura, 1987):

$$G_{ijkl}^r = \frac{1}{8\pi} [\bar{G}_{ikjl} + \bar{G}_{jkil}], \quad (2.9)$$

and the non-zero components of \bar{G}_{ijkl} (see **Appendix B**) for a transversely isotropic system are given by Lin and Mura (1973).

However, in SCA, embedding a pore into an effective medium already containing the pore itself implies that the interactions of pores are taken into account twice. Bruner (1976) criticized that the self-consistent method might cause an overestimate of the elastic interactions between pores. To avoid the double-counting pore interactions in SCA, one can introduce the pores into the rock sequentially, with pore $n + 1$ considered to be added into a reference medium which has the effective elastic properties with n pores. In this way, pore $n + 1$ feels the elastic effect of n pores, but not vice versa (Jaeger et al., 2007). In the DEM, a small amount of inclusions of one phase is incrementally added to a background host medium iteratively. The process is continued until the desired proportion of the constituents is reached. The change in effective elastic stiffness dC due to an increase of the i th component dv is (Hornby, 1994; Xu, 1998):

$$\frac{d}{dv}(C^{DEM}(v)) = \frac{1}{1-v}(C^r - C^{DEM}(v)) \times [I + G^r(C^r - C^{DEM}(v))]^{-1}. \quad (2.10)$$

An important conceptual difference between the DEM and SCA schemes is that the DEM scheme treats each constituent asymmetrically with a preferred host matrix, whereas the SCA scheme does not identify any specific host material but treats the composite as an aggregate of all the constituents (Mavko et al., 2009).

2.6.1 DEM and SCA to Biot-Gassmann Consistency

As previously mentioned in the introduction, we now employ the Biot-Gassmann consistency to test whether DEM and SCA handle the elastic interactions in a physically sound way. We can observe from Figure 2.5 that the saturated stiffness C_{11} by DEM and SCA are not in agreement with those predicted by applying Brown-Korrington's relations to the dry C_{11} and C_{33} computed with DEM and SCA (Figure 2.5(a) and (b)). This demonstrates that DEM and SCA are not consistent with Biot-Gassmann theory, which also implies that the pores and cracks interactions simulated by DEM and SC lack of physical foundation.

2.7 T-matrix to Characterize Elastic Interactions

2.7.1 T-matrix Formulation

Estimating effective elastic constant of composites can be considered as a many-body problem, and T-matrix approach of quantum scattering theory can be used to attack such a many-body problem. Based on multiple-point correlation functions, the T-matrix language explicitly takes into account the elastic interactions between inclusions to compute the effective elastic properties. The integral equation for effective elastic constants of macroscopically homogeneous materials with statistical fluctuation of properties at the microscopic level is very similar to the Lippmann-Schwinger-Dyson equation of multiple scattering in quantum mechanics (Mavko et al., 2009). The effective stiffness C_T^* of the cracked, porous medium using T-matrix approach is formulated by Jakobsen et al. (2003, 2004):

$$C_T^* = C^0 + \langle T_1 \rangle \left(I - \langle T_1 \rangle^{-1} X \right)^{-1}, \quad (2.11)$$

where

$$\langle T_1 \rangle = \sum_{r=1}^N v^r t^r, \quad (2.12)$$

$$t^r = \delta C^r (I - G^r \delta C^r)^{-1}, \quad (2.13)$$

and

$$\delta C^r = C^r - C^0. \quad (2.14)$$

Here, X is the second-order correction for the effects of inclusion tensor.

$$X = - \sum_{r=1}^N \sum_{s=1}^N v^r t^r G_d^{rs} v^s t^s, \quad (2.15)$$

where G_d^{rs} represents the two-point interaction between the r th set and s th set of inclusions. The fourth-rank tensor G_d^{rs} can be obtained in the same way as G^r (see equation 2.9) except that the aspect ratio of the inclusion α_r is set as the aspect ratio of spatial distribution α_d .

The definition of the aspect ratio of inclusion α_r and aspect ratio of spatial distribution α_d are schematically displayed in Figure 2.6. In fact, the concept of aspect ratio of spatial distribution represents the conditional probability of finding another inclusion given the position of an inclusion. Figure 2.7 is an example to show that the individual crack in the two rocks has the same aspect ratio, but organized in a different way. If $\alpha_d < 1$, it indicates that the probability of an inclusion showing up

in the X (vertical) direction is higher than the probability of finding an inclusion in the Y direction. Ponte-Castaneda and Willis (1995) pointed out that the maximum value for aspect ratio of spatial distribution α_d should satisfy the relationship $\alpha_{d(\max)} = \alpha_r / v$, where v is the volume concentration of inclusion.

It is evident to see that the first-order T-matrix formulation is in agreement with the dilute estimate of Eshelby's formulation under the constant displacement condition. In Figure 2.8, the dashed straight lines represent the stiffness-based NIA predictions, and the solid lines, exhibiting non-linear relationship with crack density, are for the high-order T-matrix predictions taking into account the elastic interactions. C11 and C33 predicted by stiffness-based NIA typically break down when crack density is over 0.15. However, the high order T-matrix can yield physically plausible estimates at high crack density. They overlap at crack density less than 0.02, but are markedly separated at high crack density. This also suggests that the stress interactions are strong and can't be ignored at high crack density.

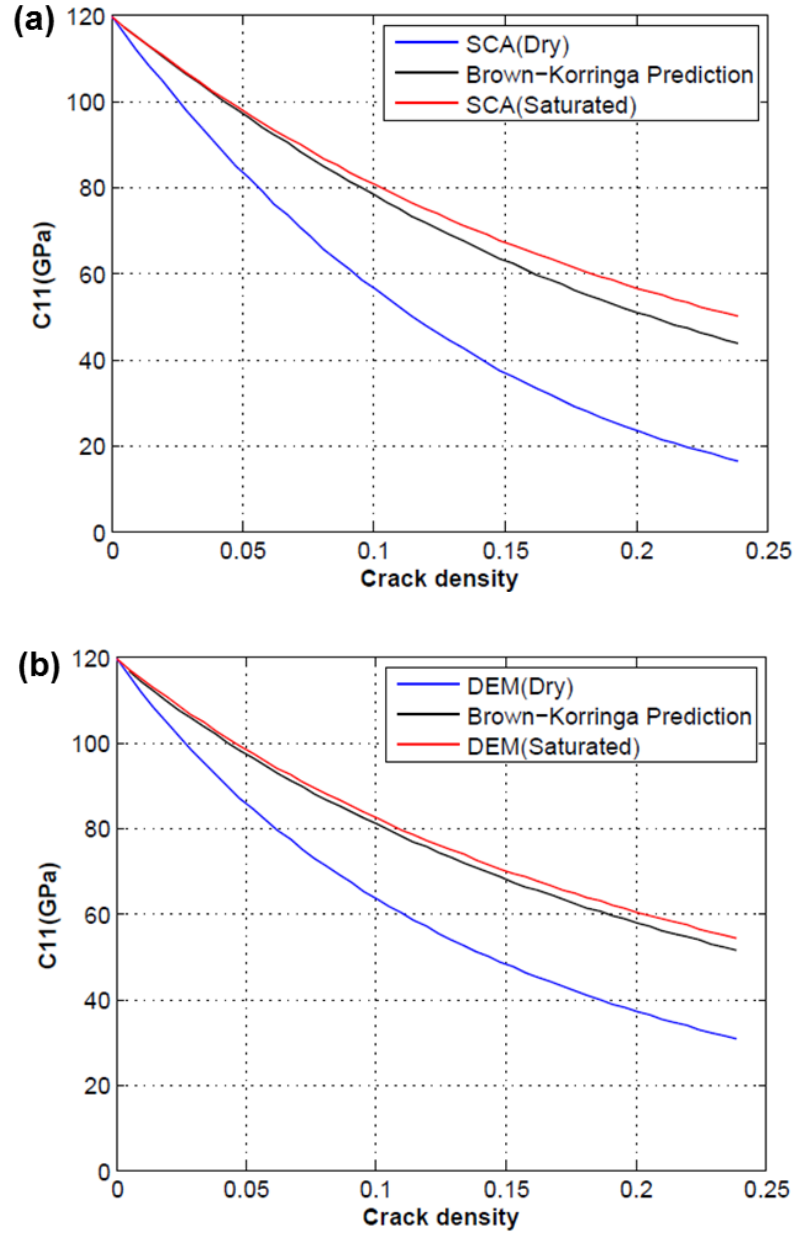


Figure 2.5. The effective elastic stiffness C_{11} as a function of crack density simulated by (a) SCA, (b) DEM. Blue line represents elastic response of dry rock simulated by DEM/SCA. Red line and black line indicate elastic stiffness for saturated rock predicted by DEM/SCA and Brown-Korringa relations, respectively.

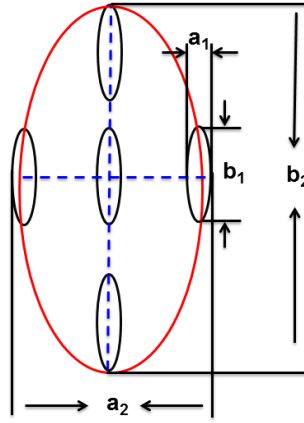


Figure 2.6. Schematic illustration of a 2D cross section through the 3D ellipsoidal crack distribution in the T-matrix model. The aspect ratio of the individual cracks is a_1/b_1 , and the aspect ratio of the crack distribution is a_2/b_2 .

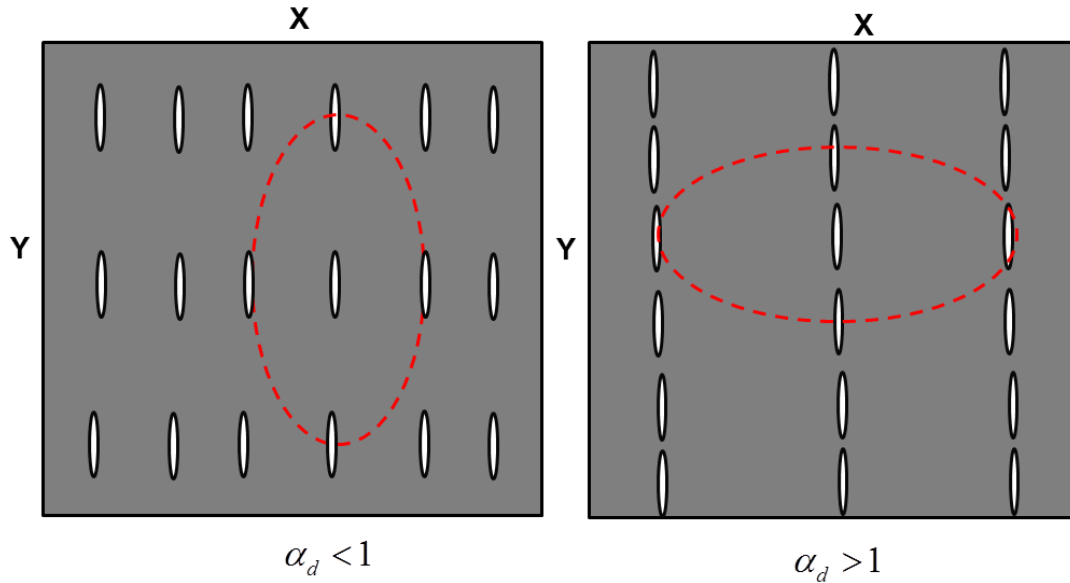


Figure 2.7. An example to illustrate the concept of aspect ratio of spatial distribution as the conditional probability to find another inclusion given the position of an inclusion. Each individual crack has the same aspect ratio, but organized in a different way. (left) aspect ratio of spatial distribution is smaller than 1; (right) aspect ratio of spatial distribution is bigger than 1.

2.7.2 Effect of Spatial Distribution on Effective Stiffness

Figure 2.9 is used to illustrate the influence of the aspect ratio of the inclusion and aspect ratio of the spatial distribution on the stiffness of C11. Clearly, compared with aspect ratio of spatial distribution, the aspect ratio of inclusion still has the dominant impact on controlling the rock's overall elastic behavior. It is also interesting to see that the elastic stiffness exhibit different sensitivity to the aspect ratio of spatial distribution when the aspect ratio of inclusion varies. Generally, the aspect ratio of spatial distribution has bigger impact on the effective elastic stiffness when the aspect ratio of inclusion is lower. This can be understood, because when the aspect ratio of the crack is smaller, local stress field can readily exhibit concentration and dilution, and the stress interactions consequently have bigger impact. We can also read that the computed elastic stiffness decrease with the increasing aspect ratio of spatial distribution. This can be explained by the variation of stress field due to the crack interactions. When the aspect ratio of the spatial distribution increases, the crack tips will approach closer and closer. As a result, the stress amplification will increase much stronger than the stress shielding, and the effective elastic stiffness will decrease accordingly. This is consistent with the numerical experiment about the stress interactions we present in the Figure 2.2, and demonstrates that the parameter “aspect ratio of spatial distribution” can successfully characterize the competing effects about stress shielding and amplification.

We also evaluate the interaction effects on both dry and brine-filled cracks and compare them in the Figure 2.9(a) and Figure 2.9(b). The results show that, for the brine-filled cracks, the elastic stiffness C11 has less sensitivity to the variation of

aspect ratio of spatial distribution. Physically, this makes sense because the brine often drastically stiffens the very compliant cracks (Schoenberg and Sayers, 1995). As a result, the stress interactions are getting weaker and have less impact on the effective elastic stiffness.

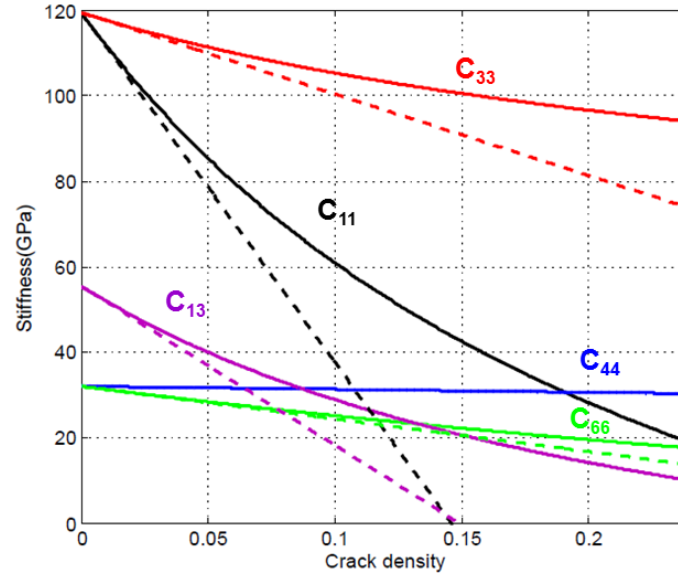


Figure 2.8. Effective elastic properties of cracked carbonate as a function of crack density. C_{11} , C_{33} , C_{13} , C_{44} , and C_{66} represent five independent elastic stiffness constants in HTI medium. The aspect ratio of the crack is set as 0.05, and the aspect ratio of spatial distribution is set as 1.0.

2.7.3 T-matrix to Biot-Gassmann Consistency

We test the Biot-Gassmann consistency on the T-matrix modeling results as shown in Figure 2.10. It turns out that the saturated stiffness C_{11} and C_{33} directly computed by T-matrix exactly matches those predicted by applying Brown-Korringa's relations to the dry C_{11} and C_{33} computed with T-matrix. It is also easy to illustrate that the

C44 and C66 do not change with fluid saturation. This indicates that T-matrix is consistent with Biot-Gassmann theory, and verifies that T-matrix characterize the crack interactions with physical foundation.

2.8 Comparison of Different Effective Medium Theories

The comparisons of T-matrix with Hudson's crack theory, compliance-based NIA, SCA, and DEM model are displayed in Figure 2.11. As expected, the several predictions largely agree with each other when the crack density is low, but there are significant differences at high crack density. This illustrates the importance of including the effects of spatial distribution when coping with non-dilute concentration of pores and cracks. The compliance-based NIA gives the best match with the T-matrix when the aspect ratio of spatial distribution is very small, which represents the crack interaction effect dominated by stress shielding. However, this should not be treated as physical equivalence. The compliance-based NIA does not take into consideration the crack interactions. Nonetheless, those pores and cracks interactions are explicitly characterized in the T-matrix formulation. Additional insight can be gained from this comparison is that the SCA and DEM prediction approach the T-matrix prediction when the aspect ratio of the spatial distribution is 1. And this is in agreement with the assumption of SCA and DEM, in which the cracks are randomly distributed and interacted.

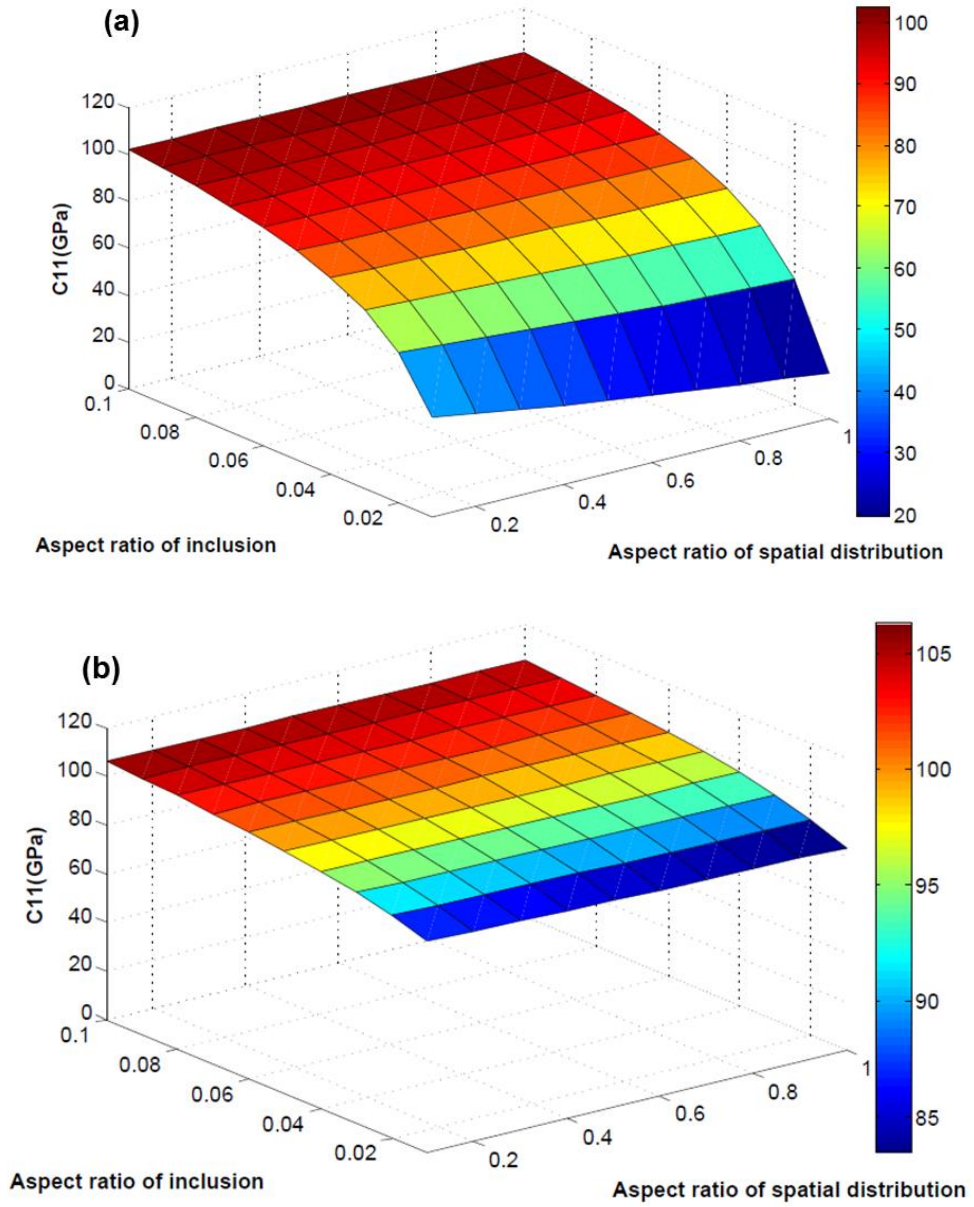


Figure 2.9. Computed elastic stiffness C_{11} as a function of aspect ratio of inclusion and aspect ratio of spatial distribution. Porosity is set as 0.01. Data are color-coded by the value of effective elastic stiffness. Cracks are assumed (a) dry, and (b) brine saturated.

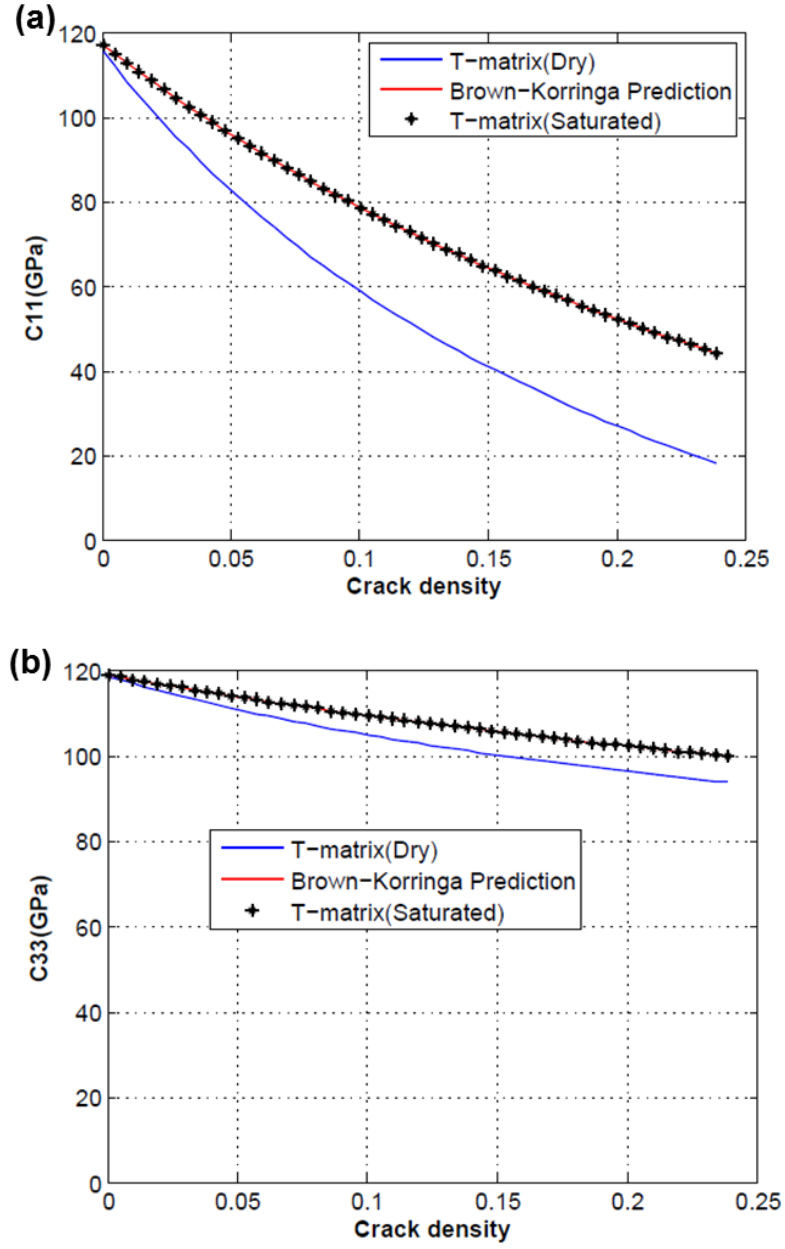


Figure 2.10. The effective elastic stiffness C_{11} (a), and C_{33} (b) as a function of crack density. Blue line represents elastic response of dry rock simulated by T-matrix. The aspect ratio of the crack is set as 0.05, and the aspect ratio of spatial distribution is set as 1.0.

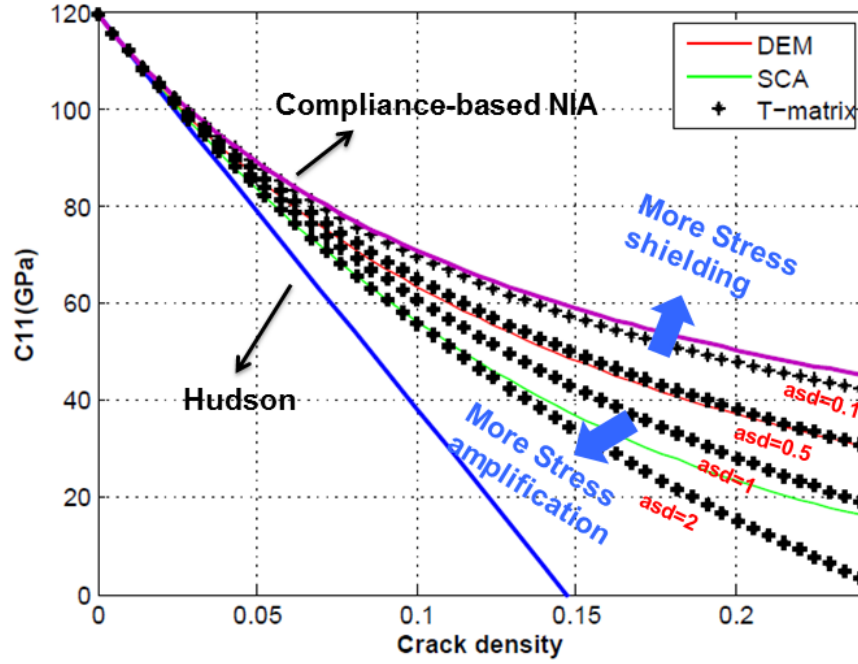


Figure 2.11. Comparison of C_{11} as a function of crack density predicted by different effective medium theories. The aspect ratio of the crack is set as 0.05. Blue line, purple line, red line and green line represents prediction by stiffness-based NIA, compliance-based NIA, DEM prediction and SC prediction, respectively. Black dashed lines indicate the T-matrix predicted with different aspect ratio of spatial distribution.

In Figure 2.12, we use a numerical example to demonstrate the effective elastic stiffness predicted by the compliance-based NIA, which appears mathematically reasonable, but is not physically reasonable. We assume the aspect ratio of the inclusion is 1.0, suggesting no anisotropy occurs in this case. When the porosity is 100%, theoretically, the effective bulk modulus of the rock should be zero as Kuster-

Toksöz model and T-matrix predicted. However, the compliance-based NIA increasingly overestimate the moduli as the porosity increases, and this overestimation is evident from the fact that it predicts finite elastic moduli when the porosity reaches 100%. Such overestimate of effective elastic stiffness-based on NIA is also reported by Hu et al. (2009) and Jaeger et al. (2007). In addition, this demonstrates that it is lack of physical foundation to assume that the elastic interactions can be ignored at large concentrations of pores.

As displayed in Figure 2.13, we also examine how the spatial distribution of cracks affects the seismic anisotropic parameters introduced for HTI media by Rüger (1997) and Tsvankin (1997). It is clear that the impacts of spatial distribution on the seismic anisotropy become increasingly important when the inclusion concentrations increase beyond the dilute limit. Generally, the seismic anisotropy will increase as the aspect ratio of spatial distribution increase. In other words, the stress amplification effect will enhance the amplitude of seismic anisotropy.

Moreover, the gamma parameter, which is a measure of shear-wave splitting, has been pointed out in many papers (e.g. Bakulin et al., 2000), is approximate to crack density which indicate the degree of fracturing. Figure 2.13(b) makes clearly that this estimation is roughly reasonable when the crack density is lower than 0.1. Nevertheless, at high crack density, when stress shielding dominates the crack interactions (aspect ratio of the spatial distribution is small), the anisotropic parameter gamma gives a significantly higher estimate of crack density ($|\gamma| < e$). From Figure 2.13, we also observe that the elliptical anisotropy $\eta = |\varepsilon - \delta|$, which is an important

parameter for P-wave time processing in anisotropic media, approximated as zero based on the compliance-based NIA. However, T-matrix for large aspect ratio of spatial distribution can typically predict positive elliptical anisotropy.

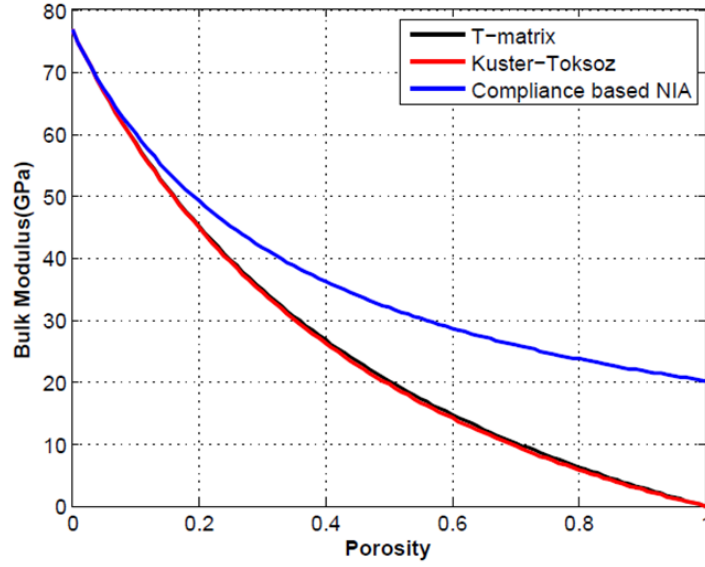


Figure 2.12. Elastic modulus of rocks containing dry, randomly distributed spherical pores, according to various effective medium theories. Red line, black line, and blue line represents predicted bulk modulus by K-T model, T-matrix, and compliance-based NIA, respectively. For T-matrix modeling, the aspect ratio of spatial distribution is set as 1.0.

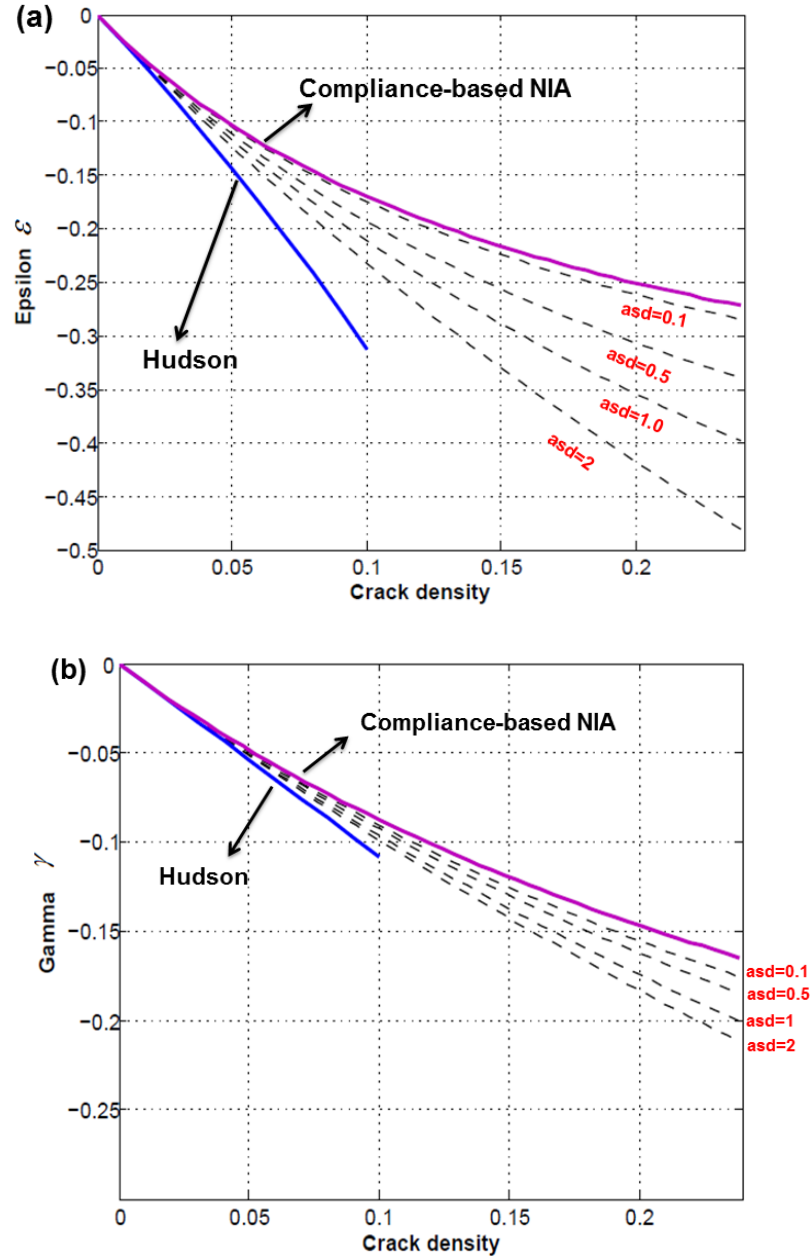


Figure 2.13. Comparisons of predictions of Thomsen's anisotropic parameters as a function of crack density: (a) Epsilon, (b) Gamma, and (c) Delta. Blue line and purple line represent prediction by stiffness-based NIA and compliance-based NIA, respectively.

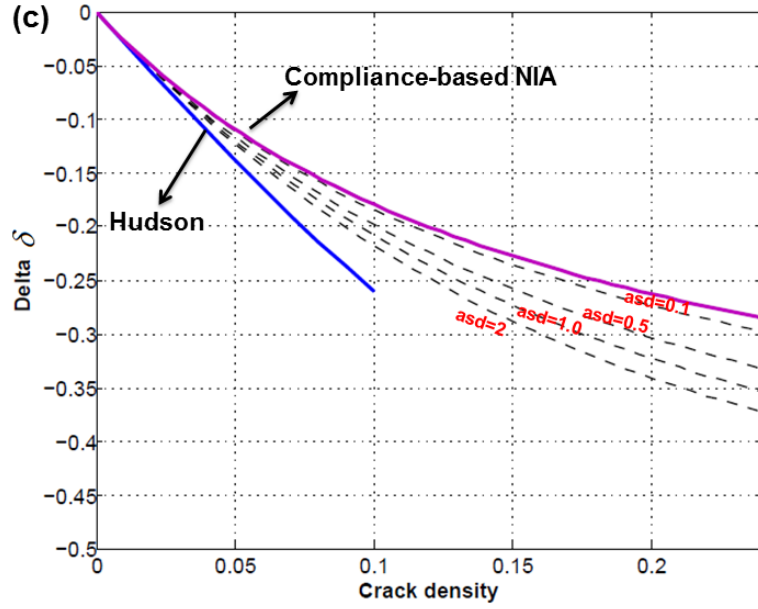


Figure 2.13 (continued). Comparisons of predictions of Thomsen's anisotropic parameters as a function of crack density: (a) Epsilon, (b) Gamma, and (c) Delta. Blue line and purple line represent prediction by stiffness-based NIA and compliance-based NIA, respectively.

2.9 Discussion

For a long time, Hudson's crack model and the compliance-based NIA (or the liner-slip theory) have been the two most popular rock physics schemes in modeling cracked rocks. We numerically demonstrate that the first-order Hudson's theory are functionally equivalent to the Eshelby's dilute estimate under the constant displacement boundary condition, and the compliance-based NIA are functionally equivalent to the Eshelby's dilute estimate under the constant load boundary condition. This may provide insight into explaining the physical discrepancy between the stiffness-based NIA and compliance-based NIA, not merely the mathematical

difference by inverting the compliance tensor into stiffness tensor. This further explains why those two popular effective media schemes are incapable of producing physically plausible estimates at high crack density.

It is also necessary to point out that the Biot-consistency can be applicable only when no porosity heterogeneity exists. Actually, we believe that no effective medium theory for rock elasticity can be Biot-consistent when pore heterogeneities are present in the rocks, because it can't handle the pore pressure equilibration induced by the stress heterogeneity. Figure 2.14 illustrates the fluid saturation effect in the case where both stiff pores (aspect ratio is 0.5) and thin cracks (aspect ratio is 0.05) are present. The saturated stiffness simulated by T-matrix clearly deviates from the prediction by Brown-Korringa's relations when cracks are present, which suggests that the T-matrix is not consistent with Biot-Gassmann theory if elastic heterogeneities exist. Since the cracks are much more compliant than the pores, fluid may flow from cracks to stiff pores, and this fluid pressure equalization is a time-dependent process. The T-matrix prediction represents the status where the fluid starts to flow (high frequency limit), and the Brown-Korringa prediction represents the status where the fluid flow reaches the maximum quantity (low frequency limit). The difference between those two statuses is considered as the dispersion effect, and this dispersion effect, as expected, is getting stronger with increasing crack density. For detailed analysis on frequency-dependent elastic response due to the fluid flow between stiff matrix porosity and compliant fractures, see Thomsen (1995), Chapman et al. (2002), Gurevich (2003), and Jakobsen and Chapman (2009).

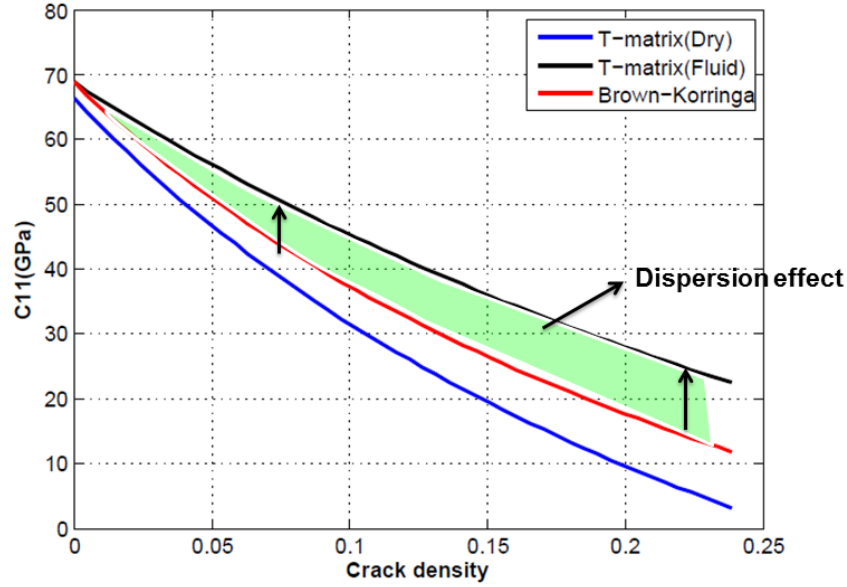


Figure 2.14. Variation of the elastic stiffness C_{11} with increasing crack density. The solid matrix is calcite and the matrix (stiff) porosity is 0.2. The aspect ratio of the matrix porosity and cracks are set as 0.5 and 0.05, respectively. The aspect ratio of spatial distribution is defined as 1.0 for T-matrix modeling. Blue line represents stiffness of dry rock, red line represents stiffness predicted by Brown-Korringa relations, and black line indicates the brine-saturated stiffness simulated by T-matrix. The shadow zone indicates the dispersion effects.

In this paper, we have proposed a clear guideline on how to select a convincing effective medium theory to characterize the elastic response for fractured, porous rock. The primary differences for the various inclusion and crack models presented here lie in their strategies for extrapolating the exact expression for deformation of a single ellipsoidal inclusion (Eshelby, 1957) to handling the elastic interactions between inclusions (Mavko, 2008). Theoretically, a good effective medium theory should

satisfy two conditions. First of all, it should work beyond dilute limit; secondly, it should characterize the pores and cracks interactions with physical foundations (or consistent with Biot-Gassmann theory). However, from the perspective of practical application, different effective medium theories can be selected according to the geological condition and pores or cracks distribution configuration. For example, DEM and SCA can work pretty well for randomly distributed pores and cracks. For not heavily cracked reservoir rocks, Hudson theory and compliance-based NIA can still be used to link crack density to the effective elastic properties with physical meaning.

The inclusion and crack model we present here is formulated on the basis of the assumption that the pore geometry is ellipsoidal. However, in real sedimentary rocks, geometry of pore and cracks are almost never ellipsoidal and often exhibit hopelessly complex and irregular microstructure. Some attempts have been made to model the effective elastic moduli when the pore shapes are not ellipsoidal (Mavko and Nur, 1978; Schoenberg, 1980; Zimmerman, 1991; Hudson and Liu, 1999). Indeed, it is impossible to create an exact physical model to mimic the elastic behavior of real porous, cracked rocks. More importantly, capturing the detailed characteristic about pores and cracks might be beyond the capability of the long-wavelength seismic data with a realistic noise level. What we are concerned more are the statistical features of the cracks or pores in the rocks. Based on micromechanics analysis, Grechka and Kachanov (2006) also concluded that a number of geometric features of cracks, such as random irregularities of fracture shapes, are insignificant for estimating the

effective elastic properties. Therefore, the current approach to treat the pore geometry as ellipsoidal is primarily still feasible to model the effective elastic properties of real rocks.

2.10 Conclusions

The spatial arrangements of pores and cracks, which are mainly controlled and organized by geological processes, can naturally cause the local elastic field variation and hence affect the effective elastic response. We use finite element modeling method to illustrate that stress amplification due to coplanar cracks significantly increases the volumetric strain, and the stress shielding due to stacked cracks significantly decreases the volumetric strain. Rather than only using the volume concentration and geometric features of pores and cracks, we suggest the elastic interactions between the pores and cracks should be taken into account to compute the effective elastic properties.

DEM and SCA implicitly handle the elastic interactions between pores and cracks, but are illustrated not Biot-Gassmann consistent. This implies that the elastic interactions simulated by DEM and SCA lack of physical foundation. T-matrix approach which takes into account the ellipsoid distribution of pores or cracks, can produce physically plausible result even at large concentration, and it is always consistent with Biot-Gassmann theory when no pore heterogeneity exists. This suggests that T-matrix explicitly characterizes the pores and crack interactions with physical foundation, and we recommend that T-matrix is a more physically reliable approach to model the effective elastic properties for the cracked, porous rock.

Numerical results further demonstrate that the varying spatial distribution of pores and cracks can significantly affect rock's elastic response and the resulting seismic anisotropy, and this impact cannot be ignored when the inclusion concentrations increases beyond the dilute limit. However, the impact of such stress interaction can be mitigated for pores with large aspect ratio or filled with liquid.

2.11 Acknowledgement

This work was sponsored by Fluids and DHI consortium of the Colorado School of Mines and University of Houston. Special thanks also go to Dr. Leon Thomsen and Dr. Enru Liu for their illuminating discussions.

2.12 Appendix A-- Evaluation of Eshelby Tensor

Eshelby tensor is generally given in terms of elliptic integrals of the first and second kinds (Eshelby, 1957; Mura, 1987). Assuming that the ellipsoid semi-axes a_1 , a_2 , a_3 are ordered as $a_1 > a_2 > a_3$, the components of the fourth-order Eshelby tensor E_{ijkl} of the r th inclusion are given by the following expressions:

$$E_{1111}^r = \frac{3}{8\pi(1-\nu)} a_1^2 I_{11} + \frac{1-2\nu}{8\pi(1-\nu)} I_1,$$

$$E_{1122}^r = \frac{3}{8\pi(1-\nu)} a_1^2 I_{12} - \frac{1-2\nu}{8\pi(1-\nu)} I_1,$$

$$E_{1133}^r = \frac{3}{8\pi(1-\nu)} a_1^2 I_{13} - \frac{1-2\nu}{8\pi(1-\nu)} I_1,$$

$$E_{1212}^r = \frac{a_1^2 + a_2^2}{16\pi(1-\nu)} I_{12} + \frac{1-2\nu}{16\pi(1-\nu)} (I_1 + I_2),$$

where ν is the Possion ratio of the matrix, and $I_1, I_2,$ and I_3 is given below as:

$$I_1 = 2\pi a_1 a_2 a_3 \int_0^\infty \frac{ds}{(a_1^2 + s)\Delta(s)},$$

$$I_{11} = 2\pi a_1 a_2 a_3 \int_0^\infty \frac{ds}{(a_1^2 + s)^2 \Delta(s)},$$

$$I_{12} = 2\pi a_1 a_2 a_3 \int_0^\infty \frac{ds}{(a_1^2 + s)(a_2^2 + s)\Delta(s)},$$

with $\Delta(s) = (a_1^2 + s)^{1/2} (a_2^2 + s)^{1/2} (a_3^2 + s)^{1/2}$. The reaming coefficients are found by simultaneous cyclic permutation of (1, 2, 3) and (a_1, a_2, a_3) .

All other non-zero components are obtained by the cyclic permutation of (1, 2, 3), and should satisfy the relationship $E_{ijkl}^r = E_{jikl}^r = E_{ijlk}^r$. The components which cannot be obtained by the cyclic permutation are zero.

If the inclusion refers to spheres, to calculate the Eshelby tensor, one can use $a_1 = a_2 = a_3$. Also, if the inclusion refers to a typical penny-shaped cracks, $a_1 = a_2 \gg a_3$.

2.13 Appendix B-- Evaluation of Tensor \bar{G}_{ijkl}

The tensor \bar{G}_{ijkl} used to calculate G_{ijkl}^r tensor for the transversely isotropic media in equation 2.9 are given by Lin and Mura (1973) and Nishizawa (1982). It has 12 non-zero elements, and they are shown by the following integral form:

$$\bar{G}_{1111} = \bar{G}_{2222} = \frac{\pi}{2} \int_0^1 \Delta(1-x^2) \{ [f(1-x^2) + h\rho^2 x^2] [(3e+d)(1-x^2) + 4f\rho^2 x^2] - g^2 \rho^2 x^2 (1-x^2) \} dx$$

$$\bar{G}_{3333} = 4\pi \int_0^1 \Delta \rho^2 x^2 \{ [d(1-x^2) + f\rho^2 x^2] [e(1-x^2) + f\rho^2 x^2] dx$$

$$\bar{G}_{1122} = \bar{G}_{2211} = \frac{\pi}{2} \int_0^1 \Delta(1-x^2) \{ [f(1-x^2) + h\rho^2 x^2] [(e+3d)(1-x^2) + 4f\rho^2 x^2] - 3g^2 \rho^2 x^2 (1-x^2) \} dx$$

$$\bar{G}_{1133} = \bar{G}_{2233} = 2\pi \int_0^1 \Delta \rho^2 x^2 \{ [(d+e)(1-x^2) + 2f\rho^2 x^2] [f(1-x^2) + h\rho^2 x^2] - g^2 \rho^2 x^2 (1-x^2) \} dx$$

$$\bar{G}_{3311} = \bar{G}_{3322} = 2\pi \int_0^1 \Delta(1-x^2) [d(1-x^2) + f\rho^2 x^2] [e(1-x^2) + f\rho^2 x^2] dx$$

$$\bar{G}_{1212} = \bar{G}_{2211} = \frac{\pi}{2} \int_0^1 \Delta(1-x^2)^2 \{ g^2 \rho^2 x^2 - (d-e)[f(1-x^2) + h\rho^2 x^2] \} dx$$

$$\bar{G}_{1313} = \bar{G}_{2323} = -2\pi \int_0^1 \Delta g \rho^2 x^2 (1-x^2) [e(1-x^2) + f\rho^2 x^2] dx$$

where

$$d = c_{11}, \quad e = (c_{11} - c_{12})/2, \quad f = c_{44}, \quad g = c_{13} + c_{44}, \quad h = c_{33},$$

$$\Delta^{-1} = [e(1-x^2) + f\rho^2 x^2] \{ [d(1-x^2) + f\rho^2 x^2] [f(1-x^2) + h\rho^2 x^2] - g^2 \rho^2 x^2 (1-x^2) \},$$

c_{ij} are elastic tensor elements of the host rock in Voigt notation, and ρ is the inverse of

aspect ratio $\rho = 1/\alpha$.

2.14 Reference

- Bakulin, A., V. Grechka, and I. Tsvankin, 2000, Estimation of fracture parameters from reflection seismic data—Part I: HTI model due to a single fracture set: *Geophysics*, 65, 1788–1802.
- Bandyopadhyay, K., 2009, *Seismic Anisotropy: Geological Causes and Its Implications to Reservoir Geophysics*: Ph.D. Thesis, Stanford University.
- Berryman, J. G., 1980, Long-wavelength propagation in composite elastic media. 1. Spherical inclusions: *Journal of the Acoustical Society of America*, 68, 1809–1819.
- Berryman, J.G., 1995, Mixture theories for rock properties, in *Rock Physics and Phase Relations: A Handbook of Physical Constants*, T.J. Ahrens, ed. American Geophysical Union, Washington, D.C., 205–228.
- Biot, M. A., 1956, Theory of propagation of elastic waves in fluid-saturated porous solid. I. Low-frequency range: *Journal of the Acoustical Society of America*, 28, 168–178.
- Brown, R. J. S., and J. Korrington, 1975, On the dependence of the elastic properties of a porous rock on the compressibility of the pore fluid: *Geophysics*, 40, 608–616.
- Bruner, W. M., 1976, "Comment on seismic velocities in dry and saturated cracked solids:" by R. J. O'Connell and B. Budiansky: *Journal of Geophysical. Research*, 81, 2573-2576.
- Budiansky, B., 1965, On the elastic moduli of some heterogeneous materials: *Journal of the Mechanics and Physics of Solids*, 13, 223–227.
- Budiansky, B., and R. J. O'Connell, 1976, Elastic moduli of a cracked solid: *International Journal of Solids and Structures*, 12, 81–97.

- Chapman, M., S. V. Zatsepin, and S. Crampin, 2002, Derivation of a microstructural poroelastic model: *Geophysical Journal International*, 151, 427–451.
- Eshelby, J. D., 1957, The determination of the elastic field of an ellipsoidal inclusion and related problems: *Proceeding of the Royal Society of London, Series, A, Mathematical and Physical Sciences*, 241, 376–396.
- Gassmann, F., 1951, Über die Elastizität poröser Medien: *Vierteljahrsschrift der Naturforschenden Gesellschaft in Zürich*, 96, 1–23.
- Grechka, V., 2007, Comparison of the non-interaction and differential schemes in predicting the effective elastic properties of fractures media: *International Journal of Fracture*, 144, 291–292.
- Grechka, V., and M. Kachanov, 2006, Effective elasticity of cracked rocks: A snapshot of the work in progress: *Geophysics*, 71, no. 6, W45–W58.
- Gurevich, B., 2003, Elastic properties of saturated porous rocks with aligned fractures: *Journal of Applied Geophysics*, 54, 203–218.
- Hoëmig, A., 1979, Elastic moduli of a non-randomly cracked body: *International Journal of Solids and Structures*, 15, 137–154.
- Hornby, B. E., L. M. Schwartz, and J. A. Hudson, 1994, Anisotropic effective-medium modeling of the elastic properties of shales: *Geophysics*, 59, 1570–1583.
- Hu, Y., and G. A. McMechan, 2009, Comparison of effective stiffness and compliance for characterizing cracked media: *Geophysics*, 74, no. 2, D49–D55.
- Hudson, J. A., 1980, Overall properties of a cracked solid: *Mathematical Proceedings of the Cambridge Philosophical Society*, 88, 371–384.

- , 1981, Wave speeds and attenuation of elastic waves in material containing cracks: *Geophysical Journal of the Royal Astronomical Society*, 64, 133–150.
- , 1994, Overall properties of a material with inclusions or cavities: *Geophysical Journal International*, 117, 555–561.
- Hudson, J. A., and E. Liu, 1999, Effective elastic properties of heavily faulted structures: *Geophysics*, 64, 479–485.
- Hudson, J. A., E. Liu, and S. Crampin, 1996, Transmission properties of a fault plane: *Geophysical Journal International*, 125, 559–566.
- Jaeger, J., Cook, N.G., and Zimmerman, R., 2007, *Fundamentals of Rock Mechanics*, 4th ed: Malden, MA: Blackwell Ltd.
- Jakobsen, M., J. A. Hudson, and T. A. Johansen, 2003, T-Matrix approach to shale acoustics: *Geophysical Journal International*, 154, 533–558.
- Jakobsen, M., 2004, The interacting inclusion model of wave-induced fluid flow: *Geophysical Journal International*, 158, 1168–1176.
- Jakobsen, M., and M. Chapman, 2009, Unified theory of global flow and squirt flow in cracked porous media: *Geophysics*, 74, no. 2, WA65–WA76
- Kachanov, M., 1992, Elastic properties of cracked solids: Critical review of some basic concepts: *Applied Mechanics Reviews*, 45, 304–335.
- Kachanov, M., I. Tsukrov, and B. Shafiro, 1994, Effective moduli of solids with cavities of various shapes: *Applied Mechanics Reviews*, 47, no. 1S, S151–S174,
- Kachanov, M., B. Shafiro, and I. Tsukrov, 2003, *Handbook of Elasticity Solutions*: KluwerAcademic Publishers.

- Kuster, G. T., and Toksoz, M. N., 1974, Velocity and attenuation of seismic waves in two-phase media: Part I. theoretical formulations: *Geophysics*, 39, 587-606.
- Liu, E., J. A., Hudson, and T. Pointer, 2000, Equivalent medium representation of cracked rock: *Journal of Geophysical Research*, 105, 2981–3000.
- Lin, S., and T. Mura, 1973, Elastic fields of inclusions in anisotropic media (II): *Physica Status Solidi (a)*, 15, 281–285.
- Mavko, G., and T. Vanorio, 2008, Observation and limitations of effective medium models for pore shape: *Stanford Rock Physics & Borehole Geophysics Project Annual report*, 114, B9: 1-14
- Mavko, G., and A. Nur, 1978, The effect of nonelliptical cracks on the compressibility of rocks: *Journal of Geophysical Research*, 83, 4459–4468.
- Mavko G., T. Mukerji, and J. Dvorkin, 2009, *The Rock Physics Handbook, Tools for Seismic Analysis in Porous Media*: Cambridge University Press
- Mura, T., 1987, *Micromechanics of Defects in Solid*: Martinus Nijhoff Pub.
- Nishizawa, O., 1982, Seismic velocity anisotropy in a medium containing oriented cracks —Transversely isotropic case: *Journal of Physics of the Earth*, 30, 341–347.
- Norris, A.N., 1985, A differential scheme for the effective moduli of composites: *Mechanics of Materials*., 4, 1–16.
- O’Connell, R. J., and B. Budiansky, 1974, Seismic velocities in dry and saturated cracked solids: *Journal of Geophysical Research*, 79, 5412–5426.
- Ponte Castañeda, P., and J. R. Willis, 1995, The effect of spatial distribution on the effective behavior of composite materials and cracked media: *Journal of Mechanics and Physics of Solids*, 43, 1919–1951.

- Rüger, A., 1997, P-wave reflection coefficients for transversely isotropic models with vertical and horizontal axis of symmetry: *Geophysics*, 62, 713–722.
- Sayers, C. M., and M. Kachanov, 1995, Microcrack-induced elastic wave anisotropy of brittle rocks: *Journal of Geophysical Research*, 100, no. B3, 4149–4156.
- Schoenberg, M., 1980, Elastic wave behavior across linear slip interfaces: *Journal of the Acoustic Society of America*, 68, 1516–1521.
- Schoenberg, M., and J. Douma, 1988, Elastic wave propagation in media with parallel fractures and aligned cracks: *Geophysical Prospecting*, 36, 571–590.
- Schoenberg, M., and C. M. Sayers, 1995, Seismic anisotropy of fractured rock: *Geophysics*, 60, 204–211.
- Teng, L., 1998, *Seismic and Rock Physics Characterization of Fractured Reservoirs*: Ph.D. Thesis, Stanford University.
- Thomsen, L., 1985, Biot-consistent elastic moduli of porous rocks: Low-frequency limit: *Geophysics*, 50, 2797–2807.
- Thomsen, L., 1995, Elastic anisotropy due to aligned cracks in porous rock: *Geophysical Prospecting*, 43, 805–829.
- Tsvankin, I., 1997, Reflection moveout and parameter estimation for horizontal transverse isotropy: *Geophysics*, 62, 614–629.
- Xu, S., 1998, Modelling the effect of fluid communication on velocities in anisotropic porous rocks: *International Journal of Solids and Structures*, 35, 4685–4707.
- Vernik, L., M. Kachanov, 2010, Modeling elastic properties of siliciclastic rocks: *Geophysics*, 75(6), E171-E182.

Walsh, J., 1965, The effects of cracks on the compressibility of rocks: *Journal of Geophysical Research*, 70, 381-389.

Willis, J. R., 1977, Bounds and self-consistent estimates for the overall properties of anisotropic composites: *Journal of the Mechanics and Physics of Solids*, 25, 185–202

Wu, T. T., 1966, The effect of inclusion shape on the elastic moduli of a two-phase material: *International Journal of Solids and Structures*, 2, 1-8.

Zimmerman, R.W., 1991, Elastic moduli of a solid containing spherical inclusions: *Mechanics of Materials*, 12, 17-24.

Chapter 3

Extended Biot Theory with Local Flow in Heterogeneous Porous Rocks

3.1 Abstract

The elastic wave energy is mainly dissipated into heat by local viscous fluid flow. The theoretical treatment reported here is aimed to quantitatively evaluate the effect of local flow on the elastic wave propagation characteristics for a wide range of frequencies. The extended Biot theory with squirt flow and mesoscopic flow, which are distinguished depending on the scale of pressure gradient, are separately explored. The dynamic poroelastic responses of heterogeneous porous media are mainly characterized by the magnitude of the dispersion and relaxation frequency. Normally, the magnitude of the dispersion is determined by the degree of heterogeneity and the elastic compressibility contrast. The characteristic frequency is dependent on the information of porous solid, fluid properties, and the mesoscopic geometry of heterogeneities. Most of those geological features are poorly determined from the available data, incurring uncertainty to understand the poroelastic behavior from geophysical measurements. I propose to use a rock physics diagnostic including the dispersion effect to interpret sonic log data. It is found that the presence of heterogeneities enhances the V_p/V_s ratio and slightly decreases the P-impedance. I recommend that a detailed interpretation of the sonic log data and seismic inversion results should account for the dispersion effect.

3.2 Introduction

The well-known Biot theory (Biot, 1956a, 1956b, 1962) describes the wave characteristic caused by the global flow of viscous fluids through permeable porous homogeneous medium. However, an essential feature of sedimentary rocks is the universal presence of heterogeneity occurring at various scales. When excited by a passing elastic wave, the compliant portions of the rock tend to contract and expand much more easily than do stiff portions, consequently producing pore pressure gradients and fluid flow. The wave induced fluid flow can be categorized as “squirt flow”, “mesoscopic flow”, and “macroscopic flow”, which are defined based on the distance over which the fluid pressure attempts to equilibrate by diffusion processes (Pride et al., 2006; Muller et al., 2010). The “squirt” and “mesoscopic” flow are often termed as local flow, whereas the “macroscopic” flow occurring at wavelength scale is often called global flow or Biot flow. In each case, the viscous flow attenuates wave energy and results in velocity dispersion. The principle goal of this chapter is to quantitatively evaluate the effect of local flow on the elastic wave propagation characteristics for a wide range of frequencies.

The squirt flow typically emphasizes on the grain-scale heterogeneities, such as loose grain contact and micro-cracks frequently occurring in the reservoir rocks. In the past decades, many lab measurements suggested that significant dispersion and attenuation observed at ultrasonic frequency is mainly caused by this microscopic squirt flow (Winkler, 1983, 1985; Murphy et al., 1984, 1986; Han, 1986; Jones, 1986; Batzle et al., 2006; Yao, 2013). On the theoretical side, a number of model theories

(Mavko and Nur, 1975, 1979; O'Connell and Budiansky, 1974, 1977; Kuster and Toksoz, 1974; Jones, 1986; Hudson, 1990; Mavko and Jizba, 1991; Dvorkin et al., 1995; Chapman et al., 2002; Jakobsen et al., 2004) have emerged, seeking to provide predictions on the velocity dispersion and attenuation resulting from the squirt flow. Although those poroelastic models can properly handle the effect of squirt flow, they generally do not take into account the effect of global flow. Consequently, to preserve the theoretical generality and completeness, it was felt necessary to characterize the wave propagation characteristics including both the effect of squirt flow and global flow in porous medium with microscopic heterogeneity. This will be investigated in section 4, and my study draws heavily on the work by Tang (2011), Yao (2013), and Yao et al. (2013).

However, the effect of squirt flow on the wave characteristics is hard to be observed at seismic exploration band (Pride et al., 2006; Mavko et al., 2009; Muller et al., 2010). It is increasingly believed that the mesoscopic flow mechanism is the dominant cause that can explain the level of loss determined from seismic wave field (Pride et al., 2004; Muller et al., 2010). Mesoscopic flow is created by the heterogeneities on a scale much larger than typical pore size but smaller than the wavelength (White, 1975; Dutta and Ode, 1979a, 1979b; Gelinsky and Shapiro, 1997; Gurevich et al., 1997; Shapiro and Muller, 1999; Muller and Gurevich, 2004; Pride et al., 2003a, 2003b; Carcione and Picotti, 2006; Muller et al., 2007). From the geological perspective, mesoscopic heterogeneities can be fractures and soft inclusions in porous matrix, patches of different immiscible fluids, and so on. A double-porosity dual-permeability model to characterize the poroelastic responses of

general porous heterogeneous composite is developed by Pride and Berryman (2003a, 2003b). In section 5, the governing equation and theoretical modeling results of the double-porosity dual-permeability (DPDP) are presented. This will also lay the theoretical foundation for the work presented in Chapter 4, 5, and 6.

One of the challenges in exploration geophysics is to interpret seismic and ultrasonic data in heterogeneous reservoir rocks due to the significant intrinsic dispersion effect. The elastic responses of the heterogeneous rock can be influenced by the wave-induced fluid flow. As such, it is critical to develop a rock physics diagnostic that takes into account the dispersion effect. In this chapter, I attempt to construct a rock physics template including dispersion effect caused by squirt flow to quantitatively interpret sonic data in a heterogeneous carbonate reservoir. Finally, in the section of discussion, some fundamental issues and potential application regarding the velocity dispersion and attenuation resulting from the wave-induced fluid flow will be discussed.

3.3 Brief Review of Biot's Theory

Wave propagation in porous saturated medium creates interactions between fluid and porous solid matrix. Energy is dissipated into heat due to the relative motion of viscous pore fluid with respect to the porous matrix of solid. This physical process consequently gives rise to velocity dispersion and wave attenuation. In this section, I briefly review Biot's linear poroelastic constitutive stress-strain relations and wave propagation in homogeneous porous media. For a complete description about Biot's theory, the reader is

referred to the original paper by Biot (1956a, 1956b, 1962), and the reformulation by Rice and Cleary (1976).

The porous solid matrix is characterized by mineral grain density ρ_s , porosity ϕ , permeability κ , solid grain bulk moduli K_s , and drained porous rock frame bulk moduli K_d . The pore fluid is characterized by bulk modulus K_f , density ρ_f , and viscosity η .

3.3.1 Poroelastic Constitutive Relations

Poroelastic constitutive laws relate the total stress field τ_{ij} and the pore pressure p_f to the deformation state of a porous medium. The stress-strain relations can be written as:

$$\tau_{ij} = 2\mu e_{ij} + \delta_{ij}(\lambda_c e - \alpha M \xi) , \quad (3.1)$$

$$p_f = -\alpha M e + M \xi , \quad (3.2)$$

where

$$\alpha = 1 - \frac{K_d}{K_s} , \text{ which is also called the Biot's coefficient;}$$

$$\frac{1}{M} = \frac{\alpha - \phi}{K_s} + \frac{\phi}{K_f} ;$$

$$\lambda_c = \lambda + \alpha^2 M ,$$

where λ and μ are Lamé parameters for the rock frame under drained condition. Here, two independent deformation fields are e_{ij} and ξ ; e_{ij} represents the strain tensor of the

solid frame; \mathbf{e} refers to the bulk strain of porous solid frame; $\xi = \nabla \cdot \mathbf{W} = -\nabla \cdot \phi(\mathbf{U} - \mathbf{u})$ refers to the increment of fluid content, with \mathbf{u} and \mathbf{U} denoting the displacement vectors of the rock frame and pore fluid.

3.3.2 Poroelastic Wave Propagation

Biot's poroelastic wave equations for porous saturated medium are given by (Biot, 1956b, 1962; Stern et al., 1985):

$$(\lambda + \alpha^2 M + \mu) \nabla(\nabla \cdot \mathbf{u}) + \mu \nabla^2 \mathbf{u} + \alpha M \nabla(\nabla \cdot \mathbf{W}) = \rho_b \frac{\partial^2 \mathbf{u}}{\partial t^2} + \rho_f \frac{\partial^2 \mathbf{W}}{\partial t^2} , \quad (3.3)$$

$$\alpha M \nabla(\nabla \cdot \mathbf{u}) + M \nabla(\nabla \cdot \mathbf{W}) = \rho_f \frac{\partial^2 \mathbf{u}}{\partial t^2} + \frac{c_m \rho_f}{\phi} \frac{\partial^2 \mathbf{W}}{\partial t^2} + \frac{F \eta}{\kappa} \frac{\partial \mathbf{W}}{\partial t} , \quad (3.4)$$

where $\rho_b = \rho_s(1 - \phi) + \rho_f \phi$; c_m is the tortuosity parameter, which is a constant depending on the pore structure (Dutta and Ode, 1979a). Here, \mathbf{F} is the frequency-dependent coefficients which characterize the drag force between the frame and the fluid (Stern et al., 1985). \mathbf{F} is expressed as:

$$F(\zeta) = \frac{1}{4} \left(\frac{\zeta T(\zeta)}{1 + 2iT(\zeta)/\zeta} \right) , \quad (3.5)$$

where $T(\zeta)$ is the Kelvin function (Stern et al., 1985)

$$T(\zeta) = \frac{ber'(\zeta) + ibei'(\zeta)}{ber(\zeta) + ibei(\zeta)} , \quad (3.6)$$

and

$$\zeta = (\omega / \omega_r)^{1/2} = \left(\frac{\omega a^2 \rho_f}{\eta} \right)^{1/2}. \quad (3.7)$$

Here a is the pore-size factor; ω is the angular frequency; ber and bei are functions of the Bessel function of the first kind. The derivatives of functions ber and bei are ber' and bei' , respectively. Solving equation 3.3 and 3.4 will yield two dilatational waves and one rotational wave, which are all dispersive.

3.4 Extended Biot Theory with Squirt Flow

3.4.1 Theoretical Formulation

To analyze the squirt flow between cracks and pores, a penny-shaped ellipsoidal inclusion and spherical cavity are used to simulate the pore-crack model as shown in Figure 3.1(Tang, 2011, 2012). In this model, the induced squirt flow causes the change of pore pressure and the variation depends on the amount of fluid flowing in and out of the pore space. Consequently, the squirt flow contribution to the saturated bulk modulus is expressed in a Gassmann-type equation (eqn. 15 & 16 of Tang (2011)) as:

$$K = K_d + \alpha^2 / [(\alpha - \phi) / K_s + \phi / K_f + S(\omega)], \quad (3.8)$$

$$S(\omega) = \frac{q}{\delta P_p V_p} = \frac{8\pi\varepsilon(1-\nu_s)}{3\mu_s} f(\zeta) \left[\frac{1/K_d - 1/K_s}{1/K_d - 1/K} - f(\zeta) \right] \left/ \left\{ 1 + \frac{4(1-\nu_s)K_f}{3\mu_s\gamma} [1 - f(\zeta)] \right\} \right., \quad (3.9)$$

where

$$f(\zeta) = \frac{2J_1(\zeta)}{\zeta J_0(\zeta)}, \quad (3.10)$$

$$\zeta = \sqrt{3i\omega\eta/K_f} / \gamma. \quad (3.11)$$

Here, J_1 and J_0 are the order one and order zero first kind Bessel functions, and ν_s is the Poisson ratio of the solid rock. As illustrated in equation 3.9, the impact of squirt flow is mainly controlled by the two parameters crack density ε and crack aspect ratio γ . The intensity of cracks determines the magnitude of squirt flow, and the aspect ratio controls the relaxation time of squirt time (Tang, 2011). After substitution of equation 3.8 and 3.9 which quantify the effect of squirt flow on the effective bulk modulus into the equation 3.3 and 3.4, the unified poroelastic wave propagation in cracked porous medium can be obtained.

However, the velocity dispersion predicted by the aforementioned Tang's model is below Gassmann's low frequency limit. Obviously, this is against the fundamental physics concerning the velocity dispersion due to local flow (Batzle et al., 2006; Mavko et al., 2009). Based on Tang's work, Yao (2013) proposed a frequency-dependent reversed fluid flow term to accurately characterize the effect of local flow on the elastic properties. At any non-zero frequency, a reversed fluid flow is hypothetically transferred from the stiffer phase to the softer phase, with the amount of $q'(f)$:

$$q'(f) = -(q_{\max} - q(f)), \quad (3.12)$$

where q_{\max} can be obtained by setting frequency $f=0$ Hz in equation 3.9. Furthermore, Yao et al. (2013) developed a frequency-dependent effective concept of “dynamic fluid modulus “ K_f ”, which is determined by an additional fluid flow term to the original fluid modulus as shown in equation 3.13, to characterize the poroelastic responses due to wave-induced fluid flow.

$$\frac{1}{K_f''} = \frac{1}{K_f} - \frac{q'/V_p}{dP_p}. \quad (3.13)$$

Now, with the introduction of this dynamic fluid modulus, the application of Gassmann’s equation can be successfully extended from homogeneous to heterogeneous media at non-zero frequencies.

$$K_{sat} = K_{dry} + \frac{\alpha^2}{(\alpha - \phi)/K_0 + \phi/K_f''}. \quad (3.14)$$

3.4.2 Shear-wave Dispersion

For the local flow mechanism, the dispersion of shear modulus can be roughly derived from the dispersion of the bulk modulus (Mavko and Jizba , 1991; Dvokin et al, 1995). The relationship can be expressed as:

$$\frac{1}{\mu_d} - \frac{1}{\mu(w)} = \frac{4}{15} \left(\frac{1}{K_d} - \frac{1}{K(w)} \right), \quad (3.15)$$

where μ_d is the effective shear modulus of dry rock and $K(\omega)$ is computed based on equation 3.8. This relationship is taken to compute the dispersion characteristics of shear-wave. Such handling about the shear modulus dispersion is not theoretically sound, but presents a practical way to physically relate the shear modulus dispersion based on the bulk modulus dispersion (Tang, 2011).

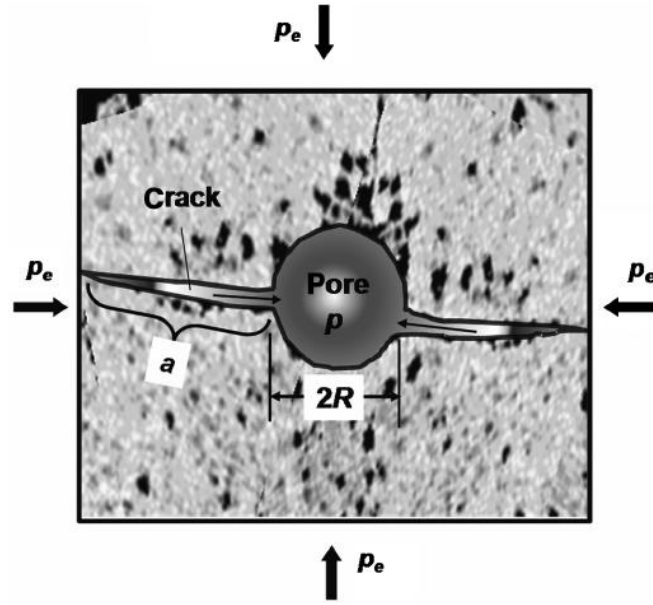


Figure 3.1. Schematic of pore-crack model to describe the squirt flow mechanism. The pore pressure change p in the pore space is caused by an external stress p_e (taken from Tang et al., 2012).

3.4.3 Numerical Results and Analysis

In this section, I quantify the effects of fluid viscosity, rock permeability, and aspect ratio on the poroelastic responses of the porous rock containing cracks using

the above described theory. Table 3.1 lists the fundamental parameters that will be used to calculate the characteristics of velocity dispersion and wave attenuation for the modeling examples presented in this section. The dry rock's elastic moduli are computed using the self-consistent model (Berryman, 1995; Mavko et al., 2009). In the following examples, the pore space was assumed to consist of a combination of stiff matrix porosity and cracks with aspect ratio 0.4 and 0.01, respectively. Figures 3.2 and 3.3 illustrate the effect of viscosity on the characteristics of the (a) dispersion and (b) attenuation for the fast and slow compressional waves. In Figure 3.2, considerable dispersion effect is observed for the fast compressional wave, and when the frequency goes to very low value, the velocity is in agreement with that predicted by Gassmann equation. Actually, both the squirt flow and Biot flow contribute to the velocity dispersion. Note that the dispersion effect caused by the squirt flow, which occurs at relatively lower frequency range, is much larger than that caused by Biot flow. In Figure 3.2 (b), the peak to the left for the each attenuation curve corresponds to energy loss caused by squirt flow, while the peak to the right corresponds to the Biot-loss maximum. Obviously, the magnitude of attenuation due to squirt flow is much higher than the Biot flow. As expected, characteristic frequency of squirt flow shifts to the lower frequency domain as the viscosity increases. The physical explanation is that the high viscosity requires longer time for the pore pressure to equilibrate. In addition, be aware that such a dependency of the characteristic frequency for squirt flow is opposite to that of the Biot flow.

In Figure 3.3, the slow P-wave exhibits fundamentally different physical behavior. For each curve, at lower frequency range, the velocity of slow P-wave is very low, approximating to zero. It then ramps up to about 800m/s at a higher frequency range. As we can see, the transitional frequency will shift to lower frequency range as fluid viscosity decreases. On the high frequency end, however, the slow P-wave becomes a truly propagating wave. The slow P-wave attenuation curves are shown in Figure 3.3 (b). Attenuation of slow P-wave is very high at lower frequency, and then decreases significantly at higher frequency. At low frequency, the slow P-wave is essentially a diffusion wave which propagates for only a short distance before being fully dissipated.

Table 3.1. Input parameters to calculate the characteristics of velocity dispersion and wave attenuation of squirt flow

Parameter	Figure 3.2 & 3.3	Figure 3.4	Figure 3.5	Figure 3.6
K_s (GPa)	37.9	37.9	37.9	85
G_s (GPa)	32.6	32.6	32.6	45
ρ_s (g/cm ³)	2.65	2.65	2.65	2.87
K_f (GPa)	2.25	2.25	2.25	2.25
ρ_f (kg/m ³)	1.05	1.05	1.05	1.05
ϕ	0.25	0.25	0.25	0.03
κ_0 (md)	1000	1000	1, 10,100,1000	100
η (cP)	1,10 ¹ ,10 ² , 10 ³	1	1	10
τ	2.4	2.4	2.4	2.4
α	0.5	0.5	0.5	0.15
ε	0.15	0, 0.05,0.10,0.15	0.15	0:0.001:0.25
γ	0.001	10 ⁻⁴ ,5*10 ⁻⁴ ,10 ⁻³ ,10 ⁻²	0.001	0.01

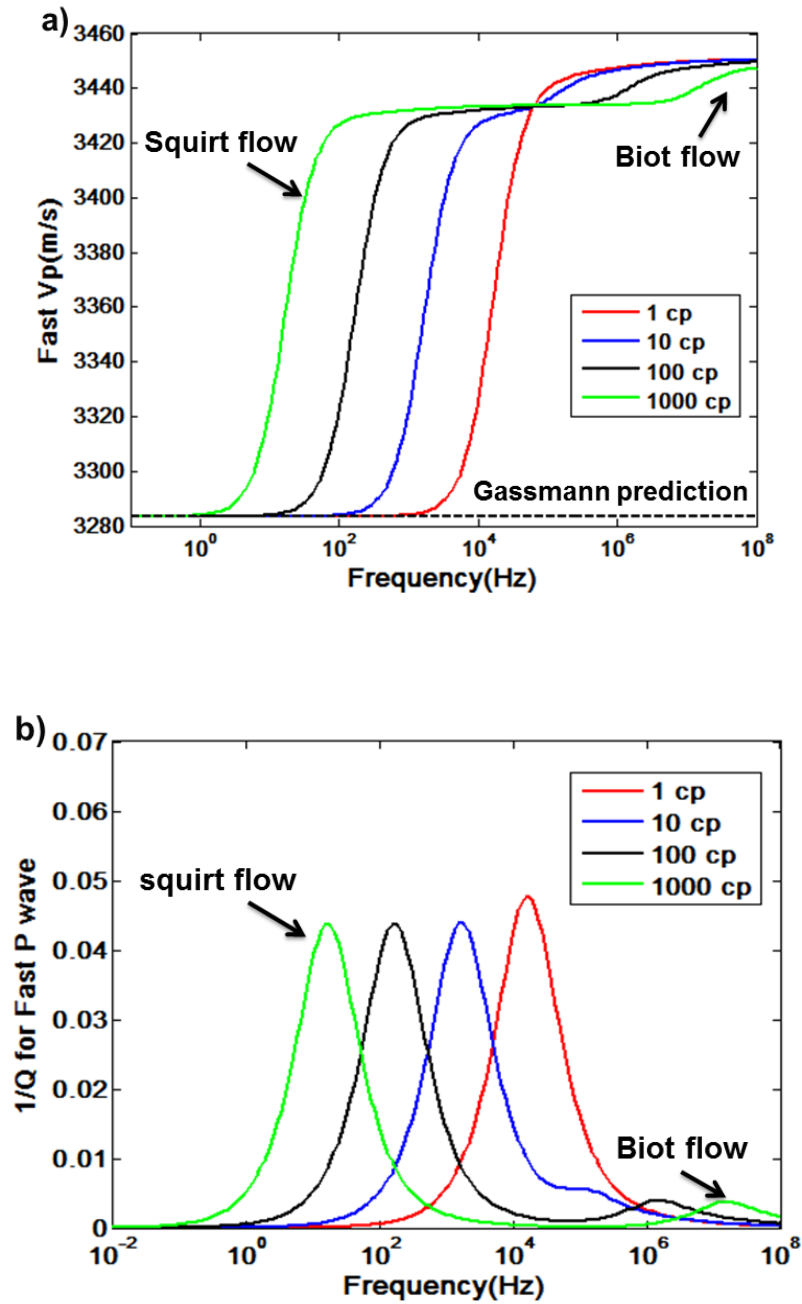


Figure 3.2. Illustration of effect of viscosity on (a) dispersion (b) attenuation of fast P-wave in a cracked porous rock. The calculated frequency range is from 10^{-2} to 10^8 Hz, plotted on logarithmic scale. The dashed line in (a) indicates the velocity predicted by Gassmann's equation.

The Figure 3.4 illustrates the effect of two important parameters characterizing the features of micro-cracks on the attenuation of fast P-wave. As dictated in the equation 3.8, the crack density determines the magnitude of dissipative energy loss, whereas the crack aspect ratio controls the shifting trend of characteristic frequency. When the crack density goes to zero, suggesting that no cracks are present in the porous medium, the dispersion and attenuation caused by the squirt flow consequently vanishes. As shown in Figure 3.4(a), the amount of attenuation increases with increasing crack density. Also, it is evident that the aspect ratio only affects the characteristic frequency of squirt flow, placing no impact on the Biot flow. The relaxation frequency of squirt flow shifts to a lower frequency range as the aspect ratio becomes smaller. Here, the aspect ratio acts like characteristic length of microscopic heterogeneity. The small aspect ratio indicates that the geometry of the crack is narrow and long. Consequently, it takes longer time for the pore pressure to equilibrate. Figure 3.5 shows the effect of permeability on the attenuation of fast P-wave. By contrast to the fact that the aspect ratio merely affects the central frequency of squirt flow and the permeability variation only determines the characteristic frequency of Biot flow. Clearly, we can observe that the higher permeability will make the characteristic frequency of Biot flow move to lower frequency domain, and hence there are more chances to affect the seismic and sonic measurements.

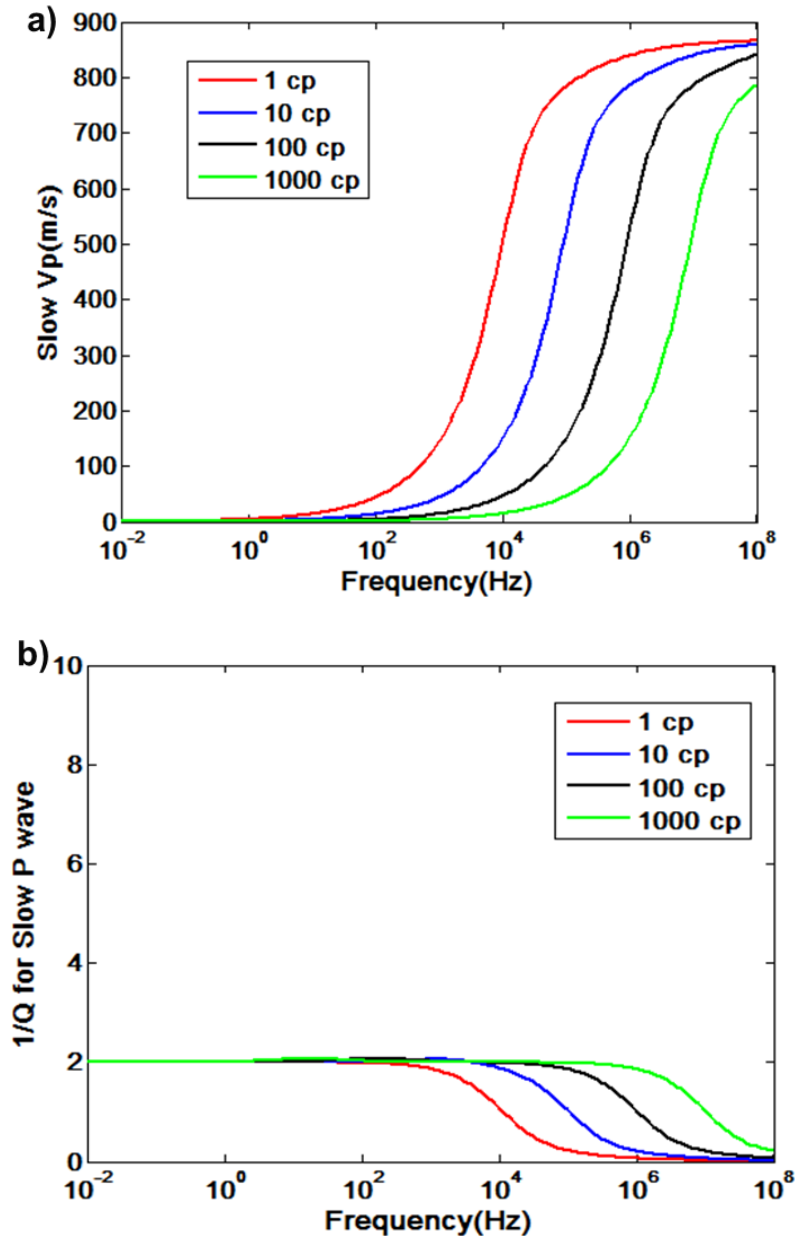


Figure 3.3. Illustration of the effect of viscosity on (a) dispersion (b) attenuation of slow P-wave in a cracked porous rock. The calculated frequency range is from 10^{-2} to 10^8 Hz, plotted on logarithmic scale.

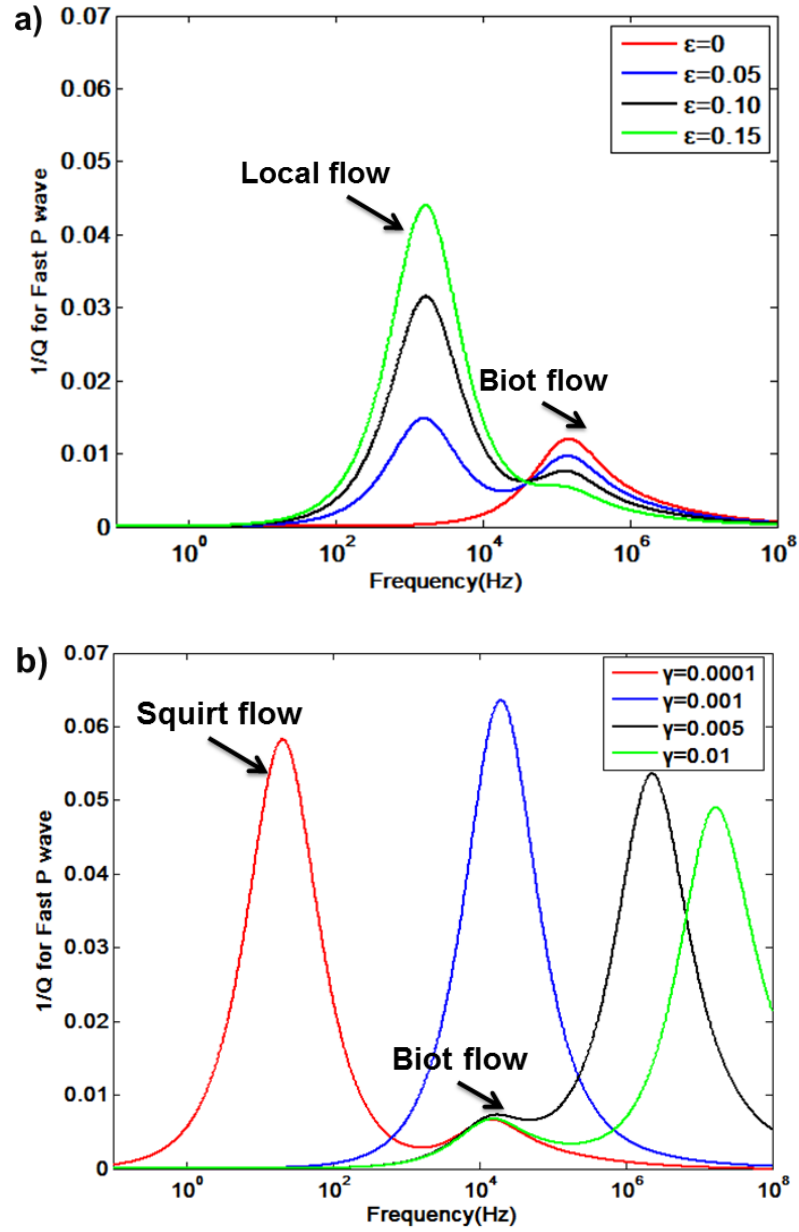


Figure 3.4. Illustration of the effect of (a) crack density and (b) aspect ratio on attenuation of fast P-wave in a cracked porous rock. The calculated frequency range is from 10^{-2} to 10^8 Hz, plotted on logarithmic scale.

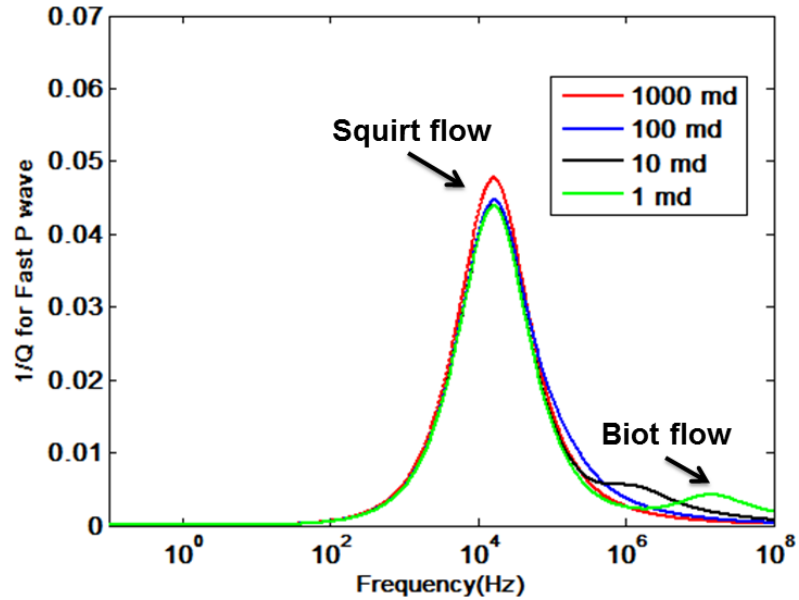


Figure 3.5. Illustration of the effect of permeability on attenuation of fast P-wave in a cracked porous rock. The calculated frequency range is from 10^{-2} to 10^8 Hz, plotted on logarithmic scale.

3.4.4 Squirt Flow Effect on Interpretation of Well Log Data

Elastic attributes such as P-impedance and V_p/V_s ratio calculated from well log data are often used to calibrate seismic interpretation in terms of rock properties. However, in heterogeneous reservoirs, those elastic properties may exhibit considerable discrepancy between seismic and sonic log frequency domain due to the dispersion effect. The simulated elastic properties of the carbonate's V_p/V_s ratio versus P-impedance at seismic and ultrasonic frequency band are displayed in Figure 3.6. The black line representing 100% brine saturated at zero frequency indicates the relaxed elastic response when the pore pressure are equilibrated, and the red line representing 100% brine saturated at 10M Hz frequency indicates the un-relaxed

elastic responses. The thin pink lines represent modeling results of different crack densities.

The rock physics modeling results explain the scattering point in terms of porosity heterogeneities and dispersion effect. The presence of strong heterogeneity in the carbonate reservoir rocks suggests that the dispersion effect caused by squirt flow should also be pronounced. The modeling results show that the dispersion effect significantly increases the V_p/V_s ratio and slightly increases the P-impedance. The scatters of the well log points sit between the brine-saturated line at zero frequency and 10M Hz frequency. This makes sense because the typical frequency range of sonic log is around 10K Hz, ranging between the seismic and ultrasonic frequency band. This also implies that not all the elastic attributes computed from sonic log data can be used to calibrate seismic interpretation, especially those approximate to red lines representing the un-relaxed elastic response. Also, this rock physics template will improve the accuracy of quantifying the effect of crack density on the elastic properties of heterogeneous carbonate.

3.5 Extended Biot Theory with Mesoscopic Flow

WIFF can also occur from spatial variations in rock compliance on a scale greater than typical pore size but less than the wavelength. Such WIFF is often called mesoscopic flow (Muller et al., 2010). In this section, we focus on Double-porosity Dual-permeability (DPDP) model which represents a more general framework to explain the velocity dispersion and attenuation due to the mesoscopic fluid flow.

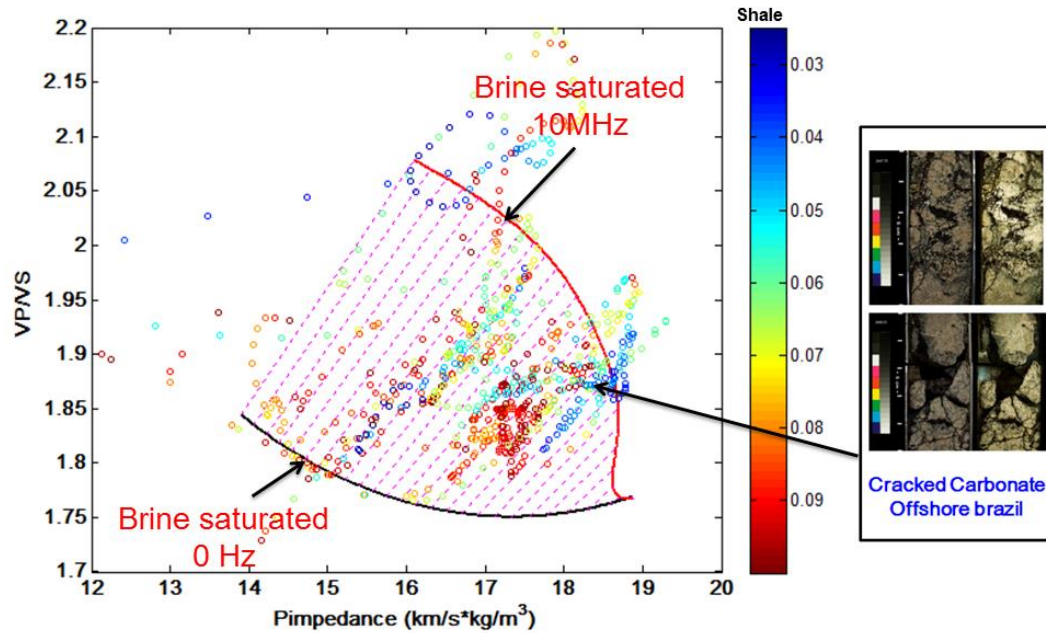


Figure 3.6. A rock physics template presented as cross-plots of V_p/V_s versus P-impedance, which is used to illustrate the dispersion effect. The parameters used to model the rock physics template are listed in Table 3.1. All of the scattering data points are from the log data in a heterogeneous carbonate reservoir, offshore Brazil. The core photos in the right of figure indicate the heavily cracked carbonates at the corresponding depth.

3.5.1 Double-porosity Dual-permeability Theory

Although various heterogeneities exist in the earth material, it is also clear that two types of heterogeneity are of particular interest to us: the heterogeneity of compressibility which accounts for the effective elastic response, and the heterogeneity of permeability which is responsible for the effective hydraulic properties. The double-porosity dual-

permeability model is to tackle on the poroelastic behavior due to the coexistences of such two types of heterogeneities. As illustrated in Figure 3.7, the heterogeneous porous media is therefore described as a composite which consists of two distinct porous phase, exhibiting contrasting hydraulic and elastic properties but saturated by a single fluid phase. One typical example to elucidate the double-porosity model is a fractured reservoir (Figure 3.8). Fracture or crack porosity normally occupies small portions of the volume, but with higher compressibility and permeability than those of the host rock.

The concept of double porosity was initially developed to describe fluid flow in a porous medium by Barrenblatt et al. (1960) and later by Wilson and Aifantis (1982). Berryman and Wang (1995, 2000) made a rigorous extension of Biot theory to formulate the phenomenological equations for the poroelastic behavior of double-porosity medium at macroscopic scale. Subsequently, Pride and Berryman (2003a, b) introduced the internal mesoscopic flow, which is transferred between the two distinct porous phases corresponding to different fluid pressure, into the double-porosity model. This provides an important energy dissipation mechanism to explain the high attenuation at seismic frequency band. Double-porosity dual-permeability model also gives a theoretical and versatile framework to model acoustic wave propagation through heterogeneous porous structures, without placing any restrictions on the mesoscopic geometry of the heterogeneity (Pride et al., 2004).

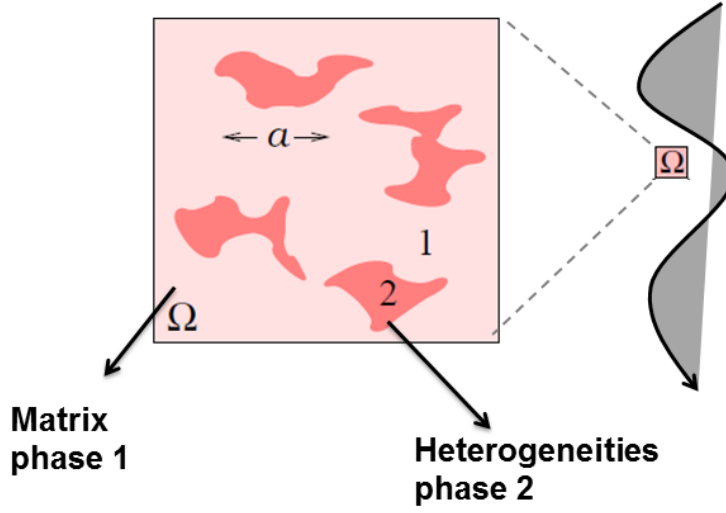


Figure 3.7. A schematic illustration of double-porosity dual-permeability model (after Pride and Berryman, 2003a). Phase 1 and Phase 2 are isotropic porous continua, and a is the characteristic length of mesoscopic scale heterogeneity.

3.5.2 Governing Equation of DPDP

The governing equation for DPDP in frequency domain is given as (Pride and Berryman, 2003a, 2003b; Pride et al., 2004):

$$\nabla \cdot \tau^D - \nabla P_c = -i\omega(\rho v + \rho_f q_1 + \rho_f q_2) \quad (3.16)$$

$$\begin{bmatrix} q_1 \\ q_2 \end{bmatrix} = -\frac{1}{\eta} \begin{bmatrix} \kappa_{11} & \kappa_{12} \\ \kappa_{12} & \kappa_{22} \end{bmatrix} \cdot \begin{bmatrix} \nabla \bar{p}_{f1} - i\omega \rho_f v \\ \nabla \bar{p}_{f2} - i\omega \rho_f v \end{bmatrix} \quad (3.17)$$

$$\begin{bmatrix} \nabla \cdot v \\ \nabla \cdot q_1 \\ \nabla \cdot q_2 \end{bmatrix} = i\omega \begin{bmatrix} a_{11} & a_{12} & a_{13} \\ a_{12} & a_{22} & a_{23} \\ a_{13} & a_{23} & a_{33} \end{bmatrix} \cdot \begin{bmatrix} P_c \\ \bar{p}_{f1} \\ \bar{p}_{f2} \end{bmatrix} + i\omega \begin{bmatrix} 0 \\ \zeta_{\text{int}} \\ -\zeta_{\text{int}} \end{bmatrix} \quad (3.18)$$

$$-i\omega \zeta_{\text{int}} = \gamma(\omega)(\bar{p}_{f1} - \bar{p}_{f2}) \quad (3.19)$$

$$-i\omega\tau^D = [G(\omega) - i\omega g(\omega)] \left[\nabla v + (\nabla v)^T - \frac{2}{3} \nabla \cdot v I \right] \quad (3.20)$$

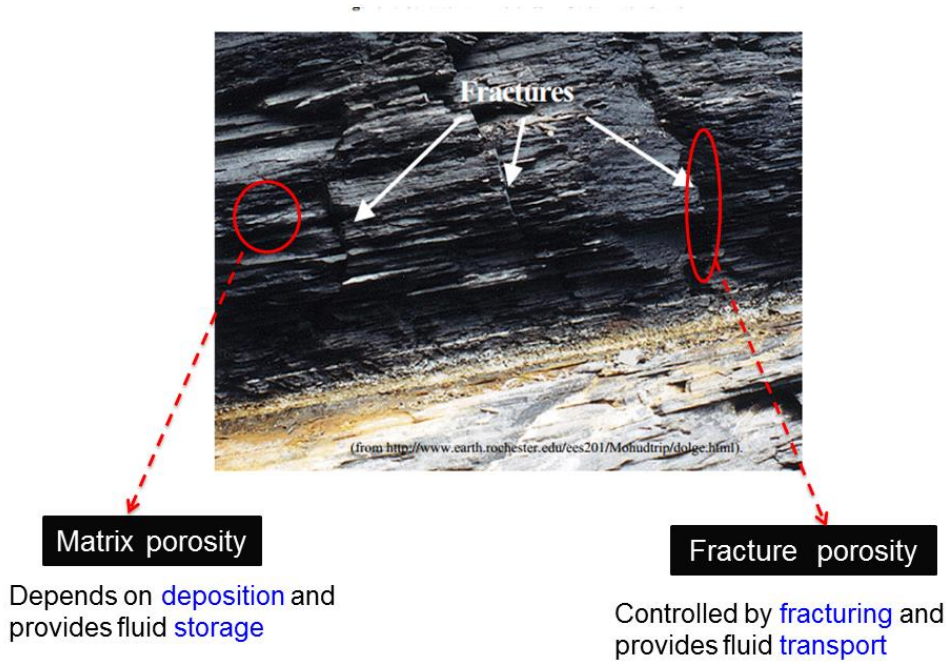


Figure 3.8. Fractured reservoirs are typical example for elucidation of double-porosity dual-permeability model. The photo is the outcrop of Marcellus shale. Taken from <http://www.earth.rochester.edu/ees201/Mohudtrip/dolge.html>

The macroscopic fields are: v , the average particle velocity of the solid grains throughout an averaging volume of the composite; q_i , the average Darcy flux across phase i ; P_c , the average total pressure in the averaging volume; τ^D , the average deviatoric stress tensor; \bar{p}_{fi} , the average fluid pressure within phase i ; and $-i\omega\zeta_{\text{int}}$, the average rate at which fluid volume is being transferred from phase 1 into phase 2 as normalized by the total volume of the averaging region; ζ_{int} indicates the internal mesoscopic flow which means the increment in fluid content to internal pore pressure

equilibration process; $G(\omega)$ is the Hilbert transform of $g(\omega)$ with low frequency limit corresponding to the drained shear modulus of the composite (Liu, 2005)

Physically, each set of the governing equation has explicit physical significance. The equation 3.16 represents the conservation of the momentum equation. Note that there are three types of fluid flow: two types of external fluid flow and one type of internal fluid flow. Equation 3.17 indicates the generalized Darcy's law corresponding to the external fluid flow at macroscopic scale. Equation 3.19 is the transport law for internal mesoscopic flow, which results in the main viscous loss for the heterogeneous pororelastic system. Equation 3.18 and 3.20 is the generalized compressibility law. Further analysis of these equations suggests that there exist three compression waves and a single shear-wave. The first type of P-wave represents the conventional fast P-wave, and the other two slow P-wave modes correspond to fluid pressure diffusion due to the external fluid flow.

The frequency-dependent relaxation coefficient $\gamma(\omega)$, which essentially controls the mesoscopic flow characteristic, is defined as:

$$\gamma(\omega) = \gamma_m \sqrt{1 - i \frac{\omega}{\omega_m}}, \quad (3.21)$$

where

$$\gamma_m = -\frac{\kappa_1 K_1^d}{\eta L_1^2} \left(\frac{a_{12} + B_0(a_{22} + a_{33})}{R_1 - B_0/B_1} \right) \left[1 + O(\kappa_1/\kappa_2) \right], \quad (3.22)$$

$$\omega_m = \frac{\eta B_1 K_1^d}{\kappa_1 \alpha_1} \left(\gamma_m \frac{V}{S} \right)^2 \left[1 + \sqrt{\frac{\kappa_1 B_2 K_2^d \alpha_1}{\kappa_2 B_1 K_1^d \alpha_2}} \right]. \quad (3.23)$$

Note that the parameters controlling the characteristic frequency are mainly dependent on the properties of phase 1 (matrix). In fact, phase 1 controls the timing of the diffusive penetration of the fluid pressure and therefore determines the dispersion effect and viscous loss. All the other coefficients in these equations, which depend on the information about porous solid, fluid properties, and the mesoscopic geometry of heterogeneities, have been discussed in detail by Pride and Berryman (2003a, 2003b) . The constants a_{ij} are all real and correspond to the high-frequency response for which no internal fluid-pressure relaxation can take place (Pride and Berryman, 2003a).

3.5.3 Reduction to Single-porosity Biot Theory

The numerical simulation about the aforementioned governing equation is obviously cumbersome, and hence the analytical expressions for the double-porosity model are derived by Pride and Berryman (2003a, 2003b) and Pride et al. (2004). Under the assumption that phase 2 is entirely embedded in phase 1, the double-porosity theory is reduced to the effective Biot theory in which the elastic moduli is defined to be frequency-dependent to incorporate the mesoscopic flow. The frequency-dependent poroelastic moduli are given as:

$$\frac{1}{K_d^*} = a_{11} - \frac{a_{13}^2}{a_{33} - \gamma / i\omega} , \quad (3.24)$$

$$B = \frac{-a_{12}(a_{33} - \gamma / i\omega) + a_{13}(a_{23} + \gamma / i\omega)}{(a_{22} - \gamma / i\omega)(a_{33} - \gamma / i\omega) - (a_{23} + \gamma / i\omega)^2} , \quad (3.25)$$

$$\frac{1}{K_u^*} = \frac{1}{K_d^*} + B \left(a_{12} - \frac{a_{13}(a_{23} + \gamma/i\omega)}{a_{33} - \gamma/i\omega} \right). \quad (3.26)$$

Here, $K_d^*(\omega)$ is the effective drained bulk modulus of the double-porosity composite; $B(\omega)$ is the effective Skempton's coefficient; $K_u^*(\omega)$ is the effective undrained bulk modulus. Since the dry rock frame is independent on fluid pressure difference, the complex frequency-dependent drained modulus $K_d^*(\omega)$ seems to be against our physical intuition. However, $K_d^*(\omega)$ actually represents the effective elastic modulus which takes into account the fluid-pressure equilibration between two distinct porous phases.

3.5.4 Numerical Examples and Analysis

Figure 3.9 illustrates the effect of viscosity and heterogeneity size on attenuation of fast P-wave velocity in a double porosity composite. Matrix rock and fluid properties for the double-porosity composite are given in Table 3.2. The remarkable peak-attenuation due to mesoscopic flow, which takes place at seismic frequency band, is several orders higher than the Biot-loss. It is easy to see that higher viscosity and larger heterogeneity size shift the peak mesoscopic attenuation to a lower frequency range. Physically, this can be understood, because both higher viscosity and larger heterogeneity size will make the pore pressure take longer time to equilibrate. All those observations are also consistent with the theoretical analysis in the equation 3.23.

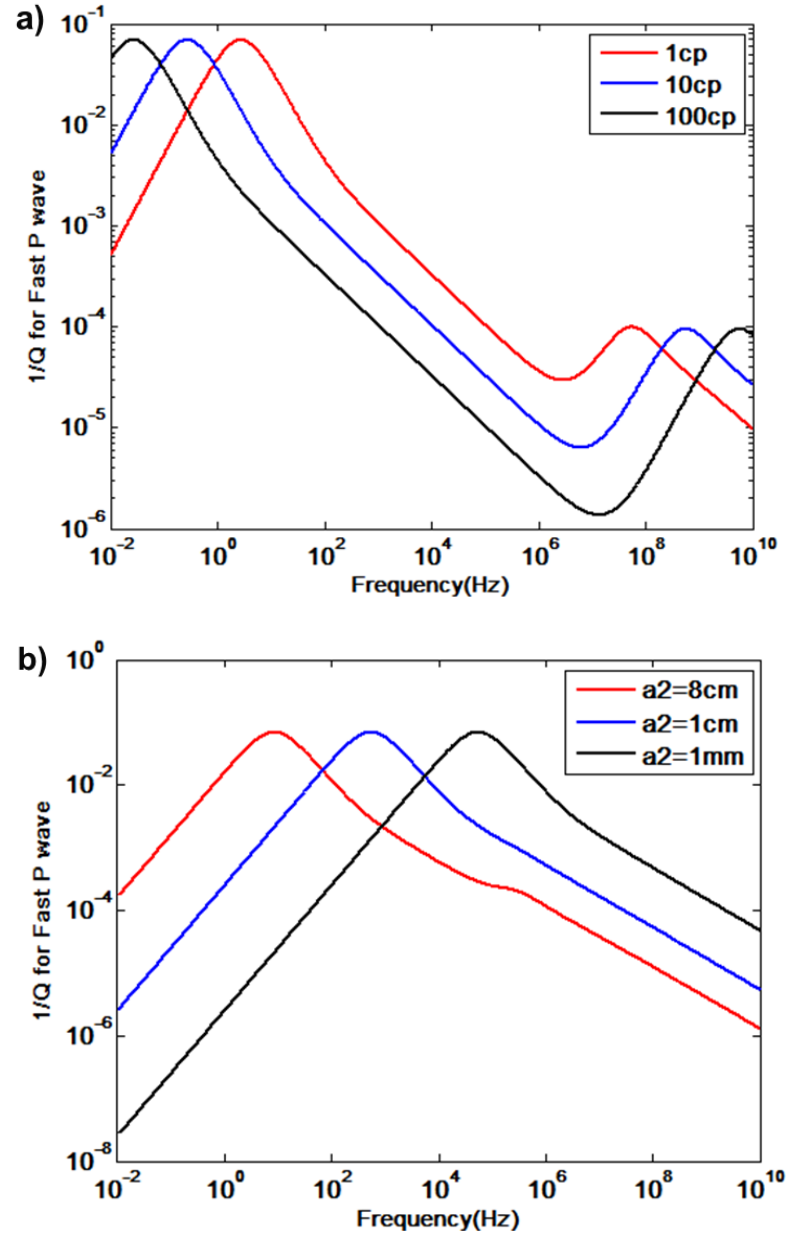


Figure 3.9. Illustration of the effect of (a) viscosity and (b) heterogeneity size on attenuation of fast P-wave in a double porosity composite. The peak to the left for each curve corresponds to mesoscopic loss, while the peak to the right corresponds to the Biot-loss.

Figure 3.10 shows the variation of P-wave attenuation with permeability and frequency. It turns out that the fast P-wave attenuation is dominated by the contribution from mesoscopic loss, and the permeability significantly affects the amplitude and peak frequency of the attenuation. Figure 3.11 shows the relationship between permeability and P-wave attenuation in the seismic exploration band. The seismic energy loss is almost linearly proportional to the permeability variation. For the reservoirs rocks with low permeability, the low-frequency component of seismic wave attenuates more, while for high permeability reservoir rocks, the high-frequency component of seismic wave has high attenuation.

Table 3.2. The related parameters for the double-porosity dual-permeability modeling in the section 3.5.

Parameter	Rock frame properties			
	Figure 3.9(a)		Figure 3.9(b)	
	Phase 1	Phase 2	Phase 1	Phase 2
K_d (GPa)	17.5	0.5	17.5	0.5
μ_d (GPa)	15.8	0.4	15.8	0.4
V	0.963	0.037	0.963	0.037
ϕ	0.10	0.30	0.10	0.30
κ (md)	100	1000	100	1000
α (m)		0.01		0.08, 0.01, 0.001
ε		0.1		0.1
τ	2.4	2	2.4	2
Pore fluid properties				
K_f (GPa)	2.25		2.25	
ρ_f (kg/m ³)	1.05		1.05	
η (cP)	1,10,100		5	

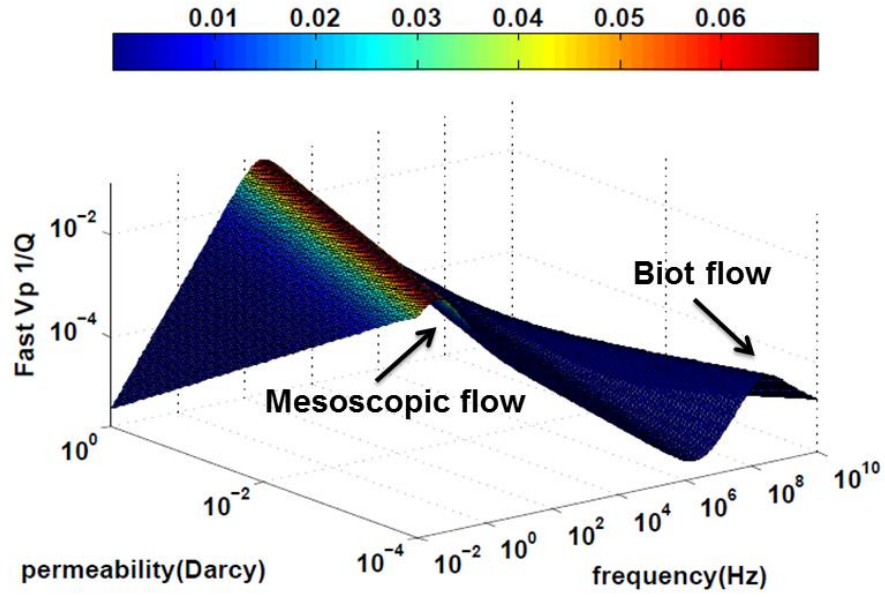


Figure 3.10. The permeability and frequency dependence on the P-wave attenuation in a double porosity composite. The heterogeneity size is assumed 10cm in this case.

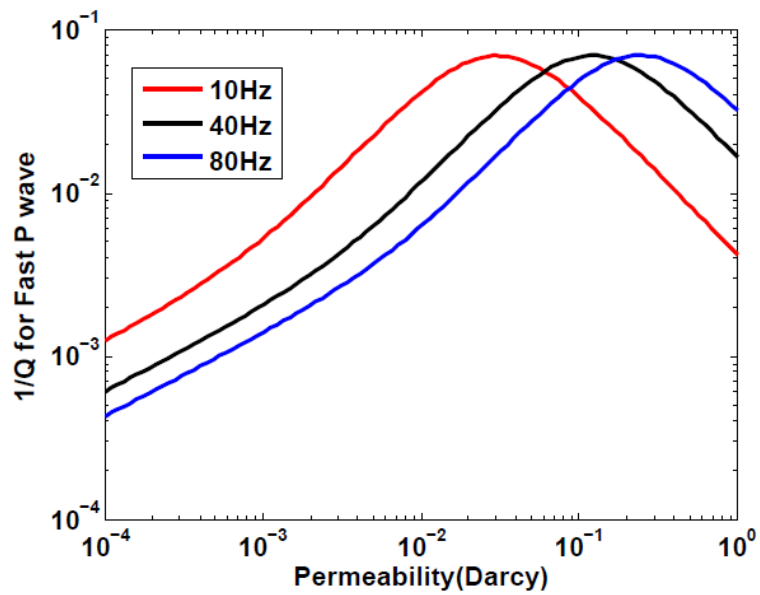


Figure 3.11. The permeability dependence of the fast P-wave attenuation in seismic exploration band. The red line, black line, and blue line represent 10Hz, 40Hz, and 80Hz, respectively.

3.6. Discussion

To essentially characterize velocity dispersion and wave attenuation, one at least needs to know two key features in the dynamic poroelastic system: the magnitude of dispersion and the characteristic frequency (Mavko et al., 2009; Yao, 2013). In this section, I will discuss the fundamental physical issues standing behind the magnitude of dispersion and characteristic frequency. Besides, the multi-scale heterogeneity and dispersion coverage will also be explored in this section.

3.6.1 What Determines Magnitude of Dispersion

The magnitude of the dispersion represents the velocity difference at the low-frequency limit and high-frequency limit. The low-frequency limit corresponds to the relaxed state where the pore pressure has sufficient time to equilibrate, the velocity is therefore consistent with Gassmann prediction. The high-frequency limit is referred as un-relaxed state where the pore pressure has no time to equilibrate, effectively making compliant pores isolated from the stiff pores and resulting in high elastic moduli predictions. Generally, the degree of dispersion is mainly dependent on the contrast between the heterogeneity phase and host phase in terms of elastic compressibility and volume fraction. Normally, the bigger contrast of elastic compressibility indicates bigger pore pressure gradients, and the volume fraction of heterogeneities directly suggests the amount of fluid flow.

It is also important to point out that the rock's overall elastic properties in drained condition can significantly affect the quantity of velocity dispersion and attenuation.

The dispersion effect can be enhanced in the more compliant rock due to the creation of more fluid pressure difference. For example, as shown in Figure 3.12, H-S lower bound and Hill average generate much higher mesoscopic flow loss than does H-S upper bound. Interestingly, the characteristic frequency is also found to be shifted due to the change of rock's overall elastic properties. This will bring uncertainty for the poroelastic modeling of WIFF, since using different effective medium theories to simulate the elastic response will yield quite different results. Strictly speaking, the dry rock's elastic properties should be measured at lab with in-situ pressure and temperature conditions.

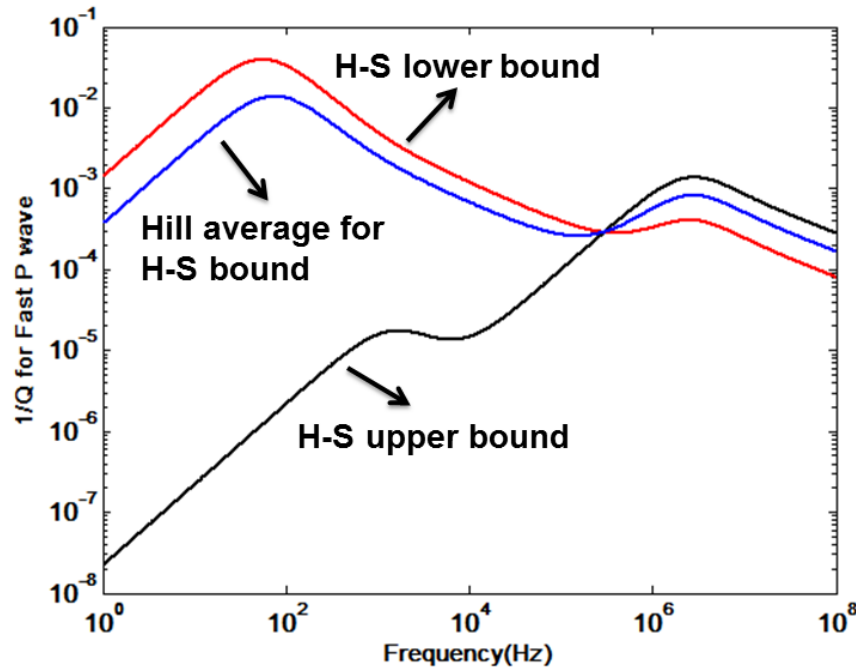


Figure 3.12. Comparisons of the effect of modeling effective elastic properties on the attenuation of fast P-wave.

Additionally, the degree of heterogeneity variation might significantly affect the dispersion characteristics. Based on some numerical investigations, Mason et al. (2007)

concluded that the heterogeneity distribution with the bigger standard deviation can result in stronger dispersion and attenuation. Meanwhile, he also pointed out that the smooth transition of local heterogeneity properties can pose weaker dispersion effect than the local heterogeneity properties with huge contrast.

3.6.2 Characteristic Frequency and Diffusion Equation

Wave-induced fluid pressure gradients equilibration can be regarded as a pore pressure diffusion process. The pore pressure diffusion equation can be expressed using Fick's law as:

$$\frac{\partial p}{\partial t} = D \cdot \nabla^2 p , \quad (3.27)$$

where p is pore pressure, and D is the hydraulic diffusivity that can be given as (Wang, 2000):

$$D = M \frac{\kappa}{\eta} = \frac{K_f}{\phi} \frac{\kappa}{\eta} . \quad (3.28)$$

When the fluid pressure has just enough time to diffuse across heterogeneous patches present in a wave period, the attenuation reaches maximum (Pride et al., 2004). As for any diffusion process, the time necessary for the fluid-pressure difference to equilibrate goes as:

$$f_c = \lambda^2 / D . \quad (3.29)$$

For Biot flow, the wavelength can be written as $\lambda = \sqrt{H/\rho}/f$, so the relaxation frequency is to be derived as:

$$f_c = \frac{H}{M} \frac{\eta}{\rho \kappa} . \quad (3.30)$$

Since $H / \rho M$ can be approximated as $\rho_f \phi^{-m}$ for many reservoir rocks (Archie, 1942; Pride et al., 2006), equation (4.30) can be written as:

$$f_c = \frac{\eta}{\rho_f \phi^{-m} \kappa} . \quad (3.31)$$

Normally, the characteristic frequency of Biot flow in typical sedimentary rocks is above 100K Hz (Bourbié et al., 1987; Muller et al., 2010; Mavko et al., 2009). Consequently, concerning the global flow at seismic exploration band, pore pressure is always relaxed and Biot attenuation is negligible.

For the mesoscopic flow, fluid pressure equilibration occurs at the time L^2 / D , where L is characteristic spatial scale of the heterogeneity within an averaging volume.

$$f_c = \frac{\kappa}{\phi L^2} \frac{K_f}{\eta} . \quad (3.32)$$

Note that the dependence of characteristic frequency on the fluid mobility κ / η for the mesoscopic flow is opposite to that of Biot flow (equation 3.31). As shown in equation (3.32), the maximum mesoscopic loss can occur anywhere within the seismic exploration band, depending on the rock's porosity and permeability, pore fluids's viscosity and bulk modulus, and characteristic length of the heterogeneity.

For the squirt flow, the pore pressure equilibration takes place at pore and grain scale. The fundamental physical standing behind is the Navier-Stokes equation and the equation of mass conservation in the fluid mechanics. As we can see in equation (3.10) and

equation (3.11), the characteristic frequency is a function of pore fluid's viscosity and bulk modulus, and the aspect ratio of the cracks. Unlike mesoscopic flow, the characteristic frequency of squirt flow is not dependent on rock's permeability. This is because the length scale for the squirt flow to take place does not exceed the grain size, and hence the pore pressure equilibration process is not affected by the permeability of the material (Wenzlau, 2009).

Except for those parameters listed in this section to determine the relaxation frequency, another very important geological feature, the spatial distribution of the pores and heterogeneities (as what we discuss in Chapter 2), possibly plays an important role in affecting the relaxation time for the pore pressure to be equilibrated.

3.6.3 Multi-scale Heterogeneities and Dispersion Coverage

For the poroelastic model presented here, I restrict our attention on the mesoscopic heterogeneity with a single dominant diffusion length, or the micro-cracks with a single aspect ratio. However, such idealization of the geometric properties of heterogeneities never satisfies the condition of real world. Multi-scale heterogeneities always coexist either in a discrete or continuous manner (O'Connell and Budiansky, 1977; Han, 2009; Yao, 2013), since randomness and statistical fluctuation are the most prominent features of subsurface rocks in nature. The velocity dispersion will consequently behave in a continuous manner, and many flow mechanisms can simultaneously take place over different frequency ranges depending on the scale and hydro-physical properties of the geological features. The possible relative positions of these different mechanisms and the

associated geological features are schematically illustrated in the Figure 3.13. Note that the velocity can be even lower than that of Gassmann prediction when there exists open boundary condition for the porous system. This might happen in subsurface. For example, seismic wave propagating in faulted zone or large patches can cause the fluid flow out of the boundary of a representative volume within seismic wavelength. However, for most of the geological conditions, the fluid cannot be escaped from the representative volume within the typical wavelength, but trapped and transferred from one part of the rock to another part.

An interesting issue is that the physical behavior of the flow mechanism is intimately related to the heterogeneity size and corresponding wavelength. For example, assuming the velocity of the rock is 3000m/s, if the heterogeneity size is 10 cm, this will be considered as mesoscopic heterogeneity when the frequency is below $f < 3 \times 10^4 \text{ Hz}$. However, if the frequency exceeds this frequency range, e.g., $f > 10^5 \text{ Hz}$, the mesoscopic flow mechanism are invalid because the heterogeneity size is now bigger than the wavelength. Actually, the scale of the heterogeneity and the corresponding WIFF are physically meaningful only when the velocity of the rock and the observational frequency are given.

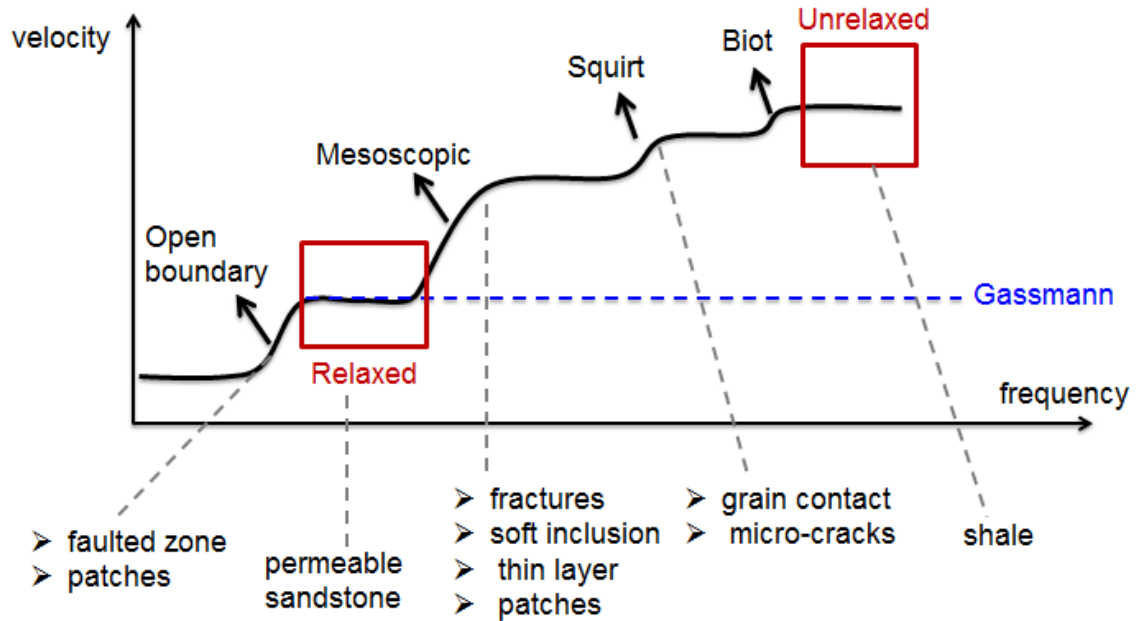


Figure 3.13. A schematic illustration of velocity dispersion associated with different mechanism. The potential geological features that cause the flow are also listed in the corresponding position.

Physically, the coexistence of mesoscopic flow, squirt flow, and global flow can cause interaction with each other, rather than acting in a linear superimposition manner as shown in Figure 3.13. In this chapter, the extended Biot theory including local flow completely ignores the coupling effect and interaction of different flow mechanism. Because of the overall complexity of interrelationship among all the physical properties affecting the fluid pressure equilibration processes and the interaction of the fluid flow at various scales, we are still far from fully understanding the dynamic poroelastic behavior of a heterogeneous porous system with multi-scale heterogeneity.

With the improvement of seismic acquisition and processing technique, it becomes increasingly important to utilize the multi-scale wave-field data for the reservoir characterization, development, and monitoring. Typical geophysical measurements often includes the surface seismic data (10^{1-2}Hz), VSP data (10^{1-3}Hz), sonic logs (10^{3-4}Hz), and lab measurements (10^{1-6}Hz). The fully integration of geophysical measurement at various scales opens the possibility for us to understand the poroelastic behavior of complex heterogeneous reservoir rocks. However, the main limitation still lies in how to remove other factors that also lead to the dispersion effect in the seismic data, such as apparent attenuation caused by interference and scattering effect. A number of studies have shown that it is difficult to discern the intrinsic attenuation from the apparent attenuation.

3.7 Concluding Remarks

This study has presented how to incorporate the poroelastic characteristic of local fluid flow, resulting from the heterogeneous nature of the porous media, into the classical Biot theory. The parameter of crack density, indicating the degree of microscopic heterogeneity, controls the magnitudes of squirt flow dispersion. The characteristic frequency of squirt flow mechanism is mainly determined by the fluid viscosity and the aspect ratio of the cracks. Numerical examples show that the impact of squirt flow can be prominent in seismic frequency band due to high viscosity and small aspect ratio of cracks. A rock physics template taking into account the dispersion effect caused by squirt flow is developed to interpret the sonic data in a heterogeneous carbonate reservoir, and

the result shows that the dispersion effect can considerably amplify the V_p/V_s ratio and slightly increase the P-impedance. The double-porosity dual-permeability model provides a theoretical framework to simulate the poroelastic response due to the presence of mesoscopic heterogeneity. The mesoscopic flow mechanism is considered to explain the significant energy loss observed in the seismic frequency band. Geometric features of heterogeneity and fluid mobility are found to significantly affect the magnitude of velocity dispersion and wave attenuation. This potentially provides a link between fluid transport properties and seismic wave signatures.

3.8 Acknowledgement

This work was sponsored by Fluids and DHI consortium of the Colorado School of Mines and University of Houston.

3.9 References

- Aki, K., and P. G. Richards, 1980, Quantitative Seismology: Theory and Methods: W. H. Freeman & Co.
- Archie, G. E., 1942, The electrical resistivity log as an aid in determining some reservoir characteristics: American Institute of Mining, Metallurgical, and Petroleum Engineers, 146, 54-67.

- Barenblatt, G. I., I. P., Zheltow, and T. N. Kochina, 1960, Basic concepts in the theory of seepage homogeneous liquids in fissured rocks: *Journal of Applied Mathematics and Mechanics*, 24, 1286–303.
- Batzle, M. L., D. H. Han, and R. Hofmann, 2006, Fluid mobility and frequency-dependent seismic velocity—Direct measurements: *Geophysics*, 71, no. 1, N1–N9.
- Berryman, J. G., 1995, Mixture theories for rock properties, in T. J. Aherens, ed., *Rock physics and phase relations: A handbook of physics constants*: American Geophysical Union, 205-228.
- Berryman, J. G., and H. F. Wang, 1995, The elastic coefficients of double-porosity models for fluid transport in jointed rock: *Journal of Geophysical Research*, 100 (24) 611-627.
- Berryman, J. G., and H. F. Wang, Elastic wave propagation and attenuation in a double-porosity dual-permeability medium: *International Journal of Rock Mechanics and Mining Sciences*, 37, 63– 78, 2000.
- Biot, M. A., 1956a, Theory of propagation of elastic waves in fluid-saturated porous solid. I. Low-frequency range: *Journal of the Acoustical Society of America*, 28, 168–178.
- , 1956b, Theory of propagation of elastic waves in a fluid-saturated porous solid. II. Higher frequency range: *Journal of the Acoustical Society of America*, 28, 179–191.
- , 1962, Mechanics of deformation and acoustic propagation in porous media: *Journal of Applied Physics*, 33, 1482–1498.

Bourbié, T., O. Coussy, and B. Zinszner, 1987, *Acoustics of Porous Media*: Editions Technip.

Carcione, J. M., and S. Picotti, 2006, P-wave seismic attenuation by slow wave diffusion: Effects of inhomogeneous rock properties: *Geophysics*, 71, no. 3, O1–O8.
Applied Physics, 33, 1482–1498.

Chapman, M., S. V. Zatsepin, and S. Crampin, 2002, Derivation of a microstructural poroelastic model: *Geophysical Journal International*, 151, 427–451

Dvorkin, J., G. Mavko, and A. Nur, 1995, Squirt flow in fully saturated rocks: *Geophysics*, 60, 97–107.

Dutta, N. C., and H. Odé, 1979a, Attenuation and dispersion of compressional waves in fluid-filled porous rocks with partial gas saturation (White model,) Part I—Biot theory: *Geophysics*, 44, 1777–1788.

———, 1979b, Attenuation and dispersion of compressional waves in fluid filled porous rocks with partial gas saturation (White model), Part II—Results: *Geophysics*, 44, 1789–1805.

Gelinsky, S., and S. A. Shapiro, 1997, Dynamic-equivalent medium approach for thinly layered saturated sediments: *Geophysical Journal International*, 128, F1–F4.

Gurevich, B., V. B. Zyrianov, and S. L. Lopatnikov, 1997, Seismic attenuation in finely layered porous rocks: Effects of fluid flow and scattering: *Geophysics*, 62, 319–324.

Gurevich, B., R. Ciz, and A. I. M. Dennehan, 2004, Simple expressions for normal incidence reflection coefficients from an interface between fluid saturated porous materials: *Geophysics*, 69, 1372–1377.

- Han, D., 1986, Effects of Porosity and Clay Content on Acoustic Properties of Sandstones and Unconsolidated Sediments: Ph.D. dissertation, Stanford University.
- Han, D., and Q. Yao, 2009, Intrinsic seismic wave attenuation - tight gas sand example: Annual Report, Fluids/DHI Consortium.
- Hudson, J. A., 1990, Overall elastic properties of isotropic materials with arbitrary distribution of circular cracks: *Geophysical Journal International*, 102, 465–469.
- Jakobsen, M., 2004, The interacting inclusion model of wave-induced fluid flow: *Geophysical Journal International*, 158, 1168–1176
- Jones, T. D., 1986, Pore fluids and frequency-dependent wave propagation in rocks: *Geophysics*, 51, 1939–1953
- Kuster, G. T., and M. N. Toksöz, 1974, Velocity and attenuation of seismic waves in two-phase media: Part I, Theoretical formulation: *Geophysics*, 39, 587–606.
- Liu, X., 2005, Seismic Wave Propagation and Modeling in Poroelastic Media with Mesoscopic Inhomogeneities: Ph.D. Thesis, The University of Adelaide.
- Mavko, G., and A. Nur, 1975, Melt squirt in the aesthenosphere: *Journal of Geophysical Research*, 80, 1444–1448.
- Mavko, G., and D. Jizba, 1991, Estimating grain-scale fluid effects on velocity dispersion in rocks: *Geophysics*, 56, 1940–1949.
- Mavko, G., and A. Nur, 1979, Wave attenuation in partially saturated rocks: *Geophysics*, 44, 161–178.
- Mavko, G., T. Mukerji, and J. Dvorkin, 2009, *The Rock Physics Handbook*, 2nd ed.: Cambridge University Press.

- Muller, T. M., and B. Gurevich, 2004, One-dimensional random patchy saturation model for velocity and attenuation in porous rocks: *Geophysics*, 69, 1166–1172.
- Muller, T. M., G. Lambert, and B. Gurevich, 2007, Dynamic permeability of porous rocks and its seismic signatures: *Geophysics*, 72, no. 5, E149–E158.
- Müller, T. M., B. Gurevich, and M. Lebedev, 2010, Seismic wave attenuation and dispersion resulting from wave-induced flow in porous rocks-A review, *Geophysics*, 75, 75A147-75A164.
- Murphy, W. F., J. N. Roberts, D. Yale, and K. W. Winkler, 1984, Centimeter scale heterogeneities and microstratification in sedimentary rocks: *Geophysical Research Letters*, 11, 697–700.
- Murphy, W. F. I., K. W. Winkler, and R. L. Kleinberg, 1986, Acoustic relaxation in sedimentary rocks: Dependence on grain contacts and fluid saturation: *Geophysics*, 51, 757–766
- O’Connell, R. J., and B. Budiansky, 1974, Seismic velocities in dry and saturated cracked solids: *Journal of Geophysical Research*, 79, 5412–5426.
- Plona, T., 1980, Observation of a second bulk compressional wave in a porous medium at ultrasonic frequencies, *Applied Physics Letters*, 36(4), 259-261.s: *Journal of Geophysical Research*, 79, 5412–5426.
- Pride, S. R., and J. G. Berryman, 2003a, Linear dynamics of double-porosity and dual-permeability materials. I. Governing equations and acoustic attenuation: *Physical Review E*, 68, 036603.
- , 2003b, Linear dynamics of double-porosity and dual permeability materials. II. Fluid transport equations: *Physical Review E*, 68, 036604.

- Pride, S. R., J. G. Berryman, and J. M. Harris, 2004, Seismic attenuation due to wave-induced flow: *Journal of Geophysical Research*, 109,B01201.
- Pride, S. R., J. H. Harris, D. L. Johnson, A. Mateeva, K. T. Nihei, R. L. Nowack, J.W. Rector, H. Spetzler, R.Wu, T. Yamamoto, J. G. Berryman, and M. Fehler, 2003, Acquisition/processing—Permeability dependence of seismic amplitudes: *The Leading Edge*, 22, 518–525.
- Stern, M., A. Bedford, and H. R. Millwater, 1985, Wave reflection from a sediment layer with depth-dependent properties: *Journal of the Acoustical Society of America*, 77, 1043–1063.
- Tang, X., 2011, A unified theory for elastic wave propagation through porous media containing cracks- An extension of Biot's poroelastic wave theory: *Science China—Earth Sciences*, 54, 1441– 1452.
- Tang, X., X. Chen, and X. Xu, 2012, A cracked porous medium elastic wave theory and its application to interpreting acoustic data from tight formations: *Geophysics*, 77, 245-252
- Walton, K., 1987, The effective elastic moduli of a random pack of spheres: *Journal of the Mechanics and Physics of Solids*, 35, 213-226.
- Wilson, R. K., and E. C. Aifantis, 1982, On the theory of consolidation with double porosity: *International Journal of Engineering Science*, 20, 1009–35.
- Winkler, K., 1983, Contact stiffness in granular porous materials: Comparison between theory and experiment: *Geophysical Research Letters*, 10, 1073–1076.
- , 1985, Dispersion analysis of velocity and attenuation in Berea sandstone: *Journal of Geophysical Research*, 90, 6793–6800

White, J. E., 1975, Computed seismic speeds and attenuation in rocks with partial gas saturation: *Geophysics*, 40, 224–232.

Yao, Q., 2013, Velocity Dispersion and Attenuation in Reservoir Rocks: Ph.D. Thesis, University of Houston.

Yao, Q., Han, D, Yan, F., and Zhao, L., 2013, Fluid substitution with dynamic fluid modulus: Facing the challenges in heterogeneous rocks, 83rd Annual Meeting, SEG, Expanded Abstracts.

Wang, H. F., 2000, Theory of Linear Poroelasticity With Applications to Geomechanics and Hydrogeology, Princeton Univ. Press, Princeton, N. J.

Wenzlau, F., 2009, Poroelastic Modelling of Wavefields in Heterogeneous Media: Ph.D. Thesis, Universität Karlsruhe (TH).

Chapter 4

Seismic Reflection Dispersion Due to Wave-induced Fluid Flow: A Theoretical Study

4.1 Abstract

Wave-induced fluid flow changes the behavior of the reflection coefficients. In this chapter, I have proposed and performed how to compute the poroelastic reflection from the boundary of heterogeneous porous media. The reflectivity approach presented here places no restrictions on the material-property contrast, the frequency, and the angle of incidence. The resulting poroelastic reflection coefficients incorporate both the influence of Biot flow and mesoscopic fluid flow. For a typical shale-sand reflector, it is found that the effect of local flow causes a variation in the reflection amplitude as high as 40%, and a maximum phase shift as high as 12 degrees at the seismic exploration frequency band. This can lead to misleading seismic imaging of the geological feature as well as quantitative interpretation of reservoir properties. However, the global flow-induced seismic dispersion characteristic, which occurs at a very high frequency range, is almost negligible.

4.2 Introduction

Seismic waves propagating in heterogeneous porous media create fluid pressure gradients and consequently induce fluid flow. During the process of fluid flow, the viscous-inertial loss takes place and dissipates mechanical energy into heat, which is

responsible for the intrinsic attenuation of seismic waves (Aki and Richards, 1980; Muller et al., 2010). The wave-induced fluid flow typically affects wave propagation characteristics (Biot, 1956a, 1956b, 1962; Pride and Berryman, 2003a, 2003b), and hence affects the behavior of reflection coefficients. The most pronounced influence is that the reflection coefficient is frequency-dependent, known as “reflection dispersion” here. It is of considerable interest to understand the poroelastic reflection signatures, which are believed to have potential in revealing reservoir properties such as saturation content and flow characteristics. Furthermore, an extensive investigation on the poroelastic reflection at a wide frequency range is critical to help us realize the physical discrepancy standing behind the different geophysical measurements at various scales, which typically include the surface seismic data (10^{0-2} Hz), VSP data (10^{2-3} Hz), sonic logs (10^{3-4} Hz), and lab measurements (10^{0-6} Hz). The present work contributes to quantifying the impact of wave-induced fluid flow on the reflection coefficients in heterogeneous reservoir rocks.

In the past decades, dissipation-related seismic attributes already have been employed to interpret seismic data as hydrocarbon indicators or to map reservoir properties (e.g., Taner et al., 1979; Klimentos, 1995; Dasgupta and Clark, 1998; Maultzsch et al., 2003; Castagna et al., 2003; Ebrom, 2004; Chapman et al., 2006; Hofmann, 2006). Based on the analysis of the experimental and field seismic data, Korneev et al.(2004) and Goloshubin et al.(2001, 2006) reported that the seismic reflection from a fluid-saturated layer shows a clear frequency-dependent amplitude response, and they further demonstrated that the theoretical formulation with a diffusive term gives a reasonable match with the physical modeling data. Generally,

much of these progresses have been driven by the development of spectral decomposition methods (Chakraborty and Okaya, 1995; Partyka et al., 1999; Castagna et al., 2003), which break down the seismic reflection signal into its component frequencies.

From a theoretical point of view, many authors (Geertsma and Smit, 1961; Stoll, 1977; White, 1977; Dutta and Ode, 1983; Bourbie et al., 1987; Gurevich & Schoenberg 1999; Gurevich et al. 2004) have studied the seismic reflection coefficients at an interface between two porous homogeneous media. The slow P-wave related to the fluid pressure diffusion is generated at the interface of poroelastic contact. Based on their calculations, the inelastic energy loss for reflection amplitudes is only significant at very high frequency. Physically, this is understandable, because the relative fluid flow with respect to the solid, namely global flow due to wavelength-scale pore-pressure equilibration, becomes negligible at low frequency. Meanwhile, the reflections at the interface between a liquid and a liquid-saturated porous solid also have been investigated extensively (Deresiewicz and Ric, 1960; de la Cruz et al. 1992; Santos et al. 1992; Denneman et al. 2002; Ciarletta and Sumbatyan 2003; Sharma 2004; Rubino et al. 2006; Dai and Kuang 2008).

However, in partially saturated rock or in fully saturated elastically heterogeneous rock, the effect of velocity dispersion and wave attenuation becomes more prominent. The viscous loss is mainly caused by an internal equilibration that takes place with fluid flowing from the more compliant high-pressure regions to the relatively stiffer low-pressure regions (Batzle et al., 2006). Based on the heterogeneities of various scale, such local low can be categorized as “squirt flow” and “mesoscopic flow”.

Squirt flow typically occurs at microscopic pore scale (Mavko and Nur, 1975; O'Connell and Budiansky, 1974; Dvorkin et al., 1995; Tang et al., 2011), while mesoscopic flow is created by the heterogeneities on a scale much larger than typical pore size but smaller than the wavelength (White, 1975; Dutta and Ode, 1979a, 1979b; Gelinsky and Shapiro, 1997; Gurevich et al., 1997; Shapiro and Muller, 1999; Pride et al., 2003a, b; Muller and Gurevich, 2004; Carcione and Picotti, 2006; Muller et al., 2007). Squirt flow is usually considered to be important at ultrasonic frequencies, while mesoscopic flow is increasingly considered as the dominant cause of fluid-related attenuation in the seismic exploration band (Pride et al., 2004; Müller et al., 2010).

To study the intrinsic attenuation effect on the reflection coefficient in a thinly layered, partially saturated reservoir with a non-dispersive overburden, Quintal et al. (2009) and Ren et al. (2009) combined the analytical solution of 1D White's model (White et al., 1975; Carcione and Picotti, 2006) and the analytical expression of reflection coefficient in visco-elastic media to obtain the reflection dispersion signatures. They further demonstrated that the analytical result is consistent with their numerical simulation result. On the other hand, rather than considering the poroelastic behavior due to the complex interaction between fluid and solid, many authors reported the impact of Q-contrast on the reflection amplitude and phase both theoretically (White, 1965; Bourbie, 1983a, 1983b; Lines et al., 2009; Morozov, 2011) and experimentally (Bourbie, 1984; Lines et al., 2012).

In general, the theoretical formulation for the reflection coefficients from the boundary of heterogeneous poroelastic media as a function of material properties,

incident angle, and frequency is very complicated. In this chapter, we seek to present an effective procedure to calculate the poroelastic reflection coefficients at arbitrary angles. In addition, it is well known that the global flow and local flow always take place simultaneously. However, studying the reflection dispersion signature including both global flow and local flow simultaneously is sparsely documented. In this chapter, to preserve the theoretical generality, the computed poroelastic reflection will incorporate the effect of local flow as well as global flow as shown in Figure 4.1.

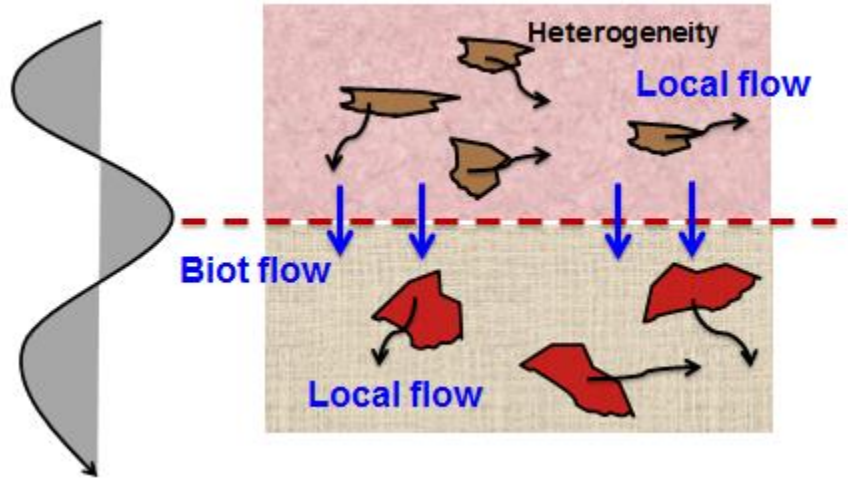


Figure 4.1. A schematic illustration of the P-wave incident upon an interface between two fluid-saturated heterogeneous porous media.

To characterize the reflection dispersion signatures, the first essential question to be addressed is how to describe the heterogeneous porous media that waves propagate through. Many poroelastic models have been proposed to explain the velocity dispersion and wave attenuation characteristics due to the inertial fluid effect. In this chapter, emphasis will be placed on the double-porosity dual-permeability model

developed by Berryman and Wang (1995, 2000), Pride and Berryman (2003a, 2003b), and Pride et al. (2004). There are several reasons to choose the double-porosity model. First of all, it represents a general framework to model wave propagation through heterogeneous porous structures, without placing any restriction on the mesoscopic geometry of the heterogeneity (Pride et al., 2004). Secondly, to highlight the effect of intrinsic loss and dispersion on reflection dispersion in the seismic frequency band, the geological heterogeneities here will be specified as mesoscopic scale. Moreover, Pride et al. (2004) showed that this theory can also be designed to simulate the dispersion effect associated with the patchy-saturation model and the squirt-flow model.

The content of this chapter is structured as follows. First, we will briefly review the wave dispersion and attenuation characteristics using double-porosity dual-permeability model. Next, we present how to use an effective procedure to calculate the poroelastic reflection in heterogeneous porous media. Following this section, a numerical example will be presented to quantitatively analyze the seismic reflection characteristics in terms of magnitude and phase angle. The difference between the elastic and poroelastic reflection coefficients will be compared in the section. Finally, we will discuss the effect of reservoir properties on the reflection dispersion signatures and explore the implications for reservoir characterization.

4.3 Effective Biot Media

To illustrate the effects of the wave-induced flow on the reflection of seismic waves, we treat the simplified problem of reflection and transmission of a plane compressional seismic wave incident with an oblique angle at a plane interface between two heterogeneous porous medium in the upper and lower half-space. If double-porosity dual-permeability model is used to describe the wave characteristics in heterogeneous porous materials, as illustrated on Figure 4.2, the incident plane compressional wave will generate four reflected wave modes and four transmitted wave modes: fast compressional wave, converted shear-wave, first-kind slow compressional wave, and second-kind slow compressional wave (Berryman and Wang, 1995, 2000; Pride et al., 2004; Dai et al., 2006). The fast compressional wave represents the conventional P-wave observed in the seismograms, and the other two slow P-wave modes are caused by the relative motion of the fluid with respect to the solid skeleton of heterogeneity phase and host phase, respectively. Mathematically, solving such a problem of plane-wave reflection and transmission in double-porosity media becomes extremely tedious, because there is a requirement of eight boundary conditions to constrain the solutions of reflections and transmission coefficients. Consequently, it was felt necessary to describe the heterogeneous porous media in a simplified way.

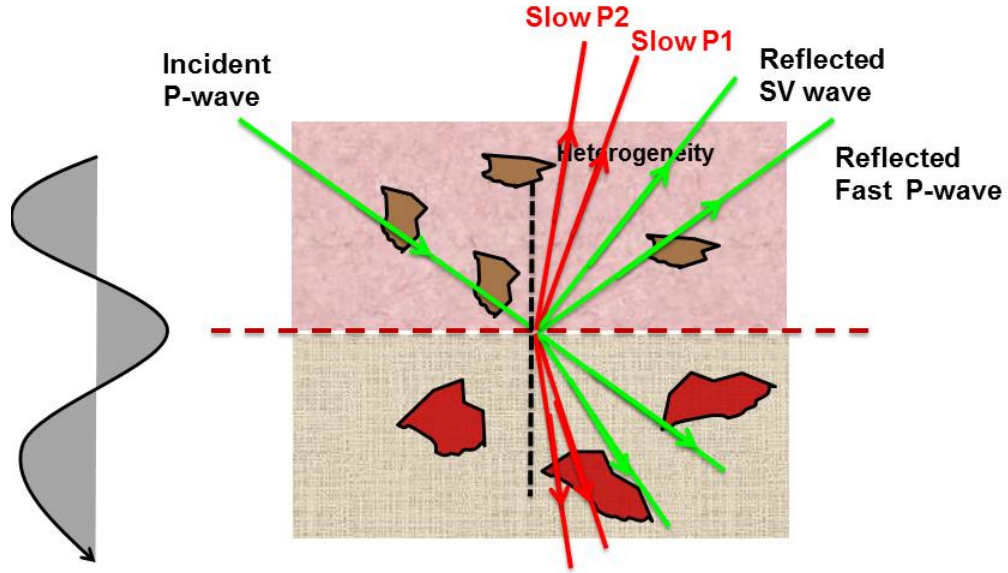


Figure 4.2. A schematic illustration of the plane wave reflection and transmission at the interface of double-porosity dual-permeability media.

As illustrated in Figure 4.3, the approach adopted in this study is to replace the heterogeneous porous medium with effectively homogeneous porous medium by reducing the internal local flow term. As a consequence, the effect of local flow is taken into account by a set of poroelastic parameters in classical Biot theory. In other words, the resulting effectively homogeneous media is mathematically expressed in the form of classical Biot theory, but it physically incorporates the frequency-dependent, wave-induced exchange of fluids between more compliant regions to relatively stiff regions. This effectively homogeneous porous media is termed as effective Biot media here. One typical example is the reduction of double-porosity theory to effective single-porosity Biot theory suggested by Pride et al (2004). With the assumption that the heterogeneity phase is totally embedded in the host phase, the

fluid motion relative to the solid skeleton of heterogeneity phase vanishes. The effect of internal flow is included in the effective drained bulk modulus, which can be derived from the original parameters of the double-porosity model. Note that the slow P-wave, which is related to the external fluid pressure equilibration, is not the original wave mode any more. It already includes the effect of internal flow exchange between the phase 1 and phase 2. The resulting undrained bulk modulus can be given as:

$$K_{sat}(\omega) = K_{dry}(\omega) + \frac{\alpha(\omega)^2}{(\alpha(\omega) - \phi) / K_s + \phi / K_f}, \quad (4.1)$$

where the $K_{dry}(\omega)$ and $\alpha(\omega)$ are the effective drained bulk modulus and Biot coefficient of the double-porosity composite, respectively.

It is necessary to point out that the workflow presented here is not limited to double-porosity model. It is applicable to any other poroelastic models which can generate the effective Biot media. The geological scenario can also be extended to patchy-saturation model, squirt flow model, etc. Indeed, many other poroelastic models (White, 1975; Dutta and Ode, 1979a, 1979b; Dvorkin et al., 1995; Gelinsky and Shapiro, 1997; Gurevich et al., 1997; Shapiro and Muller, 1999; Johnson, 2001; Chapman et al., 2002; Muller and Gurevich, 2004; Carcione and Picotti, 2006; Muller et al., 2007) can be considered to model the wave dispersion and attenuation characteristic in effective Biot media with different geological conditions. For example, rather to use the effective drained bulk modulus, Yao (2013) proposed to use effective fluid modulus to account for the frequency-dependent internal flow effect, which can be expressed as:

$$K_{sat}(\omega) = K_{dry} + \frac{\alpha^2}{(\alpha - \phi) / K_s + \phi / K_f(\omega)}. \quad (4.2)$$

The importance of the concept of effective Biot media lies in that it allows for the local flow loss, but does not require analysis of a second slow-wave. This is critical to the later treatment in this chapter, since the problem of solving the reflection coefficients from the boundary of heterogeneous porous media can be transformed to the problem of solving the reflection coefficients from the boundary of effective Biot media. Consequently, the problem of wave propagation characteristic and plane wave boundary can be casted in the framework of classical Biot theory.

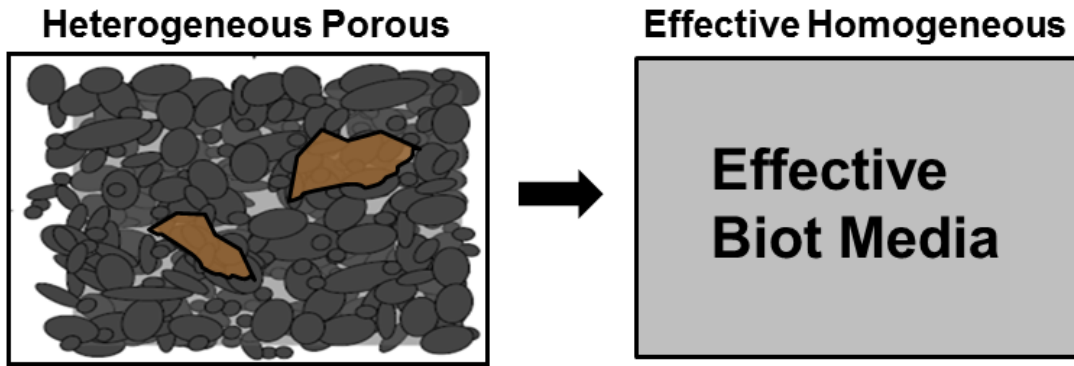


Figure 4.3. Schematic of the concept of effective Biot media that is simplified from heterogeneous porous media.

4.4 Reflection Coefficients from the Boundary of Effective Biot Media

Here, we use the aforementioned effective Biot theory reduced from the double-porosity model to describe the heterogeneous porous materials. As previously described, it represents a general framework to simulate the poroelastic response due to mesoscopic flow, which is considered to explain the significant energy loss

observed in the seismic frequency band. Following the notation presented in the last chapter, the poroelastic wave equations in effective Biot media are given as:

$$(\lambda^* + \alpha^{*2} M^* + \mu^*) \nabla(\nabla \bullet \mathbf{u}) + \mu^* \nabla^2 \mathbf{u} + \alpha^* M^* \nabla(\nabla \bullet \mathbf{W}) = \rho_b \frac{\partial^2 \mathbf{u}}{\partial t^2} + \rho_f \frac{\partial^2 \mathbf{W}}{\partial t^2}, \quad (4.3)$$

$$\alpha^* M^* \nabla(\nabla \bullet \mathbf{u}) + M^* \nabla(\nabla \bullet \mathbf{W}) = \rho_f \frac{\partial^2 \mathbf{u}}{\partial t^2} + \frac{c_m \rho_f}{\phi} \frac{\partial^2 \mathbf{W}}{\partial t^2} + \frac{F \eta}{\kappa^*} \frac{\partial \mathbf{W}}{\partial t}. \quad (4.4)$$

Here, the frequency-dependent effective elastic parameters which incorporate the local flow effects are given as:

$$\frac{1}{\mu_d} - \frac{1}{\mu^*} = \frac{4}{15} \left(\frac{1}{K_d} - \frac{1}{K_d^*} \right) \quad (4.5)$$

$$\alpha^* = 1 - K_d^* / K_s; \quad (4.6)$$

$$\frac{1}{M^*} = \frac{\alpha^* - \phi}{K_s} + \frac{\phi}{K_f}; \quad (4.7)$$

$$\frac{1}{\kappa^*} = \frac{\nu_1}{\kappa_1} + \frac{\nu_2}{\kappa_2}, \quad (4.8)$$

where K_d^* is defined in equation 3.24, which can be calculated from the parameters in the double-porosity model; ν_1 and ν_2 are the volume fraction of phase 1 and phase 2, respectively; and κ_1 and κ_2 are the permeability of the phase 1 and phase 2, respectively.

The geometry for the reflection from the boundary of effective Biot media is shown in Figure 4.4. The properties of the upper medium are indicated by the subscript 1, and those of the lower medium by the subscript 2. The incident wave is

taken to be a fast P-wave of angular frequency, with an incident angle α with respect to the normal to the boundary. At the interface, the incident wave is reflected into medium 1 and transmitted into medium 2, and in both media the fast P-wave, slow P-wave and SV-wave are generated.

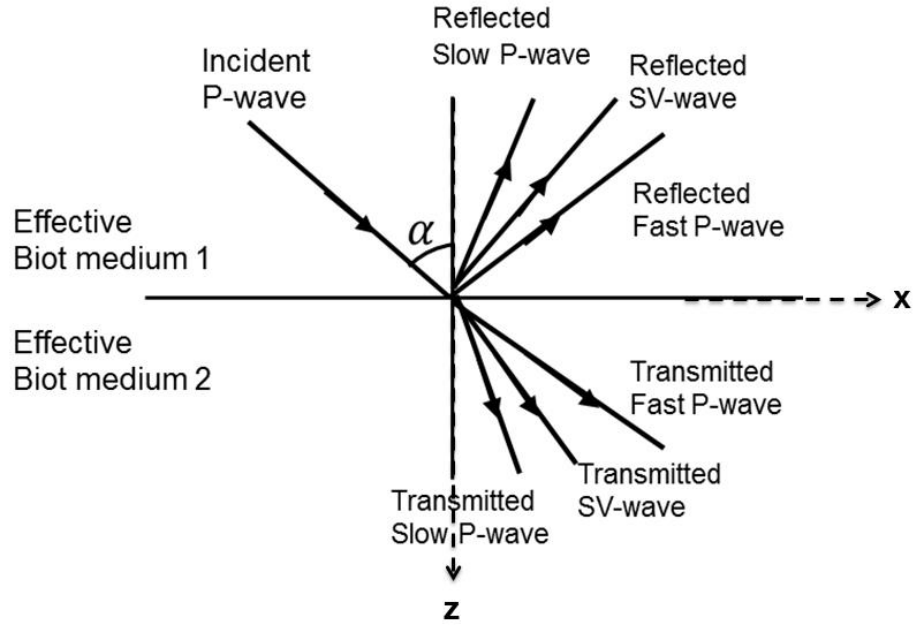


Figure 4.4. Reflection and transmission of a compressional plane wave at an interface between two effective Biot medium. The effective single-porosity Biot medium is reduced from double-porosity medium.

In order to solve the seismic reflection and transmission at the interface of effective Biot medium, we have the boundary conditions as follows (Deresiewicz, 1960; Dutta and Ode, 1983; Bourbie, 1987; Dai et al., 2006):

1. Continuity of the horizontal solid matrix displacement : $u_x^1 = u_x^2$, (4.9a)

2. Continuity of the normal solid matrix displacement: $u_z^1 = u_z^2$, (4.9b)

$$3. \text{ Continuity of the total normal stress: } \sigma_{zz}^1 = \sigma_{zz}^2, \quad (4.9c)$$

$$4. \text{ Continuity of the total shear stress: } \sigma_{xz}^1 = \sigma_{xz}^2, \quad (4.9d)$$

$$5. \text{ Continuity of the increments of fluid content: } W_z^1 = W_z^2, \quad (4.9e)$$

$$6. \text{ Continuity of the fluid pressure: } p_f^1 = p_f^2. \quad (4.9f)$$

The angle-incident seismic reflection coefficients can be calculated through solving the Zoeppritz-style equations:

$$GR = P, \quad (4.10)$$

where R is 6×1 vector of the unknown reflection and transmission coefficients and is given by:

$$R = \begin{pmatrix} R_{P1P1} \\ R_{P1P2} \\ R_{P1S} \\ T_{P1P1} \\ T_{P1P2} \\ T_{P1S} \end{pmatrix}, \quad (4.11)$$

where R_{P1P1} , R_{P1P2} and R_{P1S} are the reflection coefficients of the fast P-, slow P- and S-waves, respectively; T_{P1P1} , T_{P1P2} , and T_{P1S} are the transmission coefficients of the fast P-, slow P- and S-waves, respectively. G is a 6×6 matrix which characterizes the angle-dependent dynamic poroelastic responses in the upper and lower half space of the effective Biot media:

$$G = \begin{pmatrix} \sin \theta_{p1}^r & \sin \theta_{p2}^r & \cos \theta_s^r & -\sin \theta_{p1}^t & -\sin \theta_{p2}^t & \cos \theta_s^t \\ \cos \theta_{p1}^r & \cos \theta_{p2}^r & -\sin \theta_s^r & \cos \theta_{p1}^t & \cos \theta_{p2}^t & \sin \theta_s^t \\ X_1 & X_2 & X_3 & X_4 & X_5 & X_6 \\ \frac{\mu_1^* \sin 2\theta_{p1}^r}{V_{p11}} & \frac{\mu_1^* \sin 2\theta_{p2}^r}{V_{p12}} & \frac{\mu_1^* \cos 2\theta_s^r}{V_{s1}} & \frac{\mu_2^* \sin 2\theta_{p1}^t}{V_{p21}} & \frac{\mu_2^* \sin 2\theta_{p2}^t}{V_{p22}} & -\frac{\mu_2^* \cos 2\theta_s^t}{V_{s2}} \\ \delta_{p11} \cos \theta_{p1}^r & \delta_{p12} \cos \theta_{p2}^r & -\delta_{s1} \sin \theta_s^r & \delta_{p21} \cos \theta_{p1}^t & \delta_{p22} \cos \theta_{p2}^t & \delta_{s2} \sin \theta_s^t \\ \frac{\alpha_1^* M_1^* + M_1^* \delta_{p11}}{V_{p11}} & \frac{\alpha_1^* M_1^* + M_1^* \delta_{p12}}{V_{p12}} & 0 & -\frac{\alpha_2^* M_2^* + M_2^* \delta_{p21}}{V_{p21}} & -\frac{\alpha_2^* M_2^* + M_2^* \delta_{p22}}{V_{p22}} & 0 \end{pmatrix}, \quad (4.12)$$

where

$$X_1 = \frac{\lambda_1^* + (\alpha_1^*)^2 M_1 + \alpha_1^* M_1^* \delta_{p11} + 2\mu_1^* (\cos \theta_{p1}^r)^2}{V_{p11}},$$

$$X_2 = \frac{\lambda_1^* + (\alpha_1^*)^2 M_1 + \alpha_1^* M_1^* \delta_{p12} + 2\mu_1^* (\cos \theta_{p2}^r)^2}{V_{p12}},$$

$$X_3 = -\frac{2\mu_1^* (\cos \theta_s^r)^2}{V_{s1}}, \quad X_4 = -\frac{\lambda_2^* + (\alpha_2^*)^2 M_2 + \alpha_2^* M_2^* \delta_{p12} + 2\mu_2^* (\cos \theta_{p1}^t)^2}{V_{p21}},$$

$$X_5 = -\frac{\lambda_2^* + (\alpha_2^*)^2 M_2 + \alpha_2^* M_2^* \delta_{p12} + 2\mu_2^* (\cos \theta_{p2}^t)^2}{V_{p22}}, \quad X_6 = -\frac{2\mu_2^* (\cos \theta_s^t)^2}{V_{s2}},$$

$$X_7 = -\frac{\lambda_1^* + (\alpha_1^*)^2 M_1 + \alpha_1^* M_1^* \delta_{p11} + 2\mu_1^* (\cos \theta_s^t)^2}{V_{p11}}.$$

P is a 6×1 vector that represents the information of the incident P-wave in the upper medium, and is given by:

$$P = \begin{pmatrix} -\sin \theta^i \\ \cos \theta^i \\ X_7 \\ \frac{\mu_1^* \sin 2\theta^i}{Vp_{11}} \\ \delta_{p11} \cos \theta^i \\ -\frac{\alpha_1^* M_1^* + M_1^* \delta_{p11}}{Vp_{11}} \end{pmatrix}. \quad (4.13)$$

The detailed derivations are carried out in Appendix A. In the above equations, Vp_{11} , Vp_{12} , Vs_1 and Vp_{21} , Vp_{22} , Vs_2 are the frequency-dependent fast P-wave velocity, slow P-wave velocity, and shear-wave velocity in the upper medium and low medium, respectively; $\lambda_i^*(i=1,2)$ and $\mu_i^*(i=1,2)$ are the frequency-dependent Lamé's parameter of the effective Biot media under drained condition; $\alpha_i(i=1,2)$ is the effective frequency-dependent Biot's coefficient which can be computed from equation 4.7, and the frequency-dependent $M_i(i=1,2)$ is computed based on equation 4.8; $\delta_{pi1}, \delta_{pi2}, \delta_{si}, (i=1,2)$ refer to the ratios of the potential for the relative fluid displacement to the rock frame displacement for the fast P-wave, slow P-wave, and shear-wave respectively; $\theta_{p1}^r, \theta_{p2}^r, \theta_s^r$ refer to the reflected angles of fast P-wave, slow P-wave, and shear-wave respectively, and $\theta_{p1}^t, \theta_{p2}^t, \theta_s^t$ refer to the transmitted angles of fast P-wave, slow P-wave, and shear-wave respectively.

Following Snell's law in effective Biot media (equation A-12 in Appendix A), they can be expressed as:

$$\theta_{p_2}^r = \theta^i, \theta_{p_2}^r = \arcsin \frac{\sin \theta^i}{V_{p_{11}}} V_{p_{12}}, \theta_s^r = \arcsin \frac{\sin \theta^i}{V_{p_{11}}} V_{s_1}$$

$$\theta_{p_1}^t = \arcsin \frac{\sin \theta^i}{V_{p_{11}}} V_{p_{21}}, \theta_{p_2}^t = \arcsin \frac{\sin \theta^i}{V_{p_{11}}} V_{p_{22}}, \theta_s^t = \arcsin \frac{\sin \theta^i}{V_{p_{11}}} V_{s_2}.$$

Note that the resulting reflection coefficients now become complex numbers due to the wave dispersion and attenuation in heterogeneous poroelastic media. Thus, we can define the reflection coefficients as:

$$R(\omega) = |R(\omega)| \exp(i\varphi), \quad (4.14)$$

where $|R(\omega)|$ indicates the magnitude, and φ indicates the phase angle for the poroelastic reflection coefficients. In the following sections, we will use these two parameters to characterize the reflection dispersion signatures.

It is necessary to point out that all the frequency-dependent poroelastic parameters in equation 4.10 are computed based on the effective single porosity Biot model reduced from double-porosity model, which suggests that the effect of local flow is incorporated into the poroelastic wave propagation. Correspondingly, the resulting reflection coefficients will also contain the responses from both global flow and local flow.

4.5 A Numerical Example

So far we have presented a theoretical formulation of the reflection and transmission of plane seismic waves at a boundary between two heterogeneous porous

rocks. In this section, we use a numerical example to quantitatively investigate the impact of wave-induced fluid flow on the seismic reflection coefficients at arbitrary angles and frequencies.

4.5.1 Geological Model

We only consider an interface with two heterogeneous porous half-spaces above and below. To mimic the realistic reservoir situation, we assume that the geological model consists of an underlain sandstone reservoir with an overburden shale layer. Both the sandstone and shale have heterogeneous porous structures which can be characterized by the double-porosity model. To obtain their elastic properties, we start with a solid rock matrix, in which the minerals are mixed using a Reuss-Voigt-Hill average. The mineral presenting in the upper medium (shale) consists of 85% clay and 15% feldspar. The mineral presenting in the lower medium (sandstone) consists of 95% quartz and 5% clay, implying that the sandstone is pretty clean. The heterogeneity phases in sandstone and shale are assumed to represent the compliant parts of the rock where the grains are unconsolidated, while the matrix phases are considered to be well consolidated. The dry rock moduli are in turn determined from the following effective medium formula (Walton, 1987; Pride et al., 2002; Pride and Berryman, 2003a)

$$K_i = (1 - \phi_i)K_s / (1 + c_i\phi_i), \quad (4.15)$$

$$G_i = (1 - \phi_i)G_s / (1 + c_i\phi_i), \quad (4.16)$$

where we take $c_1=5$ and 4 for the well consolidated host phase, $c_2=150$ and 100 for the poorly consolidated heterogeneity phase, in sandstone and shale respectively.

Matrix rock and fluid properties for the overlying shale and underlying sandstone are given in Table 4.1 and Table 4.2, respectively. Phase 1 and phase 2 refer to the host phase and heterogeneity phase, respectively; K_s and μ_s are the bulk and shear moduli (in GPa) for the mineral matrix; K_d and μ_d are the bulk and shear moduli of the drained rock frame; ρ_s is the density of mineral matrix; ϕ is the porosity; τ is the tortuosity parameter; κ is the permeability; and V indicates the volume fraction of the phase 1 or phase 2. For the sake of simplicity, the geometry of the heterogeneity phase is assumed as penny-shaped, and a and ε are used to represent the radius and aspect ratio of heterogeneity respectively. As for the fluid properties, K_f , ρ_f , and η are the bulk modulus, density, and viscosity of the pore fluid respectively.

Table 4.1. The related parameters for rock frame properties of upper medium and lower medium.

Parameter	Rock frame properties			
	Upper (shale)		Lower(sandstone)	
	Phase 1	Phase 2	Phase 1	Phase 2
K_d (GPa)	22.0	4.2	11.9	0.6
μ_d (GPa)	6.9	1.5	10.3	0.4
V	0.93	0.07	0.96	0.04
ϕ	0.05	0.06	0.25	0.30
κ (md)	0.01	100	10	1000
α (m)		0.05		0.08
ε		0.1		0.1
τ	2.4	2	2.4	2

Table 4.2. The related parameters for the pore fluid properties of upper medium and lower medium.

Parameter	Pore fluid properties	
	Upper (shale)	Lower(sandstone)
K_f (GPa)	2.25	2.5
ρ_f (kg/m ³)	1.05	1.05
η (cP)	1	5

4.5.2 Velocity Dispersion and Attenuation Characteristics

The fast P-wave and the corresponding 1/Q for the upper and lower medium are plotted against frequency in Figure 4.5. We observe considerable velocity dispersion for the heterogeneous sandstone at a low frequency range of 10-100Hz. By contrast,

the overburden shale exhibits little dispersion effect, and the transitional frequency occurs at very low frequency (below 1 Hz). The mesoscopic flow is responsible for such dispersion effects. Moreover, there is a slight ramp-up in the fast P-wave for both the upper medium and lower medium centered at a much higher frequency, which is caused by the Biot flow. In Figure 4.5 (b), the peak to the left for each attenuation curve corresponds to the frequency when the mesoscopic heterogeneities structure just has time to equilibrate in one cycle, while the peak to the right corresponds to the Biot-loss maximum. Such a dependence of the characteristic frequency for mesoscopic fluid flow is opposite to that of the Biot flow. It is also easy to find that the local viscous flow contributes to most of the dissipative energy, whereas the global flow plays a dominant role in the energy dissipation for the high frequency domain.

The slow P-wave dispersion and attenuation ($1/Q$) as a function of frequency are displayed in Figure 4.6. The slow P-wave can influence fast P-wave reflection amplitudes, which carry information about the porous media away from the interface to distant receivers. The shear-wave dispersion and the corresponding $1/Q$ for the upper and lower medium are plotted against frequency in Figure 4.7, respectively. Compared with the fast P-wave dispersion and attenuation shown in Figure 4.5, the shear-wave dispersion effect due to mesoscopic flow is much smaller than that of fast P-wave. Nonetheless, it is interesting to note that the shear-wave dispersion and attenuation caused by Biot flow is larger than the corresponding fast P-wave dispersion.

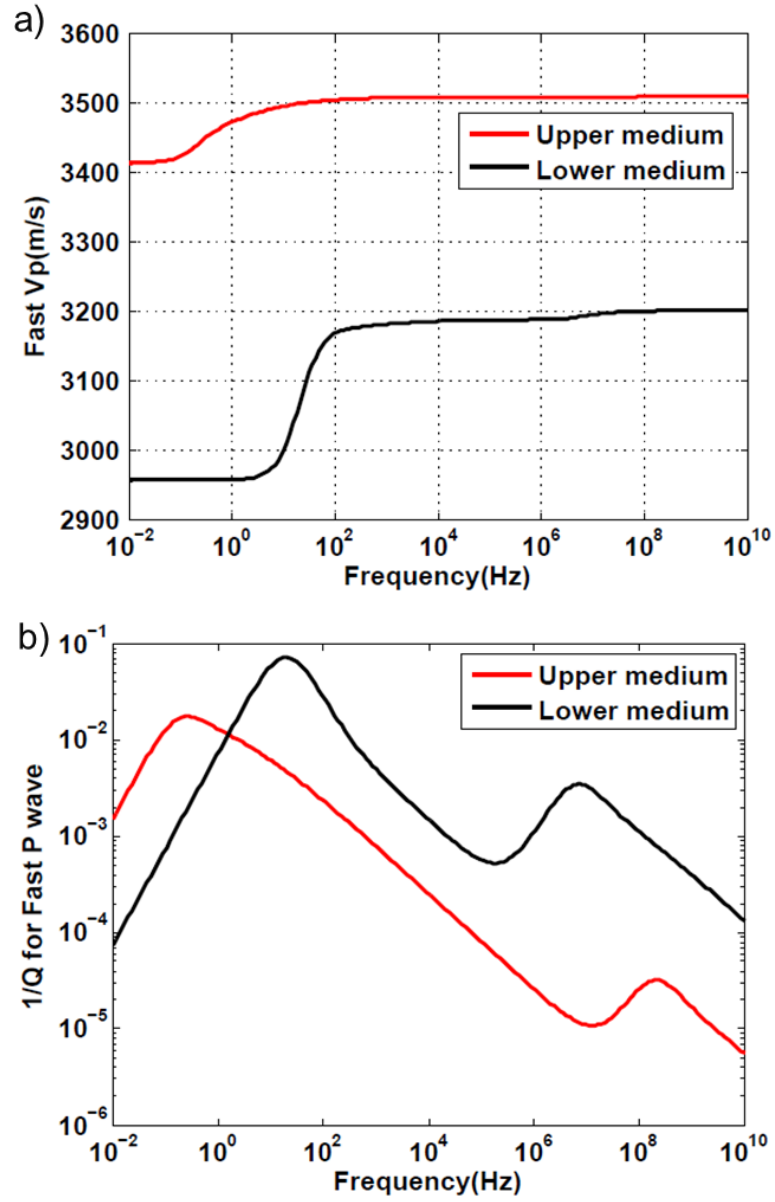


Figure 4.5. (a) Phase velocity dispersion (b) Attenuation of the effective fast P-wave in the upper and lower double-porosity medium.

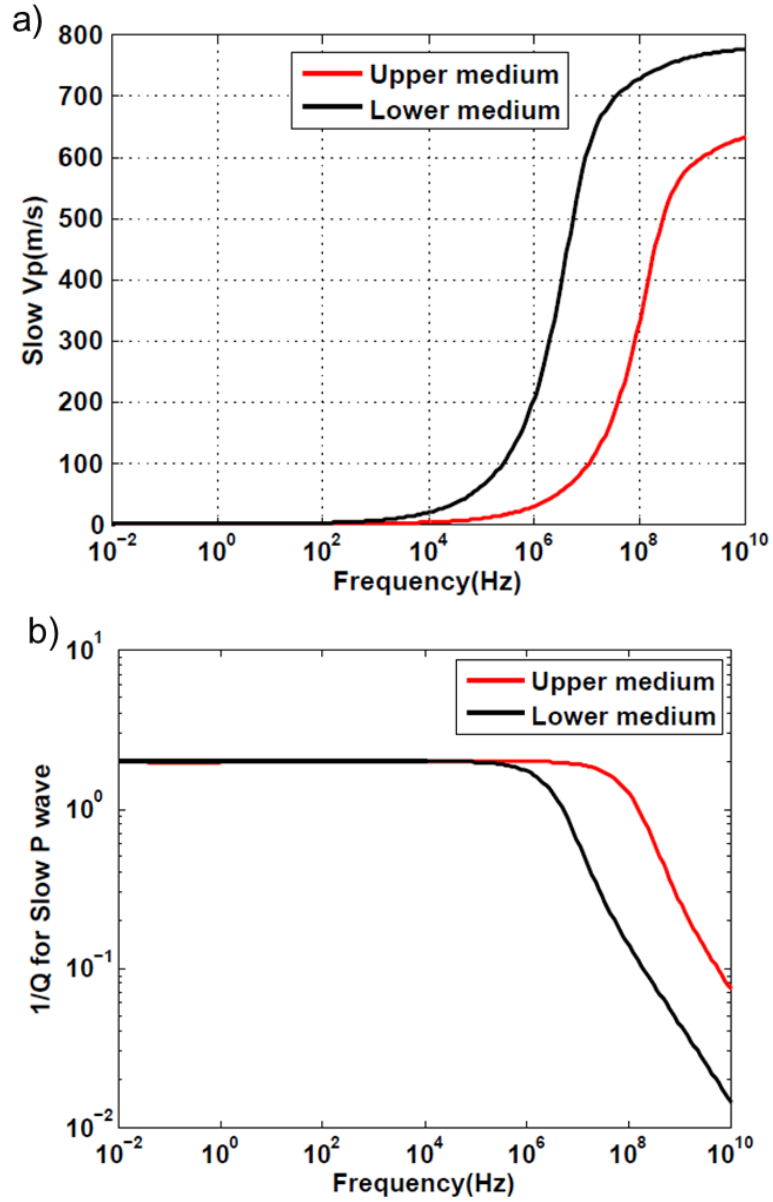


Figure 4.6. (a) Phase velocity dispersion (b) Attenuation of effective slow P-waves in the upper and lower double porosity medium. The elastic properties of the rock and the fluids are given in Table 4.1.

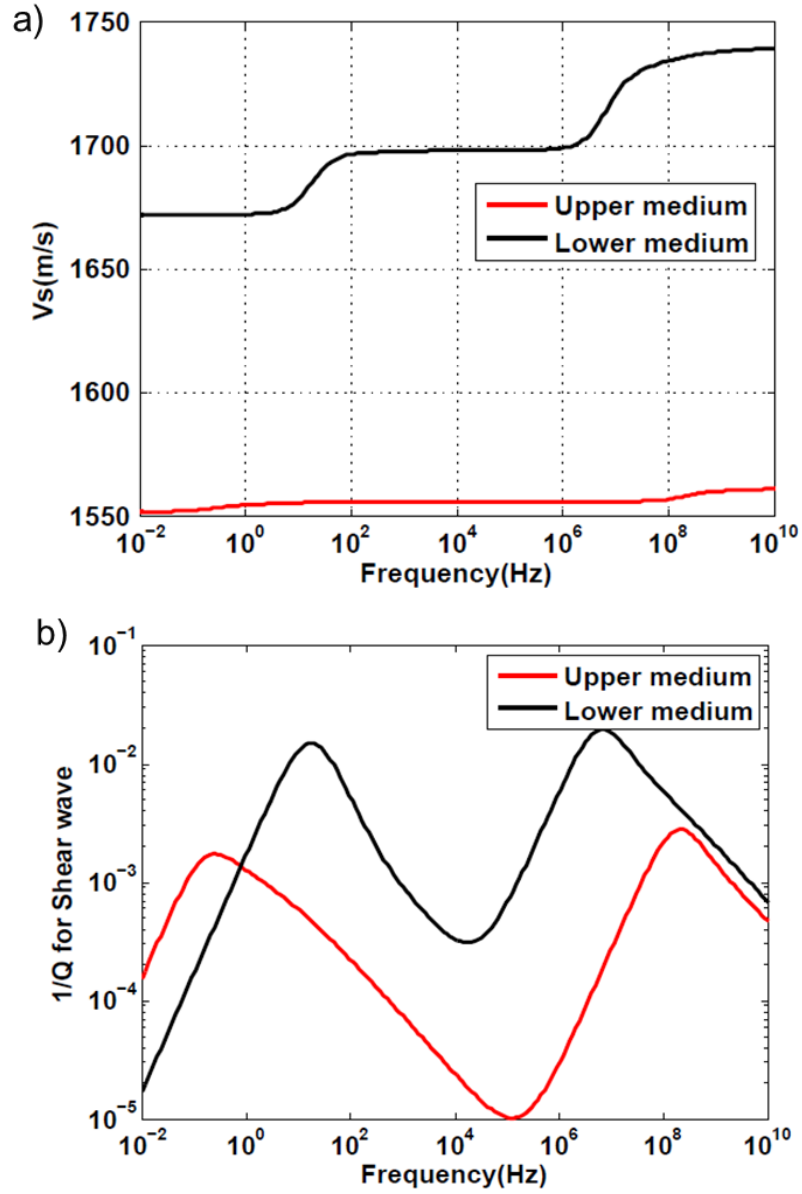


Figure 4.7. (a): Phase velocity dispersion (b): Attenuation of effective S-waves in the upper and lower double porosity medium. The elastic properties of the rock and the fluids are given in Table 4.1.

4.5.3 Reflection Dispersion Signatures

For the given set of parameters, Figure 4.8 shows the computed reflection amplitude and phase variation of fast PP-wave as a function of frequency and incident angle. In the amplitude versus incident-angle domain, Figure 4.8(a) shows that the reflection magnitude increases with an increase of incident angle, which agrees with traditional class III AVO response. In the amplitude versus frequency domain, the low frequency bright spot channel occurring at the seismic frequency band is intimately associated with the physical discrepancy between the characteristic frequency of the overburden shale and underlain reservoir sandstone. Generally, the amplitude versus incident-angle (AVA) relationship is mainly influenced by the contrast in elastic properties such as P-impedance and V_p/V_s ratio. However, the amplitude versus frequency (AVF) relationship contains the information about heterogeneities properties and fluid mobility. Figure 4.8(b) shows the phase shift of the poroelastic reflection compared with that of elastic reflection. It is found that the phase variation is also dependent on the frequency, and a non-negligible phase shift which can be as high as 12 degrees occurs in the seismic exploration band. Nonetheless, the phase variation shows little sensitivity to the incident angle change. The combination of seismic reflection (both amplitude and phase angle) variation with incident angle and frequency as shown in Figure 4.8 has potential to reveal more reservoir properties.

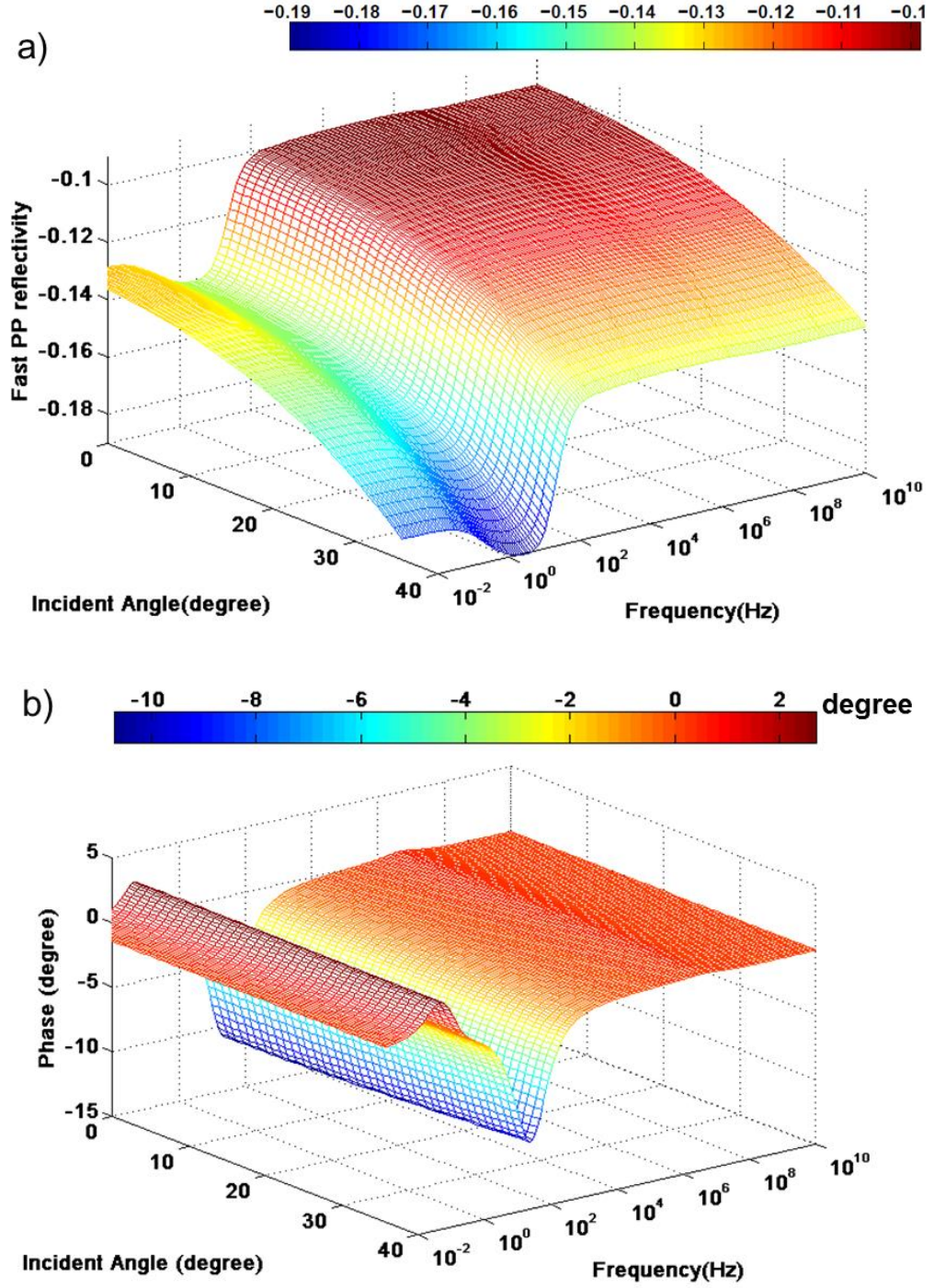


Figure 4.8. (a) Reflection amplitude and (b) phase variation of fast PP as a function of frequency and incidence angle. Phase variation here indicates the deviation of the phase in the poroelastic reflection from the constant phase in the elastic reflection.

Now, we are going to give a detailed analysis regarding the fast PP reflectivity dispersion characteristics (Figure 4.9) at normal incident angle. In Figure 4.9(a), the red line indicates the elastic reflection coefficient which is computed from the classical Zoeppritz equation. The saturated rock's elastic response for elastic reflection is computed using Gassmann equation, which suggests that the elastic reflections coefficients do not include any intrinsic dispersion effects. As we can observe, the elastic reflection is consistent with the poroelastic reflection only at the frequency band as low as 10^{-2} Hz. Such consistency physically makes sense, because Biot flow becomes negligible at very low frequency, and local flow does not induce a dispersion effect at very low frequency. It can be concluded that the porous dissipative media acts as elastic media at very low frequency ($<10^{-2}$ Hz). The reflectivity dispersion occurring at roughly 0.01-100 Hz is believed to be caused by mesoscopic flow, and the maximum dispersion effect at the seismic frequency domain can reach as much as 40%. This huge dispersion effect should not be ignored when using seismic reflections for quantitative seismic interpretation. Moreover, the negligible reflectivity dispersion occurring at about 10^6 Hz (ultrasonic lab frequency band) is believed to be associated with Biot flow.

Figure 4.9(b) plots the phase variation against the frequency at normal incident angle. The phase angle of the poroelastic reflection is consistent with that of elastic reflection at both the low frequency and high frequency limit. A phase advance occurs at 10^{-3} Hz to around 10^{-1} Hz, but then a noticeable phase delay takes place at a broad frequency range from 10^{-1} Hz to 10^5 Hz. Both of these phase shifts are mainly caused by local flow. It is believed that the small phase advance occurring at ultrasonic

frequency band is closely related to the dispersion caused by Biot flow. Note that the local flow can influence the phase angle to a considerable degree, and consequently affect the seismic waveform. This implies that phase shift can lead to uncertainty for seismically imaging the precise location of the geological feature of interest. In addition, the significant discrepancy of the seismic amplitude and phase variation between surface seismic band and sonic log band also suggests that we should be more cautious about seismic-to-synthetic well tie in heterogeneous reservoir rocks.

Figure 4.10 shows the AVO relationship with different frequencies in the seismic exploration band. For the purpose of reservoir evaluation, seismic reflection amplitude can be often interpreted to indicate porous volume or other reservoir properties. However, we demonstrate that the wave-induced fluid flow can strongly affect the seismic reflection amplitude. Be aware that the field reflection observations which are often centered around 40-60 Hz already represent the reflection dispersion effect. That is to say, in heterogeneous reservoir rocks, the classical seismic reflection interpretation based on Zoeppritz equation might be misleading. For example, for the given geological model, if we use the dispersive seismic reflection amplitude to estimate porosity, the result will be considerably underestimated.

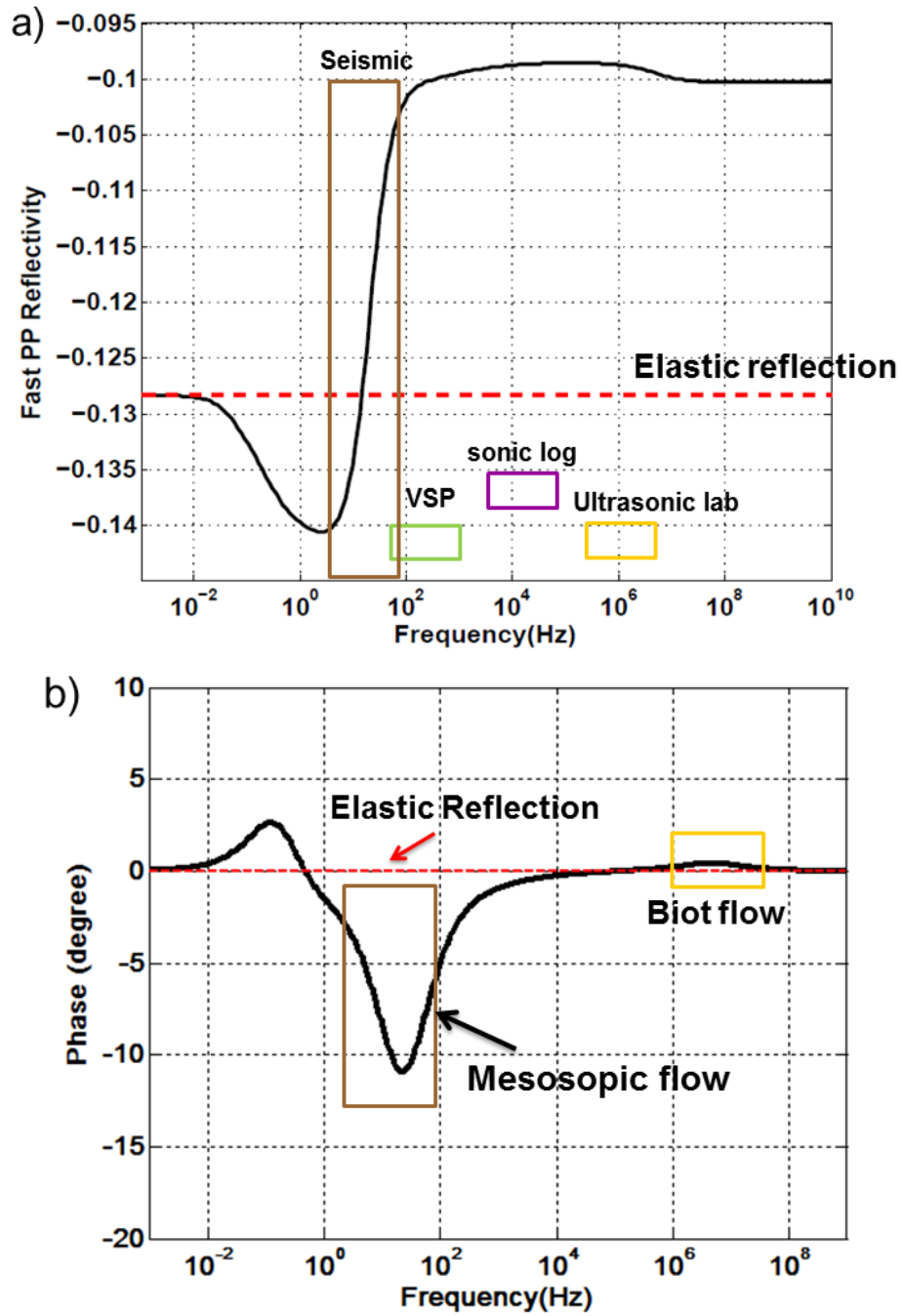


Figure 4.9. Reflection (a) amplitude and (b) phase of fast PP as a function of frequency at normal incidence angle. The red dashed line indicates (a) amplitude and

(b) phase computed for elastic reflection. The frequency bands for seismic, VSP, sonic log, and ultrasonic lab are highlighted in the plot.

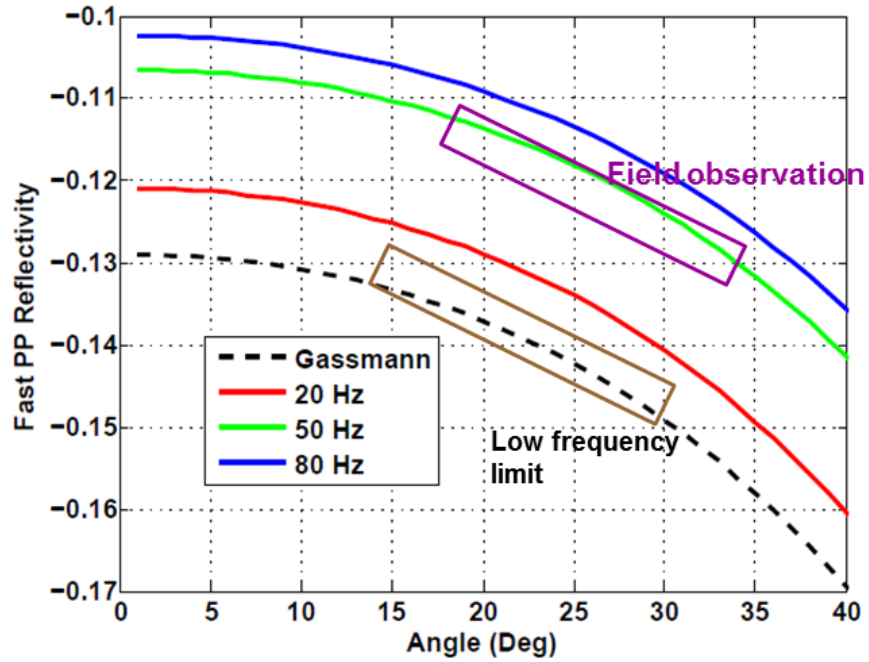


Figure 4.10. AVO relationship with different frequency in the seismic band. The central frequency band for the field observation is often centered at around 40-60 Hz. The black dash line indicates the reflection computed from Zoeppritz equation, which often represents the low frequency limit for the poroelastic reflection.

Figure 4.11 shows the converted PS reflection as a function of frequency. PS reflectivity is zero at normal incident angle, which is physically understandable because no PS conversion occurs at normal incident angle. At non-zero incident angle, we observe that the PS reflection presents similar dispersion trend as the fast PP reflectivity does. However, it should be noted that the relative dispersion effect for

PS reflection is bigger than that of fast PP reflection. In particular, the dispersion effect due to Biot flow is more evident. Additionally, we find that PS reflection has a larger dispersion effect for far offset than near offset for the given geological model.

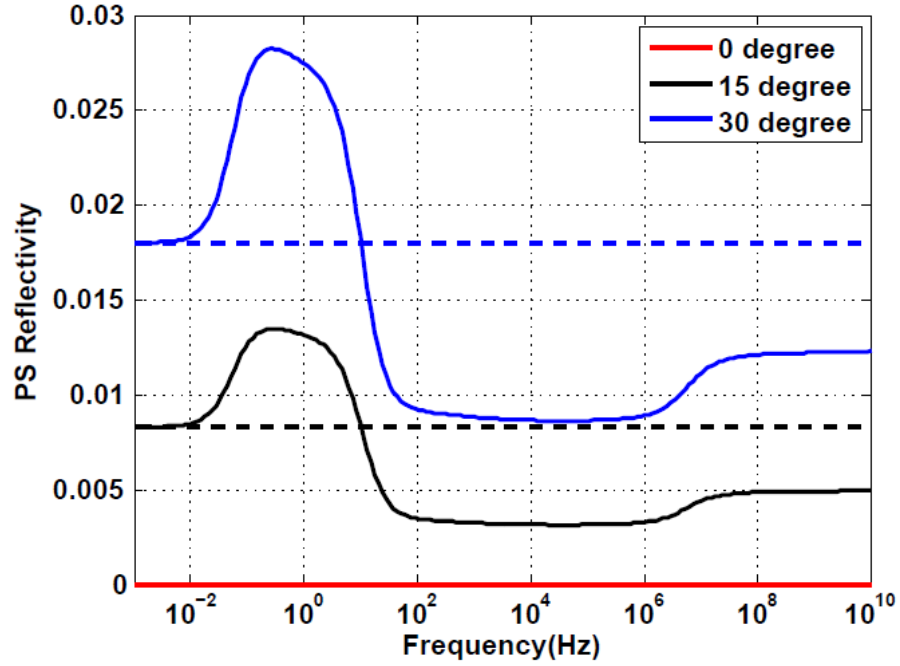


Figure 4.11. Comparisons of PS reflectivity dispersion at incident angles of 0 degree, 15 degrees, and 30 degrees. The dashed line indicates the PS reflection coefficients computed based on the Zoeppritz equation.

4.6 Discussion

The double-porosity model we employed here is based on the idealization that the heterogeneous porous media can be meaningfully reduced to just two distinct porous phases with a single dominant diffusion length and contrasting properties. The idealization of the model may limit its application on some complex heterogeneous

reservoirs, which often involves mixing many porous phases and multi-scale heterogeneities in a random manner. Moreover, to generate the effective Biot media from the double-porosity model, the heterogeneity phase 2 is assumed entirely embedded in host phase 1. This implies that the volume fraction of phase 2 is much smaller compared with that of phase 1, which may not meet the conditions of real rocks in some geological scenarios. However, the real challenge concerning the practical implementation of this methodology is the difficulty in prescribing appropriate physical parameters, such as heterogeneity size, tortuosity, bulk modulus in the drained condition, etc.

Similar to any other sedimentary rocks, shale more or less contains heterogeneities to some extent. Such heterogeneities may come from the presence of micro-cracks or organic material related to hydrocarbon generation (Hornby et al., 1994; Vernik et al., 1994; Jakobsen et al., 2003; Bandyopadhyay, 2009), compositional variation due to different depositional environments, and so forth. As a consequence, shales are naturally dispersive materials, even they might behave elastically in seismic exploration band due to their very low permeability characteristics (Batzle et al., 2006). To investigate the frequency-dependent reflection variations due to patchy-saturated rocks, Ren et al. (2009a, 2009b) and Liu et al. (2011) assume that the overlying shale is non-dispersive. However, in this study, to preserve the generality of poroelastic reflection in heterogeneous poroelastic media, the overburden shale is considered as a dispersive medium including mesoscopic heterogeneity. Even the dispersion effect is not appreciable and occurs in very low frequency domain, as we can see in Figure 4.5. The permeability of shale in our designed geological model is

given as 0.01md, but the permeability of shales can vary enormously, from nanodarcy range to microdarcy range. Figure 4.12 illustrates how the permeability of the overburden shale influences the reflection amplitude. It turns out that the reflection dispersion curve merely shows noticeable change at the low frequency domain (<10 Hz, with seismic amplitude getting stronger as the permeability of the overburden shale decreases. In addition, it is worth noting that the velocity and flow characteristic in the shale also exhibit anisotropy. The dispersion and attenuation in the direction parallel to the layers are quite different from those perpendicular to the layers. However, in this study only the case of isotropy is discussed. The plane wave propagation going across the anisotropic poroelastic contact should be investigated in the future.

As we know, the reflection dispersion feature is intimately related to the contrast of attenuation across the interface. On the other hand, it is also essential to understand the material's attenuation attributes from the poroelastic reflection signatures. Figure 4.13 shows the comparison of reflection amplitude and phase with frequency-dependent $1/Q$ ($=1/Q_{\text{lower}}-1/Q_{\text{upper}}$) contrast across the interface. It is interesting to see that attenuation contrast controls the reflection amplitude with frequency. If $1/Q < 0$, which suggests the attenuation in the upper medium is higher than that in the low medium, the amplitude increases with frequency. However, when the attenuation contrast changes from negative to positive, which occurs around 2 Hz, the corresponding reflection amplitude starts decreasing with frequency. Meanwhile, the Biot flow exerts an opposite influence on the relationship of attenuation contrast with

reflection amplitude. At the frequency domain ranging from 10^6 - 10^8 Hz, the attenuation contrast is positive, but the reflection amplitude increases with frequency.

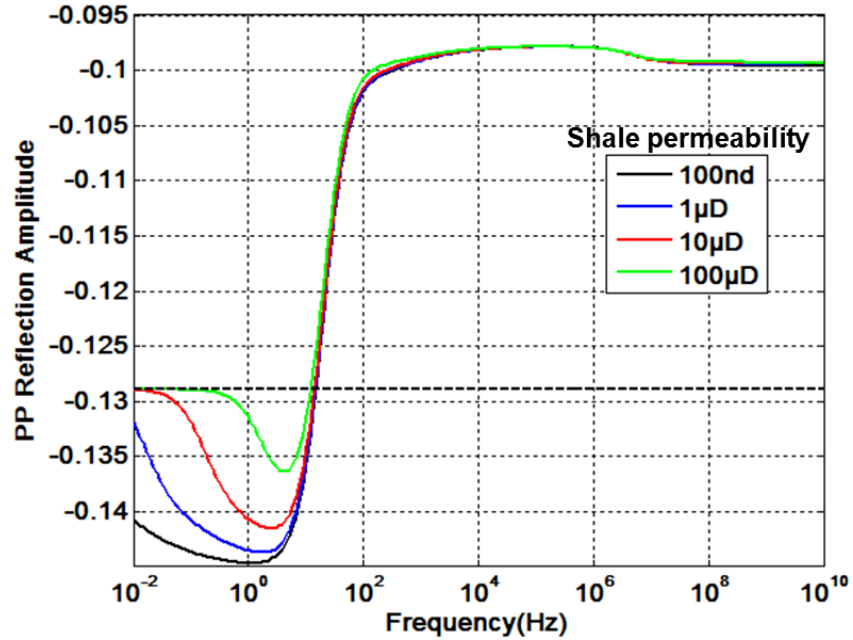


Figure 4.12. The effect of permeability of overburden shale on PP reflection dispersion at normal incident angle.

Additionally, it is clear to see that the attenuation contrast peak corresponds to the frequency range where the reflection amplitude exhibits the most rapid change with frequency (the slope of the tangential line). Figure 4.13b illustrates that phase shift is closely related to attenuation contrast, especially when local flow controls the reflection dispersion effect. However, at the frequency range where the global flow dominates, the phase shift and attenuation contrast have an opposite trend with frequency.

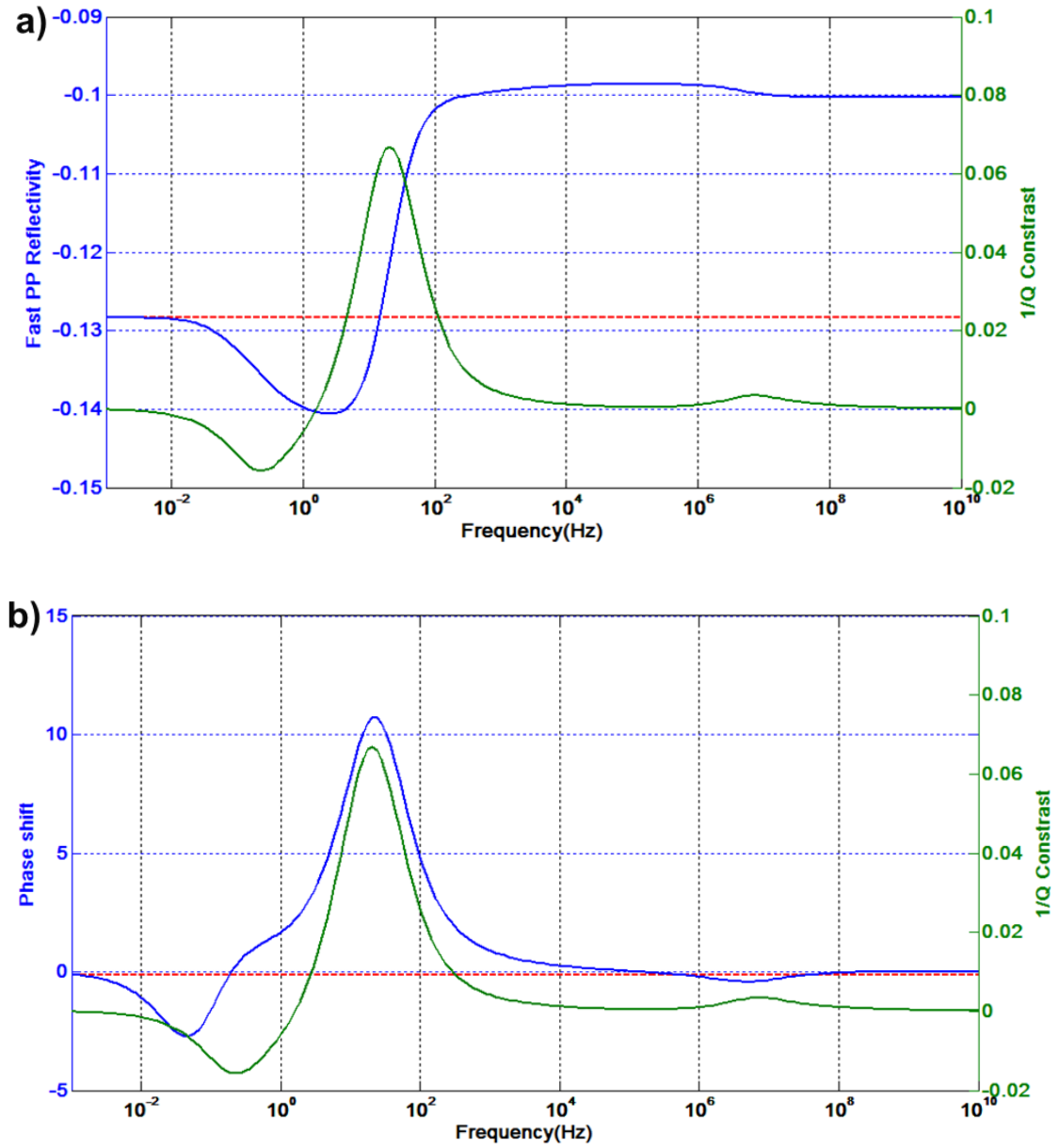


Figure 4.13. Comparison of (a) reflection amplitude and (b) phase shift with attenuation contrast as a function of frequency at normal incidence angle. The red dashed line indicates (a) amplitude and (b) phase computed for elastic reflection.

One question might be raised is, after we obtain the frequency-dependent velocity, what if we calculate reflection coefficients based on the classical Zoeppritz equation for each single-frequency component? What is the difference for this result compared with the poroelastic reflection computed based on the methodology proposed here? The result of comparison is shown in Figure 4.14. They still show certain differences at a wide frequency range. It turns out that the latter can capture the amplitude-versus-frequency trend caused by local flow, but it is incapable of characterizing the reflection dispersion signatures caused by Biot flow. More importantly, the reflection calculated based on the classical Zoeppritz equation cannot give the phase variation with frequency, which is an inseparable part of the poroelastic reflection feature. However, the key point we want to emphasize here is that, from a theoretical point of view, the classical Zoeppritz equation is not applicable for calculating the reflection coefficients in the heterogeneous and dissipative media, because the well-known assumption for the Zoeppritz equation is that the medium is elastic and non-dissipative (Aki and Richards, 1980). Before going into the further details, let us step back and see what is the physically distinctive difference between the classical Zoeppritz equation and equation 4.10 presented here. From a perspective of energy conservation, the classical Zoeppritz equation only takes into account the conservation of elastic energy. To be specific, the total energy of particle motion, including the volume of integral of kinetic energy and elastic strain energy throughout the elastic medium, has been hold constant (Aki and Richards, 1980). However, the “poroelastic Zoeppritz equation” not only includes the elastic energy but also the dissipative energy, which comes from the pore pressure diffusion caused by both

global and local viscous flow. Here, we do not perform the analysis of energy conservation. Interested readers can refer Dutta and Ode (1983), in which they systematically study the energy conservation in the boundary of the fluid-saturated porous media.

Furthermore, the methodology to compute poroelastic reflection coefficient here is distinct from the derivation of reflection coefficients in the visco-elastic media (White, 1965; Bourbie, 1983a, 1983b; Riedel et al., 2003; Lines et al., 2009; Ren et al., 2009; Quintal et al., 2009; Liu et al., 2011; Morozov, 2011). Even though the velocity and attenuation input in their method is sometimes considered as frequency-dependent, the dynamic interaction regarding the fluid flow between the upper and lower porous medium is ignored.

The seismic reflection dispersion characteristics include the responses of both mesoscopic flow and Biot flow. However, the possible interaction and coupling effect between mesoscopic flow and Biot flow are ignored. The seismic dispersion signatures discussed in the present study cover a wide range of frequency bands. Regarding its real field application, an integrated study of seismic, VSP, and sonic log at different scales is helpful to fully reveal the reservoir properties and heterogeneity information. Finally, it is necessary to point out that the present study focuses on the theoretical modeling. Lab measurements and field observations need to be investigated in the future to verify the theoretical work.

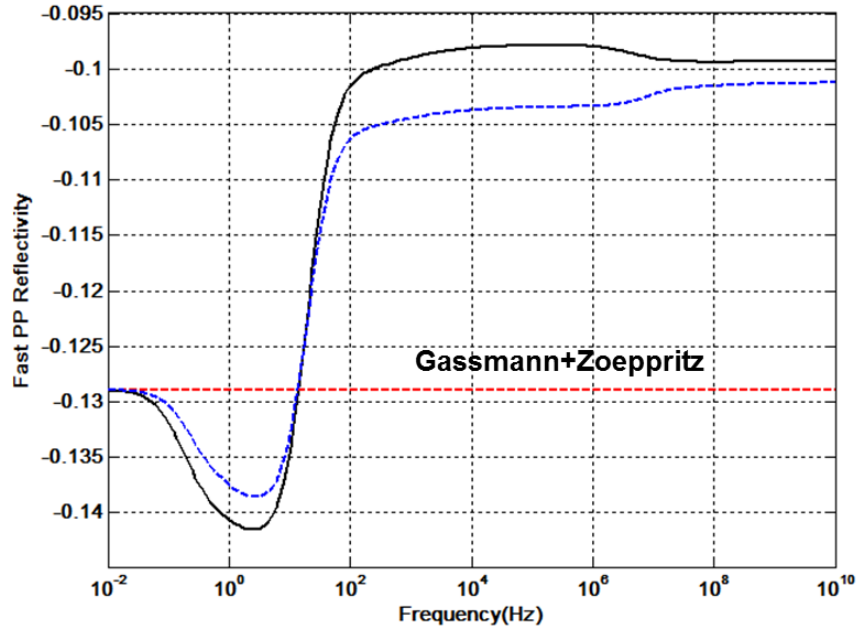


Figure 4.14. Comparison of poroelastic reflection (black line) and reflection calculated based on classical Zoeppritz equation for each-frequency component (blue dashed line) at normal incidence angle.

4.7 Conclusions

In the present work, we have quantified the impact of wave-induced fluid flow on the reflection at the interface between two heterogeneous porous media. The poroelastic reflection not only depends on the elastic properties contrast and incident angle, but also relies on the information about observational frequency, fluid mobility, and heterogeneity features. It is found that the poroelastic reflection is identical to the elastic reflection only when frequency goes as low as 10^{-2} Hz, and they deviate significantly from each other at a wide frequency range. Seismic reflection exhibits negligible dispersion effect due to Biot flow. However, the local flow can cause

significant amounts of dispersion for seismic reflections in the exploration band. Such dispersion effects can't be ignored, because the classical quantitative seismic interpretation might be misleading. For example, the weakening seismic reflection amplitude due to intrinsic dispersion and attenuation can yield an underestimate of the porosity in reservoir rocks. Also, the phase variation caused by local flow can bring uncertainty for seismically imaging the geological structure. Additionally, for a wide frequency range, the significant discrepancy of the seismic amplitude and phase variation at surface seismic, VSP, and sonic log frequency bands also suggests that the full integration of geophysical measurements at various scales in heterogeneous reservoir rocks should be more cautious. The implication for reservoir characterization is encouraging, which leaves open the possibility of using frequency-dependent seismic attributes to indicate geological heterogeneity features and fluid mobility information.

4.8 Acknowledgement

This work was sponsored by Fluids and DHI consortium of the Colorado School of Mines and University of Houston.

4.9 Appendix

SEISMIC REFLECTION COEFFICIENTS FROM THE BOUNDARY OF EFFECTIVE BIOT MEDIA

In order to facilitate computations, we consider Helmholtz decomposition of the two displacement vectors \mathbf{u} and \mathbf{W} in the form:

$$\begin{cases} \mathbf{u} = \nabla \varphi_s + \nabla \times \psi_s \\ \mathbf{W} = \nabla \varphi_f + \nabla \times \psi_f \end{cases}, \quad (\text{A-1})$$

where φ_s, ψ_s are the potential functions associated with the displacement vectors of rock frame, and φ_f, ψ_f are the potential functions associated with the displacement vectors of fluid with respect to the solid frame.

As the geometry is illustrated in Figure 4.3, we consider the seismic reflections at the interface of two effective Biot media. For two-dimensional plane-wave propagation, the displacement potentials of the incident, reflected, and transmitted waves can be written in the form:

$$\text{Incident P wave: } \begin{cases} \varphi_s^i = A_{s1}^i e^{ik_{p1}^i (\sin \theta^i x + \cos \theta^i z) - i\omega t} \\ \varphi_f^i = A_{f1}^i e^{ik_{p1}^i (\sin \theta^i x + \cos \theta^i z) - i\omega t} \end{cases}, \quad (\text{A-2})$$

$$\text{Reflected P wave: } \begin{cases} \varphi_s^r = \varphi_{s1}^r + \varphi_{s2}^r = A_{s1}^r e^{ik_{p1}^r (\sin \theta_{p1}^r x - \cos \theta_{p1}^r z) - i\omega t} + A_{s2}^r e^{ik_{p2}^r (\sin \theta_{p2}^r x - \cos \theta_{p2}^r z) - i\omega t} \\ \varphi_f^r = \varphi_{f1}^r + \varphi_{f2}^r = A_{f1}^r e^{ik_{p1}^r (\sin \theta_{p1}^r x - \cos \theta_{p1}^r z) - i\omega t} + A_{f2}^r e^{i\omega t - ik_{p2}^r (\sin \theta_{p2}^r x - \cos \theta_{p2}^r z) - i\omega t} \end{cases}, \quad (\text{A-3})$$

$$\text{Reflected SV wave: } \begin{cases} \psi_s^r = B_s^r e^{ik_s^r (\sin \theta_s^r x - \cos \theta_s^r z) - i\omega t} \\ \psi_f^r = B_f^r e^{ik_s^r (\sin \theta_s^r x - \cos \theta_s^r z) - i\omega t} \end{cases}, \quad (\text{A-4})$$

Transmitted P wave:

$$\begin{cases} \varphi_s^t = \varphi_{s1}^t + \varphi_{s2}^t = A_{s1}^t e^{ik_{p1}^t (\sin \theta_{p1}^t x + \cos \theta_{p1}^t z) - i\omega t} + A_{s2}^t e^{ik_{p2}^t (\sin \theta_{p2}^t x + \cos \theta_{p2}^t z) - i\omega t} \\ \varphi_f^t = \varphi_{f1}^t + \varphi_{f2}^t = A_{f1}^t e^{ik_{p1}^t (\sin \theta_{p1}^t x + \cos \theta_{p1}^t z) - i\omega t} + A_{f2}^t e^{ik_{p2}^t (\sin \theta_{p2}^t x + \cos \theta_{p2}^t z) - i\omega t} \end{cases}, \quad (\text{A-5})$$

$$\text{Transmitted SV wave: } \begin{cases} \psi_s^t = B_s^t e^{ik_s^t (\sin \theta_s^t x + \cos \theta_s^t z) - i\omega t} \\ \psi_f^t = B_f^t e^{ik_s^t (\sin \theta_s^t x + \cos \theta_s^t z) - i\omega t} \end{cases}, \quad (\text{A-6})$$

where the superscripts i , r , t denote the incident, reflection and transmission waves respectively; k_{p1}^i is the wave number of the incident fast compressional wave; k_{p1}^r , k_{p2}^r , and k_s^r are the wave numbers of two reflected compressional and reflected shear-wave in the effective Biot medium 1, respectively; k_{p1}^t , k_{p2}^t , and k_s^t are the wave numbers of two transmitted compressional and transmitted shear-wave in the effective Biot medium 2, respectively; $A_{s1}^m(m=i,r,t)$ and A_{f1}^m denote, respectively, the potential amplitude of fast compression wave associated with the displacement of rock frame and relative fluid flow; $A_{s2}^m(m=i,r,t)$ and A_{f2}^m denote, respectively, the potential amplitude of second compression wave associated with the displacement of rock frame and relative fluid flow; $B_s^m(m=r,t)$ and B_f^m denote, respectively, the potential amplitude of shear-wave associated with the displacement of rock frame and relative fluid flow.

Following the earlier work by Deresiewicz (1960), Dutta and Ode (1979, 1983), and Dai et al. (2006), the potential of the rock frame displacement is related to that of the relative fluid flow displacement by a constant. Therefore, we have such relationship in medium 1,

$$\frac{A_{f1}^i}{A_{s1}^i} = \delta_{p11}, \quad \frac{A_{f1}^r}{A_{s1}^r} = \delta_{p11}, \quad \frac{A_{f2}^r}{A_{s2}^r} = \delta_{p12}, \quad \text{and} \quad \frac{B_f^r}{B_s^r} = \delta_{s1}; \quad (\text{A-7})$$

And similarly, in medium 2, we have

$$\frac{A_{f1}^t}{A_{s1}^t} = \delta_{p21}, \quad \frac{A_{f2}^t}{A_{s2}^t} = \delta_{p22}, \quad \text{and} \quad \frac{B_f^t}{B_s^t} = \delta_{s2}; \quad (\text{A-8})$$

where

$$\tau_{pij} = \frac{\lambda_i^* + (\alpha_i^*)^2 M_i^* + 2\mu_i^* - \rho_{bi} V_{pij}^2}{\rho_{fi} V_p^2 - \alpha_i^* M_i^*} (i=1,2; j=1,2),$$

$$\tau_{si} = \frac{\mu_i^* - \rho_{bi} V_{si}^2}{\rho_{fi} V_{si}^2} (i=1,2).$$

Here, $i=1$ refers to the upper medium 1, and $i=2$ refers to the lower medium 2; $j=1$ refers to the fast P-wave, and $j=2$ refers to the slow P-wave. Consequently, $V_{p_{11}}$, $V_{p_{12}}$, V_{s_1} and $V_{p_{21}}$, $V_{p_{22}}$, V_{s_2} are the frequency-dependent fast P-wave velocity, slow P-wave velocity, and shear-wave velocity in the upper medium and low medium, respectively.

If we substitute (A-7) and (A-8) into (A-2), (A-3), (A-4), (A-5), and (A-6), we consequently have six unknown amplitudes of the displacement potentials A_{s1}^r , A_{s2}^r , B_s^r , A_{s1}^t , A_{s2}^t , and B_s^t , which correspond to the potential amplitudes of reflected fast compressional wave, reflected slow compressional wave, reflected shear-wave, transmitted fast compressional wave, transmitted slow compressional wave, and transmitted shear-wave respectively. Also, they are related to the six boundary conditions listed in the equation 4.9.

Consequently, from the equations in A1-A8, we can relate the potential function to the displacement in medium 1 and medium 2.

For medium 1, we have:

$$\left\{ \begin{aligned} u_{1x} &= \frac{\partial(\varphi_s^i + \varphi_s^r)}{\partial x} - \frac{\partial\psi_s^r}{\partial z} = \frac{\partial(\varphi_s^i + \varphi_{s1}^r + \varphi_{s2}^r)}{\partial x} - \frac{\partial\psi_s^r}{\partial z} \\ u_{1z} &= \frac{\partial(\varphi_s^i + \varphi_s^r)}{\partial z} + \frac{\partial\psi_s^r}{\partial x} = \frac{\partial(\varphi_s^i + \varphi_{s1}^r + \varphi_{s2}^r)}{\partial z} + \frac{\partial\psi_s^r}{\partial x} \\ W_{1x} &= \frac{\partial(\varphi_f^i + \varphi_f^r)}{\partial x} - \frac{\partial\psi_f^r}{\partial z} = \frac{\partial(\delta_{p11}\varphi_s^i + \delta_{p11}\varphi_{s1}^r + \delta_{p12}\varphi_{s2}^r)}{\partial x} - \delta_{s1} \frac{\partial\psi_s^r}{\partial z} \\ W_{1z} &= \frac{\partial(\varphi_f^i + \varphi_f^r)}{\partial z} + \frac{\partial\psi_f^r}{\partial x} = \frac{\partial(\delta_{p11}\varphi_s^i + \delta_{p11}\varphi_{s1}^r + \delta_{p12}\varphi_{s2}^r)}{\partial z} + \delta_{s1} \frac{\partial\psi_s^r}{\partial x} \end{aligned} \right. \quad (\text{A-9})$$

Similarly, for medium 2, we have:

$$\left\{ \begin{aligned} u_{2x} &= \frac{\partial\varphi_s^t}{\partial x} - \frac{\partial\psi_s^t}{\partial z} = \frac{\partial(\phi_1^t + \phi_2^t)}{\partial x} - \frac{\partial\psi_s^t}{\partial z} \\ u_{2z} &= \frac{\partial\varphi_s^t}{\partial z} + \frac{\partial\psi_s^t}{\partial x} = \frac{\partial(\phi_1^t + \phi_2^t)}{\partial z} + \frac{\partial\psi_s^t}{\partial x} \\ W_{2x} &= \frac{\partial\varphi_f^t}{\partial x} - \frac{\partial\psi_f^t}{\partial z} = \frac{\partial(\delta_{p21}\phi_1^t + \delta_{p22}\phi_2^t)}{\partial x} - \delta_{s2} \frac{\partial\psi_s^t}{\partial z} \\ W_{2z} &= \frac{\partial\varphi_f^t}{\partial z} + \frac{\partial\psi_f^t}{\partial x} = \frac{\partial(\delta_{p21}\phi_1^t + \delta_{p22}\phi_2^t)}{\partial z} + \delta_{s2} \frac{\partial\psi_s^t}{\partial x} \end{aligned} \right. \quad (\text{A-10})$$

Following the boundary conditions listed in the equation (4.9a)-(4.9f) and on the basis of the poroelastic stress-strain relationship, we have:

$$u_{1x} = u_{2x} \quad (\text{A-11a})$$

$$u_{1z} = u_{2z} \quad (\text{A-11b})$$

$$(\lambda_1^* + \alpha_1^{*2} M_1^*)(u_{1x,x} + u_{1z,z}) + 2\mu_1 u_{1z,z} + \alpha_1 M_1^*(W_{1x,x} + W_{1z,z}) = (\lambda_2^* + \alpha_2^{*2} M_2^*)(u_{2x,x} + u_{2z,z}) + 2\mu_2^* u_{2z,z} + \alpha_2^* M_2^*(W_{2x,x} + W_{2z,z}) \quad (\text{A-11c})$$

$$\mu_1^*(u_{1x,z} + u_{1z,x}) = \mu_2^*(u_{2x,z} + u_{2z,x}) \quad (\text{A-11d})$$

$$W_{1z} = W_{2z} \quad (\text{A-11e})$$

$$\alpha_1^* M_1^*(u_{1x,x} + u_{1z,z}) + M_1^*(W_{1x,x} + W_{1z,z}) = \alpha_2^* M_2^*(u_{2x,x} + u_{2z,z}) + M_2^*(W_{2x,x} + W_{2z,z}) \quad (\text{A-11f})$$

Note that the boundary conditions require that the phase factors must be equal at the $z=0$ for all x and t , and hence we have:

$$k_{p1}^i \sin \theta^i x = k_{p1}^r \sin \theta_{p1}^r = k_{p2}^r \sin \theta_{p2}^r = k_s^r \sin \theta_s^r = k_{p1}^t \sin \theta_{p1}^t = k_{p2}^t \sin \theta_{p2}^t = k_s^t \sin \theta_s^t. \quad (\text{A-12})$$

Equation A-12 is also the statement of Snell's law for reflection and transmission in effective Biot media.

Now, we substitute equation (A-2 to A-10) into the boundary condition (A-11a to A-11f) and set $z=0$ (for all x and t). Then we can obtain the following equation:

$$\begin{pmatrix} \frac{\sin \theta_{p1}^r}{V_{p11}} & \frac{\sin \theta_{p2}^r}{V_{p12}} & \frac{\cos \theta_s^r}{V_{s1}} & -\frac{\sin \theta_{p1}^r}{V_{p21}} & -\frac{\sin \theta_{p2}^r}{V_{p22}} & \frac{\cos \theta_s^r}{V_{s2}} \\ \frac{\cos \theta_{p1}^r}{V_{p11}} & \frac{\cos \theta_{p2}^r}{V_{p12}} & -\frac{\sin \theta_s^r}{V_{s1}} & \frac{\cos \theta_{p1}^r}{V_{p21}} & \frac{\cos \theta_{p2}^r}{V_{p22}} & \frac{\sin \theta_s^r}{V_{s2}} \\ Y_1 & Y_2 & Y_3 & Y_4 & Y_5 & Y_6 \\ \frac{\mu_1^* \sin 2\theta_{p1}^r}{(V_{p11})^2} & \frac{\mu_1^* \sin 2\theta_{p2}^r}{(V_{p12})^2} & \frac{\mu_1^* \cos 2\theta_s^r}{(V_{s1})^2} & \frac{\mu_2^* \sin 2\theta_{p1}^r}{(V_{p21})^2} & \frac{\mu_2^* \sin 2\theta_{p2}^r}{(V_{p22})^2} & -\frac{\mu_2^* \cos 2\theta_s^r}{(V_{s2})^2} \\ \delta_{p11} \frac{\cos \theta_{p1}^r}{V_{p11}} & \delta_{p12} \frac{\cos \theta_{p2}^r}{V_{p12}} & -\delta_{s1} \frac{\sin \theta_s^r}{V_{s1}} & \delta_{p21} \frac{\cos \theta_{p1}^r}{V_{p21}} & \delta_{p22} \frac{\cos \theta_{p2}^r}{V_{p22}} & \delta_{s2} \frac{\sin \theta_s^r}{V_{s2}} \\ \frac{\alpha_1^* M_1^* + M_1^* \delta_{p11}}{(V_{p11})^2} & \frac{\alpha_1^* M_1^* + M_1^* \delta_{p12}}{(V_{p12})^2} & 0 & -\frac{\alpha_2^* M_2^* + M_2^* \delta_{p21}}{(V_{p21})^2} & -\frac{\alpha_2^* M_2^* + M_2^* \delta_{p22}}{(V_{p22})^2} & 0 \end{pmatrix} \begin{pmatrix} R_1 \\ R_2 \\ R_3 \\ R_4 \\ R_5 \\ R_6 \end{pmatrix} = \begin{pmatrix} -\frac{\sin \theta^i}{V_{p11}} \\ \frac{\cos \theta^i}{V_{p11}} \\ Y_7 \\ \frac{\mu_1^* \sin 2\theta^i}{(V_{p11})^2} \\ \delta_{p11} \frac{\cos \theta^i}{V_{p11}} \\ -\frac{\alpha_1^* M_1^* + M_1^* \delta_{p11}}{(V_{p11})^2} \end{pmatrix} \quad (\text{A-13})$$

where

$$Y_1 = \frac{\lambda_1^* + (\alpha_1^*)^2 M_1 + \alpha_1^* M_1^* \delta_{p11} + 2\mu_1^* (\cos \theta_{p1}^r)^2}{(V_{p11})^2},$$

$$Y_2 = \frac{\lambda_1^* + (\alpha_1^*)^2 M_1 + \alpha_1^* M_1^* \delta_{p12} + 2\mu_1^* (\cos \theta_{p2}^r)^2}{(V_{p12})^2},$$

$$Y_3 = -\frac{2\mu_1^* (\cos \theta_s^r)^2}{(V_{s1})^2}, \quad Y_4 = -\frac{\lambda_2^* + (\alpha_2^*)^2 M_2 + \alpha_2^* M_2^* \delta_{p12} + 2\mu_2^* (\cos \theta_{p1}^r)^2}{(V_{p21})^2},$$

$$Y_5 = -\frac{\lambda_2^* + (\alpha_2^*)^2 M_2 + \alpha_2^* M_2^* \delta_{p12} + 2\mu_2^* (\cos \theta_{p2}^r)^2}{(V_{p22})^2}, \quad Y_6 = -\frac{2\mu_2^* (\cos \theta_s^r)^2}{(V_{s2})^2},$$

$$Y_7 = -\frac{\lambda_1^* + (\alpha_1^*)^2 M_1 + \alpha_1^* M_1^* \delta_{p11} + 2\mu_1^* (\cos \theta^i)^2}{(V_{p11})^2};$$

and R_1 , R_2 , R_3 , R_4 , R_5 , and R_6 represent the amplitude ratio for the potentials of reflected fast P-wave, reflected slow P-wave, reflected S-wave, transmitted fast P-wave, transmitted slow P-wave, and transmitted S-wave, respectively. Here, we define the reflection coefficients and transmission coefficients as the amplitude ratios for the matrix displacement. Therefore, based on the equation A-1, we can convert the amplitude ratio for the potentials to the amplitude ratio for the displacement. The Zoeppritz-style reflection and transmission coefficients of elastic waves from the boundary of effective Biot media are given in equation 4.10.

4.10 References

- Aki, K., and P. G. Richards, 1980, *Quantitative Seismology: Theory and Methods*: W. H. Freeman & Co.
- Batzle, M. L., D. H. Han, and R. Hofmann, 2006, Fluid mobility and frequency-dependent seismic velocity—Direct measurements: *Geophysics*, 71, no. 1, N1–N9.
- Berryman, J. G., and H. F. Wang, 1995, The elastic coefficients of double-porosity models for fluid transport in jointed rock: *Journal of Geophysical Research*, 100 (24), 611-627.
- Berryman, J. G., and H. F. Wang, 2000, Elastic wave propagation and attenuation in a double-porosity dual-permeability medium: *International Journal of Rock Mechanics and Mining Sciences*, 37, 63– 78.

- Biot, M. A., 1956a, Theory of propagation of elastic waves in fluid-saturated porous solid. I. Low-frequency range: *Journal of the Acoustical Society of America*, 28, 168–178.
- , 1956b, Theory of propagation of elastic waves in a fluid-saturated porous solid. II. Higher frequency range: *Journal of the Acoustical Society of America*, 28, 179–191.
- , 1962, Mechanics of deformation and acoustic propagation in porous media: *Journal of Applied Physics*, 33, 1482–1498.
- Bourbié, T., 1983, Effects of attenuation on reflections: Ph.D. thesis, Stanford University.
- Bourbié, T., and A. Gonzalez-Serrano, 1983, Synthetic seismograms in attenuating media: *Geophysics*, 48, 1575–1587.
- Bourbié, T., and A. Nur, 1984, Effects of attenuation on reflections: Experimental test: *Journal of Geophysical Research*, 89, 6197–6202.
- Carcione, J. M., and S. Picotti, 2006, P-wave seismic attenuation by slow wave diffusion: Effects of inhomogeneous rock properties: *Geophysics*, 71, no. 3, O1–O8.
- Castagna, J. P., S. Sun, and R. W. Seigfried, 2003, Instantaneous spectral analysis: Detection of low-frequency shadows associated with hydrocarbons: *The Leading Edge*, 22, 120–127.
- Chakraborty, A., and D. Okaya, 1995, Frequency-time decomposition of seismic data using wavelet-based methods: *Geophysics*, 60, 1906–1916.
- Chapman, M. E., E. Liu, and X. Li, 2006, The influence of fluid-sensitive dispersion and attenuation on AVO analysis: *Geophysical Journal International*, 167, 89–105.

- Ciarletta, M., and M.A. Sumbatyan, 2003, Reflection of plane waves by the free boundary of a porous elastic half-space: *Journal of Sound and Vibration*, 259, 253–264.
- Dai, Z., and Z. Kuang, 2006, Reflection and transmission of elastic waves from the interface of fluid-saturated porous solid and a double porosity solid: *Transport in Porous Media*: 65(2), 237–264
- Dai, Z.J., and Z. Kuang, 2008, Reflection and transmission of elastic waves at the interface between water and a double porosity solid: *Transport in Porous Media*, 72, 369–392.
- Dasgupta, R., and Clark, R.A., 1998, Estimation of Q from surface seismic reflection data: *Geophysics*, 63, 2120–2128
- de la Cruz, V., J. Hube, and T.J.T. Spanos, 1992, Reflection and transmission of seismic-waves at the boundaries of porous-media: *Wave Motion*, 16, 323–338.
- Deresiewicz, H., and Rice, J. T., 1960, The effect of boundaries on wave propagation in liquid-filled porous solid: I. Reflection of plane waves at a true plane boundary: *Bulletin of the Seismological Society of America*, 50, 599-607.
- Dvorkin, J., G. Mavko, and A. Nur., 1995, Squirt flow in fully saturated rocks: *Geophysics*, 60, 97–107.
- Denneman, A. I. M., G. G. Drijkoningen, D. M. J. Smeulders, and K. Wapenaar, 2002, Reflection and transmission of waves at a fluid/porous-medium interface: *Geophysics*, 67, 282–291.

- Dutta, N. C., and H. Odé, 1979a, Attenuation and dispersion of compressional waves in fluid-filled porous rocks with partial gas saturation (White model,) Part I—Biot theory: *Geophysics*, 44, 1777–1788.
- , 1979b, Attenuation and dispersion of compressional waves in fluid filled porous rocks with partial gas saturation (White model), Part II—Results: *Geophysics*, 44, 1789–1805.
- Dutta, N. C., and H. Odé, 1983, Seismic reflections from a gas-water contact: *Geophysics*, 48, 148–162.
- Ebrom, D., 2004, The low frequency gas shadow on seismic sections: *The Leading Edge*, 23(8), 772.
- Geertsma, J., and D. C. Smit, 1961, Some aspects of elastic wave propagation in fluid-saturated porous solids: *Geophysics*, 26, 169–181.
- Gelinsky, S., and S. A. Shapiro, 1997, Dynamic-equivalent medium approach for thinly layered saturated sediments: *Geophysical Journal International*, 128, F1–F4.
- Goloshubin, G.M., Daley, T.M., and Korneev, V.A., 2001, Seismic low-frequency effects in gas reservoir monitoring VSP data, SEG Meeting: San Antonio, TX.
- Goloshubin, G., C. Van Shuyver, V. Korneev, D. Silin, and V. Vingalov, 2006, Reservoir imaging using low frequencies of seismic reflections: *The Leading Edge*, 25, 527–531.
- Gurevich, B., V. B. Zyrianov, and S. L. Lopatnikov, 1997, Seismic attenuation in finely layered porous rocks: Effects of fluid flow and scattering: *Geophysics*, 62, 319–324.

- Gurevich, B., and Schoenberg, M., 1999, Interface conditions for Biot's equations of poroelasticity: *Journal of the Acoustical Society of America*, 105, 2585–2589.
- Gurevich, B., R. Ciz, and A. I. M. Denneman, 2004, Simple expressions for normal incidence reflection coefficients from an interface between fluid saturated porous materials: *Geophysics*, 69, 1372–1377.
- Hofmann, H., 2006, Frequency-dependent Elastic and Anelastic Properties of Clastic Rocks: Ph.D. Thesis, Colorado School of Mines.
- Hornby, B. E., L. M. Schwartz, and J. A. Hudson, 1994, Anisotropic effective-medium modeling of the elastic properties of shales: *Geophysics*, 59, 1570–1583.
- Innanen, K., 2011, Inversion of the seismic AVF/AVA signatures of highly attenuative targets: *Geophysics*, 76, no. 1, R1–14.
- Jakobsen, M., J. A. Hudson, and T. A. Johansen, 2003, T-Matrix approach to shale acoustics: *Geophysical Journal International*, 154, 533–558.
- Johnson, D. L., 2001, Theory of frequency-dependent acoustics in patchy saturated porous media: *Journal of the Acoustical Society of America*, 110, 682–694.
- Korneev, V. A., G. M. Goloshubin, T.M. Daley, and D. B. Silin, 2004, Seismic low-frequency effects in monitoring fluid-saturated reservoirs: *Geophysics*, 69, 522–532.
- Lines, L., F. Vasheghani, and S. Treitel, 2008, Reflections on Q: *CSEG Recorder*, 33, December, 36–38.
- Lines, L., K. Innanen., F. Vasheghani., J. Wong., C. Sondergeld., S. Treitel., and T. Ulrych., 2012, Experimental Confirmation of “Reflections on Q”: 82nd Annual International Meeting, SEG, Expanded Abstracts, Las Vegas.

- Mavko, G., and A. Nur, 1975, Melt squirt in the aesthenosphere: *Journal of Geophysical Research*, 80, 1444–1448.
- Mavko, G., and D. Jizba, 1991, Estimating grain-scale fluid effects on velocity dispersion in rocks: *Geophysics*, 56, 1940–1949.
- Mavko, G., T. Mukerji, and J. Dvorkin, 2009, *The Rock Physics Handbook*, 2nd ed.: Cambridge University Press.
- Morozov, I., 2011, Anelastic acoustic impedance and the correspondence principle: *Geophysical Prospecting*, 59, 24–34.
- Muller, T. M., and B. Gurevich, 2004, One-dimensional random patchy saturation model for velocity and attenuation in porous rocks: *Geophysics*, 69, 1166–1172.
- Muller, T. M., G. Lambert, and B. Gurevich, 2007, Dynamic permeability of porous rocks and its seismic signatures: *Geophysics*, 72, no. 5, E149–E158.
- Müller, T. M., B. Gurevich, and M. Lebedev, 2010, Seismic wave attenuation and dispersion resulting from wave-induced flow in porous rocks- A review: *Geophysics*, 75, A147-A164.
- O’Connell, R. J., and B. Budiansky, 1974, Seismic velocities in dry and saturated cracked solids: *Journal of Geophysical Research*, 79, 5412–5426.
- Odebeatu, E., J. Zhang, M. Chapman, E. Liu, and Y. Li, 2006, Application of spectral decomposition to detection of dispersion anomalies associated with gas saturation: *The Leading Edge*, 25, 206–210.
- Partyka, G., J. Gridley, and J. Lopez, 1999, Interpretational applications of spectral decomposition in reservoir characterization: *The Leading Edge*, 18, 353–360.

- Pride, S. R., and J. G. Berryman, 2003a, Linear dynamics of double-porosity and dual-permeability materials. I. Governing equations and acoustic attenuation: *Physical Review E*, 68, 036603.
- , 2003b, Linear dynamics of double-porosity and dual permeability materials. II. Fluid transport equations: *Physical Review E*, 68, 036604.
- Pride, S. R., J. G. Berryman, and J. M. Harris, 2004, Seismic attenuation due to wave induced flow: *Journal of Geophysical Research*, 109, no. B1, B01201.
- Pride, S. R., E. Tromeur, and J. G. Berryman, 2002, Biot slow-wave effects in stratified rock: *Geophysics*, 67, 271–281.
- Ren, H., G. Goloshubin, and F. J. Hiltermann, 2009, Poroelastic analysis of amplitude-versus-frequency variations: *Geophysics*, 74, no. 6, N41–N48.
- Riedel, M., S. E. Dosso, and L. Beran, 2003, Uncertainty estimation for amplitude variation with offset AVO inversion: *Geophysics*, 68, 1485–1496
- Rubino, J.G., C.L. Ravazzoli, and J.E. Santos, 2006, Reflection and transmission of waves in composite porous media: a quantification of energy conversions involving slow waves: *Journal of the Acoustical Society of America*, 120, 2425– 2436.
- Santos, J.E., J.M. Corbero, C.L. Ravazzoli, and J.L. Hensley, 1992, Reflection and transmission coefficients in fluid-saturated porous-media: *Journal of the Acoustical Society of America*, 91, 1911–1923.
- Sharma, M.D., 2004, 3-D wave propagation in a general anisotropic poroelastic medium: reflection and refraction at an interface with fluid: *Geophysical Journal International*, 157, 947–958.
- Stoll. R. D., 1977, Acoustic waves in ocean sediments: *Geophysics*, 42, 715-725.

- Taner, M. T., F. Koehler, and E. Sheriff, 1979, Complex seismic trace analysis: *Geophysics*, 44, 1041–1063.
- Tang, X., 2011, A unified theory for elastic wave propagation through porous media containing cracks- An extension of Biot's poroelastic wave theory: *Science China—Earth Sciences*, 54, 1441– 1452.
- Vernik, L., 1994. Hydrocarbon-generation-induced microcracking of source rocks: *Geophysics*, 59, 555–563.
- Walton, K., 1987, The effective elastic moduli of a random pack of spheres: *Journal of the Mechanics and Physics of Solids*, 35, 213-226.
- White, J. E., 1965, Reflections from lossy media: *The Journal of the Acoustical Society of America*, 38, 604–607.
- White, J. E., 1975, Computed seismic speeds and attenuation in rocks with partial gas saturation: *Geophysics*, 40, 224–232.
- White, J. E.. and Dean. A., 1977, Effects of Huid saturation on seismic reflections *Geophysics*, 42, 191.
- Yao, Q., 2013. Velocity Dispersion and Attenuation in Reservoir Rocks: Ph.D. Thesis, University of Houston.

Chapter 5

Poroelastic Seismic Analysis and Its Implications for Reservoir Imaging and Characterization

5.1 Abstract

The classical seismic interpretation linking signature of amplitude-versus-offset (AVO) to lithology and fluid prediction is based on the assumptions of elasticity. I extend this interpretation to heterogeneous porous media based on an analysis of frequency- and angle-dependent poroelastic reflectivity. I further demonstrate that the AVO response at the interface is strongly impacted by the reflection dispersion behavior: the bright spot (Class III AVO) get brighter at lower frequency, the dim spot (Class I AVO) get dimmer at lower frequency, and the Class II AVO reservoir exhibit significant phase distortion in frequency domain. The seismic synthetics computed from poroelastic reflection suggest that wave-induced fluid flow distorts the energy and phase distribution of the reflected seismic wiggles, thereby bringing uncertainty to seismically imaging the geological structure and quantitative seismic interpretation for reservoir properties. In addition, the poroelastic seismic response yields the connections between seismic signatures and hydraulic properties. It is found that, for the permeability that ranges from 10^{-3} D to 10^{-1} D, the reflection amplitude almost linearly decreases with permeability. For Class III AVO reservoir environment, high fluid mobility zones usually enhance the seismic amplitude; while

for Class I AVO reservoir environment, high fluid mobility zones weakens the seismic amplitude.

5.2 Introduction

Amplitude variations with offset (AVO), which have been successfully used as direct hydrocarbon indicators and to provide estimates of elastic properties (e.g., Ostrander, 1984; Rutherford and Williams, 1989; Castagna and Backus, 1993), are developed under the assumption that the rocks are purely elastic. However, the Earth materials, especially the sedimentary rocks which are of interest to petroleum industry, by their very nature, always show viscoelastic behavior (O'Connell and Budiansky, 1974; Aki and Richards, 1980; Batzle et al., 2006). In heterogeneous porous media, the wave-induced fluid flow causes velocity dispersion and attenuation (Müller et al., 2010), and hence leads to frequency-dependent reflection coefficients (Dutta and Ode, 1983; Bourbie et al., 1987; Gurevich et al. 2004; Korneev et al., 2004; Goloshubin et al., 2006; Ren et al., 2009). Neglecting the dispersion behavior of reflectivity will bias our understanding of reservoir properties. The principal goal of this chapter is to quantify the poroelastic impact on seismic analysis under different reservoir scenarios, thereby providing insights to improve reservoir imaging and characterization.

With the development of spectral decomposition technique (Chakraborty and Okaya, 1995; Partyka et al., 1999; Castagna et al., 2003), the frequency-dependent seismic attributes have been often utilized for recognition of hydrocarbon reservoirs. Nevertheless, it is not clear whether these observations are associated with the true poroelastic response or whether they just represent the processing artifacts (Ebrom 2004;

Chapman et al., 2006). Therefore, it is necessary to propose a practical recipe to guide the interpretation of frequency-dependent seismic signatures. In this chapter, we are going to propose three Amplitude-Versus-Frequency (AVF) anomalies corresponding to different reservoir environments. This part will be presented in the section 3 of this chapter. In addition, the poroelastic effect on the amplitude-versus-offset (AVO) and phase-versus-offset (PVO) will be presented in the section 4 of the chapter.

So far, we only focus on the reflectivity behavior across the porelastic contact. However, the true seismic response is a combination of source wavelet and interface reflectivity. The seismic synthetics computed from the poroelastic reflection and its associated characteristics, such as central frequency and RMS amplitude, will be explored in the section 5 of this chapter. Moreover, permeability is a major control of fluid flow, and in turn significantly affects the frequency-dependent seismic signatures. In section 6, we will discuss the relationships between permeability and seismic attributes and the possibility of extracting permeability information from poroelastic seismic response.

To facilitate our analysis, we construct three geological scenarios which correspond to the three classical AVO anomalies defined by Rutherford and Williams (1989). Model 1 refers to large increase for the underlying lithology (sandstone) relative to overlying lithology (shale), which corresponds to the Class I AVO response; Model 2 refers to weak reflectivity at normal incidence, which corresponds to the Class II AVO response; Model 3 refers to larger decrease in the acoustic impedance for the underlying lithology compared with overlying lithology, which

corresponds to the Class III AVO response. For each geological scenario, the parameters for the matrix properties are given in Table 5.1, and the fluid properties for the underlying sandstone and overlying shale are the same as that given in the Table 4.2. Based on the double-porosity dual-permeability model, the computed P-impedance and V_p/V_s ratio versus frequency are displayed in Figures 5.1 and 5.2. It turns out that, concerning the P-impedance which controls AVO intercept, sandstone has bigger dispersion effect than the overburden shale. Additionally, among the three geological scenarios, the model 3 sandstone has the largest dispersion effect. This can be understood, because reservoir rock in model 3 which shows a Class III AVO anomaly, is much more compliant and therefore creates more fluid pressure change. Also, as displayed in Figure 5.2, the V_p/V_s ratio for the sandstone of model 3 exhibits a biggest variation with frequency, implying that AVO gradient for model 3 is more sensitive to frequency variation.

5.3 Spectral Signatures of Poroelastic Reflectivity

In this section, we analyze the spectral signatures of the poroelastic reflection at normal incident angle under different reservoir circumstances. We follow the same procedure presented in Chapter 4 to compute the poroelastic reflection for the given geological scenario. The scatters for the real and imaginary part of the complex reflection coefficients are displayed in Figure 5.3. Correspondingly, based on equation 4.14, the magnitude and phase angle of the fast PP reflection coefficients at normal incident angle are calculated and plotted as a function of frequency in Figure 5.4. As expected, the magnitude and phase variation with frequency caused by local

flow are significant, while the impact of global flow is almost negligible. Following the similar classification schemes for poroelastic reflection proposed by Ren et al. (2009), we can classify their spectral signatures based on their reflectivity dispersion behavior in the seismic exploration band.

Table 5.1. The related parameters for rock frame properties of upper medium and lower medium corresponding to three types of AVO responses.

Parameter	Rock frame properties			
	Upper (shale)		Lower(sandstone)	
	Phase 1	Phase 2	Phase 1	Phase 2
Type 1 (Class I AVO)				
K_d (GPa)	23.2	3.0	24.3	1.91
μ_d (GPa)	8.8	1.1	25.6	2.1
V	0.97	0.03	0.96	0.04
ϕ	0.05	0.08	0.12	0.15
Type 2 (Class II AVO)				
K_d (GPa)	20.4	3.0	15.5	1.1
μ_d (GPa)	7.7	1.1	17.1	1.2
V	0.97	0.03	0.96	0.04
ϕ	0.08	0.08	0.18	0.22
Type 3 (Class III AVO)				
K_d (GPa)	17.4	3.0	11.9	0.6
μ_d (GPa)	6.5	1.1	10.3	0.4
V	0.97	0.03	0.96	0.04
ϕ	0.15	0.08	0.25	0.30

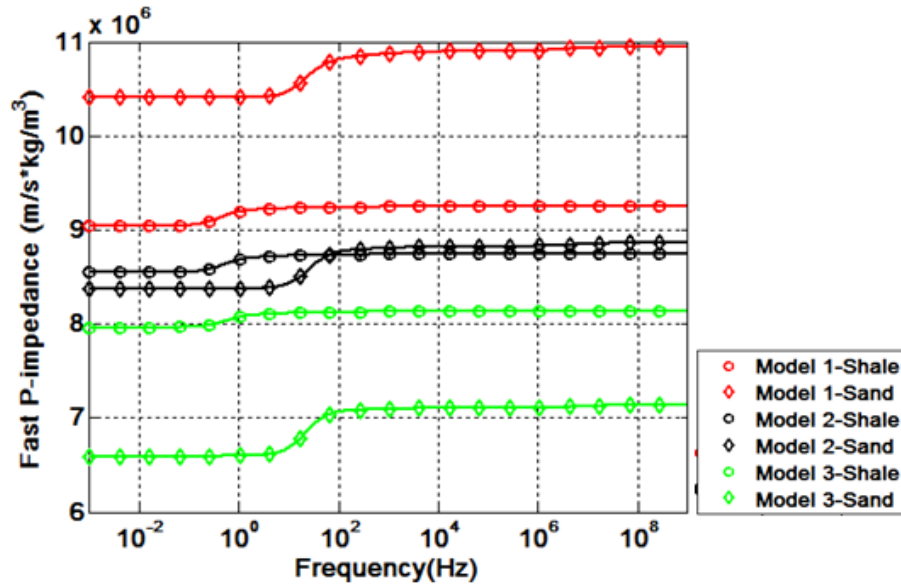


Figure 5.1. P-impedance versus frequency for the overburden shale (circle) and underlain sandstone (diamond) in Model 1 (red), Model 2 (black), and Model 3 (green).

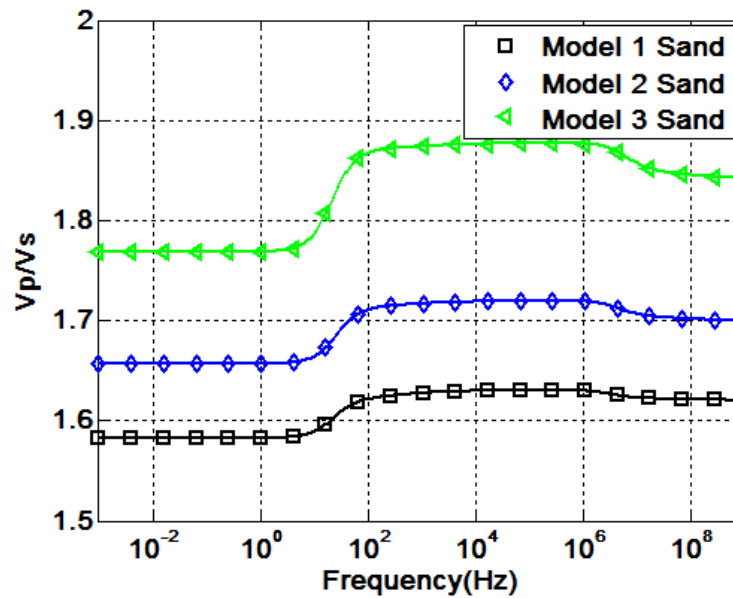


Figure 5.2. Vp/Vs ratio versus frequency for Model 1 sand (square), Model 2 sand (diamond), and Model 3 sand (triangle).

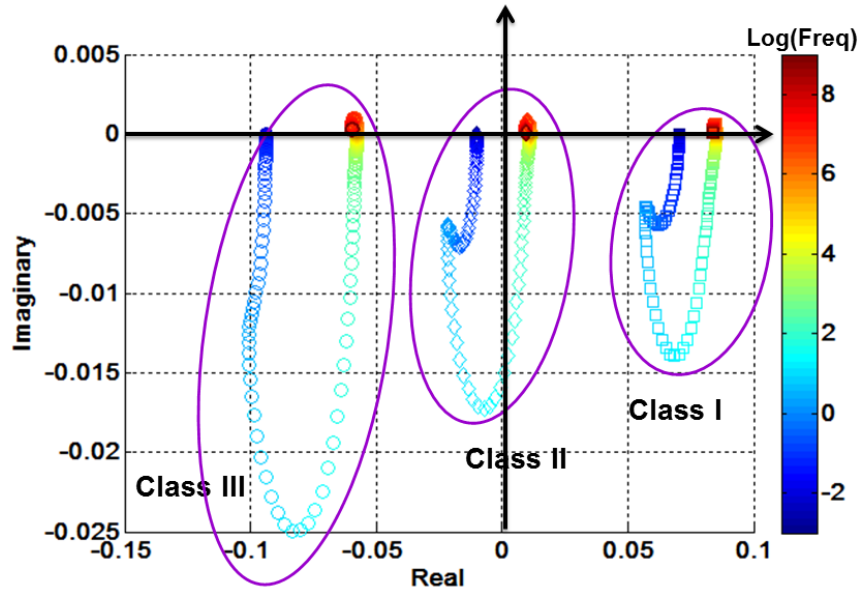


Figure 5.3. Scatters for the real and imaginary part of the poroelastic reflection coefficients at normal incident angle. The data points are color coded by log of the frequency.

5.3.1 Class I AVF--Low-frequency Dim-out

As we can see in Figure 5.4(a), for model 1 which represents the Class I AVO response, the peak amplitude of fast PP reflection decreases with frequency in the seismic exploration band. This is termed as Class I AVF--low-frequency dim-out reservoir. The phase also presents a variation compared with the elastic reflection, and the maximum phase shift is around 8 degrees. The reservoir rocks for the low-frequency dim-out reservoirs are often associated with consolidated rocks, exhibiting relatively low porosity. That is why we observe relatively small dispersion effect for the reflection magnitude and phase. However, for far-offset angle gather, when the

reflection coefficients turn into negative, the seismic amplitude decreases with frequency as shown on Figure 5.6(a). Consequently, the low-frequency dim-out reservoir will become low frequency bright spot.

5.3.2 Class II AVF--Phase-reversal Reservoir

A phase-reversal reservoir corresponds to the classical class II AVO response, in which the acoustic impedance of the reservoir rocks is slightly lower than that of the overburden lithology at zero frequency (Gassmann limit). However, as the frequency increases, the impedance of the reservoir sand becomes larger than that of the overburden shale (Figure 5.1). This is because the dispersion effect of the reservoir rock is much stronger than that of the overburden shale. Consequently, the real part of the reflection coefficient jumps from negative to positive at about 60 Hz as shown in Figure 5.3, while the imaginary part keeps as negative. Correspondingly, an apparent phase shift takes place in the seismic exploration band as depicted in Figure 5.4(b). It is worth noting that a distinct phase shift does not necessarily indicate a complete phase reversal. As illustrated in Figure 5.4(b), the 180 degree phase reversal takes place at about 10^5 Hz. More importantly, the apparent phase shift in the seismic frequency band can significantly distort the seismic waveform. However, due to the very weak seismic amplitude for class 2 AVO, the spectral signatures on seismic signal might be masked by the realistic noise level.

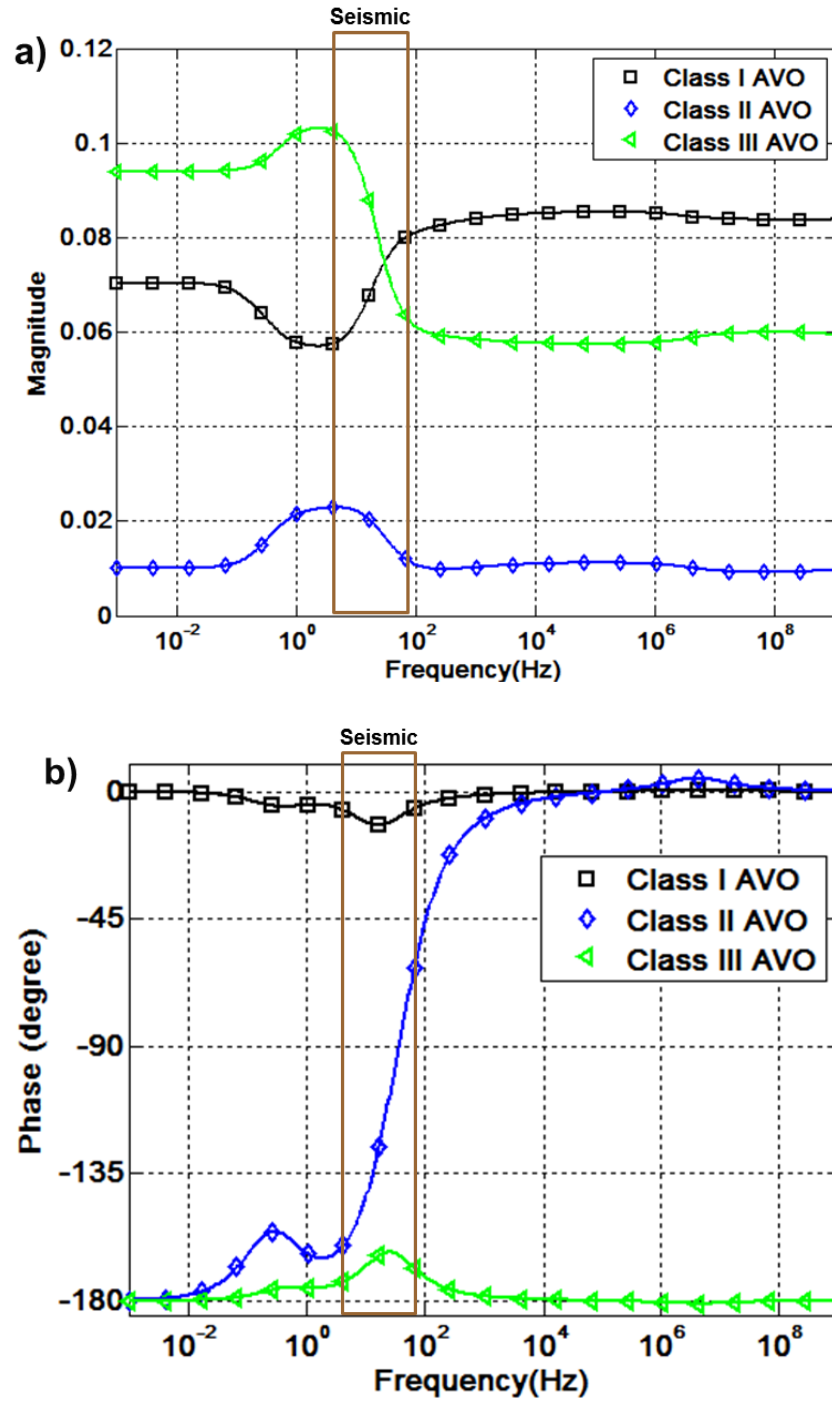


Figure 5.4. (a) Magnitude and (b) Phase angle of fast PP versus frequency for the geological scenario corresponding to Class 1 AVO (square), Class 2 AVO (diamond), and Class 3 AVO (triangle).

5.3.3 Class III AVF--Low-frequency Bright-spot

The low-frequency bright-spot corresponds to the spectral signatures of reservoir rocks having Class III AVO response. As illustrated in the Figure 5.4 (a), the trough amplitude increases with frequency, and the seismic amplitude is enhanced in the low frequency domain due to the local flow effect. To a certain degree, this might explain the low-frequency seismic anomalies observed in shallow unconsolidated sandstone reservoir that are fully saturated or partially saturated (Goloshubin et al., 2001; Castagna et al., 2003; Korneev et al, 2004; Ren et al., 2009).

Low-frequency bright spot reservoir rocks are often unconsolidated, porous and permeable. Therefore, as depicted in Figure 5.4, its dispersion effect is relatively bigger than that of the low-frequency dim-out reservoirs. Additionally, the noticeable phase shift potentially influences the seismic waveform.

5.4 Poroelastic Effect on Angle-dependent Reflectivity

Figures 5.5 and 5.6 show relationships of the amplitude versus incident angle (AVA) and phase versus incident angle (PVA) for specific frequencies in the seismic exploration band. The “Gassmann” curve represents elastic reflection coefficient. We summarized the key messages for the poroelastic effect on angle-dependent reflectivity that corresponds to Class I, Class II, and Class III AVO response, respectively.

Class I AVO:

The seismic reflection magnitude increases with frequency when the incident angle is smaller than 25 degrees. However, it exhibits an opposite trend when the incident angle exceeds 25 degrees. Note that in Figure 5.5(a), the trough of the curve indicates the phase reversal phenomenon. For the elastic reflection, it is clear to see that the phase reversal occurs at 25 degrees as shown on Figure 5.5(a). However, for the poroelastic reflection, the phase reversal is found to show up at different incident angles. In general, the incident angle for phase reversal taking place increases with frequency. The phase angle for each frequency component keeps pretty constant when the incident angle is smaller than 20 degrees or bigger than 30 degrees. However, they exhibit a significant variation between 20 to 30 degrees. The elastic reflection directly shows a polarity reversal at 25 degrees, while the phase angle for the poroelastic reflection varies with frequency in a continuous manner.

Class II AVO:

As we see in Figure 5.5(b), when the incident angle is smaller than 5 degrees, the elastic reflection shows weaker amplitude than that of the poroelastic reflection. However, when the incident angle goes beyond 30 degrees, the elastic reflection has stronger amplitude than that of poroelastic reflection. The phase angle variation with frequency is shown in Figure 5.6(b). It turns out that the phase angle shows considerable variation for near and middle offset seismic reflection, but shows very small variation for the far offset seismic reflection. In the model 2, the high-frequency reflectivity shows bigger phase variation than low-frequency reflectivity. Moreover,

the phase for the high-frequency reflectivity varies more sharply with incident angle than that of low frequency reflectivity.

Class III AVO:

The poroelastic effect does not change the curve shape of classical Class III AVO relationship, but make the poroelastic AVO response significantly deviate from the elastic AVO response. The seismic amplitude for the poroelastic reflection is weaker than that of elastic reflection. The phases angle with different frequency all show very small variation with incident angle .

Frequency-dependent AVO Gradient

The AVO gradients for Class I AVO, Class II AVO, and Class III AVO all decrease with frequency. This is consistent with what we observe from the frequency-dependent V_p/V_s ratio which controls the AVO gradient variation. As shown in Figure 5.2, the dispersion effect of V_p/V_s ratio for the underlying sandstone is stronger than that of overburden shale, and the V_p/V_s ratio contrast consequently decreases with frequency. As a result, AVO gradient decreases with frequency for these three classical AVO responses.

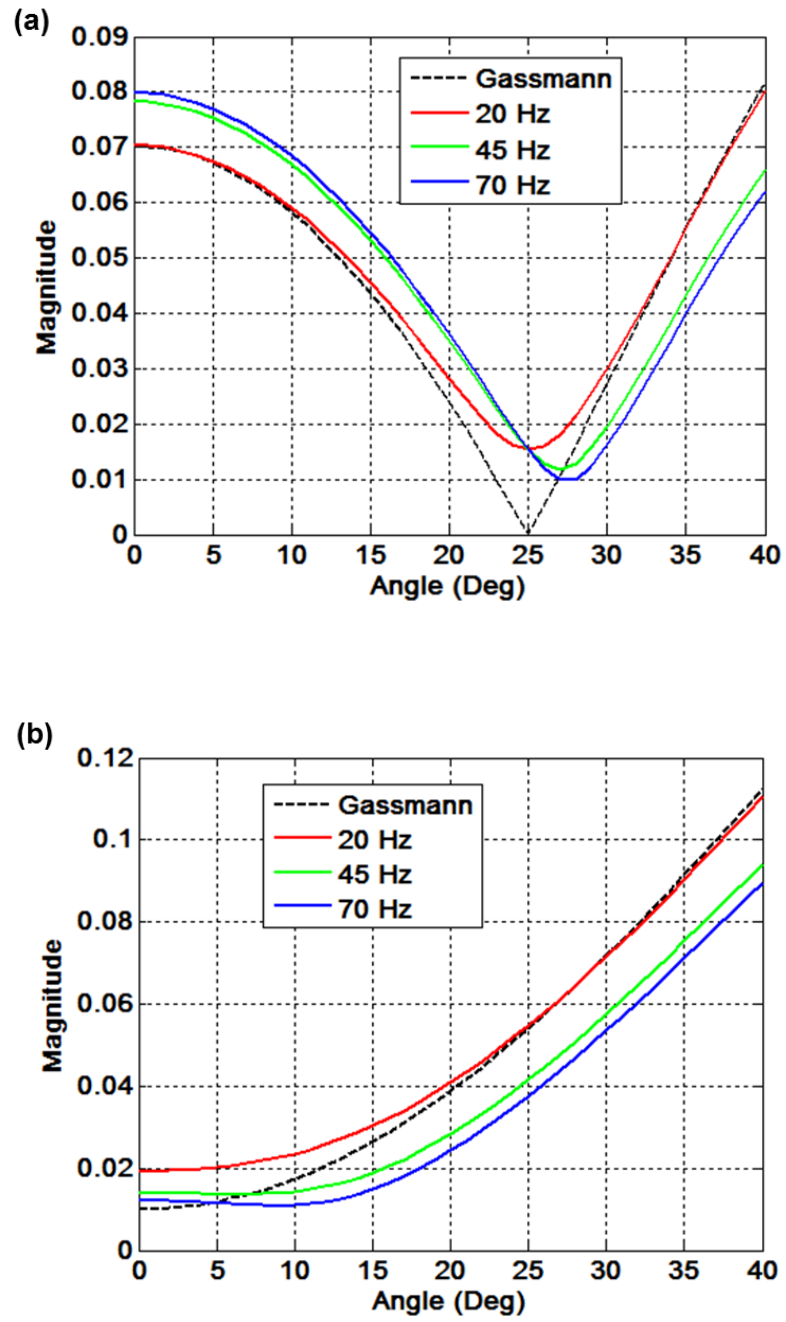


Figure 5.5. Magnitude of fast PP reflectivity versus incident angle with specific seismic frequency band for (a) Class I AVO model and (b) Class II AVO model.

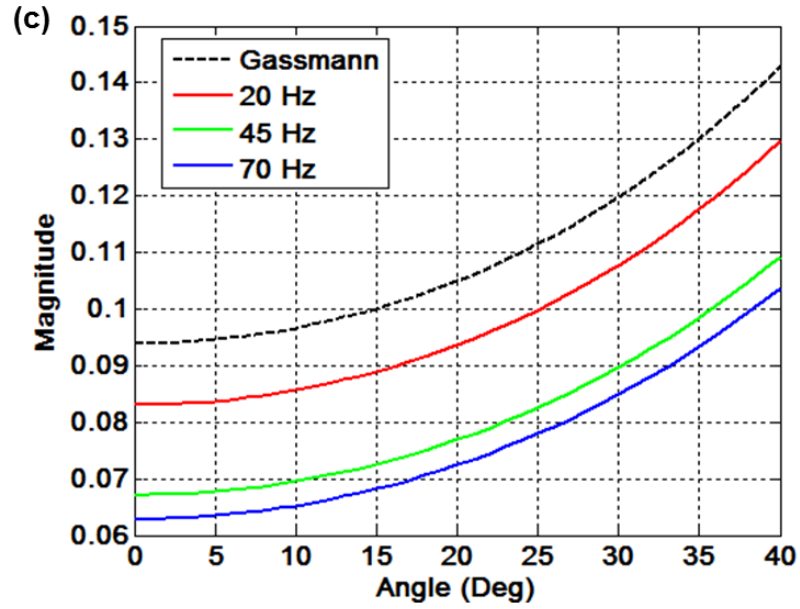


Figure 5.5(continued). Magnitude of fast PP reflectivity versus incident angle with specific seismic frequency band for (c) Class III AVO model.

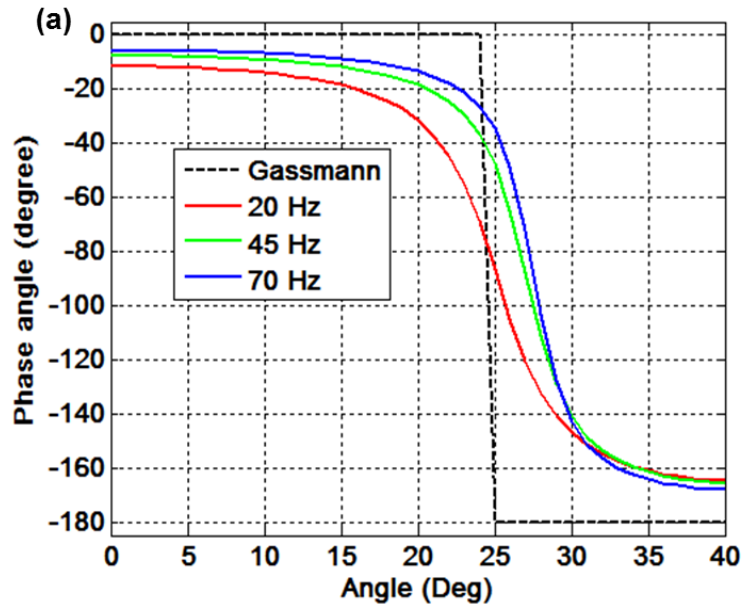


Figure 5.6. Phase angle of fast PP reflectivity versus incident angle with specific seismic frequency band for (a) Class I AVO model.

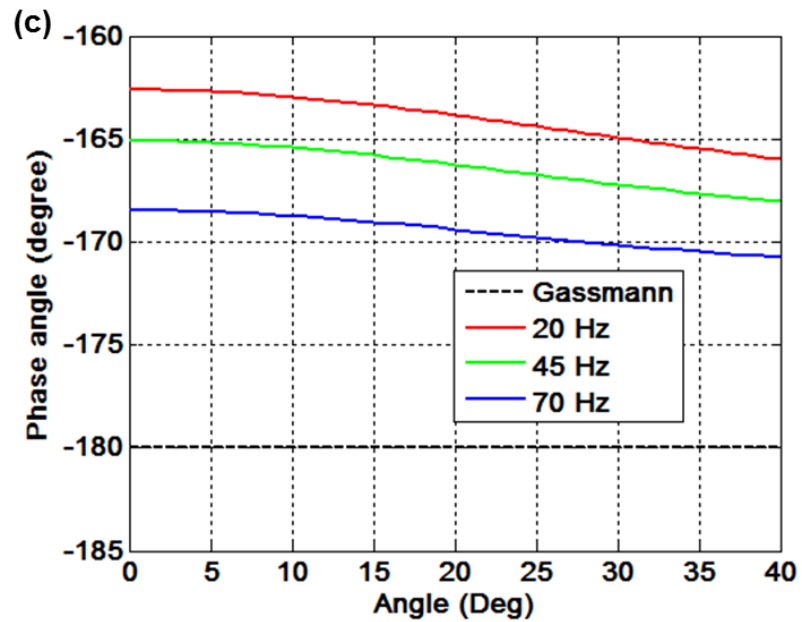
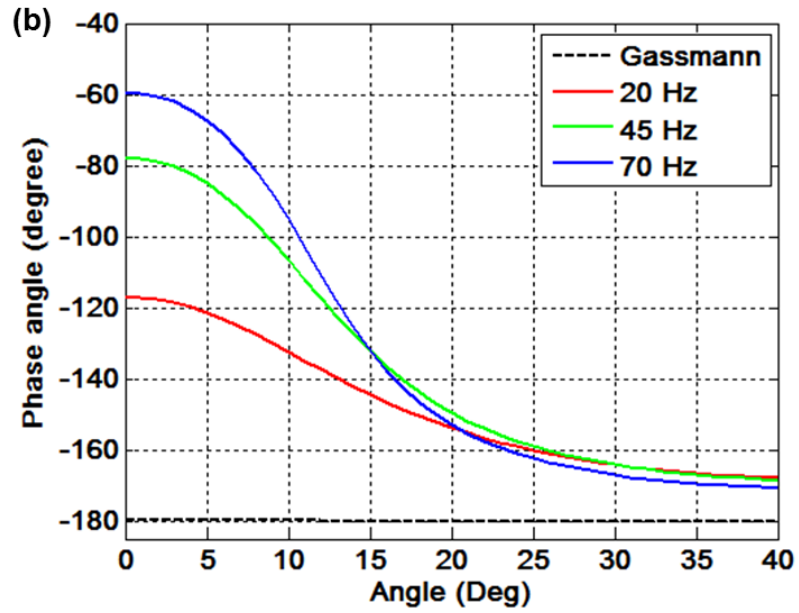


Figure 5.6 (continued). Phase angle of fast PP reflectivity versus incident angle with specific seismic frequency band for (b) Class II AVO model and (c) Class III AVO model.

5.5 Poroelastic Effect on Seismic Wavelet

In this section, we carry out the analysis of poroelastic effect on the synthetic seismic responses. As we know, convolution can be used to model the filtering of seismic energy by the various rock layers in the Earth, and it can be written in the frequency domain as:

$$S(f) = R(f)W(f), \quad (5.1)$$

where $W(f)$ can be considered as the wavelet after Fourier transform; and $R(f)$ is the frequency-dependent poroelastic reflection defined in equation 4.14. Correspondingly, the seismic trace in the time domain can be obtained after inverse Fourier transform of equation 5.1:

$$S(t) = \int_{-\infty}^{\infty} R(f)W(f)e^{i2\pi ft} df. \quad (5.2)$$

Ricker wavelets with different central frequencies used to generated synthetic seismic trace are shown in Figure 5.7. We compute the poroelastic impulse responses at normal and 30 degrees incident angle, which respectively represent the seismic responses at near offset and far offset. A series of impulse responses convolved from the Ricker wavelet with different central frequencies under different geological scenarios are presented in this section. We call the seismic response computed from the poroelastic reflection as “poroelastic seismic response”, and the seismic response computed from the elastic reflection is referred to “elastic seismic response”. It is found that the poroelastic effect affects the seismic impulse responses in terms of both seismic amplitude and phase angle. This finding is particularly interesting, because it demonstrates that the poroelastic reflection due to wave-induced fluid flow not only

affects the quantitative seismic interpretation, but also influences the accuracy of seismic imaging. Be aware that we are still concentrating on the interface effect, and the propagation effect due to the attenuation caused by wave-induced fluid flow is not discussed here. As we will show later in this section, under different reasonable geological circumstances, the poroelastic effect shows quite different impact on seismic responses.

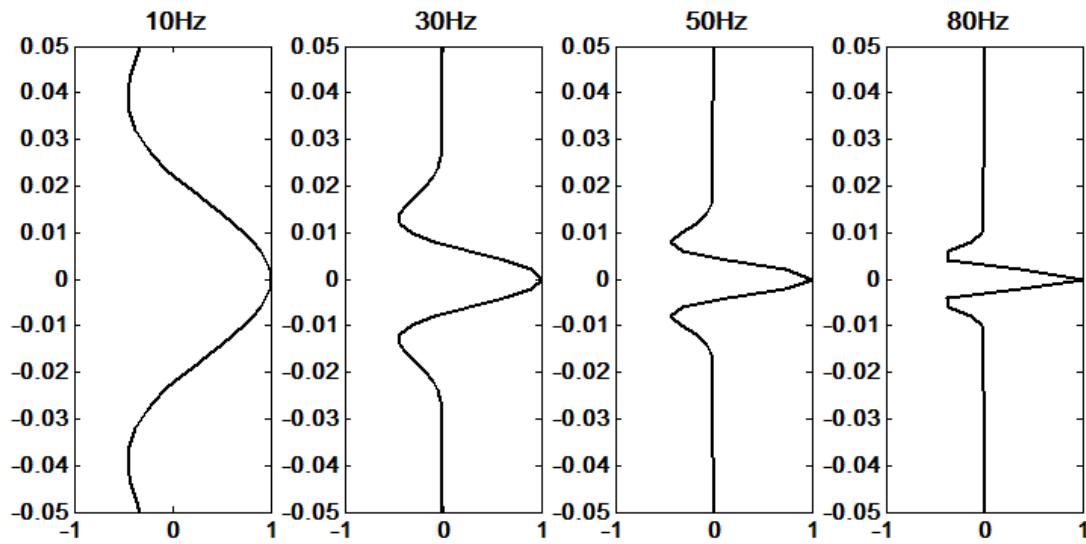


Figure 5.7. Ricker wavelets with different central frequencies used to simulate synthetic seismic trace.

Model 1

For the geological scenario associated with Class I AVO response, the comparison of elastic seismic response and poroelastic seismic response at normal and 30 degrees incident angle are shown in Figures 5.8 and 5.9, respectively. At normal incident angle, there is a noticeable phase shift for all the four poroelastic seismic synthetics.

Concerning the seismic amplitude as shown in Figure 5.10, the RMS (root-mean-square) amplitude for the poroelastic impulse responses is bigger than that of elastic impulse responses. Additionally, the amplitude differences increase with the central frequency of source wavelet. This is mainly due to the low-frequency dim-spot for Class I AVF. However, as illustrated in Figure 5.8(b), the frequency content of the poroelastic seismic response shows no appreciable change.

The poroelastic impact on the seismic responses becomes pronounced for the large incident angle. As shown on Figure 5.11, it turns out that the RMS amplitude discrepancy between the elastic impulse response and porelastic impulse response increases with frequency, and can reach as high as 65%. More importantly, the significant phase shift will influence the accuracy of seismically imaging the geological structure. Additionally, reflection dispersion causes central frequency of the poroelastic impulse response shift to lower frequency domain with a remarkable degree, and consequently distorts the frequency content of the seismic data.

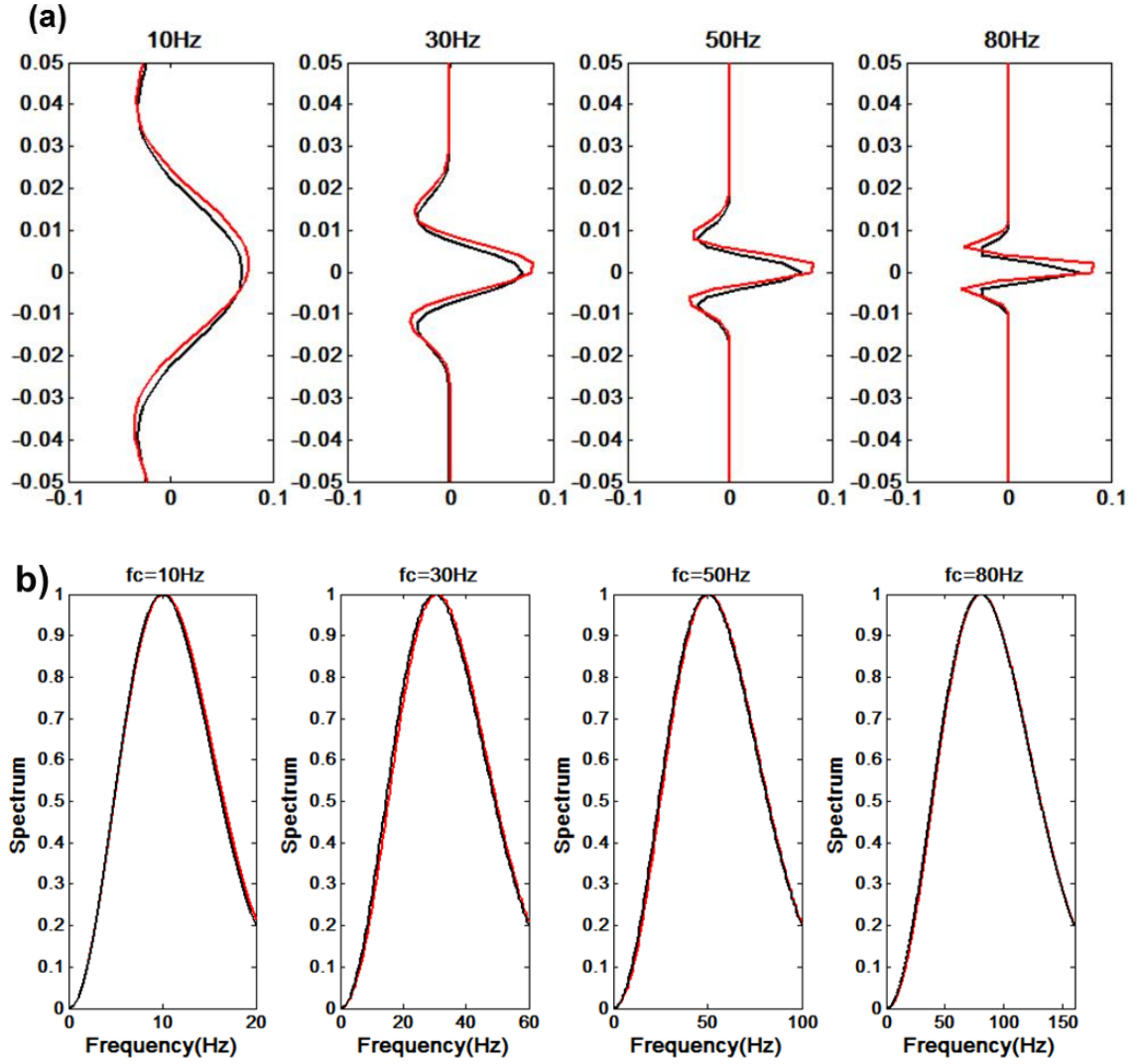


Figure 5.8. (a) Model 1 (Class I AVO) impulse responses convolved with 10-, 30-, 50-, and 80-Hz Ricker wavelets; black lines indicate synthetic seismic computed from elastic reflections at normal incident angle; red lines indicate synthetic seismic computed from poroelastic reflections at normal incident angle. (b) Normalized spectrum comparisons for impulse responses convolved with elastic reflection (black line) and poroelastic reflection (red line).

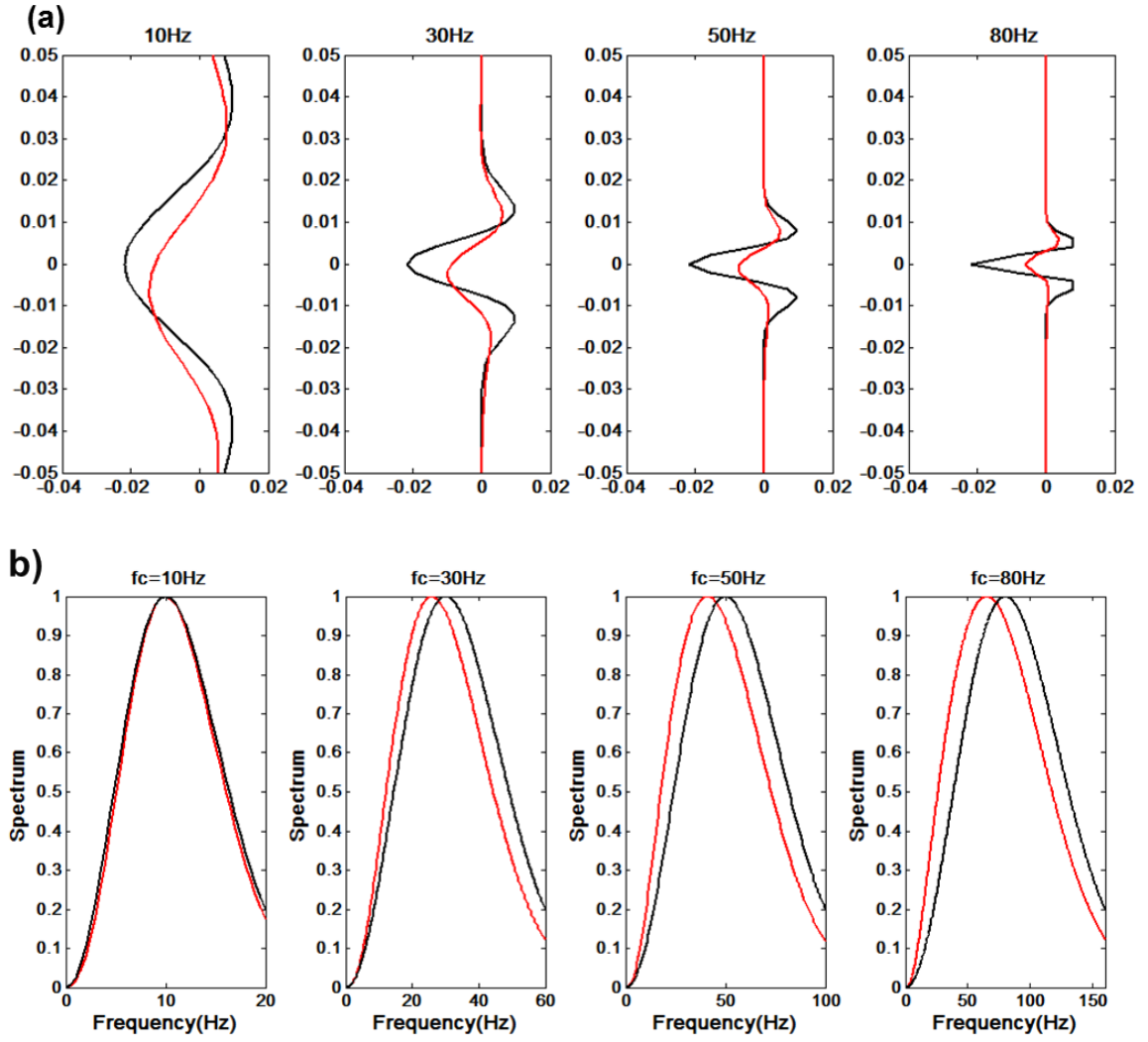


Figure 5.9. (a) Model 1 (Class I AVO) impulse responses convolved with 10-, 30-, 50-, and 80-Hz Ricker wavelets; black lines indicate synthetic seismic computed from elastic reflection at 30 degrees incident angle; red lines indicate synthetic seismic computed from poroelastic reflections at 30 degrees incident angle. (b) Normalized spectrum comparisons for impulse responses convolved with elastic reflection (black line) and poroelastic reflection (red line).

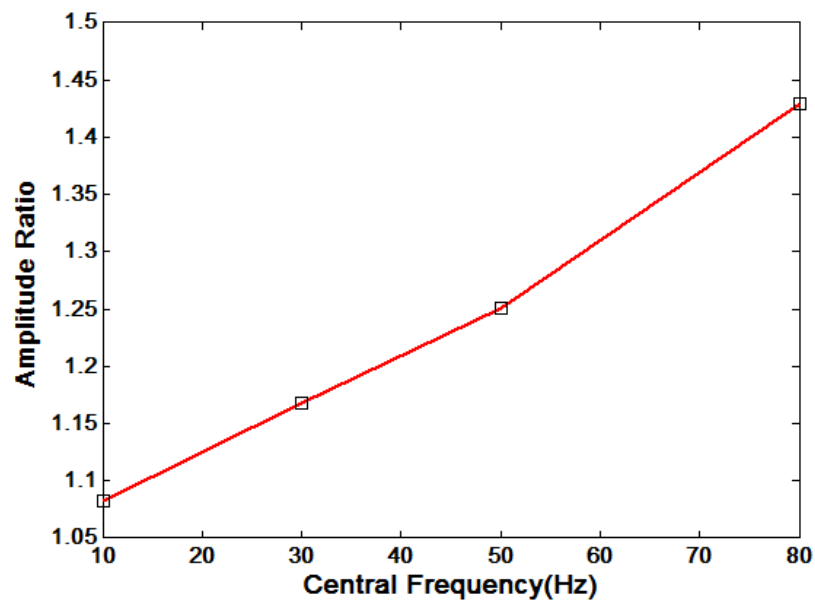


Figure 5.10. RMS amplitude ratio of poroelastic impulse responses over elastic impulse responses at normal incident angle for Class I AVO geological scenario.

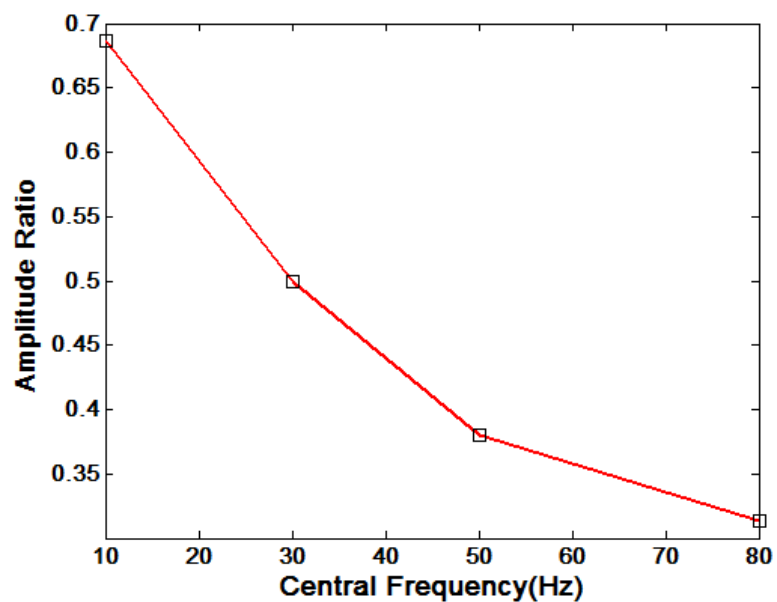


Figure 5.11. RMS amplitude ratio of poroelastic impulse responses over elastic impulse responses at 30 degrees incident angle for Class I AVO geological scenario.

Model 2

For the geological scenario associated with Class II AVO response, the comparisons of elastic seismic responses and poroelastic seismic responses are shown in Figures 5.12 and 5.13. At normal incident angle, the poroelastic reflection considerably modifies the shape of the seismic wavelet. There exists a phase reversal trend when the central frequency of the source wavelet increases from 10Hz to 80 Hz. This is mainly caused by the phase reversal phenomenon associated with Class II AVF. Also, as illustrated in Figure 5.14, the RMS amplitude for the poroelastic impulse response is weakened at low frequency domain, but is enhanced at high frequency domain. Note that this result seems to contradict the reflectivity amplitude variation trend with frequency at normal incident angle. The possible explanation is that the significant phase variation changes the RMS amplitude of seismic trace. Additionally, as illustrated in Figure 5.13(b), the central frequency of the poroelastic seismic response shifts to lower frequency domain, except the source wavelet centered at 10Hz which is shifted to a slightly higher frequency domain. At 30 degrees incident angle, it is found that the elastic responses and poroelastic responses are pretty consistent with each other. Generally, the RMS amplitudes of the poroelastic responses are smaller than that of elastic impulse responses as shown on Figure 5.15. This is because, at this incident angle, reflection amplitude of high frequency component is smaller than that of low frequency component (Figure 5.6(b)). Moreover, as illustrated in Figure 5.15(b), the central frequency of poroelastic response slightly shifts to the lower frequency domain.

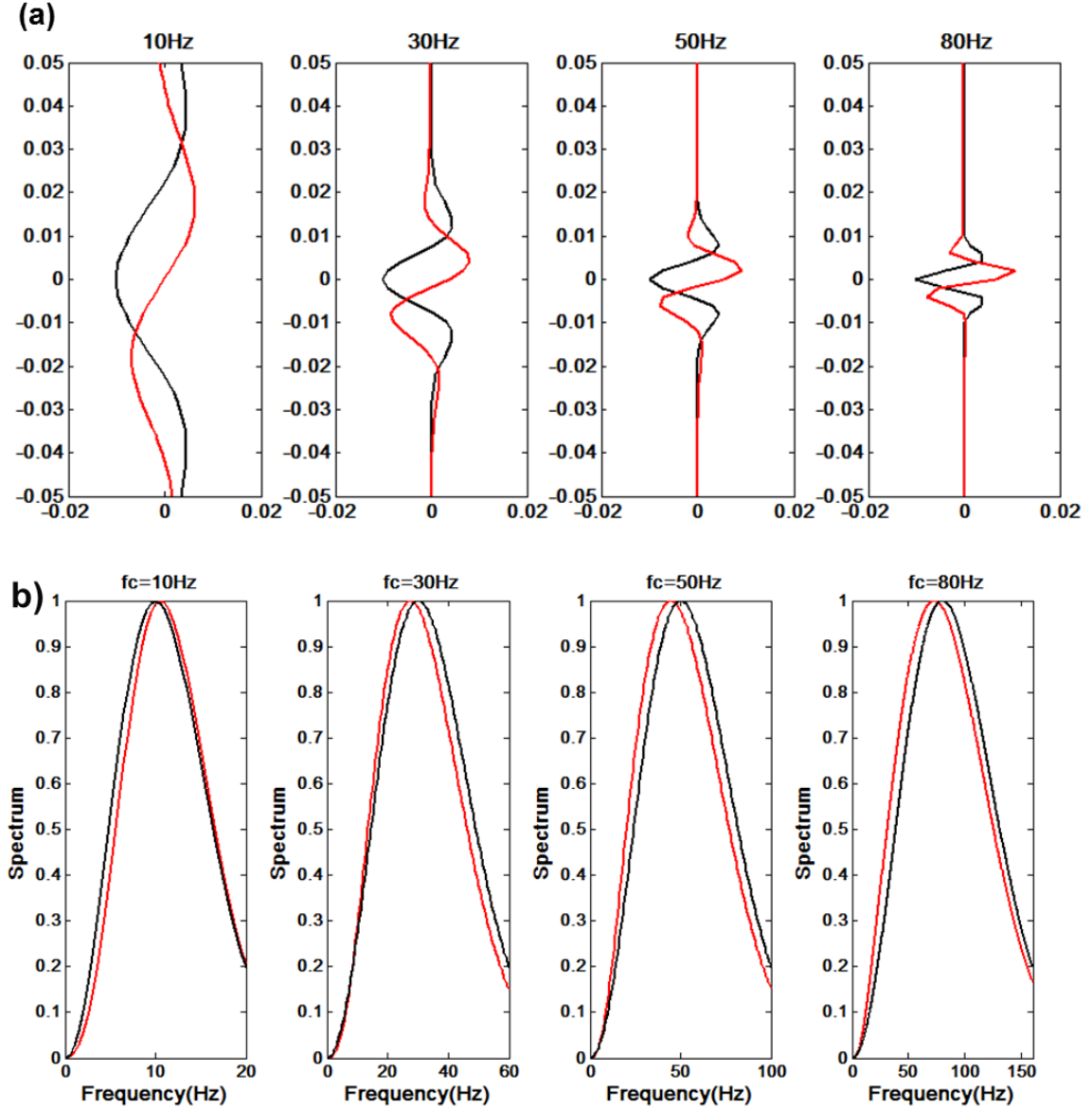


Figure 5.12. (a) Model 2 (Class II AVO response) impulse responses convolved with 10-, 30-, 50-, and 80-Hz Ricker wavelets; black lines indicate synthetic seismic computed from elastic reflections at normal incident angle; red lines indicate synthetic seismic computed from poroelastic reflections at normal incident angle. (b) Normalized spectrum comparisons for impulse responses convolved with elastic reflection (black line) and poroelastic reflection (red line).

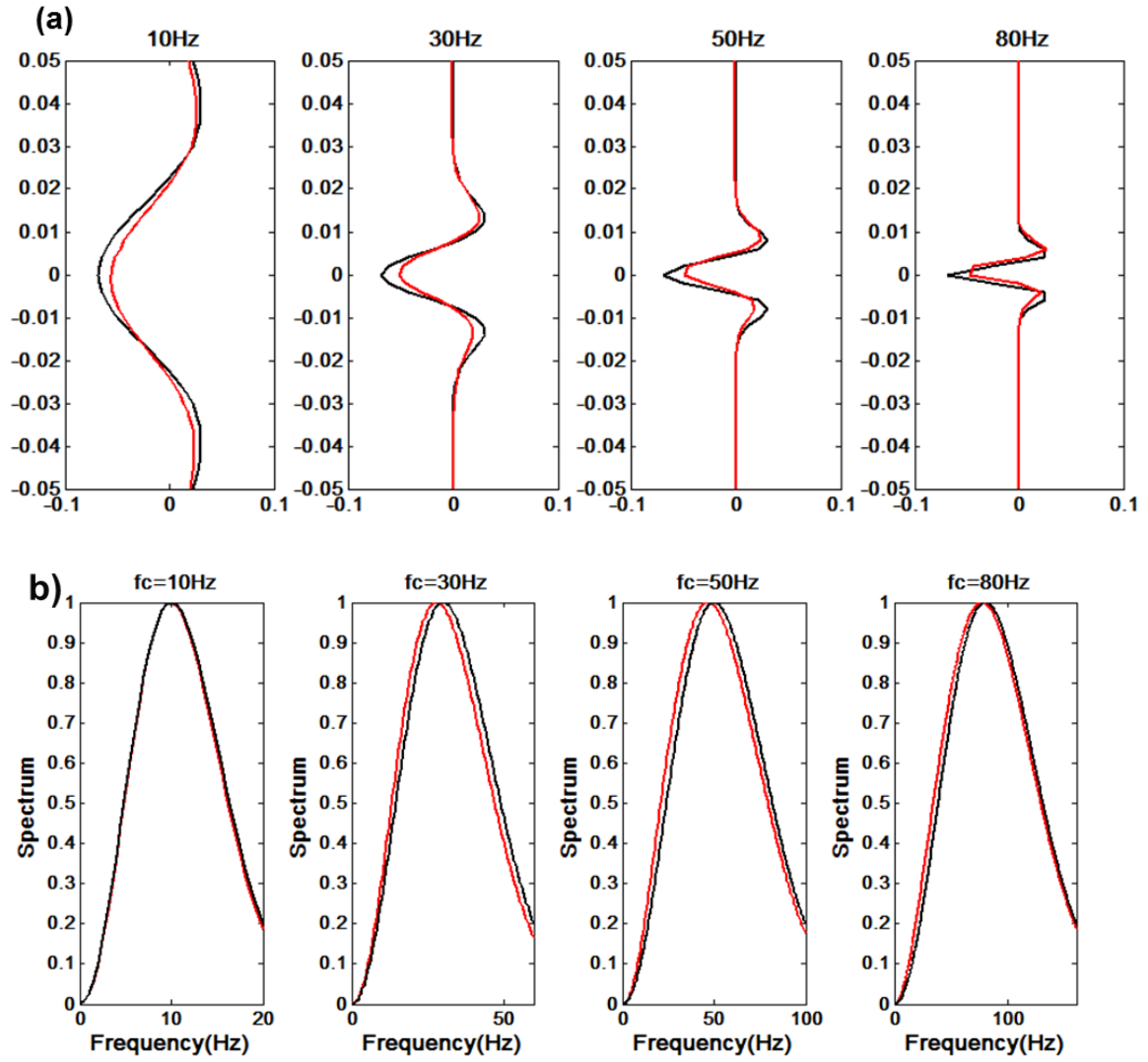


Figure 5.13. (a) Model 2 (Class II AVO response) impulse responses convolved with 10-, 30-, 50-, and 80-Hz Ricker wavelets; black lines indicate synthetic seismic computed from elastic reflection at 30 degrees incident angle; red lines indicate synthetic seismic computed from poroelastic reflections at 30 degrees incident angle. (b) Normalized spectrum comparisons for impulse responses convolved with elastic reflection (black line) and poroelastic reflection (red line).

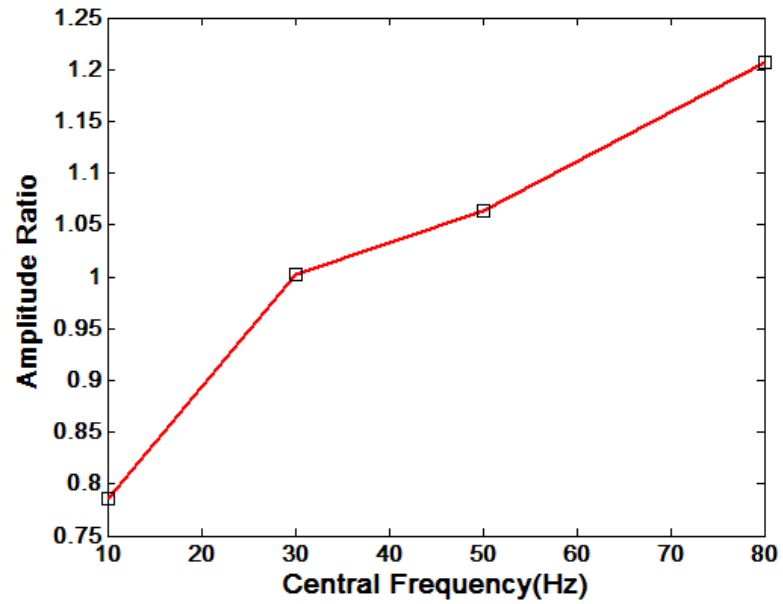


Figure 5.14. RMS amplitude ratios of poroelastic impulse responses over elastic impulse responses at normal incident angle for Class II AVO geological scenario.

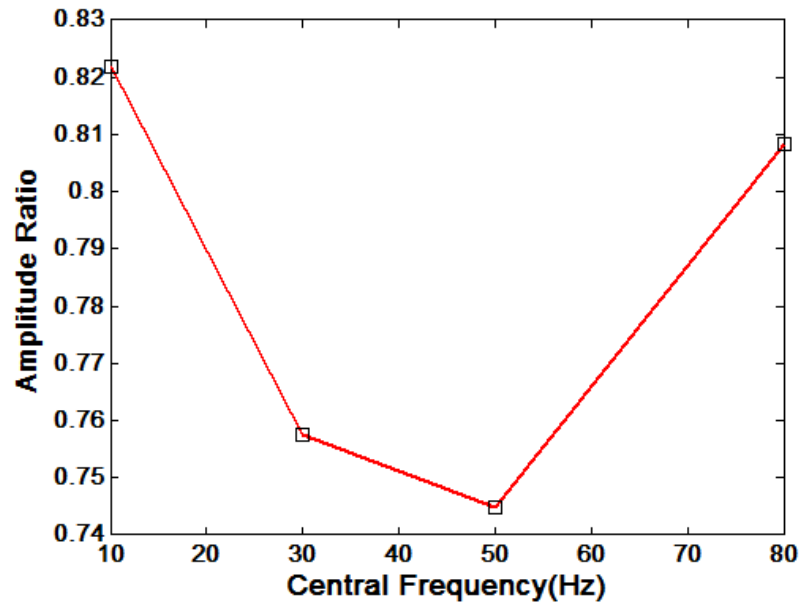


Figure 5.15. RMS amplitude ratios of poroelastic impulse responses over elastic impulse responses at 30 degrees incident angle for Class II AVO geological scenario.

Model 3

The poroelastic responses for the geological scenario associated with Class III AVO at normal and 30 degree incident angle are shown in Figure 5.16 and 5.17, respectively. At both normal and 30 degrees incident angle, the waveforms of the poroelastic impulse response are quite consistent with those of the elastic impulse responses. However, as illustrated in the Figure 5.18 and Figure 5.19, there is a non-negligible amplitude decay caused by the poroelastic effect, and this impact is more influential at normal incident angle. This is intimately associated with the low-frequency bright-spot which corresponds to Class III AVF. As a result, such a discrepancy will bring uncertainty for quantitative seismic amplitude interpretation in terms of porosity, water saturation, and so forth.

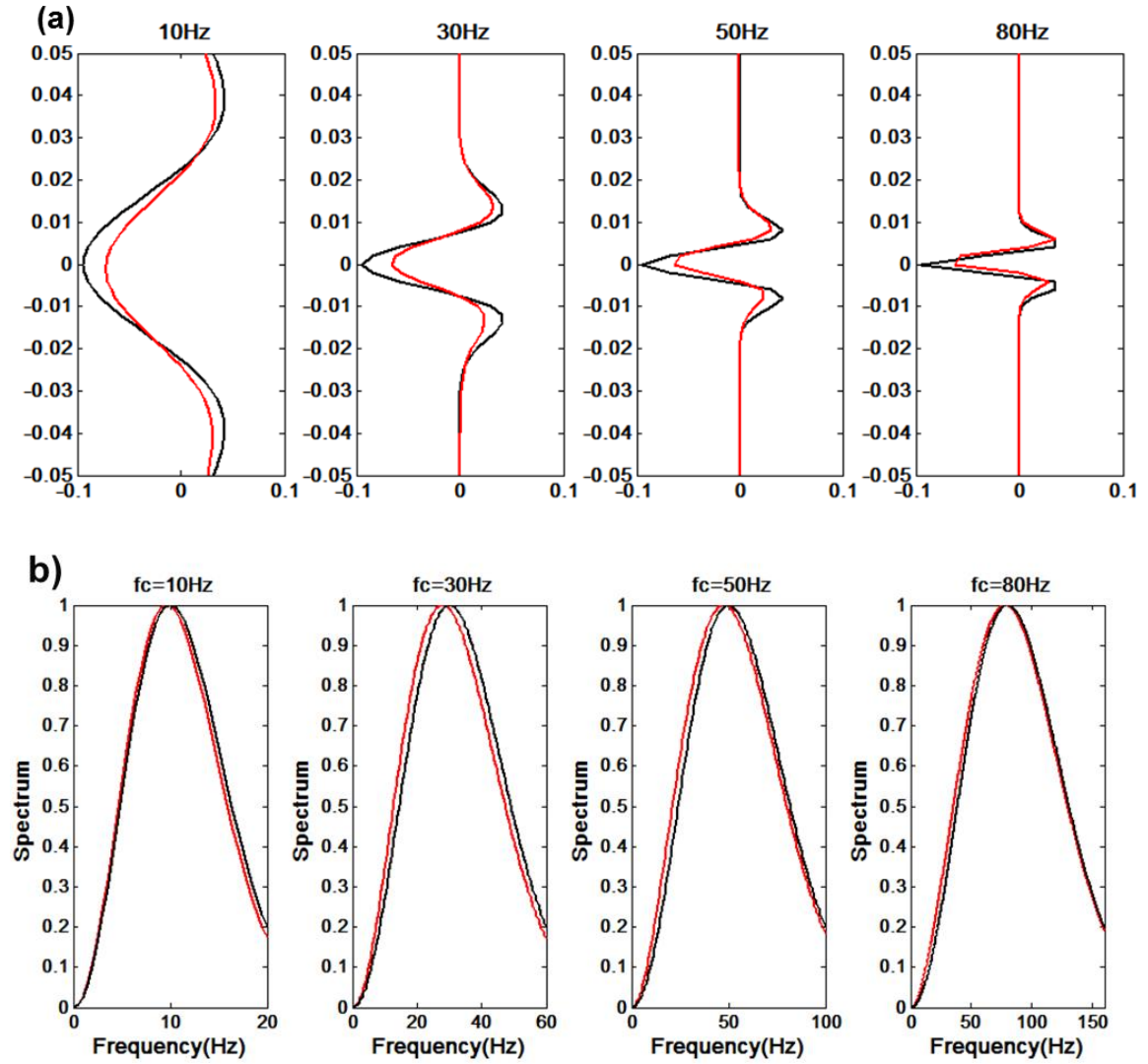


Figure 5.16. (a) Model 3 (Class III AVO response) impulse responses convolved with 10-, 30-, 50-, and 80-Hz Ricker wavelets; black lines indicate synthetic seismic computed from elastic reflection at normal incident angle; red lines indicate synthetic seismic computed from poroelastic reflections at normal incident angle. (b) Normalized spectrum comparisons for impulse response convolved with elastic reflection (black line) and poroelastic reflection (red line).

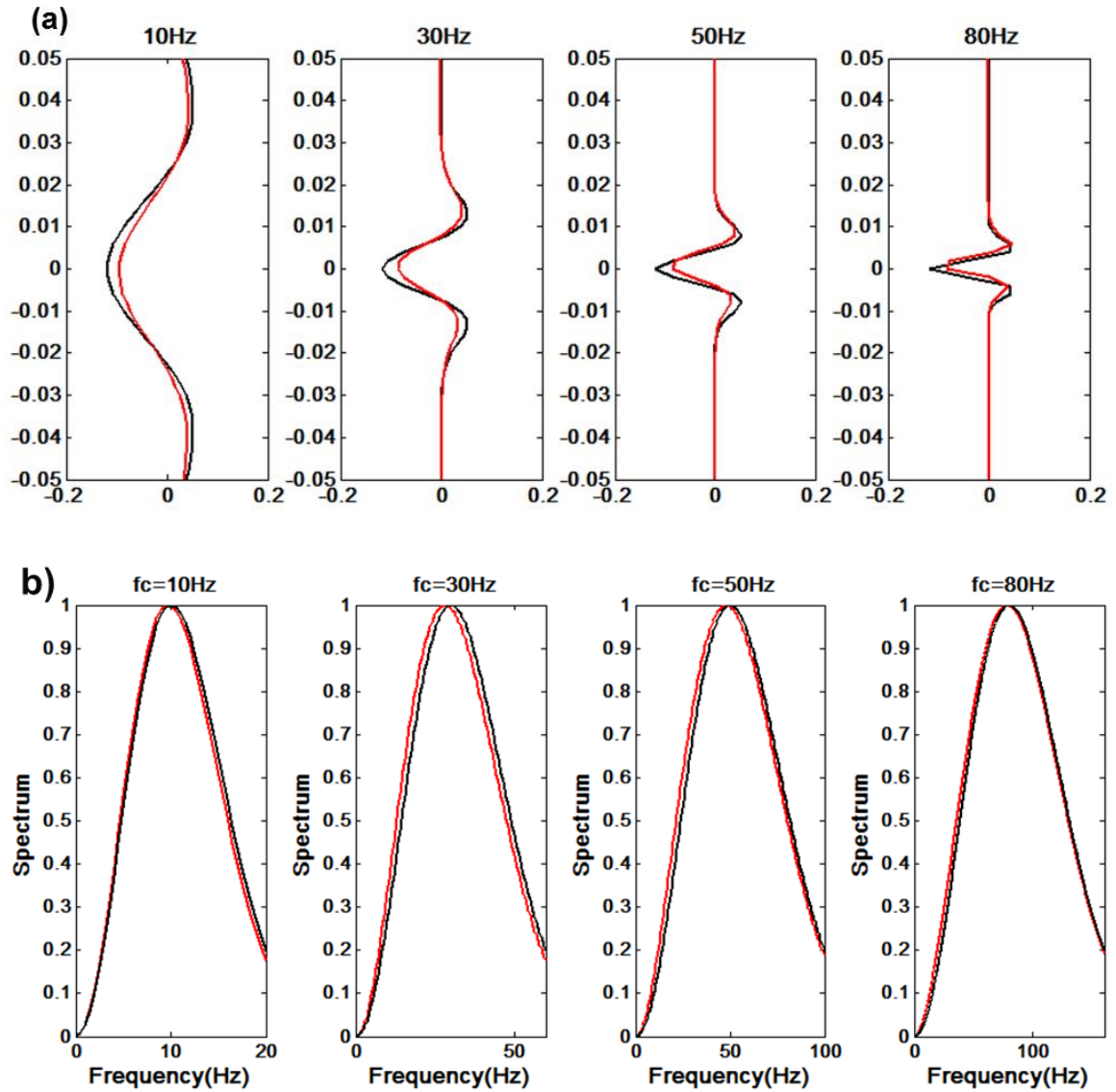


Figure 5.17. (a) Model 3 (Class III AVO response) impulse responses convolved with 10-, 30-, 50-, and 80-Hz Ricker wavelets; black lines indicate synthetic seismic computed from elastic reflection at 30 degrees incident angle; red lines indicate synthetic seismic computed from poroelastic reflections at normal incident angle. (b) Normalized spectrum comparisons for impulse responses convolved with elastic reflection (black line) and poroelastic reflection (red line).

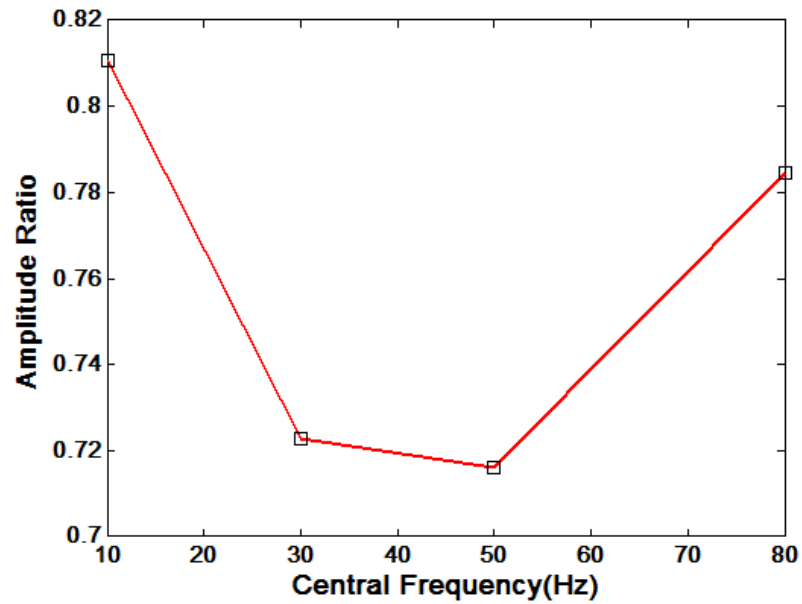


Figure 5.18 RMS amplitude ratios of poroelastic impulse responses over elastic impulse responses at normal incident angle for Class III AVO geological scenario.

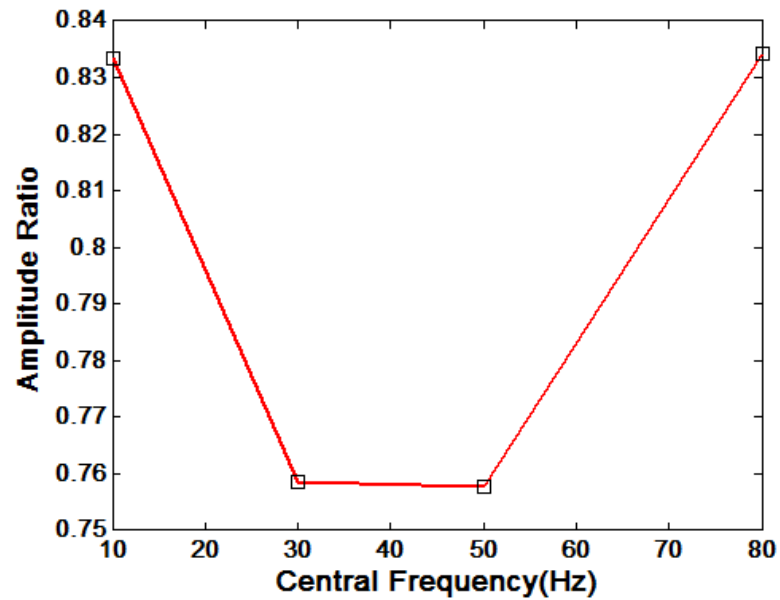


Figure 5.19 RMS amplitude ratios of poroelastic impulse responses over elastic impulse responses at 30 degrees incident angle for Class III AVO geological scenario.

5.6 Permeability Impact on Seismic Properties

In this section, we investigate the effect of permeability on poroelastic seismic attributes for different reservoir scenarios.

5.6.1 High Permeability Dim-spot Reservoir

Given the geological scenario of model 1, the magnitude and phase angle of fast PP reflectivity plotted as a function of frequency are shown in Figure 5.20. The lower permeability makes the minimum reflection amplitude and peak phase variation take place at lower frequency domain. Figure 5.21 illustrates the relationship of reflection amplitude and phase angle versus permeability. Clearly, high permeability weakens the seismic reflection amplitude and mitigates the phase variation in the seismic exploration band. The seismic responses are not sensitive to permeability variation at very low and high permeability ranges. In other words, the characteristic frequency of heterogeneous structure which corresponds to both very low and high permeability is beyond the seismic exploration band. However, for the permeability that ranges from $10^{-3} D$ to $10^{-1} D$, the reflection amplitude almost linearly decreases with permeability. In addition, the high-frequency component of reflection amplitude tends to be stronger. For example, when the permeability is $10^{-2} D$, the high-frequency amplitude is 25% stronger than the low-frequency amplitude. Figure 5.22 illustrates the poroelastic seismic responses for reservoir rocks with different permeability. As expected, the seismic amplitude evidently decreases with an increase of permeability. Also, it is interesting to see that the amplitude of elastic response is stronger than that

of poroelastic seismic response with higher permeability, but it is weaker than that of poroelastic seismic response with lower permeability.

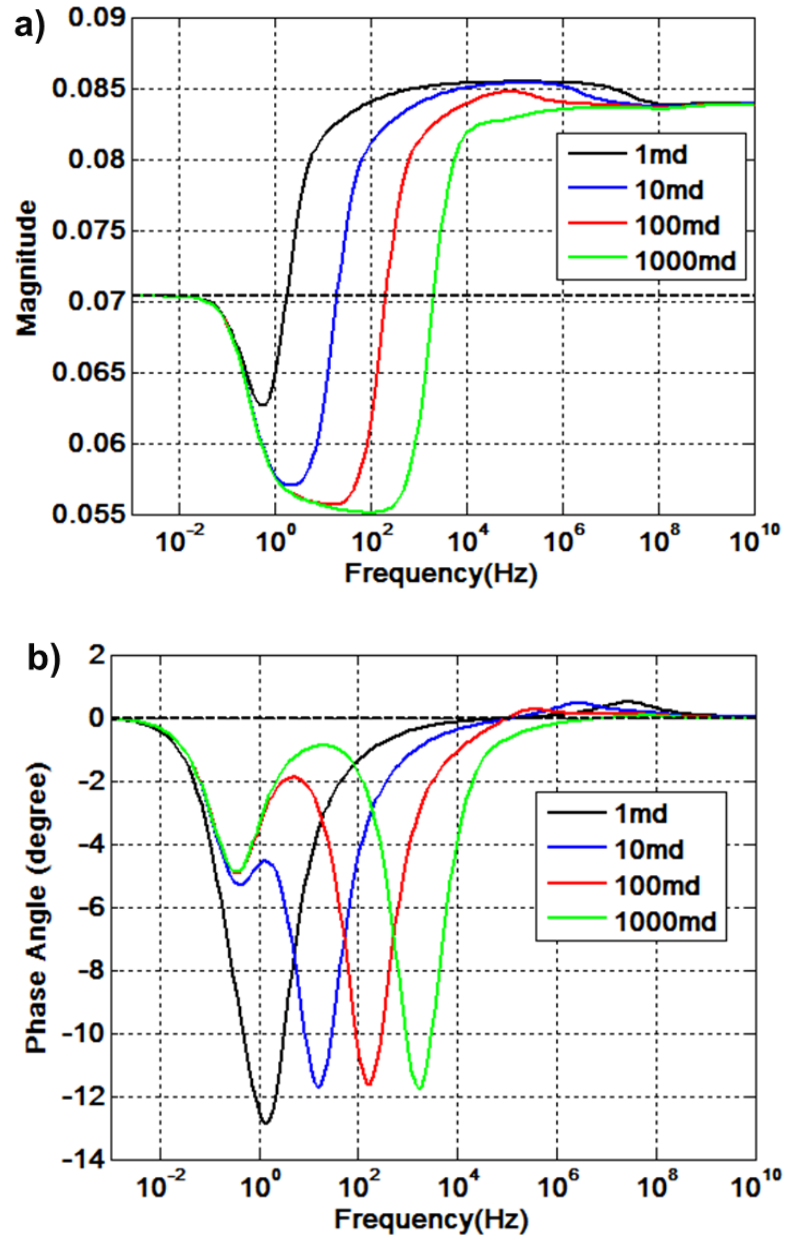


Figure 5.20. (a) Magnitude and (b) phase angle of fast PP poroelastic reflection versus frequency at normal incident angle with different matrix permeability k_1 . The

geological scenario corresponds to Class I AVO response. The black dashed line indicates the amplitude and phase angle of elastic reflection.

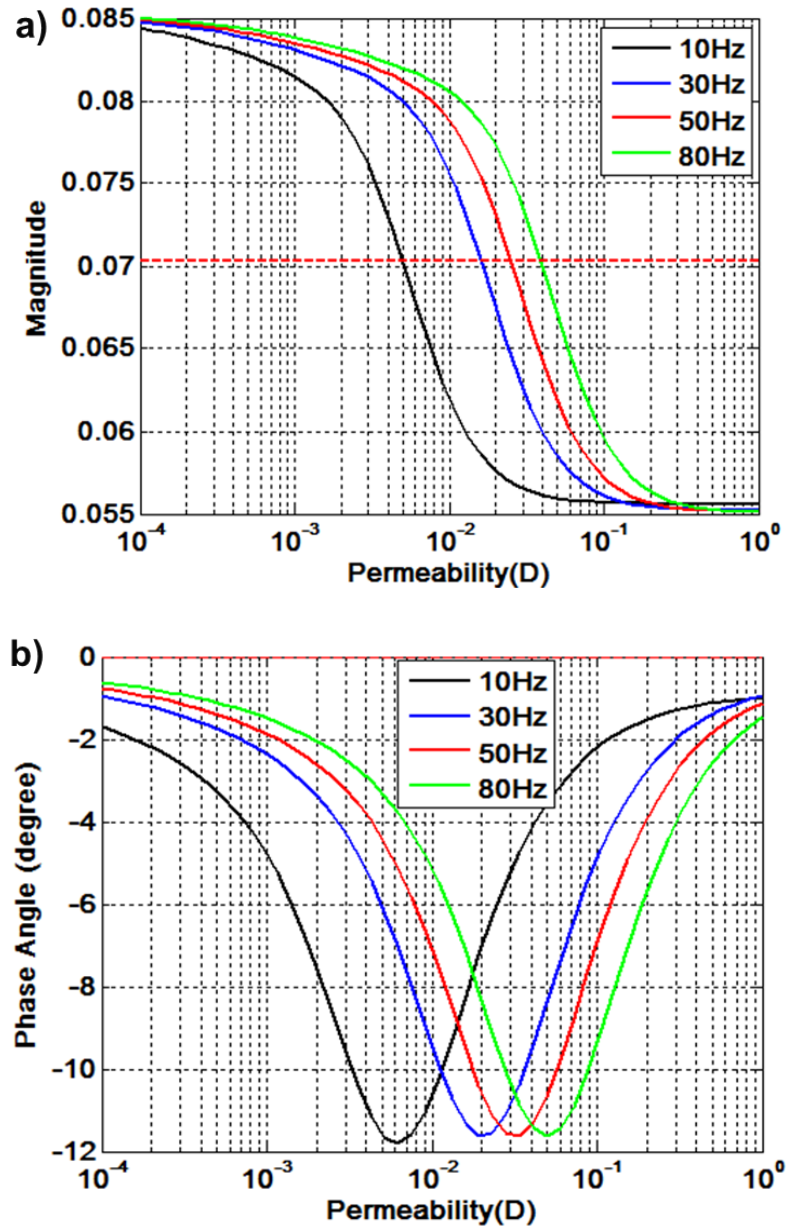


Figure 5.21. (a) Magnitude and (b) phase angle of fast PP poroelastic reflection versus permeability at normal incident angle for specific frequencies. The geological scenario corresponds to Class I AVO response. The red dashed line indicates the amplitude and phase angle of elastic reflection.

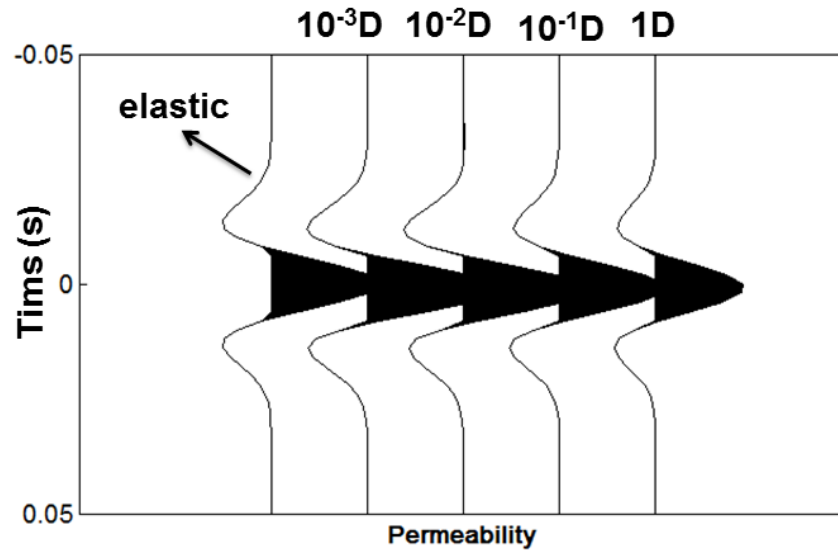


Figure 5.22. Poroelastic seismic synthetics (30-Hz Ricker wavelet) at normal incident angle for permeabilities ($10^{-3}D$, $10^{-2}D$, $10^{-1}D$, and $1D$). The left-most trace indicates the elastic seismic response. The geological scenario corresponds to Class I AVO response.

5.6.2 Permeability-dependent Phase-reversal Reservoir

Figure 5.23 illustrates the effect of permeability on the reflection amplitude and phase angle for the geological circumstance corresponding to Class II AVO response. It turns out that the significant phase variation complicates the amplitude-versus-frequency relationship. Figure 5.24 illustrates the relationship of both reflection

amplitude and phase angle with permeability variation. In general, the high permeability enhances the reflection amplitude. But for very low permeability range, say from 10^{-4} D to 10^{-3} D, the seismic amplitude slightly decreases with an increase of permeability. Additionally, be aware that the seismic amplitude for reservoir rocks with 1 D permeability is 2 times stronger than the reservoir rocks with 10^{-3} D. As illustrated in Figure 5.24(b), the most prominent feature for this geological scenario is that the phase angle exhibits a reversal trend when permeability varies in a wide range. In seismic exploration band, the poroelastic reflection have an almost zero phase angle for the low permeability rock, while the phase angle approaches to negative 180 degrees when the permeability goes to 1 D. The synthetic poroelastic seismic responses are displayed in Figure 5.25, the seismic trace exhibits a dramatic variation in terms of both amplitude and phase angle. The phase polarity for the poroelastic seismic synthetic goes from positive to negative when permeability changes from 10^{-3} D to 1 D. Also, the seismic energy of poroelastic reflection for high-permeability reservoir rocks is much higher than the case with low permeability rock.

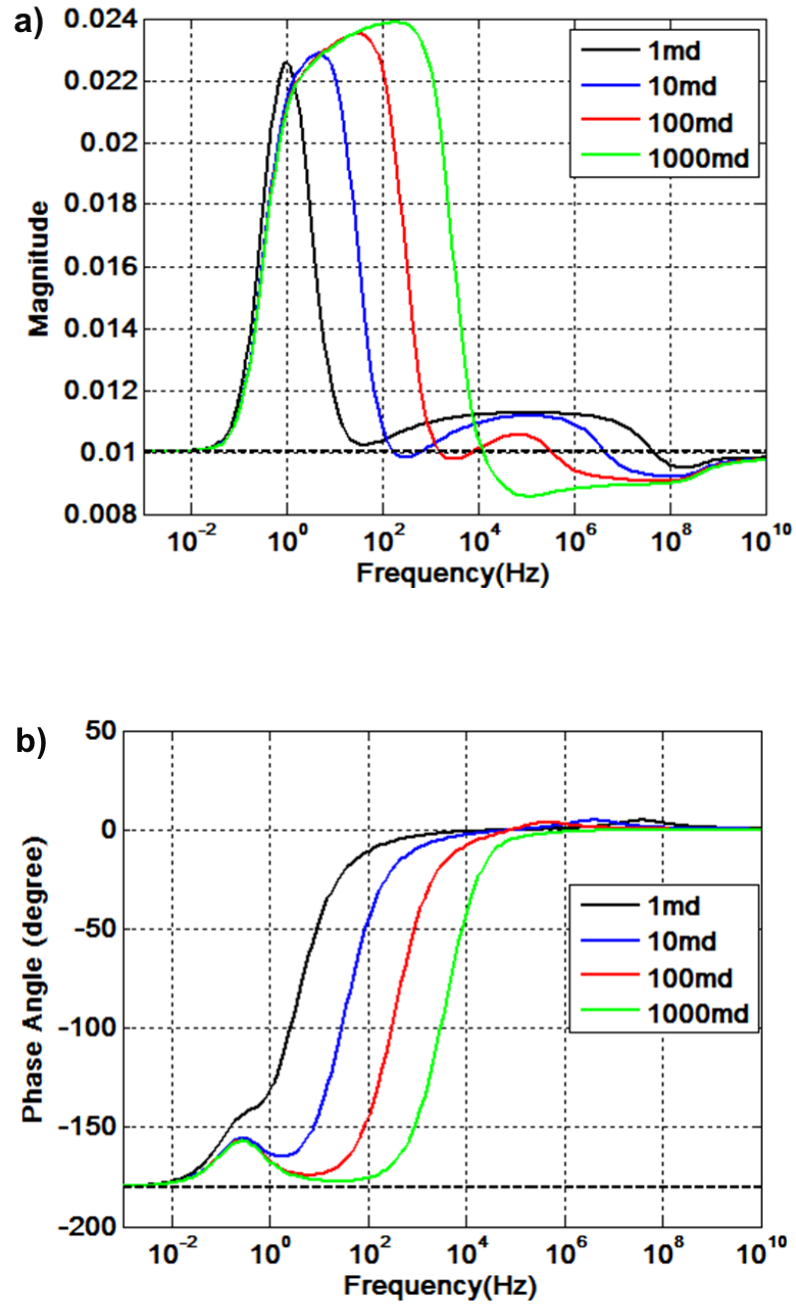


Figure 5.23 (a) Magnitude and (b) phase angle of fast PP poroelastic reflection versus frequency at normal incident angle with different matrix permeability k_1 . The geological scenario corresponds to Class II AVO response. The black dashed line indicates the amplitude and phase angle of elastic reflection.

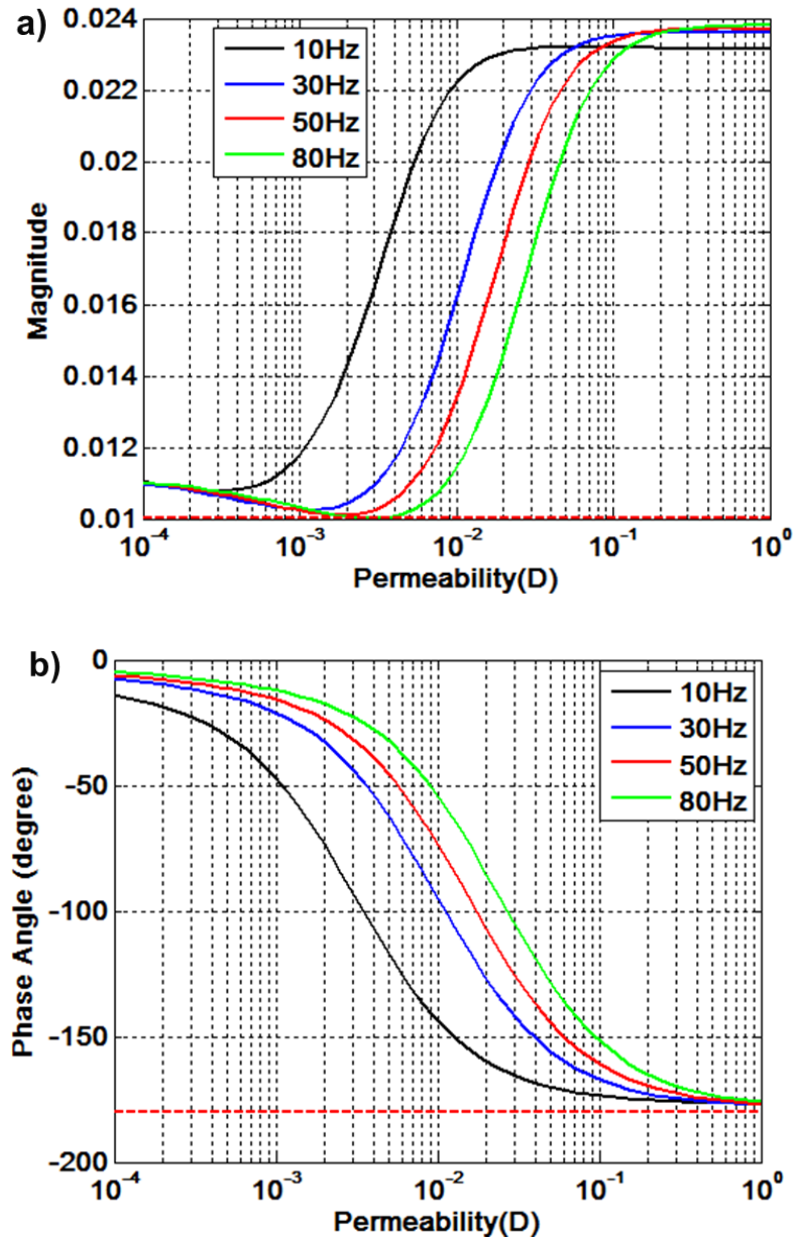


Figure 5.24 (a) Magnitude and (b) phase angle of fast PP poroelastic reflection versus permeability at normal incident angle for specific frequencies. The geological scenario corresponds to Class II AVO response. The red dashed line indicates the amplitude and phase angle of elastic reflection.

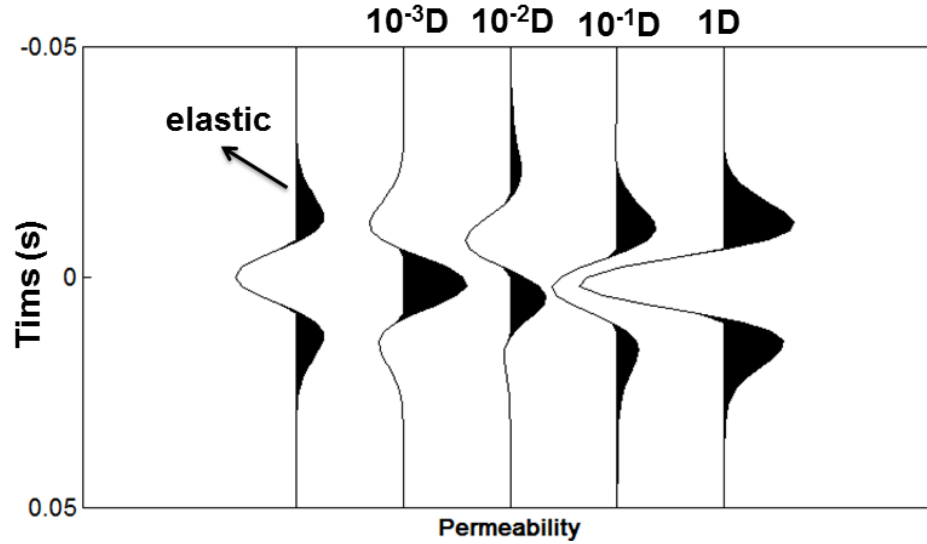


Figure 5.25 Poroelastic seismic synthetics (30-Hz Ricker wavelet) at normal incident angle for 4 permeabilities ($10^{-3} D$, $10^{-2} D$, $10^{-1} D$, and $1 D$). The left-most trace indicates the elastic seismic response. The geological scenario corresponds to Class II AVO response.

5.6.3 High Permeability Bright-spot Reservoir

Figures 5.26 and 5.27 illustrate the effect of permeability on the reflection amplitude and phase angle for the geological scenario corresponding to Class III AVO response. Similar to the poroelastic response for Class I AVO reservoir rocks, the reflection is not sensitive to permeability variation in the both very low and high permeability ranges. For permeability ranging from $10^{-3} D$ to $10^{-1} D$, we find that the seismic amplitude increases with permeability in an almost linear manner. Consequently, seismic reflections present a bright spot for the reservoir rocks having high permeability. The poroelastic seismic synthetic as shown on Figure 5.28 clearly shows an amplitude increase trend with an increase of permeability.

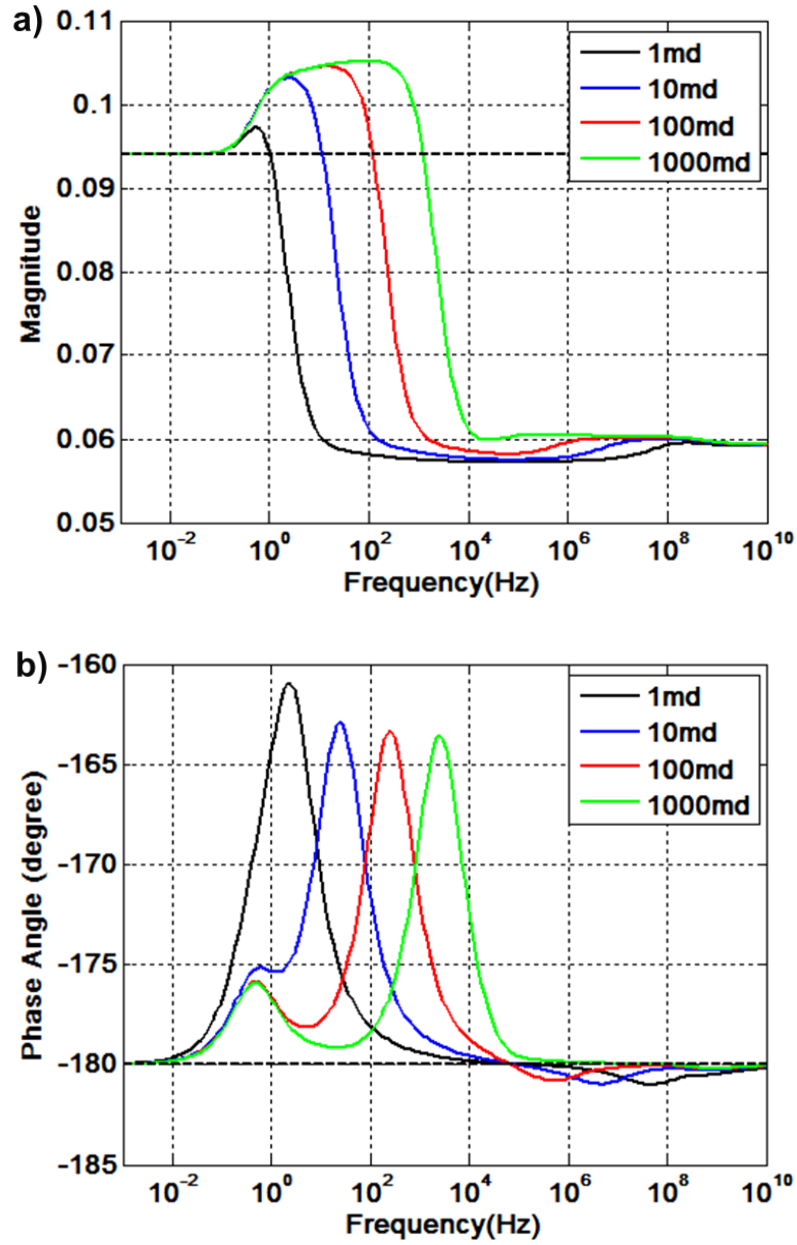


Figure 5.26. (a) Magnitude and (b) phase angle of fast PP poroelastic reflection versus frequency at normal incident angle with different matrix permeability k_1 . The geological scenario corresponds to Class III AVO response. The black dashed line indicates the amplitude and phase angle of elastic reflection.

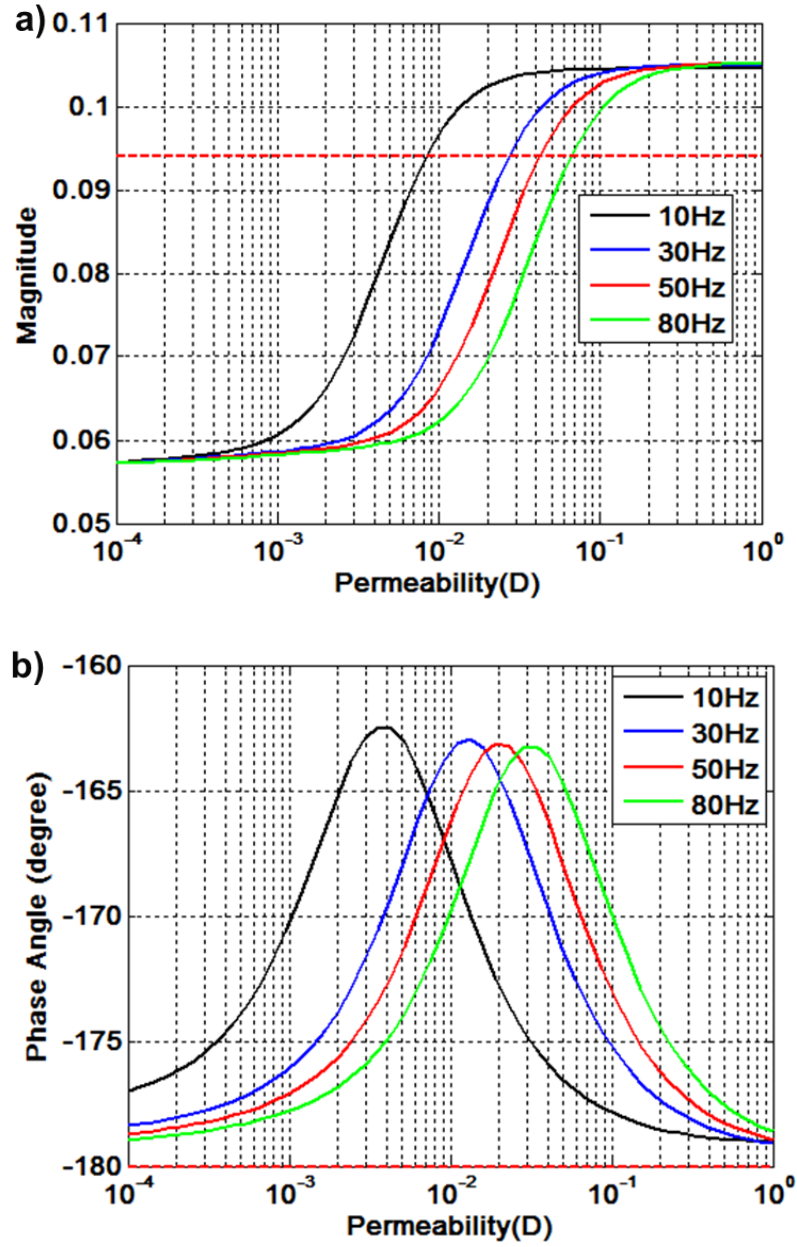


Figure 5.27. (a) Magnitude and (b) phase angle of fast PP poroelastic reflection versus permeability at normal incident angle for specific frequencies. The geological scenario corresponds to Class III AVO response. The red dashed line indicates the amplitude and phase angle of elastic reflection.

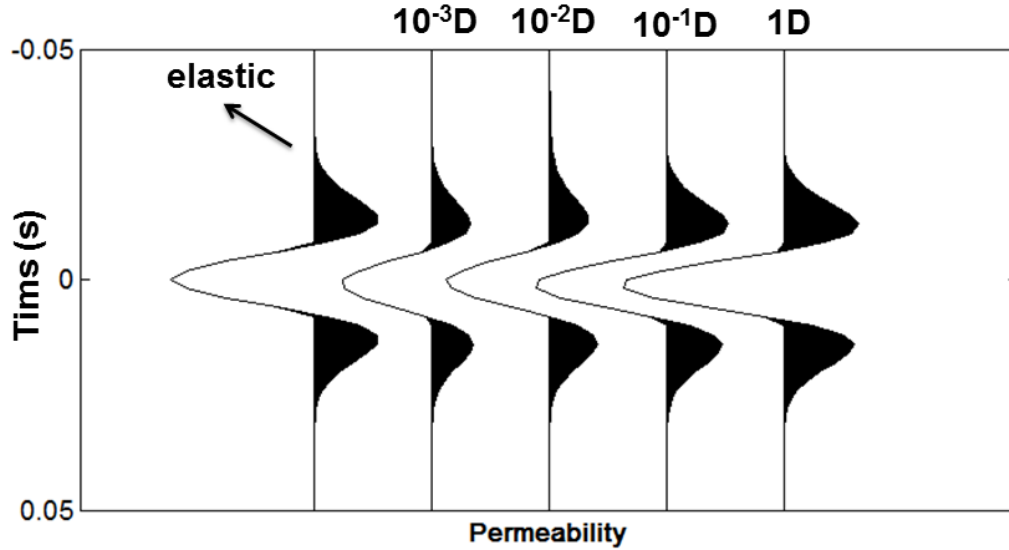


Figure 5.28. Poroelastic seismic synthetics (30-Hz Ricker wavelet) at normal incident angle for 4 permeabilities ($10^{-3} D$, $10^{-2} D$, $10^{-1} D$, and $1 D$). The left-most trace indicates the elastic seismic response. The geological scenario corresponds to Class III AVO response.

5.6.4 Seismic-sensitive Permeability Zone

In this section, we demonstrate that seismic reflection is a function of permeability for each frequency component. Interestingly, it is found that the curve shape of amplitude-permeability relationship is similar to that of velocity dispersion relationship. Correspondingly, the curve shape of phase-permeability relationship is similar to that of attenuation-frequency relationship. Permeability appears to behave in a similar way as frequency does. Indeed, it is believed that the varying permeability can be considered to mimic the frequency effect. In other words, to emulate dispersive effects, it is possible to merely change the permeability or fluid viscosity

rather than changing the observational frequency. From a phenomenological perspective, the high permeability corresponds to low frequency, where the pore pressure tends to be equilibrated; the low permeability corresponds to high frequency, where the pore pressure is difficult to be equilibrated. That is why the low-frequency bright-spot corresponds to high-permeability bright-spot for the Class III AVF reservoir environment, while the low-frequency dim-spot corresponds to high-permeability dim-spot for Class I AVF reservoir environment.

Besides, the characteristic frequency of mesoscopic flow is given in equation 4.32:

$$f_c = \frac{\kappa}{\phi L^2} \frac{K_f}{\eta} .$$

Consequently, it is easy to define this seismic-sensitive permeability:

$$\kappa_s = \frac{f_s}{\phi L^2} \frac{K_f}{\eta} . \quad (5.3)$$

It has a clear physical explanation: for a given frequency at seismic exploration band, the seismic-sensitive permeability corresponds to the mesoscopic heterogeneities structure, which just causes the pore pressure to equilibrate in one cycle given by seismic frequency band f_s . If the reservoir permeability is not in the vicinity of seismic-sensitive permeability, the seismic attributes are not sensitive to the permeability variation. However, it is not easy to predict the seismic-sensitive permeability, since the average heterogeneity size is usually poorly determined.

5.7 Combined Effect of VTI Anisotropy and WIFF on Reflection Coefficients

One explicit assumption in our study is that we restrict our consideration to the case of isotropic medium. The presence of anisotropy will make the wave propagation characteristic in heterogeneous poroelastic medium more complicated. Here, we give a simple analysis regarding the impact of the VTI anisotropy on the poroelastic reflection.

Ruger (1997) showed that a vertical transversely isotropic term could be added to the Aki-Richards' equation using Thomsen's weak anisotropic parameters δ and ε :

$$R_{VTI}(\theta) = R_{is}(\theta) + \frac{\Delta\delta}{2} \sin^2 \theta + \frac{\Delta\varepsilon}{2} \sin^2 \theta \tan^2 \theta, \quad (5.4)$$

where $\Delta\delta = \delta_2 - \delta_1$, $\Delta\varepsilon = \varepsilon_2 - \varepsilon_1$; $R_{VTI}(\theta)$ is the anisotropic AVO response and $R_{is}(\theta)$ is the isotropic AVO response.

To facilitate the analysis, we can add a poroelastic term on the reflection coefficients as:

$$R_{VTI}(\theta, f) = R_{is}(\theta) + \frac{\Delta\delta}{2} \sin^2 \theta + \frac{\Delta\varepsilon}{2} \sin^2 \theta \tan^2 \theta + R_{flow}(\theta, f), \quad (5.6)$$

Remember that the anisotropy in underlying sandstone is usually much weaker than the overburden shale. This is especially true if the overburden shale is organic rich (Vernik et al., 1994; Bandyopadhyay, 2009; Yan et al., 2011). That is to say, we have both $\Delta\delta = \delta_2 - \delta_1 < 0$ and $\Delta\varepsilon = \varepsilon_2 - \varepsilon_1 < 0$. Therefore, when the reflection coefficient is positive, the VTI anisotropy weakens the seismic amplitude; when the reflection coefficient is negative, it enhances the amplitude. However, the poroelastic effect will enhance the seismic amplitude when the reflection coefficient is positive,

but it weakens the seismic amplitude when the reflection coefficient is negative. Hence, as illustrated in Figure 5.29, it is interesting to see that the anisotropy and WIFF have an opposite effect on seismic amplitude for the given geological scenario discussed here. The combined effects depend on both the extent of anisotropy and heterogeneity of the reservoir rocks. The quantitative evaluation of combined effect will be investigated in the future study.

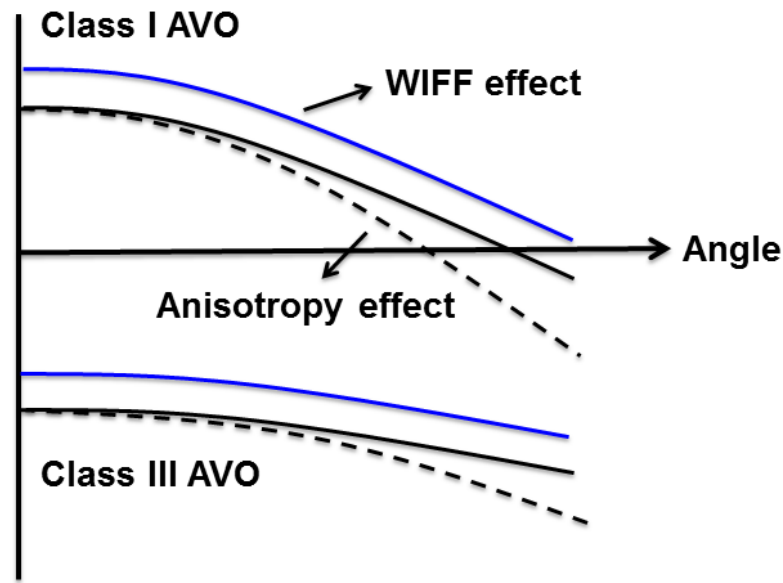


Figure 5.29. A schematic illustration of the VTI Anisotropy and WIFF impact on the reflection coefficients.

Nevertheless, several points should be discussed here:

- 1) The anisotropic effect is negligible at near incident angle, but the WIFF effect might be nonnegligible.
- 2) The anisotropic effect increases with an increase of incident angle, but the WIFF effect only increases slightly according to the previous analysis.

- 3) If the reservoir anisotropy is stronger than the overburden anisotropy, e.g. the unconventional organic-rich shale reservoirs, both the WIFF and anisotropy effect will influence the seismic amplitude in the same direction.

5.8 Discussion

In Chapter 4, we demonstrate the extent of phase shift is intimately related to the amount of attenuation ($1/Q$) contrast across the poroelastic contact. Here, we will discuss what factors decide the polarity of the phase shift, namely, phase advance or phase delay. First of all, as illustrated in Figure 5.30, the phase shifts due to effect of local flow and global flow always have an opposite trend. For example, for Model 1, the local flow yields a phase delay in the seismic frequency domain, while the global flow clearly gives rise to a phase advance in the ultrasonic frequency domain. The similar phenomenon is observed for the dispersion behavior of Model 3. Secondly, it is evident to see that the phase shift for Model 1 and Model 3 have an opposite trend. The Biot flow-induced phase shift can be explained by the equation of poroelastic reflection coefficients in Biot media (Bourbie et al., 1987).

$$R = \frac{1-Z}{1+Z} (1 + \theta_0) \exp(i \tan^{-1} \theta_0), \quad (5.6)$$

$$\theta_0 = \frac{Z^2 \sqrt{2} (m_1 - m_2)^2 \phi_1 \phi_2 \sqrt{\omega / \omega_1^c}}{1 - Z^2 g_1 + Z g_2 \sqrt{\omega_2^c / \omega_1^c}}, \quad (5.7)$$

where R indicates the reflection coefficients at normal incident angle in Biot media; ω_1^c and ω_2^c represent the characteristic frequency of the upper medium and lower

medium, respectively; and Z is the ratio of the acoustic impedance in the lower medium over that in the upper medium. Here, m can be expressed as:

$$m_i = \frac{\alpha_i M_i}{\lambda_i + 2\mu_i} (i = 1, 2), \quad (5.8)$$

where α and M are the coefficients of Biot theory (see Chapter 3).

It is clear that the phase angle is determined by θ_0 , in which the polarity is controlled by the impedance ratio as dictated in equation 5.8. In other words, the polarity of phase shift at normal incident angle is controlled by the polarity of elastic reflection coefficients. This explains why the phased shift caused by global flow shows an opposite trend for Model 1 and Model 3. It is believed that the phase shift generated by local flow is also controlled by impedance contrast across the interface. However, such a dependence on the impedance contrast for the phase shift caused by local flow is opposite to that caused by global flow. This also explains why we observe the phase-shift behavior of Class II AVO scenario is consistent with that of Class III AVO scenario in the frequency range when the sandstone impedance is smaller than the overburden shale impedance (Figure 5.4(b)). However, when the dispersion effect cause the impedance of sandstone exceeds the impedance of overburden shale, the phase-shift behavior of Class II AVO scenario is gradually in agreement with Class I AVO scenario (Figure 5.4(b)).

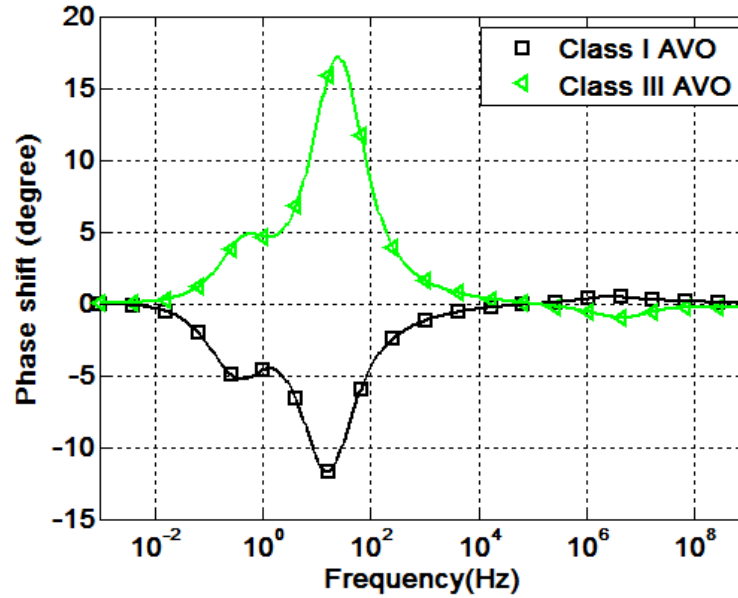


Figure 5.30. Phase-shift versus frequency for the geological scenario corresponding to Class 1 AVO (black square) and Class 3 AVO (green triangle).

It is well known that the AVO gradient information is strongly dependent on the V_p/V_s ratio. Therefore, the shear-wave dispersion characteristics play an important role in understanding the frequency-dependent AVO signatures. Shear-wave dispersion caused by global flow can be calculated on the basis of Biot's poroelastic wave propagation (Biot 1956a, 1956b; 1962). Despite the fact that S-wave dispersion and attenuation due to local flow has been experimentally observed (Batzle et al., 2006; Adam et al., 2006; Han and Yao, 2009) and numerical simulated (Masson and Pride, 2007; Rubino et al., 2009; Wenzlau et al., 2010; Quintal et al., 2012), physical mechanism standing behind it is not very clear yet. Many poroelastic models have been proposed to quantify P-wave attenuation in fully-saturated elastically heterogeneous media or partial-saturated media, however no analytical solution

concerning the S-wave attenuation is developed. In this study, to characterize the shear-wave dispersion caused by local flow, we use Mavko-Jizba relationship (Mavko and Jizba, 1991) to roughly estimate the shear modulus dispersion from the bulk modulus dispersion. The accurate description about the shear-wave dispersion in a heterogeneous porous composite should be investigated in the future.

The poroelastic seismic response is a combined product of source wavelet and poroelastic reflection. As we demonstrate in section 5, even sometimes the reflectivity show significant dispersion, the central frequency content is difficult to be shifted. Consequently, to facilitate the application of poroelastic reflection, it is better to look at the reflectivity spectrum rather than spectrum of seismic data. To achieve this goal, we can first de-convolve the seismic wavelet into the reflectivity series, and then perform spectral decomposition on those reflectivity series.

5.9 Conclusions

In the present work, we have extended our analysis from the classical AVO study to frequency and angle-dependent poroelastic reflectivity, thereby providing new insights for reservoir imaging and characterization. Our conclusion can be summarized as follows:

- 1) According to the spectral signatures of poroelastic reflection under different geological circumstances, we classify three types of amplitude-versus-frequency features: Class I AVF refers to low-frequency dim-out reservoirs;

Class II AVF refers to phase-reversal reservoirs; and Class III AVF refers to low-frequency bright-spot reservoirs.

- 2) . I further demonstrate that the AVO response at the interface is strongly impacted by the reflection dispersion behavior: the bright spot (Class III AVO) get brighter at lower frequency, the dim spot (Class I AVO) get dimmer at lower frequency, and the Class II AVO reservoir exhibit significant phase distortion in frequency domain.
- 3) Poroelastic effect due to WIFF does not change the AVO trend, but slightly diminishes the AVO gradient. More importantly, it makes the phase angle of seismic reflectivity vary with offset, while phase angle is considered to be constant for elastic reflection. For Class I and Class III AVO, the phase variation is small and generally increases with incident angle. For Class II AVO, a dramatic phase variation takes place from near offset to far offset.
- 4) We demonstrate that the poroelastic reflection can significantly affect the seismic responses. It not only influences the RMS amplitude of seismic wiggles, but also yields a noticeable phase shift compared with purely elastic seismic responses. This suggests an accurate seismic imaging and a quantitative seismic interpretation should be calibrated by the poroelastic effect. However, in most case, the central frequency of poroelastic seismic response is still controlled by source wavelet.
- 5) It is found that, for certain permeability ranges (10^{-3} D to 10^{-1} D), seismic amplitude can exhibit an almost linear relationship with permeability variation. For Class III AVO reservoir environment, high fluid mobility zones usually

enhance the seismic amplitude; whereas for Class I AVO reservoir environment, high fluid mobility zones weakens the seismic amplitude.

- 6) We suggest all detailed reservoir imaging and characterizations work, especially for highly heterogeneous or patchy-saturated reservoirs, should attempt to account for dispersion effect due to WIFF. Nevertheless, this is not an easy task in the real world because of the difficulty in prescribing appropriate physical parameters.

5.10 Acknowledgement

This work was sponsored by Fluids and DHI consortium of the Colorado School of Mines and University of Houston.

5.11 Reference

Adam, L., Batzle, M. and Brevik, I., 2006, Gassmann's fluid substitution and shear modulus variability in carbonates at laboratory seismic and ultrasonic frequencies: *Geophysics*, 71, F173-F183.

Aki, K., and P. G. Richards, 1980, *Quantitative Seismology: Theory and Methods*: W. H. Freeman & Co.

Bandyopadhyay, K., 2009, *Seismic Anisotropy: Geological Causes and Its Implications to Reservoir Geophysics*: Ph.D. Thesis, Stanford University.

Bourbié, T., O. Coussy, and B. Zinszner, 1987, *Acoustics of Porous Media*: Editions Technip.

- Castagna, J. P., and Backus, M. M., Eds., 1993, Offset dependent reflectivity: Theory and practice of AVO analysis: Society of Exploration Geophysics., Investigation in Geophysics. 8.
- Castagna, J. R., Swan, H. W., and Foster, D. J., 1998, Framework for AVO gradient and intercept interpretation: *Geophysics*, 63, 948–956
- Castagna, J. P., S. Sun, and R. W. Seigfried, 2003, Instantaneous spectral analysis: Detection of low-frequency shadows associated with hydrocarbons: *The Leading Edge*, 22, 120–127.
- Chakraborty, A., and D. Okaya, 1995, Frequency-time decomposition of seismic data using wavelet-based methods: *Geophysics*, 60, 1906–1916.
- Chapman, M. E., E. Liu, and X. Li, 2006, The influence of fluid-sensitive dispersion and attenuation on AVO analysis: *Geophysical Journal International*, 167, 89–105.
- Dasgupta, R., and Clark, R.A., 1998, Estimation of Q from surface seismic reflection data: *Geophysics*, 63, 2120–2128.
- Dutta, N. C., and H. Odé, 1983, Seismic reflections from a gas-water contact: *Geophysics*, 48, 148–162.
- Ebrom, D., 2004, The low frequency gas shadow on seismic sections: *The Leading Edge*, 23(8), 772.
- Goloshubin, G.M., Daley, T.M., and Korneev, V.A., 2001, Seismic low-frequency effects in gas reservoir monitoring VSP data, SEG Meeting: San Antonio, TX.
- Goloshubin, G., D. Silin, V. Vingalov, J. Takkand, and M. Latfullin, 2008, Reservoir permeability from seismic attribute analysis: *The Leading Edge*, 27, 376–381.

- Goloshubin, G., C. Vanschuyver, V. Korneev, D. Silin, and V. Vingalov, 2006, Reservoir imaging using low frequencies of seismic reflections: *The Leading Edge*, 62, 319–324.
- Gurevich, B., R. Ciz, and A. I. M. Denneman, 2004, Simple expressions for normal incidence reflection coefficients from an interface between fluid saturated porous materials: *Geophysics*, 69, 1372–1377.
- Han, D., and Q. Yao, 2009, Intrinsic seismic wave attenuation - tight gas sand example: Annual Report, Fluids/DHI Consortium.
- Jones, T. D., 1986, Pore fluids and frequency-dependent wave propagation in rocks: *Geophysics*, 51, 1939–1953.
- Korneev, V. A., G. M. Goloshubin, T.M. Daley, and D. B. Silin, 2004, Seismic low-frequency effects in monitoring fluid-saturated reservoirs: *Geophysics*, 69, 522–532.
- Masson, Y. J., and S. R. Pride, 2007, Poroelastic finite-difference modeling of seismic attenuation and dispersion due to mesoscopic-scale heterogeneity: *Journal of Geophysical Research*, 112, B03204.
- Müller, T. M., B. Gurevich, and M. Lebedev, 2010, Seismic wave attenuation and dispersion resulting from wave-induced flow in porous rocks-A review, *Geophysics*, 75, 75A147-75A164.
- O’Connell, R. J., and B. Budiansky, 1974, Seismic velocities in dry and saturated cracked solids: *Journal of Geophysical Research*, 79, 5412–5426.
- Ostrander, W.1., 1984, Plane-wave reflection coefficients for gas sands at nonnormal angles of incident: *Geophysics*, 49, 1637-1648.

- Partyka, G., J. Gridley, and J. Lopez, 1999, Interpretational applications of spectral decomposition in reservoir characterization: *The Leading Edge*, 18, 353–360.
- Ren, H., G. Goloshubin, and F. J. Hiltermann, 2009, Poroelastic analysis of amplitude-versus-frequency variations: *Geophysics*, 74, no. 6, O1–O8.
- Rubino, J. G., C. L. Ravazzoli, and J. E. Santos, 2009, Equivalent viscoelastic solids for heterogeneous fluid-saturated porous rocks: *Geophysics*, 74, no. 1, N1–N13.
- Rutherford, S. R., and Williams, R. H., 1989, Amplitude-versus-offset variations in gas sands: *Geophysics*, 54, 680–688.
- Rüger, A., 1997, P-wave reflection coefficients for transversely isotropic models with vertical and horizontal axis of symmetry: *Geophysics*, 62, 713–722.
- Quintal, B., H. Steeb, M. Frehner, S. M. Schmalholz, and E. H. Saenger, 2012, Pore fluid effects on S-wave attenuation caused by wave-induced fluid flow: *Geophysics*, 77, no. 3, L13–L23.
- Vernik, L., 1994. Hydrocarbon-generation-induced microcracking of source rocks: *Geophysics*, 59, 555–563.
- Wenzlau, F., J. B. Altmann, and T. M. Müller, 2010, Anisotropic dispersion and attenuation due to wave-induced fluid flow: Quasi-static finite element modeling in poroelastic solids: *Journal of Geophysical Research*, 115, B07204.

Chapter 6

Poroelastic Seismic Interpretation: A Real Case Study

6.1 Abstract

In this chapter, we present a field case study regarding the seismic reflection dispersion due to wave-induced fluid flow in a heterogeneous carbonate reservoir, offshore Brazil. We propose and implement a workflow to illuminate the poroelastic reflection characteristics from real seismic, by removing the background frequency trend that is attributed to both propagation effect of attenuation and tuning effect. We found that the poroelastic reflection from the interface of interest at the location of well A and well B exhibits considerably different frequency behavior. We explain that such a discrepancy is likely to be caused by the fact that the fluid mobility in the underlain grainstone at well A is remarkably different from that in the underlain packstone at well B. The case study here promises a solution to determine hydraulic properties from field seismic, which is often considered to be extremely challenging.

6.2 Introduction

The poroelastic reflection, representing primarily contrast of the poroelastic responses between individual layers, contains information about the dispersive and attenuative characteristics of the heterogeneous rocks. It consequently alters the amplitude, phase as well as frequency content of seismic wiggles. Understanding and interpreting poroelastic reflection signatures is of great interest, because they potentially convey the important

message about rock's fluid mobility and heterogeneity features, which cannot be gained from classical seismic interpretation on the basis of the elasticity.

In the past decades, the poroelastic reflection signatures such as “low frequency anomaly” already have been employed to interpret field data by correlating spectral anomalies to the presence of hydrocarbon reservoirs (e.g., Taner et al., 1979; Klimentos, 1995; Dasgupta and Clark, 1998; Maultzsch et al., 2003; Castagna et al., 2003; Ebrom, 2004; Rapoport et al., 2004; Korneev et al., 2004; Goloshubin et al., 2006; Tai, 2009). However, most of them are qualitative and empirical. The aim of the work reported here is to quantitatively understand and analyze the seismic reflection dispersion due to the wave induced fluid flow through a case study in a heterogeneous carbonate reservoir, Campos Basin, Offshore Brazil.

Since the poroelastic reflection is a function of frequency, it naturally comes up with using spectral decomposition methods (Chakraborty and Okaya, 1995; Partyka et al., 1999; Castagna et al., 2003), which break down the seismic signal into its component frequencies, to analyze the reflection dispersion signatures. However, it is not an easy task, because many factors can contribute to the seismic spectral anomalies. Two most prominent contributions probably come from the propagation effect of attenuation and tuning effect. In addition to influencing the seismic reflectivity at the poroelastic contact, attenuation can significantly affect the wave propagation by decaying the seismic amplitude and modifying the frequency and phase content of the propagating wavelet (Jones, 1986; Samec and Blangy, 1994). Moreover, the seismic amplitude can exhibit considerable variation with frequency due to the tuning effect (Widess, 1973). Hence, to

study the reflection dispersion due to WIFF on the basis of seismic spectral signatures, it is important to separate the seismic spectral variation due to the tuning and attenuation effect. In this chapter, we use the non-stationary convolution model (Clark, 1968; Margrave, 1998) to take into account the propagation effect of attenuation and tuning effect on the 1D seismic trace.

The detailed procedures to associate the poroelastic reflection to the reservoir rock and fluid properties are introduced in Chapter 4. However, when dealing with the real field data, the main difficulty lies in prescribing appropriate physical parameters, such as quantitative description of pore structure, heterogeneity features, fluid mobility information, and so on. Theoretically, all those physical parameters should be calibrated by core information, lab measurement, or well log measurement. But in the real world, it is often unrealistic to accurately obtain all the necessary parameters for the modeling or inversion work. In this study, we integrate surface seismic, well log data, core measurement, FMI imaging, petrophysical interpretation, and geological information to fully characterize the reservoir rock and fluid properties as much as possible.

The primary goal of this study is to demonstrate the methodology defined in Chapter 4 on a real case study. This chapter is organized as follows: First, we provide a descriptive overview of the geologic background and data sets. The reflection from the interface between the contrasting heterogeneous lithofacies will be also investigated; Then, to highlight the spectral anomaly in seismic data due to the poroelastic reflection, we perform the non-stationary convolution model to isolate the seismic dispersion signature that is caused by propagation effect of attenuation and tuning

effect; Finally, we theoretically simulate the poroelastic reflection coefficient to understand the seismic spectral signatures that are observed from the real seismic data.

6.3 Background and Reservoir Properties Description

6.3.1 Geological Background

The studied field is a Cretaceous carbonate reservoir located at the Campos Basin, which was formed during the breakup of Gondwana when Africa was separated from South America about 120 to 130 Ma (Mohriak and Dewey, 1987; Mohriak et al., 1987; Ogiesoba et al., 2011). The acknowledged depositional environments pertaining to the Cretaceous strata in the Campos Basin is a series of epi-continental rift lake basins during Barremian-Aptian time, with or without occasional marine incursions dependent on location. These incursions become important during a period of transition between rifting and drifting and a thick evaporitic unit was deposited in upper Aptian (115 Ma). As marine conditions became established in the Albian, deposition occurred mainly within a large carbonate platform/shelf comprising a number of sub-environments. Proximally, Albian carbonates are deposited from higher energy shallower-water conditions in the early Albian (112–108 Ma), to lower energy lagoonal or central platform settings by late Albian times (102–100 Ma) (Ogiesoba et al., 2011; Zhao et al., 2013). During the Cenomanian/Turonian (100–90 Ma), this platform was gradually drowned and marl and shale sediments took over in an outer-neritic environment. During the late Cretaceous, the deeper marine conditions became established, with the deposition of fine-grained clastics and turbidites in bathyal to abyssal environments.

In this study, emphasis will be placed on the seismic reflection between the Albian carbonate and the overburden marlstone. The near-angle stacked seismic data in the target zone is shown in Figure 6.1, and the observations from well A and B are displayed as a function of depth in the Figures 6.2 and 6.3, respectively. The oil accumulations are mainly trapped in the Albian carbonates formation, and underlies the marlstone formation. The interpreted horizons are highlighted on the seismic section as shown on Figure 6.1, in which the purple line indicates the reflection (peak amplitude) from the boundary between the overlying marlstone and underlying Albian carbonate. Our attention will be concentrated on the characteristic of this reflection at the location of well A as well as well B. As marked on the stacked seismic image, well A is located at the position of CDP 367, and well B is located at the position of CDP 211. The blue line refers the reflection (peak amplitude) at the interface between the porous upper limestone unit and the tight lower dolostone unit within the Albian carbonate formation.

6.3.2 Lithofacies and Heterogeneity Description

As displayed in Figure 6.2, the marlstone is found between the depths of 2611m to 2721m in the well A and 2350m to 2396m in the Well B. Marlstone represents lime-rich mud or muddy limestone which contains variable amounts of clays and silt. It is often related to the lacustrine/rift lake environments, which represent low energy, basinal setting with frequent occurrences of water fills.

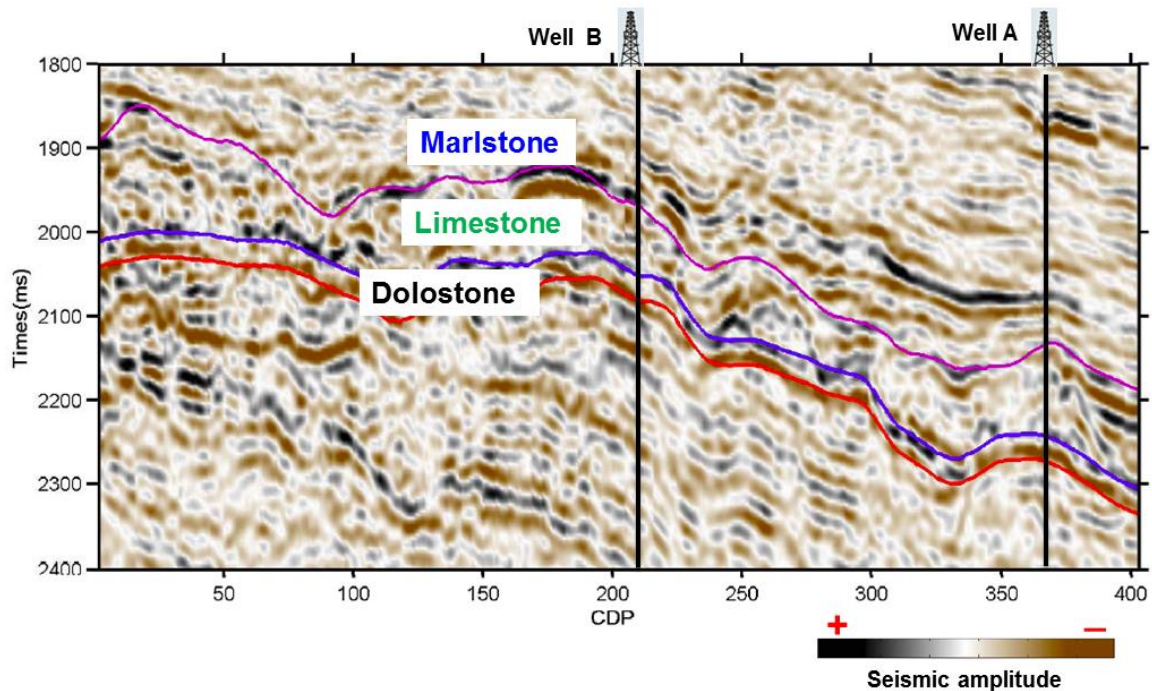


Figure 6.1. Section of the near-angle stacked seismic data. Well A is located at the position of CDP 367, and well B is located at the position of CDP 211.

The lithofacies delineation is based on the analysis of well log, interpretation of FMI imaging log, and core description. It is found that the limestone occurring in the Albian carbonate formation in well A (2721m-2883m) is quite different from that in well B (2396m-2547m), and this is mainly caused by the different depositional environment. The Albian limestone formation in the well A is more related to the higher energy setting, possibly at platform margins or highs where shoaling and spillover generated ooid and skeletal grainstone due to dominant influence of wave and/or current activity. By contrast, the depositional setting of limestone formation in the well B is more associated with the low energy environment, possibly in a lagoonal or central platform setting dominated by bedded to laminated sediments such as peloidal-bioclastic packstone. The core and

cuttings description also show that the pore fabric of Albian limestone unit of well A is grain-supported and lacks mud, while the grain size in Albian limestone unit of well B is much smaller and part of the intergrain spaces is filled with mud.

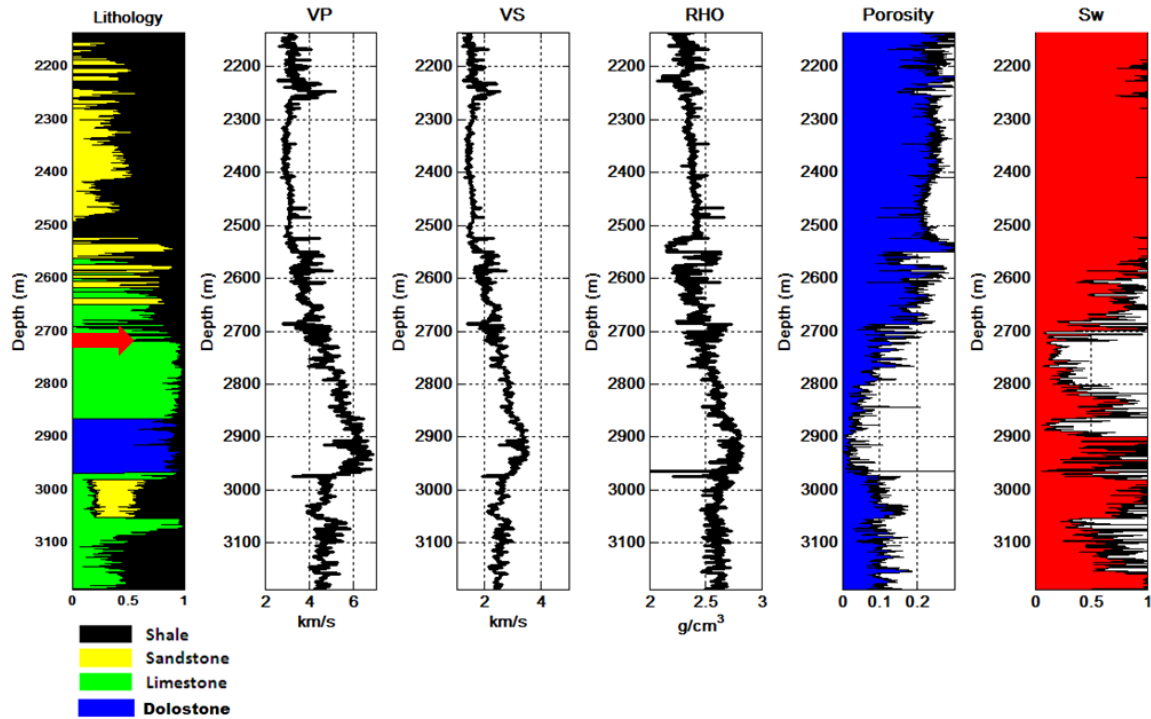


Figure 6.2. Log data from well A in the carbonate reservoir offshore Brazil provide by Maersk Oil. The lithology content, P-wave velocity, S-wave velocity, density, bulk porosity, and water saturation are displayed as a function of time converted from depth.

Additionally, based on the petrophysical interpretation of lithology content (most left column in the Figure 6.2 and 6.3), more shale content is found in the Albian limestone unit of well B. Instead, the Albian limestone unit in well A is much cleaner with less shale content. In order to facilitate the further analysis, according to the Dunham classification system for carbonate sedimentary rocks (Dunham, 1962), we define the

Albian limestone unit in well A as grainstone, and the Albian limestone unit in well B as packstone. The lithofacies correlation of well A and well B is displayed in Figure 6.4.

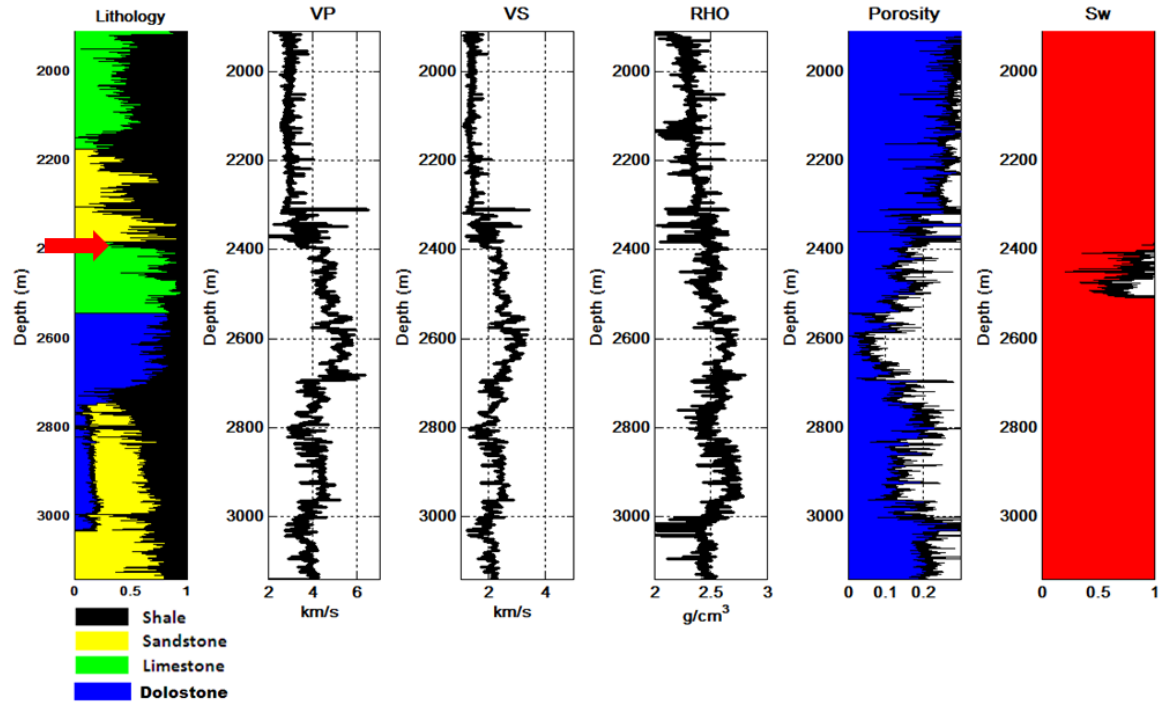


Figure 6.3. Log data from well B in the carbonate reservoir offshore Brazil provided by Maersk Oil. The lithology content, P-wave velocity, S-wave velocity, density, bulk porosity, and water saturation are displayed as a function of time converted from depth.

Geological observations from the FMI imaging log and core description suggest that the overburden marlstone and Albian carbonate reservoir are both highly heterogeneous, which are likely due to the extensive diagenesis after deposition, such as dissolution, compaction, dolomitization, and fracturing. The strong heterogeneities can be illustrated by the OMRI-CAST imaging log in Figure 6.5. Figure 6.5(a), (b), and (c) indicate that vuggy porosity and potentially open fractures frequently occur in the

marlstone formation. Another pronounced feature in the marlstone formation is that the carbonate mud is often mixed with siliciclastic, exhibiting extreme variation in terms of grain size and sediment origin. Figure 6.5(d), (e), and (f) correspond to the Albian limestone formation, in which we can observe complex fracture network and variable degrees of vuggy/moldic porosity. In general, for the heterogeneous porosity in carbonates, vugs or moldic porosities are often formed from dissolution processes by selectively dissolving grains composed of unstable minerals (Lucia, 1999; Zhao et al., 2013), and the fracturing is closely related to overburden and differential compaction, massive dissolution and collapse.

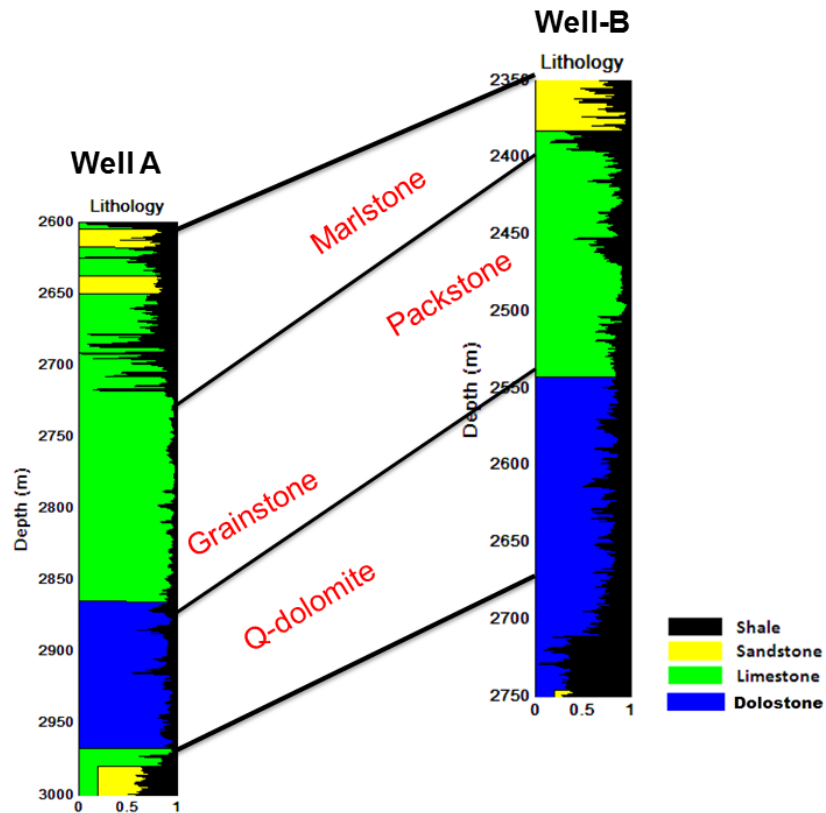


Figure 6.4. Lithofacies correlation between the well A and well B.

6.3.3 Fluid Mobility Characteristics

In a fully saturated rock, fluid mobility, which characterizes fluid's ability to move with the rock, is defined as (Bourbie et al., 1987; Batzle et al., 2006):

$$M = \frac{k}{\eta}, \quad (6.1)$$

where k is permeability and η is viscosity. For heterogeneous porous rocks, the fluid mobility often determines where the characteristic frequency to take place. For example, if fluid mobility is low, pore pressure takes a longer time to be equilibrated, and the characteristic frequency consequently shifts to lower frequency domain. The properties of fluids in reservoir rocks are listed in Table 6.1, where the viscosity is estimated based on the equations in Standing (1962) and McCain (1990).

Figure 6.6 illustrates a cross plot between permeability and total porosity for the Albian carbonate based on the core analysis. The ooid grainstone presents higher permeability (several hundreds md) for the given porosity, which is mainly due to the bigger grain size of the grain-dominated fabric. Instead, the muddy limestone has very lower permeability (most below 1md). This can be understood, because most of the porosities in the muddy limestone are micro-porosity and act as a kind of separate vugs (Lucia, 1999; Han, 2004), which contribute little to the effective permeability. The permeability-porosity cross-plot of packstone is sitting between the grainstone and muddy limestone and exhibit considerably scattering relationship, which is likely to be caused by the variable size and mud content in the packstone.

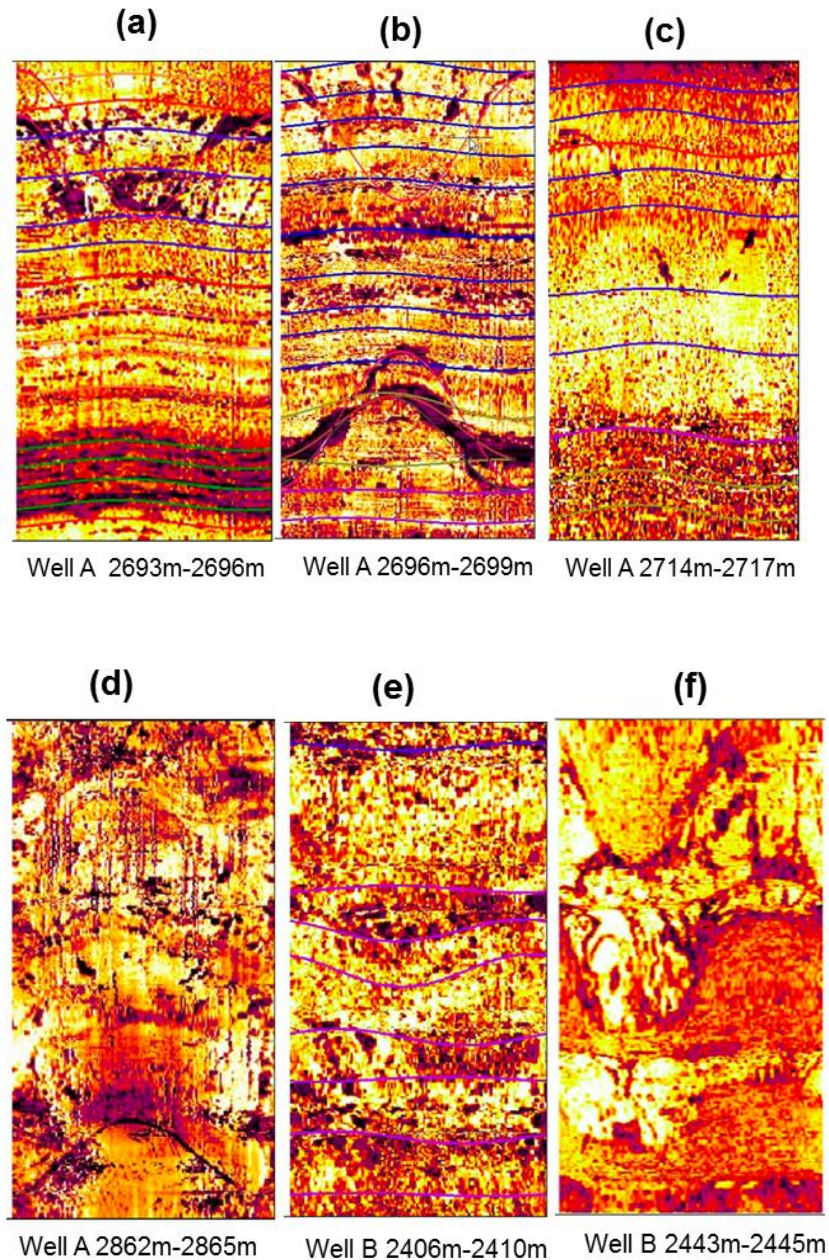


Figure 6.5. OMRI-CAST borehole images in well A and well B used to illustrate the strong heterogeneities in the overburden marlstone and underlain limestone. Here, (a), (b), and (c) correspond to the marlstone formation, and (c), (d), and (e) correspond to the limestone formation. The data and interpretation are provided by Maersk Oil.

Table 6.1. Properties of fluids in reservoir rock from lab measurements.

	Bulk Modulus (GPa)	Shear Modulus (GPa)	Density (g/cm ³)	API	Viscosity (cp)
Brine	3.0	0	1.05		
Oil	2.1	0	0.93	27	10.7

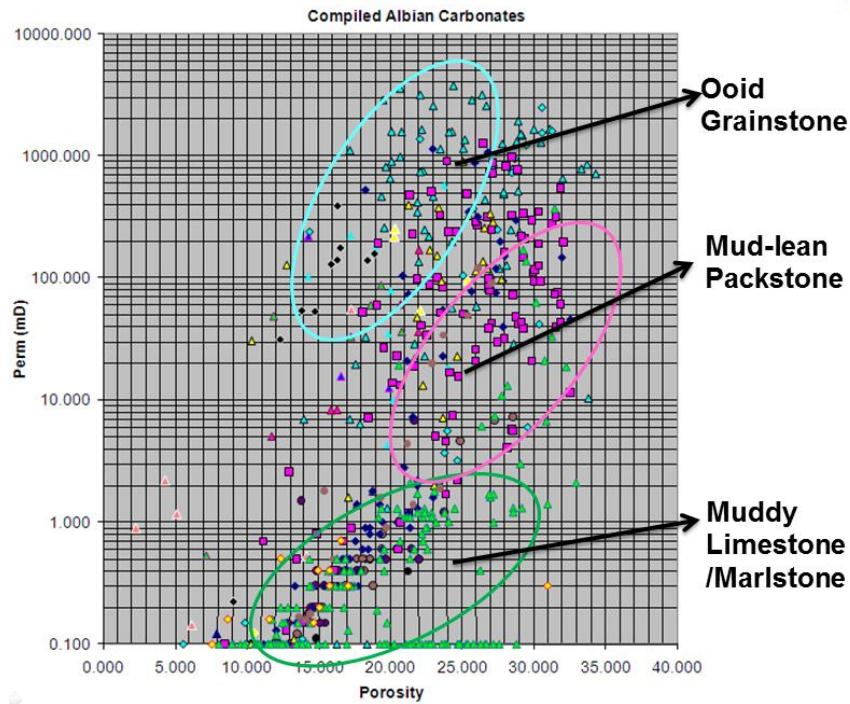


Figure 6.6. Permeability-porosity are cross-plotted for the Albian carbonate reservoir rocks. The permeability and porosity measurements are based on the core analysis.

6.4 Illuminating the Poroelastic Reflections from Real Seismic

In order to illuminate the poroelastic reflection from real seismic data, it is critical to separate the other factors that might affect the frequency behavior of the propagating

wavelet. Here, we assume that seismic frequency content is mainly influenced by the propagation effect of attenuation, tuning effect, and poroelastic reflection effect. Therefore, to bring out the poroelastic reflection effect from real seismic data, it is necessary to remove the background spectral contents that come from the propagation effect of attenuation and tuning effect. In this study, we use the non-stationary convolution model, which takes into account the propagation effect of attenuation and tuning effect, to compute the synthetic attenuated seismic trace. Then we compare the spectral of synthetic seismic with real seismic at interface of interest (the reflection at the interface between the overburden marlstone and Albian limestone). The workflow we propose to illuminate the seismic frequency characteristic caused by poroelastic reflection is summarized in Figure 6.7.

6.4.1 Non-stationary Convolution Model for Attenuated Seismic Trace

To compute the synthetic seismic from the velocity and density log, we use a convolution model that includes the source signature and the non-stationary effects of dissipation as predicted by the constant-Q model (Futterman, 1962; Kjartasson, 1979). Be aware that it does not explicitly accounts for multiples or stratigraphic filtering (. The non-stationary convolution model in the frequency domain (Margrave, 1998; Margrave and Lamourex, 2002) can be expressed as:

$$S(\omega) = W(\omega) \int_{-\infty}^{\infty} \alpha_Q(\tau, \omega) r(\tau) e^{i\omega[t-\tau]} d\tau , \quad (6.2)$$

where $W(\omega)$ is the fourier transform of wavelet; $r(\tau)$ is the reflectivity sequence and the constant-Q transfer function is:

$$\alpha_Q(\tau, \omega) = e^{-\omega\tau/2Q + iH(\omega\tau/2Q)}, \quad (6.3)$$

where the real and imaginary components in the exponential part are connected through the Hilbert transform H . As a consequence, the attenuated 1D seismic trace in time domain can be obtained after inverse Fourier transformation on equation 6.2.

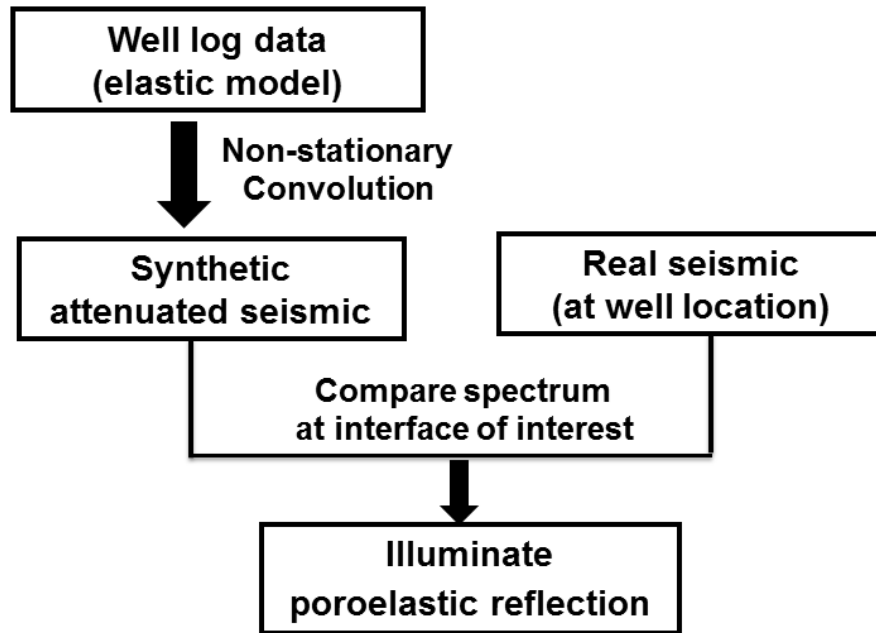


Figure 6.7. Schematic illustration of a workflow used to illuminate the poroelastic reflection from real seismic data.

6.4.2 Comparison of Spectral Signatures

A comparison of field near-angle stacked seismic at the location of well A, with synthetic seismic trace computed from log data, is illustrated in Figure 6.8. The synthetic seismic trace is created from a zero phase Ricker wavelet with central frequency 25 Hz. As expected, the real seismic data have a pretty good match with the synthetic seismograms; the strong reflections are especially well correlated. The elastic modeling result are in agreement with the visco-elastic modeling result when Q is 2000. However, small Q can cause a significant energy loss for seismic trace, especially when Q is 30 and 10. Figure 6.9 shows the spectral decomposition results for the field seismic data as well as the attenuated seismic trace. It turns out that the propagation effect of attenuation gradually shifts the overall trend of peak frequency to lower frequency domain with an increase of depth. We also notice that the shifting trend of peak frequency (highlighted in Figure 6.9 (a)) of real seismic matches best with the that of synthetic attenuated seismic trace (highlighted in Figure 6.9 (c)) with $Q=100$. It should be noted that the Q value employed here is considered to roughly represent the attenuation effect during wave propagation. As we can see, if Q is too high (e.g. =2000), there still exists considerable high frequency component in the deeper depth; if Q is too small (e.g. =30), the high frequency component decreases so sharply that the central frequency shifts to very low frequency domain in the deeper depth. Both of these are not consistent with what we observe in the field seismic. That is why we take $Q=100$ to roughly represent the attenuation effect during wave propagation. Accordingly, we compare the spectrum of real seismic data with the synthetic seismograms for the reflection event at the interface

of overburden marlstone with underlain Albian limestone, which ranges from 2.1-2.15s in the seismic trace. The difference of corresponding seismic spectral signatures between the field seismic trace and synthetic attenuated seismic trace is shown on Figure 6.10. Clearly, the attenuated seismic trace presents a peak frequency at 30Hz, while the peak frequency of field seismic takes place at around 20 Hz. We will demonstrate such salient discrepancy is likely to be caused by the reflection dispersion due to the wave-induced fluid flow.

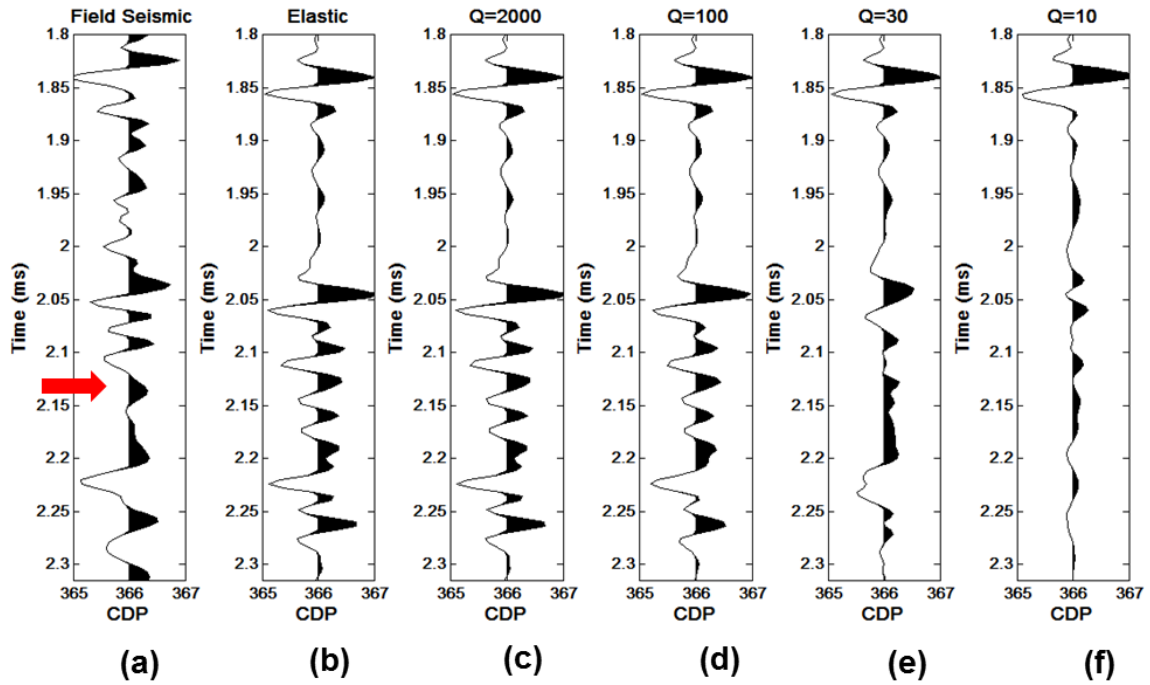


Figure 6.8. Comparisons of field seismic data at location of well A (CDP 366) with synthetic seismic trace at normal incident angle. (a) Field near-angle stacked seismic, (b) elastic, (c) $Q=2000$, (d) $Q=100$, (e) $Q=30$, and (f) $Q=10$.

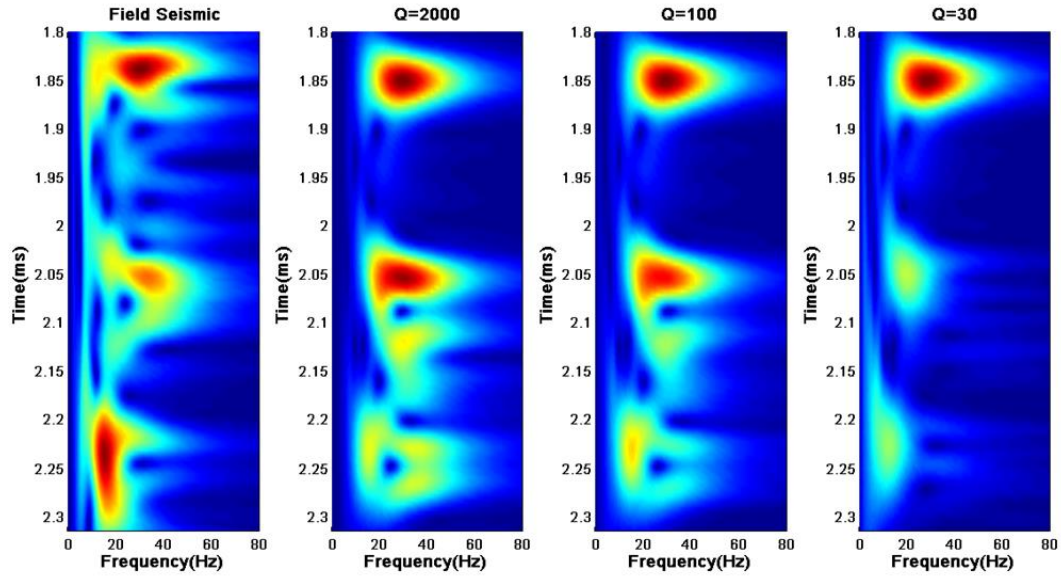


Figure 6.9. Spectral decomposition results of field seismic data at location of well A and attenuated seismic trace with different Q .

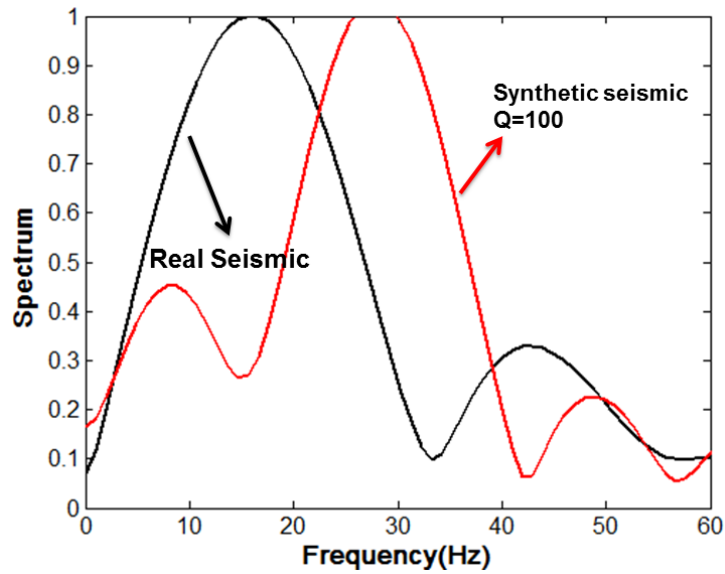


Figure 6.10. Comparison of normalized seismic spectral signatures at the interface of interest for: (a) real seismic at the location of well A, and (b) the attenuated seismic trace ($Q=100$).

Similarly, a comparison of the field seismic trace at well location B with synthetic seismic trace computed from well log B is illustrated in Figure 6.11. The corresponding seismic spectral signature is displayed in Figure 6.12. We can observe that the seismic energy is lost during the wave propagation, but the peak frequency does not exhibit an obvious shift. It is also can be noticed that the spectral signatures of field seismic match best with the attenuated seismic trace when the Q is 100. Nonetheless, as shown in Figure 6.13, we do not observe the evident seismic spectral anomaly at the depth around 1.95-2.0 s, which corresponds to the reflection at the interface between the overburden marlstone with the underlain packstone.

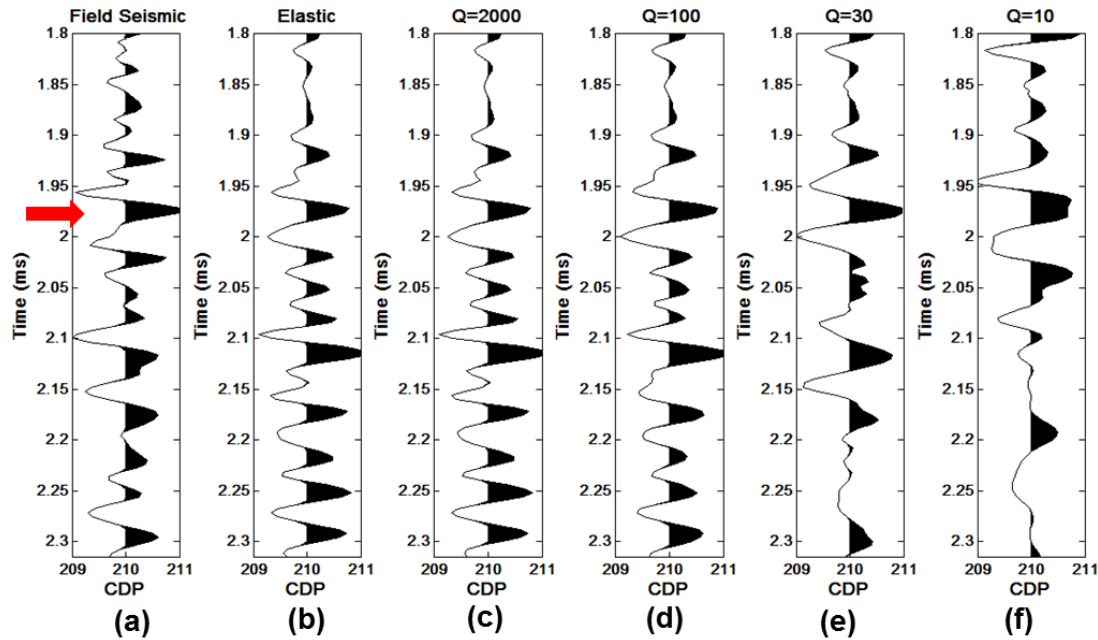


Figure 6.11. Comparisons of field seismic data at location of well B (CDP 211) with synthetic seismic trace at normal incident angle. (a) Field near-angle stacked seismic, (b) elastic, (c) $Q=2000$, (d) $Q=100$, (e) $Q=30$, and (f) $Q=10$.

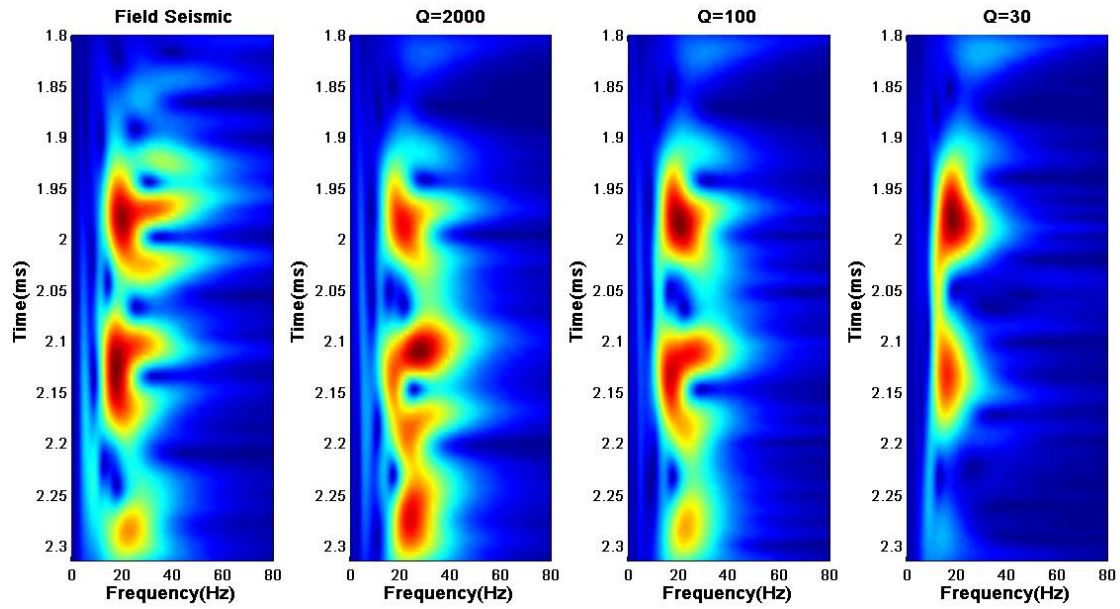


Figure 6.12. Spectral decomposition results of field seismic data at location of well B and attenuated seismic trace with different Q.

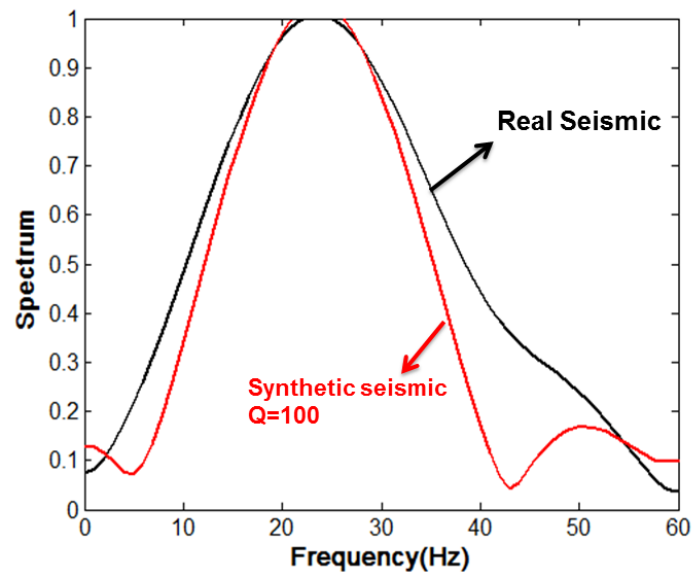


Figure 6.13. Comparison of seismic spectral signatures at the interface of interest for: (a) real seismic at the location of well B, and (b) the attenuated seismic trace (Q=100).

6.5 Poroelastic Seismic Reflection Analysis Based on Theoretical Modeling

In the last section, by comparing the spectral signature of field seismic data with the synthetic attenuated seismograms, we observe a significant low frequency shifting for the reflection of interest at the location of well A. However, no noticeable phase shift is observed for the case at the location of well B. The purpose of this section is to use poroelastic reflection to interpret and analyze this observation.

6.5.1 Velocity Dispersion and Attenuation Characteristics

In this section, we use double-porosity dual-permeability theory to model the velocity dispersion and attenuation characteristics for the overburden marlstone and underlain Albian carbonate. The minerals presenting in the rock are mixed using a Reuss-Voigt-Hill average. We begin with a solid rock matrix having the properties of this mixture, which can be referenced to the lithology interpretation of well log data. The mineral matrix in the upper medium (marlstone) consists of 60% calcite, 25% quartz, and 15% clay, and the mineral matrix in the lower medium (limestone) consists of 95% calcite and 5% clay. The values of the mineral bulk modulus K_s , shear modulus μ_s , and density ρ_s used in the computations are listed in Table 6.2.

The dry-rock elastic moduli are computed using the differentiated effective medium theory in carbonate rocks (Xu and Payne, 2009; Mavko et al., 2009; Zhao et al., 2013). In this case, the pore space is assumed to consist of a combination of stiff pores (matrix porosity) and soft pores (micro-fractures) with aspect ratio 0.15 and 0.005, respectively. Therefore, in the double-porosity dual-permeability system, the

host phase mainly consists of matrix porosity with lower permeability, while the heterogeneity phase includes the compliant micro-fractures and has higher permeability. The properties of the host phase (phase 1) and the heterogeneity phase (phase 2) for the marlstone and limestone are given in Table 6.3. Note that the only difference for the Albian limestone at well A and well B is the matrix permeability of the host phase. As previously illustrated in Figure 6.6, the Albian limestone unit in the well A is more accurately described as grainstone, and the permeability is consequently set as 200 md. By contrast, the Albian limestone unit in the well B is more associated with packstone, and the permeability is consequently set as 40 md. In addition, K_d and μ_d are the bulk and shear moduli of the drained rock frame; ρ_s is the density of mineral matrix; ϕ is the porosity; τ is the tortuosity parameter; κ is the permeability; V indicates the volume fraction of the heterogeneities. For the sake of simplicity, the geometry of the heterogeneity phase is assumed as penny-shaped, with a and ε representing the size and aspect ratio of heterogeneities, respectively. For the fluid properties (Table 6.4), K_f , ρ_f , and η are the bulk modulus, density, and viscosity of the pore fluid respectively.

Table 6.2. Mineral bulk modulus K_s , shear modulus μ_s , and density ρ_s used in the calculations (references in Mavko et al., 2009).

Mineral	K_s (GPa)	μ_s (GPa)	ρ_s (g/cm ³)
Calcite	76.8	32.0	271
Quartz	39	44	2.65
Clay	25	9	2.55

Table 6.3. The related parameters for rock frame properties of upper medium (marlstone) and lower medium (limestone).

Parameter	Rock frame properties			
	Upper (marlstone)		Lower (limestone)	
	Phase 1	Phase 2	Phase 1	Phase 2
K_d (GPa)	17.8	8.0	31.7	5.1
μ_d (GPa)	14.6	7.0	19.1	4.4
V	0.92	0.08	0.80	0.20
ϕ	0.04	0.05	0.12	0.15
κ (md)	0.1	100	200(A)/40(B)	1000
α (m)	0.05	0.05	0.05	0.05
ε	0.1	0.1	0.1	0.1
τ	2.4	2	2.4	2

Table 6.4. The related parameters for the pore fluid properties of upper medium (marlstone) and lower medium (limestone).

Parameter	Pore fluid properties	
	Upper (marlstone)	Lower (limestone)
K_f (GPa)	3.0	2.5
ρ_f (kg/m ³)	1.05	1.0
η (cP)	5	10

The calculated frequency-dependent fast P-, slow P-, and shear-wave velocity and attenuation for the lithology to be investigated are shown in Figures 6.14, 6.15, and 6.16, respectively. We observe that the three lithofacies to be investigated all show significant dispersion and attenuation. The considerable velocity increase found at the

lower frequency range corresponds to the dispersion effect due to the mesoscopic flow, while the slight ramp at the ultrasonic frequency corresponds to the Biot flow-induced dispersion effect. The transitional frequency of the overburden marlstone, underlain grainstone at well A, and underlain packstone at well B differs from each other. This is mainly caused by the distinct differences of fluid viscosity and permeability among the three lithofacies. As expected, the velocity dispersion effect and wave attenuation due to mesoscopic flow are much higher than that induced by Biot flow. Moreover, the modeling velocity at high frequency is generally in agreement with the observed well logging data, suggesting that the modeling study reflects the realistic elastic properties of the reservoir rocks to a certain degree.

6.5.2 Seismic Reflection Dispersion Analysis

Fast PP normal reflection coefficient for the interface of interest at the location of well A and well B is plotted against frequency as shown in Figure 6.17. The seismic reflectivity dispersion occurring at lower frequency corresponds to the mesoscopic flow, while the reflection dispersion taking place at higher frequency is caused by the Biot flow. It is found that the seismic reflection exhibits a significant dispersion effect at the interface of overburden marlstone and underlain grainstone at the position of well A. However, the seismic reflection dispersion effect is mitigated for the interface of overburden muddy limestone and underlain packstone at the position of well B. Such a discrepancy is mainly attributed to the difference of characteristic frequency between the grainstone and packstone.

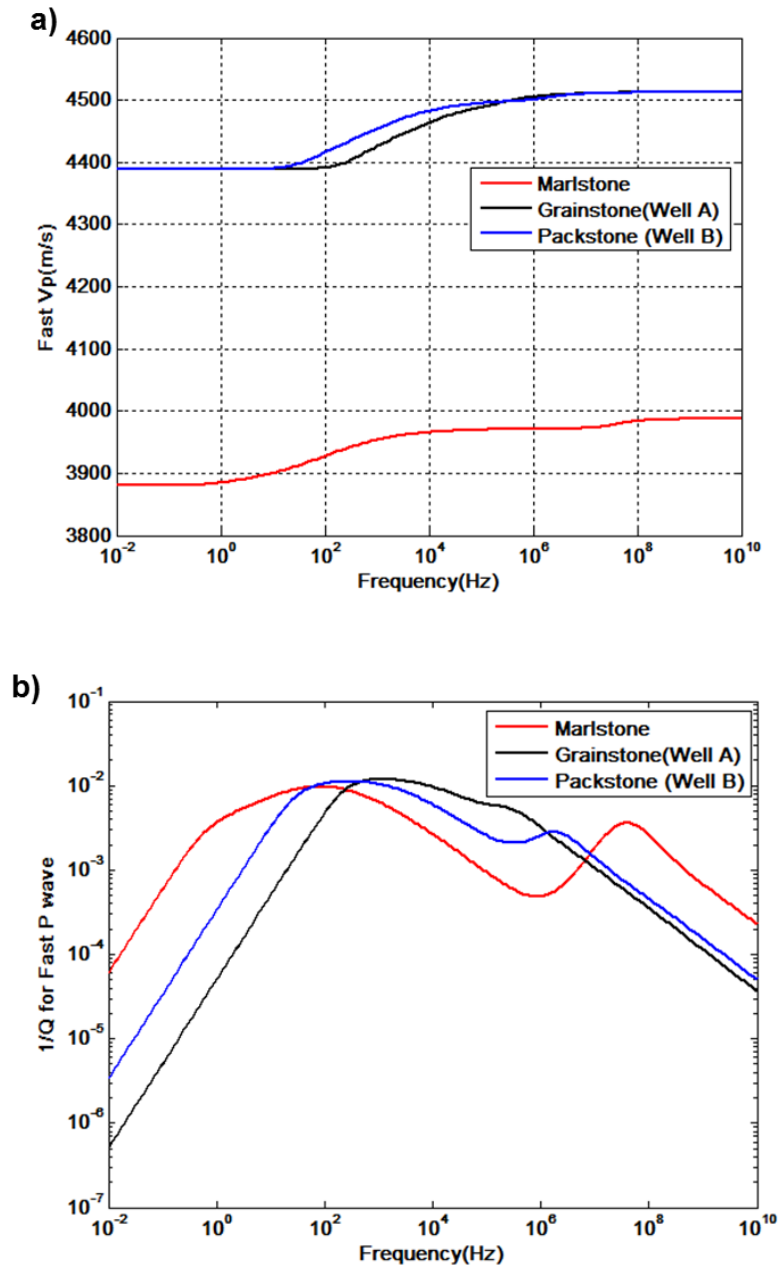


Figure 6.14. (a) Phase velocity dispersion (b) Attenuation of the effective fast P-wave for the overburden muddy limestone, the underlain grainstone at well A, and the underlain packstone at well B.

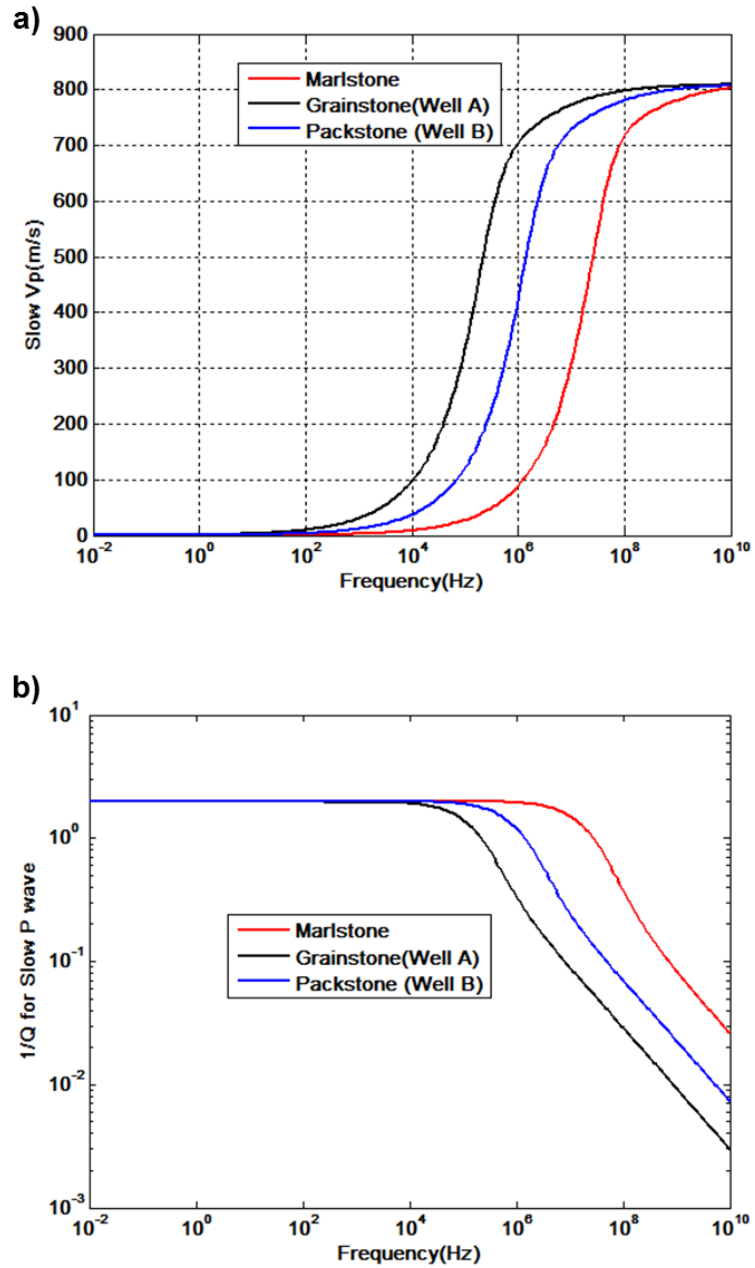


Figure 6.15. (a) Phase velocity dispersion (b) Attenuation of the effective slow P-wave for the overburden muddy limestone, the underlain grainstone at well A, and the underlain packstone at well B.

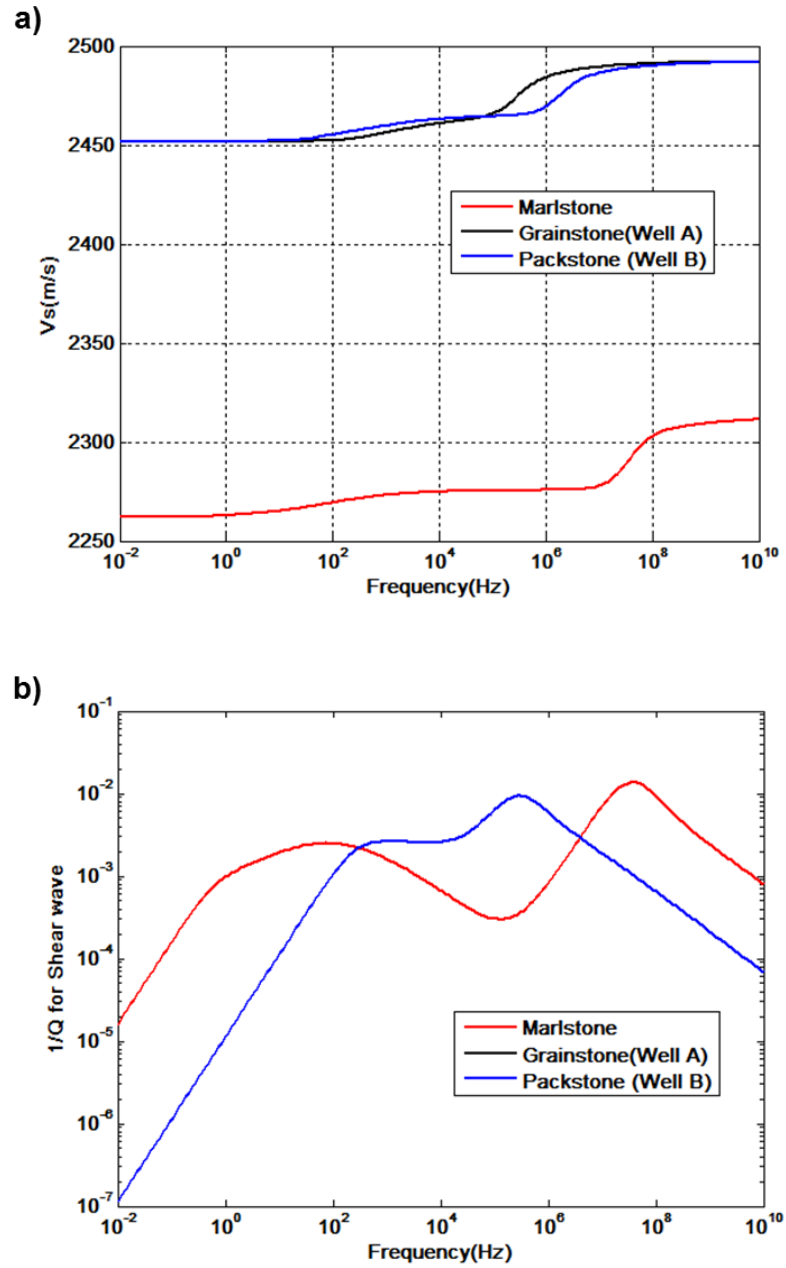


Figure 6.16. (a) Phase velocity dispersion (b) Attenuation of the effective shear-wave for the overburden muddy limestone, the underlain grainstone at well A, and the underlain packstone at well B.

The amplitude-versus-angle relationship at the seismic exploration band is illustrated in Figures 6.18 and 6.19, respectively. Clearly, from 10 Hz to 50 Hz, seismic reflection at the interface of marlstone and grainstone (at well A) presents an evident decrease due to the wave-induced fluid flow. However, negligible dispersion effect can be observed at the interface of marlstone and packstone (at well B). Consequently, based on the spectrum of the seismic data before the interface of interest (time window is around 60ms) and the modeling poroelastic reflection, we can compute the spectrum signature of the interface of interest. The results are displayed on Figures 6.20 and 6.21, respectively. It turns out that the spectrum of poroelastic modeling is roughly in agreement with that of real seismic at both well A and well B. Although the curve shape of the poroelastic reflection spectrum is still different from that observed from the field seismic, the central frequency shifting trend shows considerable consistence. We believe that this likely explains the seismic spectral signature differences observed from the interface of interest at well A and well B.

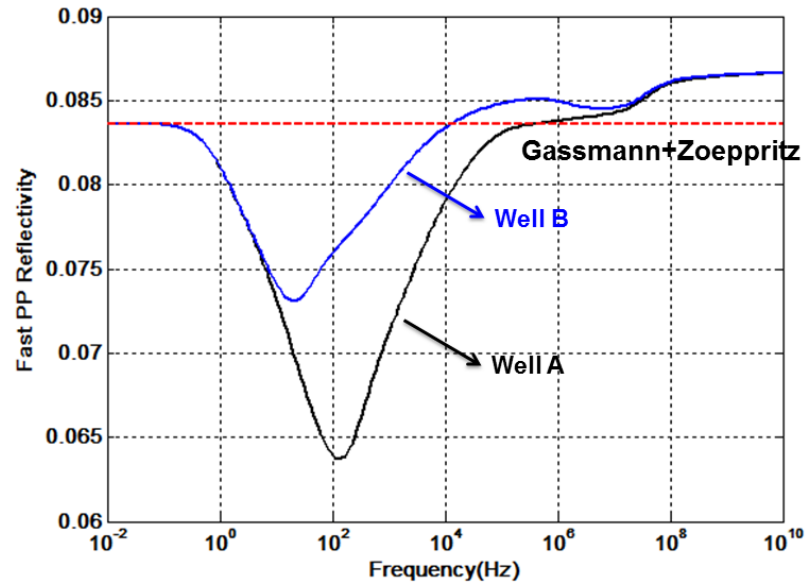


Figure 6.17. Fast PP reflectivity for the interface of interest at the position of well A and well B as a function of frequency at normal incidence angle. The dashed line indicates PP reflection coefficients computed based on Zoeppritz equation.

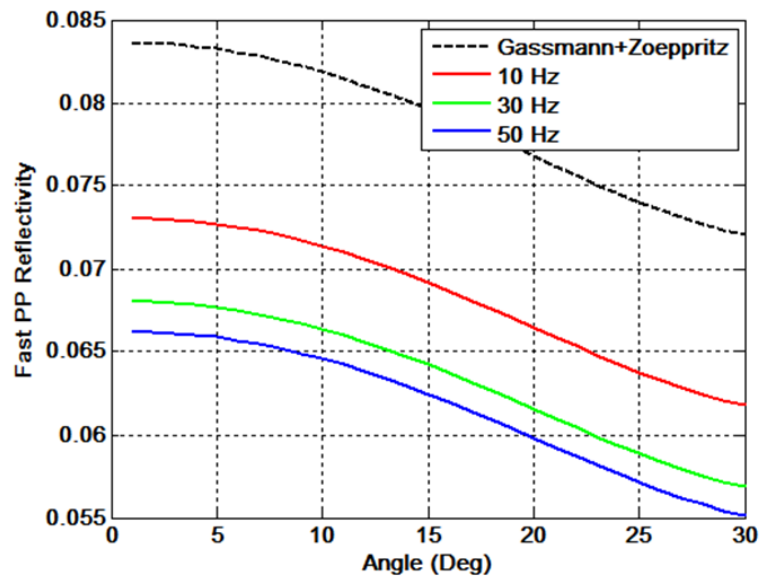


Figure 6.18. Fast PP reflectivity for the interface of interest at well A as a function of incident angle with different frequency in the seismic exploration band.

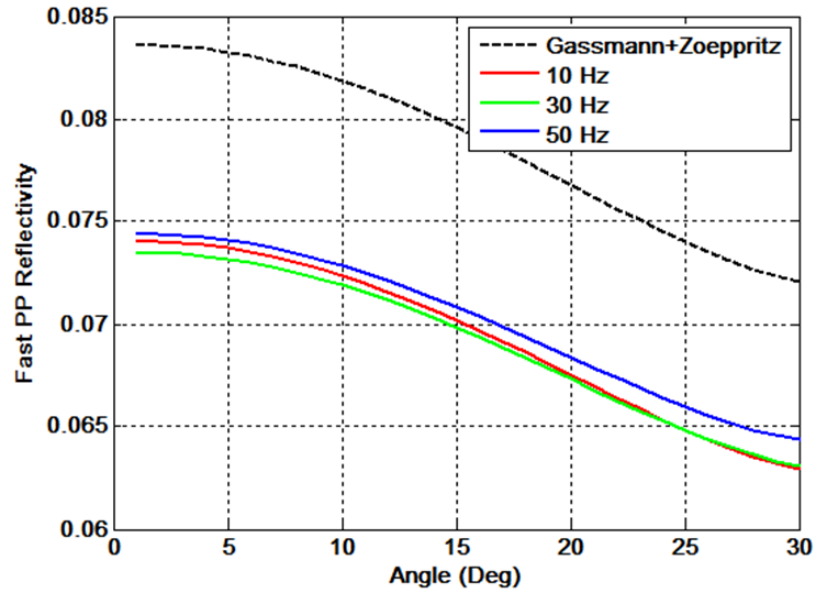


Figure 6.19. Fast PP reflectivity for the interface of interest at well B as a function of incident angle with different frequency in the seismic exploration band.

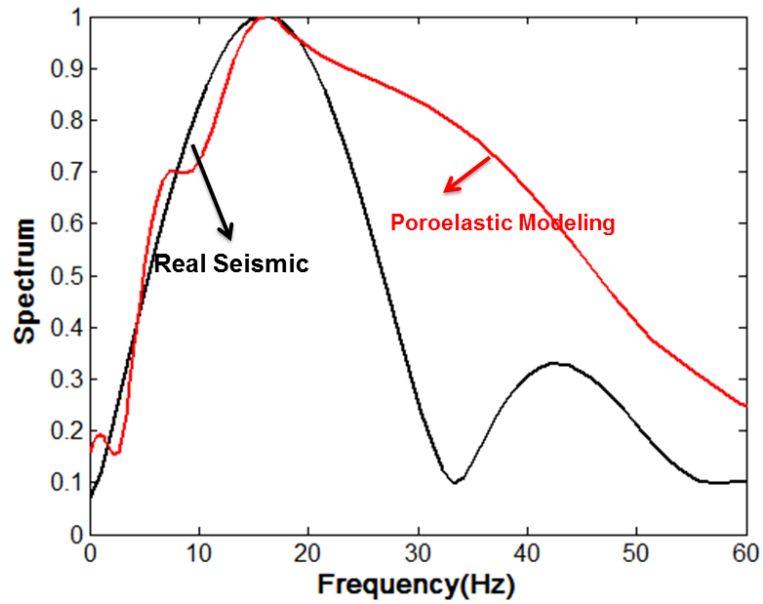


Figure 6.20. A comparison of normalized seismic spectral signatures at the interface of interest between real poroelastic modeling seismic at the location of well A.

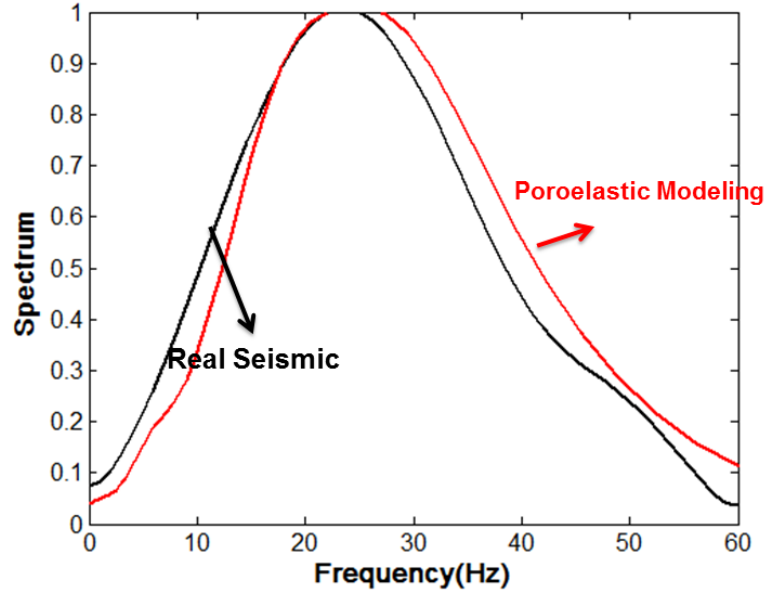


Figure 6.21. A comparison of normalized seismic spectral signatures at the interface of interest between real poroelastic modeling seismic at the location of well B.

6.6 Discussion

The seismic reflection at the interface of overburden limestone with underlain Albian limestone presents low-frequency bright spot at well A, but not exhibit frequency anomaly at well B. Based on our analysis, such a discrepancy is mainly caused by the different characteristic frequency range between the overburden and underlain lithology. As we know, the characteristic frequency, where the maximum loss due to mesoscopic flow occurs, can be expressed as:

$$f_c = \frac{k}{\phi L^2} \frac{K_f}{\eta}. \quad (6.4)$$

Here, L indicates the characteristic length of heterogeneity and is a function of α . In general, the porosity, fluid bulk modulus, and fluid mobility (k/η) can be quantified or roughly estimated from well log or lab measurement based on the geological understanding of the reservoir properties. However, the heterogeneity size which is often poorly determined from the geological observation can significantly influence the characteristic frequency range and consequently affect the seismic reflection dispersion signatures. Be aware that the theoretical modeling we perform here is not to exactly match the spectral signature of real field seismic with modeling poroelastic reflection, but to give insights on how the reservoir properties like fluid mobility alter the frequency contents of seismic reflection.

As we demonstrated in the section 3, understanding and interpretation of seismic reflection dispersion due to wave induced fluid flow is strongly dependent on how to bring out the poroelastic reflection from field seismic. Nonetheless, in addition to the attenuation, tuning effect, and poroelastic reflection that typically cause the variation of frequency behavior in seismic data, many other factors can also affect the seismic frequency contents, such as geological structure, multiples, converted waves, and improper stacking. In this study, we assume all those other factors do not play an important role in influencing the seismic spectral signatures. Besides, here I am only concerned with the effect of intrinsic attenuation on reflection dispersion signatures. However, the observed field seismic reflections may include both the contribution of intrinsic attenuation and scattering attenuation due to the presence of extensive heterogeneities. At the present time, the techniques that can reliably separate the total

inferred loss into scattering and intrinsic portions are generally not available (Pride et al., 2004).

Note that the seismic data we use is near-angle stacked gather. This is because we want to minimize the propagation effect due to attenuation. In general, far offset suggests more seismic amplitude decaying and more distortions for the seismic wavelet. The problem will therefore get more complicated. Additionally, the constant-Q model we employ to account for the effect of attenuation during wave propagation is independent of frequency, while this is in conflict with the frequency-dependent Q when we calculate the poroelastic reflection. The former plays an important role during wave propagation while the latter takes effect on the poroelastic interface. Theoretically, they should be consistent with each other. Nonetheless, for the sake of simplicity, we use the constant-Q model to account for the propagation effects of attenuation.

All those factors may potentially bring additional ambiguities for the poroelastic reflection interpretation. For potential future applications, some specific processing technologies to preserve the frequency contents of seismic data and illuminate the poroelastic reflection need to be developed.

6.7 Conclusions

To illuminate the poroelastic reflection characteristics from real seismic, we have compared the spectral signature of field seismic with the synthetic seismic that takes into account the propagation effect of attenuation and tuning effect. It is found that the central

frequency of seismic reflection from the boundary of overburden marlstone and underlain limestone shifts to the lower frequency domain at the location of well A, while the case at the location of well B does not exhibit noticeable departure. We attribute such discrepancy to the distinct difference of fluid mobility between grainstone at well A and packstone at well B. We demonstrate that fluid mobility can significantly affect the poroelastic reflection signatures. In this case, the high fluid mobility in the reservoir rocks can enhance the seismic amplitude in the low frequency domain, while for the low fluid mobility reservoir rocks, we do not observe appreciable change of seismic amplitude in the exploration band. The work reported here leaves open the possibility of indicating reservoir quality from dissipation-related seismic attributes.

6.8 Acknowledgement

We thank Maersk oil for permission to use the data. Special thanks also go to Geoscience Team of Maersk oil Houston Inc for the seismic, well log interpretation and core description.

6.9 Reference

Bourbié, T., and A. Gonzalez-Serrano, 1983, Synthetic seismograms in attenuating media: *Geophysics*, 48, 1575–1587.

Bourbié, T., and A. Nur, 1984, Effects of attenuation on reflections: Experimental test: *Journal of Geophysical Research*, 89, 6197–6202.

Clark, G. K. C., 1968, Time-varying deconvolution filters: *Geophysics*, 33, 936-944.

Castagna, J. P., S. Sun, and R. W. Siegfried, 2003, Instantaneous spectral analysis: Detection of low-frequency shadows associated with hydrocarbons: *The Leading Edge*, 22, 120–127.

Chakraborty, A., and D. Okaya, 1995, Frequency-time decomposition of seismic data using wavelet-based methods: *Geophysics*, 60, 1906–1916.

Dunham, R. J., 1962, Classification of carbonate rocks according to depositional texture: in W. E. Ham, eds., *Classification of Carbonate Rocks*: American Association of Petroleum Geologists Memoir, 108-121.

Futterman, W. I., 1962, Dispersive body waves: *Journal of Geophysical Research*, 67, 5279–5291.

Han, D., 2004, Velocity of carbonate rocks: Annual Report, Rock Physics and Fluid Consortium.

Kjartansson, E., 1979, Constant Q-wave propagation and attenuation: *Journal of Geophysical Research*, 84, 4737-4748.

Lucia, F. J., 1999, *Carbonate Reservoir Characterization*: New York, Springer-Verlag.

Margrave G. F., 1998, Theory of nonstationary linear filtering in the Fourier domain with application to time-variant filtering: *Geophysics*, 63, 244-259.

Margrave, G. F. and Lamoureux, M. P., 2002, Gabor deconvolution: CREWES Annual Research Report, 13.

McCain, W. D., 1990, Properties of Petroleum Fluids, 2nd ed.: PennWell Publishing Company, Tulsa , Oklahoma.

Mohriak, W. U., and J. F. Dewey, 1987, Deep seismic reflectors in the Campos basin, offshore Brazil: *Geophysical Journal of the Royal Astronomical Society*, 89, 133–140.

Mohriak, W. U., G. D. Karner, and J. F. Dewey, 1987, Subsidence history and tectonic evolution of the Campos basin, offshore Brazil (abs.): *American Association of Petroleum Geologists Bulletin*, 71, 594

Ogiesoba, O. C., W. Wright, F. Wang, M. V. Popini, M. P. Franco, A. T. Lourenco, and G. B. D. da Silva, 2011, Seismic conditioning and attenuation of high-angle coherent noise in a mixed carbonate and siliciclastic setting, Campos Basin, offshore Brazil: A case study: *Geophysics*, 76, no. 5, B199–B212.

Odebeatu, E., J. Zhang, M. Chapman, E. Liu, and Y. Li, 2006, Application of spectral decomposition to detection of dispersion anomalies associated with gas saturation: *The Leading Edge*, 25, 206–210.

Partyka, G., J. Gridley, and J. Lopez, 1999, Interpretational applications of spectral decomposition in reservoir characterization: *The Leading Edge*, 18, 353–360.

Pride, S. R., J. G. Berryman, and J. M. Harris, 2004, Seismic attenuation due to wave-induced flow: *Journal of Geophysical Research*, 109,B01201.

Samec, P.,and Blangy, 1. P.,1992, Viscoelastic attenuation, anisotropy and AVO: *Geophysics*, 57, 441-450.

Standing, M. B., 1962, Oil systems correlations: in Frick, T. C., ed., Petroleum Production Handbook, Volume II: McGraw-Hill Book Co.

White, J. E., 1965, Reflections from lossy media: The Journal of the Acoustical Society of America, 38, 604–607.

Widess, M.B., 1973, How thin is a thin bed?: Geophysics, 38, 1176-1180.

Tai, S., 2009, Analysis of Frequency Characteristics of Seismic Reflections in Thin Layer Zone: Methods and Applications: Ph.D. Thesis, University of Houston.

Zhao, L., Nasser, M. and Han, D., 2013, Quantitative geophysical pore type characterization and geological implications in carbonate reservoir: Geophysical Prospecting, 61(4), 827-841.